TIME-FREQUENCY ENTANGLED TWO-PHOTON STATES AND MEASUREMENTS

by

SOFIANE MERKOUCHE

A DISSERTATION

Presented to the Department of Physics
and the Division of Graduate Studies of the University of Oregon
in partial fulfillment of the requirements
for the degree of
Doctor of Philosophy

June 2022

DISSERTATION APPROVAL PAGE

Student: Sofiane Merkouche

Title: Time-Frequency Entangled Two-Photon States and Measurements

This dissertation has been accepted and approved in partial fulfillment of the requirements for the Doctor of Philosophy degree in the Department of Physics by:

Michael G. Raymer	Chair
Brian J. Smith	Advisor
David J. Wineland	Core Member
Timothy Cohen	Core Member
Andrew H. Marcus	Institutional Representative

and

Krista Chronister	Vice Provost for Graduate Studies

Original approval signatures are on file with the Division of Graduate Studies of the Univeristy of Oregon.

Degree awarded June 2022

DISSERTATION ABSTRACT

Sofiane Merkouche

Doctor of Philosophy

Department of Physics

June 2022

Title: Time-Frequency Entangled Two-Photon States and Measurements

Quantum entanglement is arguably the one feature that decisively distinguishes quantum from classical physics, and thus plays a crucial role both in understanding the fundamental nature of reality, and in providing advantages over classical protocols in the most promising applications of quantum physics. Pairs of photons entangled in the various degrees of freedom of the light field are readily available and well-studied as a platform for quantum fundamentals and applications. However, the inherently multimode nature of optical entanglement has yet to be fully explored and harnessed, particularly when it comes to quantum measurements which project onto entangled states. In this dissertation we describe a proof-of-principle experiment which takes advantage of the high-dimensional time-energy entanglement of photons to herald a multitude of Bell states. In addition, we give a theoretical model for using the nonlinear optical effect of sum-frequency generation to implement projective measurements onto high-dimensional

entangled states, and propose an experimental platform to test some of the key features of this model. The work presented here serves as an important step to complete the toolkit for using high-dimensional entanglement for quantum information science.

This dissertation contains previously published and unpublished material.

CURRICULUM VITAE

NAME OF AUTHOR: Sofiane Merkouche

GRADUATE AND UNDERGRADUATE SCHOOLS ATTENDED:

University of Oregon, Eugene, OR
University of Nevada, Las Vegas, NV

DEGREES AWARDED:

Doctor of Philosophy, Physics, 2022, University of Oregon
Bachelor of Science, Physics, 2014, University of Nevada, Las Vegas
Bachelor of Arts, Music, 2014, University of Nevada, Las Vegas

AREAS OF SPECIAL INTEREST:

Quantum optics, quantum information, quantum entanglement

PROFESSIONAL EXPERIENCE:

Graduate Research Assistant, University of Oregon, 2015-2022

Energy Analyst, SolarCity, 2014-2015

Undergraduate Research Assistant, University of Nevada, Las Vegas, 2013-2014

Academic Tutor, University of Nevada, Las Vegas, 2007-2012

GRANTS, AWARDS AND HONORS:

Promising Scholars Award, University of Oregon, 2015

Tutor of the Year Award, University of Nevada, Las Vegas, 2011

PUBLICATIONS:

Merkouche, S., Thiel, V., Davis, A. O. C., and Smith, B. J. "Heralding Multiple Photonic Pulsed Bell Pairs via Frequency-Resolved Entanglement Swapping", *Phys. Rev. Lett.* **128**, 063603 (2022).

Merkouche, S., Thiel, V., and Smith, B. J. "Spectrally resolved four-photon interference of time-frequency-entangled photons", *Phys. Rev. A* **105**, 023708 (2022).

Merkouche, S., Thiel, V., and Smith, B. J. "Positive operator-valued measure for two-photon detection via sum-frequency generation", *Phys. Rev. A* **103**, 043711 (2021).

Kühn, B., Vogel, V., Thiel, V., **Merkouche, S.**, and Smith, B. J., "Gaussian versus Non-Gaussian Filtering of Phase-Insensitive Nonclassicality", *Phys. Rev. Lett.* **126**, 173603 (2021).

Landes, T., Allgaier, M., **Merkouche, S.**, Smith, B. J., Raymer, M. G., and Marcus, A. H., "Experimental feasibility of molecular two-photon absorption with isolated time-frequency-entangled photon pairs", .Phys. Rev. Research **3**, 033154 (2021).

Raymer, M. G., Landes, T., Allgaier, M., **Merkouche, S.**, Smith, B. J., and Marcus, A. H., "How large is the quantum enhancement of two-photon absorption by time-frequency entanglement of photon pairs?", *Optica* **8**, 757-758 (2021).

Landes, T., Raymer, M. G., Allgaier, M., **Merkouche, S.**, Smith, B. J., and Marcus, A. H., "Quantifying the enhancement of two-photon absorption due to spectral-temporal entanglement", *Opt. Express* **29**, 20022-20033 (2021).

ACKNOWLEDGEMENTS

I would like to thank first and foremost my advisor, Dr. Brian Smith, who has been an invaluable mentor, inspiration, and friend throughout my time as a PhD student. Your extensive breadth and depth of knowledge of physics and optics have been a guiding light, and your work-hard, play-hard approach has made this challenging journey one of growth and enjoyment. I would like to thank to an equal extent my collaborator and other mentor Valérian "Dr. Val" Thiel. Your wizardry in the lab, your wit, and your French "je ne sais quoi" are dearly missed by all in the group. I will miss working with the two of you and I genuinely hope there are future chances for reconnecting.

I would not have made it this far without the guidance of Dr. Michael Raymer, who has been, for good reason, a teacher not only to me, but probably to half the people I have come to interact with in this field. I am lucky to have had the opportunity to learn from you directly. Dr. Markus Allgaier, Matthew Brown, Sarah Ashby, Tiemo Landes, Amy Soudachanh, Mostafa El Demery, Clark Embleton, Jack Lichtmann, Kevin Eckrosh, it really is an amazing group we have. I have learned from each and every one of you, and I hope we continue to grow and achieve great things.

Finally, I would like to thank all of my amazing friends and family who make me realize every day how lucky I am to have their love and support. They say, "May your acknowledgments section always be too small to hold all your loved ones", and that couldn't be more true for me. Thank you all.

I dedicate this dissertation to my parents, Karim and Karima, without whose love and support my success would not be possible.

TABLE OF CONTENTS

LIST OF FIGURES

CHAPTER I

BACKGROUND AND MOTIVATION

1.1. The quantum nature of light

Ever since its early days at the beginning of the twentieth century, quantum mechanics has been intimately connected to the study of electromagnetic phenomena. It was while attempting to develop a theory of blackbody radiation that Max Planck had to posit the quantization of radiation energy emitted and absorbed within a cavity in discrete units [4]. Shortly thereafter Albert Einstein was able to famously explain the photoelectric effect by generalizing Planck's idea to postulate that light itself is made up of photons, a contribution which was later to earn him the Nobel Prize [5]. Over the next few decades, rapid developments in quantum theory culminated in Paul Dirac's and Richard Feynman's formulations of quantum electrodynamics, the first of the quantum field theories which form the basis of the standard model, our best explanation of the fundamental workings of the Universe [6, 7].

It was not until the 1960's, however, that the ideas of the quantum theory of electromagnetic radiation became refined into what is known today as the field of quantum optics. This can be credited to two major developments. One of these was the quantum theory of optical coherence put forward by Roy Glauber in 1963, for which he was awarded the Nobel Prize in 2005. Glauber's work established a direct relationship between the coherence properties of the light field and statistical correlations in photodetection [8]. The other was the development of the laser by Theodore Maiman in 1960 [9]. The laser was the first source of coherent

light at optical frequencies, opening up an array of new branches of fundamental research and applications.

Today the field of quantum optics is distinguished in being a prolific testbed for the most fundamental implications of quantum theory. From the first observation of sub-Poissonian photon statistics in 1974 [10], to the first realization of quantum state tomography in 1993 [11], to the first demonstration of quantum teleportation in 1997 [12], to one of the first loophole-free tests of Bell's inequality in 2015 [13], several of the most spectacular demonstrations of the quantum nature of reality, with deep philosophical implications, have been performed using light. This prominence of the role of quantum optics in revealing the fabric of reality is largely thanks to the developments which allowed generation and verification of quantum states of light with no classical counterpart.

Beyond fundamental research, quantum optics is also the breeding grounds for some of the most promising applications of quantum mechanics today. The field of quantum information science (QIS) is founded on studying and exploiting the quantum nature of information at the fundamental level, extending the ideas of Claude Shannon on classical information theory to the quantum regime. It is widely accepted that photons will be the carriers of information in this quantum internet, establishing links of entanglement between distant quantum computers [14]. In addition, quantum light offers an enhancement in precision measurements by way of increased sensitivity, from the use of squeezed light for gravitational wave detection [15], to the use of entanglement for increasing the signal-to-noise ratio in target detection via quantum illumination [16, 17].

1.2. Entanglement: from bug to feature

One of the most striking phenomena of quantum theory is the concept of entanglement, correlations between distant objects which defy the assumptions, inherent in classical physics, of locality and realism. Locality holds that a system can only be influenced by its immediate surroundings, while realism holds that the properties of a system do not depend on the measurements made on that system. In the famous paper by Einstein, Podolsky, and Rosen (EPR) [18], it was shown that quantum mechanics is inconsistent with these assumptions, and allowed for what Einstein termed "spooky action at a distance" [19]. On this basis, the EPR paper concluded that quantum mechanics did not provide a complete description of reality.

In a striking turn of events, John Stewart Bell showed in 1964 that the EPR paradox, as it came to be known, was more than just a philosophical thought experiment. In his paper, Bell derived a statistical inequality which all correlations of the local realistic kind must obey, and which quantum entanglement could violate [20, 21]. It was not long afterwards that the first experimental tests of the Bell inequality began to be performed using pairs of entangled photons, each time conclusively violating local realistic assumptions and further corroborating the quantum mechanical predictions.

With the reality of quantum entanglement firmly established, today it is widely accepted as an important feature of the theory, and beyond revealing some of the most surprising fundamental aspects of reality, it can be harnessed to accomplish unprecedented tasks. Entanglement is now identified as a quantum resource, which can be quantified [22]. It is the crucial link between the nodes of a quantum network, which allows for the distribution of quantum information

between multiple parties. It can be used to accomplish quantum key distribution (QKD), enabling protocols for cryptography whose security is guaranteed by the laws of physics [23]. Furthermore, quantum entanglement enables the measurement of physical parameters, such as optical phase, beyond what is classically achievable, reaching down to the Heisenberg limit [24].

1.3. The state-measurement duality and entangled measurements

Another distinguishing feature of quantum theory is the important role that measurement plays in obtaining physical results. The mathematical language of quantum mechanics is linear algebra. The most general formulation of the theory holds that the state of a system is described by an operator $\hat{\rho}$ acting on a vector space called a Hilbert space, obeying certain constraints. Meanwhile, a quantum measurement is also represented by a set of operators $\{\hat{\Pi}_n\}$ acting on the same Hilbert space. The connection to the results of measurements performed on a system is then obtained by the Born rule, which states that the probability of obtaining measurement outcome n, given that the state $\hat{\rho}$ was prepared, is given by

$$p_n = \mathrm{Tr}\left(\hat{\rho}\hat{\Pi}_n\right), \tag{1.1}$$

where $\mathrm{Tr}(\cdot)$ denotes the trace.

This duality between states and measurements in quantum theory is succinctly distilled in what is called the *retrodictive approach*. Given a measurement outcome n with a corresponding operator $\hat{\Pi}_n$, one may define the retrodicted quantum state

$$\hat{\rho}_n = \frac{\hat{\Pi}_n}{\mathrm{Tr}\left(\hat{\Pi}_n\right)}, \tag{1.2}$$

which corresponds to the quantum state that would have led to measurement outcome n with unit probability (assuming an ideal measurement device [25]). Based on this retrodicted state, one may ascribe to the measurement operator $\hat{\Pi}_n$ all of the attributes that one associates with a quantum state. For example, the measurement $\hat{\Pi}_n$ is a pure measurement if the state $\hat{\rho}_n$ is a pure state. In that limit it corresponds to an ideal projective Von Neumann measurement [26].

Things get particularly interesting when we consider measurements on two quantum particles. For just as two particles may be in an entangled state, so can a joint measurement on two particles be said to be entangled, in the sense that it projects the two particles onto an entangled state. The best-known such entangled measurement is the Bell-state measurement, which projects the incoming particles onto one of the Bell states, which are the maximally entangled states that form a basis for the Hilbert space associated with two particles. To appreciate the state-measurement duality in the context of entanglement, it is perhaps most instructive to consider the quantum teleportation scenario.

It is known that it is impossible in general to copy an arbitrary quantum state of one system onto another. This is known as the no-cloning theorem [27]. Remarkably, Charles Bennett and coauthors showed in 1993 that one could, however, teleport an arbitrary quantum state of a system possessed by one party, Alice, onto a system possessed by another party, Bob, provided Alice and Bob share entanglement, and in a way that necessarily results in the erasure of the original quantum state of Alice's system [28].

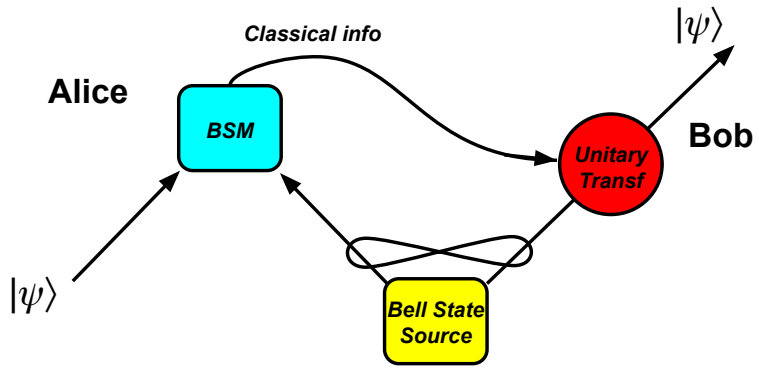

FIGURE 1.1. Quantum teleportation protocol, see text for description. BSM: Bell state measurement.

A rough outline of the quantum teleportation protocol is as follows: Alice and Bob share a maximally entangled state of two particles between them, a Bell state. Alice is also in possession of a particle in an arbitrary quantum state $|\psi\rangle$ to be teleported to Bob. The key step for teleportation is for Alice to perform a joint measurement on this particle and her half of the Bell state. This joint measurement is a Bell-state measurement, projecting the two particles onto a Bell state, meanwhile resulting in Bob's particle assuming the state $|\psi\rangle$, up to a simple transformation. What should be appreciated here is the symmetry of the entire process: we start with three particles, one in a quantum state $|\psi\rangle$ and two in a Bell state, and we end with the same three particles with one in the quantum state $|\psi\rangle$ and two in a Bell state[1]. What has changed is which two particles are in the Bell state, and the final Bell state is entirely due to the Bell state measurement. The schematic of the teleportation protocol in Fig. 1.1 makes this symmetry clear.

In a recent article [29], Nicolas Gisin notes

[1]Note that, when quantum teleportation is implemented using photons, only one photon remains (the one in the quantum state $|\psi\rangle$, since the Bell state measurement destroys the two measured photons.

> . . . entanglement is exploited twice in quantum teleportation. Firstly, entanglement is the "quantum teleportation channel", i.e. entanglement between distant systems. Second, entanglement appears in the eigenvectors of the joint measurement that Alice, the sender, has to perform jointly on the quantum state to be teleported and her half of the "quantum teleportation channel", i.e., entanglement enabling entirely new kinds of quantum measurements. I emphasize how poorly this second kind of entanglement is understood.

Indeed, interest in quantifying the entanglement inherent in joint measurements is a rather recent development. Although this kind of entanglement has been recognized since the early 1990s[2] [30], the first papers that propose a way to certify that a quantum measurement is entangled, that is, has entangled eigenstates, were not published until 2011 [31, 32]. Subsequently it was shown experimentally that the entanglement inherent in Bell state measurements can be certified [33].

Another related quantum protocol is that of entanglement swapping, shown schematically in Fig. 1.2. In this case, Alice produces one pair of entangled particles, A_1 and A_2, and Bob produces another entangled pair, B_1 and B_2. Alice sends particle A_2 and Bob sends particle B_2 to a third party, Charlie. Charlie in turn performs a Bell-state measurement on these independent particles. As expected, the measured particles A_2 and B_2 are now projected onto an entangled state. More surprisingly, the particles A_1 and B_1, which have never interacted and are still in Alice's and Bob's possession, respectively, also become projected onto an entangled state! Effectively, as a result of the measurement, the entanglement

[2] In fact, Charles Bennett has noted that it was this work which inspired the conception of quantum teleportation

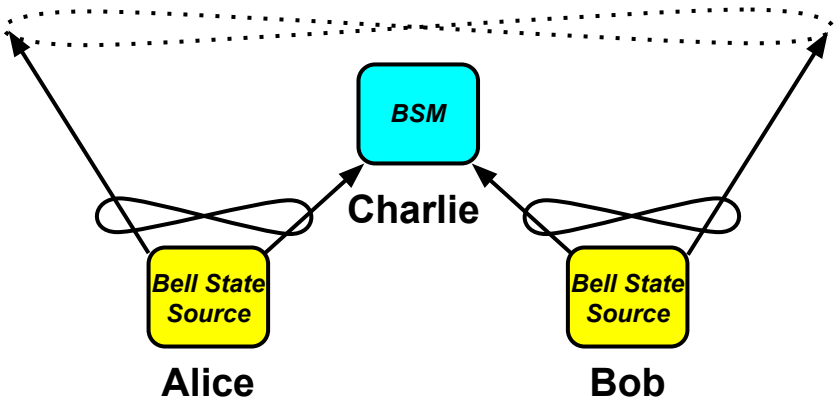

FIGURE 1.2. Entanglement swapping protocol, see text for description.

has been teleported, or swapped [34]. The most important use of entanglement swapping is as a quantum repeater, serving to extend the range of entanglement in the presence of loss and noise. However, it is also a spectacular demonstration not only of the non-locality inherent in entangled quantum states, but also of that induced by measurement, and in this work we will show an extension of this protocol to make use of the high-dimensional nature of the entanglement present in quantum states of light.

1.4. Optical quantum information encoding and entanglement

One of the benefits of using light for quantum information encoding is the inherently high information capacity offered by the degrees of freedom of light. The electromagnetic field can be decomposed into modes which are solutions to Maxwell's equations, such that each mode is uniquely specified by four variables, typically chosen as the three spatial degrees of freedom, and the polarization of light. There are two main approaches to taking advantage of this in quantum optics.

The first approach is called the continuous variable, or CV, approach. Here a fixed number of modes of light is considered, and each mode is treated as a quantum harmonic oscillator whose quantum state can encode information. One can associate with each mode two non-commuting observables, $\hat{X}$ and $\hat{P}$, analogous to position and momentum of a classical system. This is known as the CV approach because these observables can take on any value in principle. Furthermore, one can entangle two modes (A and B) such that their respective observables are correlated: $\langle \hat{X}_A - \hat{X}_B \rangle = 0$, $\langle \hat{P}_A + \hat{P}_B \rangle = \text{constant}$. This is analogous to the position and momentum entanglement considered in the original EPR paper. Finally, the energy spectrum of each mode is discrete, with equally-spaced energy levels, precisely the discrete energies which Planck postulated and which Einstein associated with the light quanta we call photons.

The second, perhaps more intuitive approach, is known as the discrete variable, or DV, approach, and it is the one considered in this work. Here a fixed number of photons is considered, whereas information is encoded in which modes they occupy. If the polarization modes are used, the state space is two-dimensional, and can encode at most a quantum bit, or qubit, of information in a single-photon state of light. This is done by associating with each polarization state of light one of the binary logical values $\{0, 1\}$. Choosing, for instance, the linear polarization states of light as the basis for encoding, we can choose $\{0 \to |H\rangle, 1 \to |V\rangle\}$ as our encoding scheme, where $|H\rangle, |V\rangle$ denote single-photon states in the horizontal and vertical polarizations, and we're using the Dirac ket notation. The most general qubit can then be represented as

$$|\psi\rangle = \alpha |H\rangle + \beta |V\rangle , \tag{1.3}$$

where α, β are complex coefficients satisfying $|\alpha|^2 + |\beta|^2 = 1$. This approach is easily accessible experimentally and has been the basis of many of the groundbreaking proof-of-principle experiments in quantum optics.

However, it is possible to use the spatial degrees of freedom to exploit a d-dimensional state space ($d > 2$), and encode a *qudit* rather than a qubit of information in a single-photon state, since the number of spatial modes are unlimited in principle. In particular, the longitudinal degree of freedom of a traveling light field, that is, the wavelength, or frequency, of the light, presents a particularly attractive mode basis to encode information. This is due in part to the mature technologies that exist for measuring light spectra, in part to the compatibility of spectral modes with optical fiber networks, and finally in part to the ease with which pairs of photons entangled in frequency and time can be generated in the laboratory. It is now well-accepted that spectral-temporal encoding of quantum information in single-photon states of light forms one of the most viable and promising paradigms for quantum information processing [35].

1.5. Expanding on the state of the art

Given that the spectral-temporal degree of freedom of light offers a platform for high-dimensional quantum information encoding, it is worth examining the available toolkit for QIS using TF-encoded states of light. After having acquired an overview of the state of the art in TF quantum information encoding, it should become more apparent what is needed to expand this toolkit, and where the work presented in this thesis fits in. To this end it is helpful to consider the three main components of a quantum experiment: state preparation, state manipulation, and measurement.

Quantum state preparation in the spectral-temporal domain is a rather mature technology by now. As previously stated, the laser has been in existence for over 60 years, allowing an exquisite amount of control over the modal properties of light. In that time, lasers have been developed across a vast range of wavelengths, and with a possessing a large range of spectral coherence properties. Continuous-wave (CW) lasers can be confined to spectral linewidths in the kHz regime at infrared frequencies [36]. Meanwhile, wavelength-tunable pulsed lasers routinely allow for the generation of ultrashort pulses with durations on the order of femtoseconds, corresponding to spectral bandwidths in the GHz range. Additionally, nonlinear optical effects such as second- and third-harmonic generation provide access to shorter wavelengths while retaining the coherence properties of the source lasers.

Since they are the ultimate source of quantum states of light, the versatility in laser spectral properties is in turn responsible for the generation of quantum states of light with well-tailored spectral properties. A key resource in this field is time-frequency entangled photon pairs, and their generation is well-studied. The use of narrow linewidth lasers, combined with appropriate non-linear optical crystals, can generate pairs of photons with ultra-broadband spectra and a high degree of entanglement, spanning over an octave in frequency [37]. At the other end, the use of pulsed lasers allows for the generation of photon pairs exhibiting no spectral entanglement, such that the detection of one of the photons heralds the other photon in a pure quantum state [38]. In between these two regimes, spectral shaping of the laser light, in combination with versatile design of nonlinear crystal properties, now permit an unprecedented degree of control over the amount of

correlations between photon pairs [2, 39]. The mechanism whereby these properties are responsible for two-photon entanglement will be addressed in the next chapter.

Manipulation of quantum states of light in the time-frequency domain has also seen great progress in the past two decades. Because the properties of a single photon consist in the classical mode it occupies, many classical methods of spectral-temporal manipulation can be carried over into the quantum regime. Chief among these is pulse shaping, whereby dispersion is used to separate the light into its spectral components, such that each of these can be addressed independently in amplitude and phase using a spatial light modulator (SLM) [40]. However, spectral amplitude shaping is inherently lossy, and although this is not a problem for classical light, this is incompatible with photonic quantum information processing, where it is desired so manipulate the modal properties without altering the photon number properties.

Such manipulation is achieved through unitary operations, acting only on the spectral and temporal phases of the optical modes. This area of the field is still in its infancy due to the technical challenges of implementing phase operations in the time domain, but some important steps have been taken towards this goal. These include frequency translation [41], bandwidth compression [42], and time lensing [43]. Furthermore, it has been shown theoretically that an arbitrary unitary transformation may be realized via a sequence of alternating time-domain and frequency-domain phase shifts within a reasonable number of steps [44].

We have already seen how quantum measurements are key players in quantum physical processes, on a par with quantum states. It is not surprising, then, that a complete toolkit for quantum information science using TF-encoded states of light should require a versatile set of measurement techniques. These

should include projective measurements both in the time basis, which are achievable through time-resolved single-photon detection, and the frequency basis, using conventional spectrometers with single-photon sensitive detectors. But furthermore, arbitrary projective measurements onto wavepacket modes are also essential, and these have been achieved at the quantum level using quantum pulse gates, which use a high-intensity shaped pulse as a gate in a non-linear interaction, implementing a pulse mode-selective frequency conversion to a register mode which can be detected with a standard single-photon detector [2, 45, 46].

However, it is also necessary to implement joint two-photon measurements. These measurements are the key requirement for quantum repeaters for the distribution of entanglement, which forms the "quantum channel" for connecting distant parties in a quantum network, as we saw in the discussion of entanglement swapping. To this end, entanglement swapping has been demonstrated using all of the available degrees of freedom of light, including polarization [47], time bins [48], transverse spatial modes [49], and most recently time-frequency modes [50]. All of these implementations rely on using a linear-optics Bell-state measurement on two photons, as we describe in the next chapter, and it is known that such a measurement (without auxiliary photons) can project onto at most a two-dimensional entangled state [51]. Reference [49] is particular among these in that multiple spatial-mode Bell states are swapped and individually characterized. However, this is done in a post-selected manner, such that information about which Bell state was swapped is only obtained after Alice and Bob compare their results.

This dissertation is concerned with expanding upon joint two-photon measurements to better utilize the capabilities afforded by the high-dimensional

nature of TF entanglement. In Chapter II we establish the theoretical framework in which to understand TF quantum information encoding in single- and two-photon states and measurements of light. In Chapter III we report on an entanglement swapping experiment that uses a spectrally multiplexed Bell-state measurement implemented by Charlie, such he can reveal to Alice and Bob ahead of time which spectrally-encoded Bell state they have swapped. This experiment is compatible with standard off-the-shelf entangled photon sources, making use of the full dimensionality of the entanglement available therein. In Chapter IV we expand on the results of the entanglement swapping experiment to show how spectrally-resolved two-photon interference can reveal entanglement even in the limit of maximally mixed quantum states, as long as they are antisymmetric upon exchange of photon labels. In Chapter V we consider theoretically the use of sum-frequency generation, a non-linear optical effect whereby a pair of photons are upconverted into a single photon, to implement two-photon measurements. We show that a mode-resolved detection of the upconverted photon can be backpropagated onto a joint measurement on the input photon pair, and describe some useful properties of the measurement operator. Finally, in Chapter VI we carry through with some the implications of the two-photon detection model presented in the previous chapter, and describe an experimental setup towards testing these implications, before concluding in Chapter VII. Chapters III and V, and the appendices associated therewith, contain previously published material co-authored by the author and reprinted with permission from all the authors.

CHAPTER II

QUANTUM OPTICS AND TWO-PHOTON ENTANGLEMENT

Since the bulk of the work described in this thesis relies on an understanding of multimode quantum optics in the single- and two-photon regime, this chapter aims to build a preliminary framework to understand this work. First, we will show how to quantize the electromagnetic field, and how the picture of photons as quantum-mechanical objects follows naturally from this quantization. Then we describe single- and two-photon states which can encode information in the spectral-temporal degree of freedom of light, and establish various quantities related to entanglement. Afterwards we describe the process of parametric down conversion, which is the most common way of generating time-frequency entangled photon pairs. Finally, we show how to model single- and two-photon detection in the quantum measurement formalism. These concepts should help to understand the subsequent chapters of this thesis.

2.1. The free quantum electromagnetic field

In this section we will follow the standard procedure for the canonical quantization of the electromagnetic field, which results in describing the normal modes of the field, which are solutions to the classical Maxwell's equations, as quantum harmonic oscillators. To this end, we express the electric and magnetic fields in terms of a monochromatic plane-wave expansion in a given quantization cavity of volume V as

$$\mathbf{E}(\mathbf{r},t) = i\sum_{\mathbf{k},\sigma} \mathbf{e}_{\mathbf{k}\sigma}\sqrt{\frac{\hbar\omega_{\mathbf{k}}}{2\epsilon_0 V}}\left[\alpha_{\mathbf{k}\sigma}u_{\mathbf{k}}(\mathbf{r})e^{-i\omega_{\mathbf{k}}t} - \alpha^*_{\mathbf{k}\sigma}u^*_{\mathbf{k}}(\mathbf{r})e^{i\omega_{\mathbf{k}}t}\right], \tag{2.1}$$

$$\mathbf{B}(\mathbf{r},t) = i\sum_{\mathbf{k},\sigma} \frac{\mathbf{k}\times\mathbf{e}_{\mathbf{k}\sigma}}{|\mathbf{k}|}\sqrt{\frac{\hbar\omega_{\mathbf{k}}}{2c^2\epsilon_0 V}}\left[\alpha_{\mathbf{k}\sigma}u_{\mathbf{k}}(\mathbf{r})e^{-i\omega_{\mathbf{k}}t} - \alpha^*_{\mathbf{k}\sigma}u^*_{\mathbf{k}}(\mathbf{r})e^{i\omega_{\mathbf{k}}t}\right]. \tag{2.2}$$

Here $\hbar$ is the reduced Planck's constant, c is the vacuum speed of light, and ϵ_0 is the vacuum permittivity. The wavevector $\mathbf{k}$ and the polarization unit vector $\mathbf{e}_{\mathbf{k}\sigma}$ satisfy $\mathbf{k}\cdot\mathbf{e}_{\mathbf{k}\sigma} = 0$, and $\sigma = \pm 1$ labels the polarization. Furthermore, $u_{\mathbf{k}}(\mathbf{r}) = e^{i\mathbf{k}\cdot\mathbf{r}}$ are the plane-wave monochromatic modes, and $\omega_{\mathbf{k}} = c|\mathbf{k}|$ are the angular frequencies of the monochromatic modes.

The Hamiltonian representing the electromagnetic energy in this volume is given classically by

$$H = \frac{\epsilon_0}{2}\int_V \mathrm{d}^3 r\left[\mathbf{E}^2(\mathbf{r},t) + c^2\mathbf{B}^2(\mathbf{r},t)\right]. \tag{2.3}$$

Using the forms of the fields in Eq. (2.1) and (2.2), and integrating over the spatial variables, we can express the Hamiltonian in terms of the expansion coefficients as

$$H = \sum_{\mathbf{k},\sigma}\frac{\hbar\omega_{\mathbf{k}}}{2}(\alpha^*_{\mathbf{k}\sigma}\alpha_{\mathbf{k}\sigma} + \alpha_{\mathbf{k}\sigma}\alpha^*_{\mathbf{k}\sigma}) \tag{2.4}$$

If we now define the canonically conjugate variables, also known as the field quadratures,

$$\begin{aligned} Q_{\mathbf{k}\sigma} &= \sqrt{\frac{\hbar}{2}}(\alpha_{\mathbf{k}\sigma} + \alpha^*_{\mathbf{k}\sigma}) \\ P_{\mathbf{k}\sigma} &= -i\sqrt{\frac{\hbar}{2}}(\alpha_{\mathbf{k}\sigma} - \alpha^*_{\mathbf{k}\sigma}), \end{aligned} \tag{2.5}$$

the Hamiltonian can be expressed in terms of these as

$$H = \sum_{\mathbf{k},\sigma} \frac{\omega_{\mathbf{k}}}{2}(Q^2_{\mathbf{k}\sigma} + P^2_{\mathbf{k}\sigma}). \tag{2.6}$$

This can be recognized as the Hamiltonian for a set of decoupled harmonic oscillators, subject to the Hamilton equations

$$\frac{\mathrm{d}Q_{\mathbf{k}\sigma}}{\mathrm{d}t} = \frac{\partial H_{\mathbf{k}\sigma}}{\partial P_{\mathbf{k}\sigma}}, \quad \frac{\mathrm{d}P_{\mathbf{k}\sigma}}{\mathrm{d}t} = -\frac{\partial H_{\mathbf{k}\sigma}}{\partial Q_{\mathbf{k}\sigma}}, \tag{2.7}$$

where $H_{\mathbf{k}\sigma} = \frac{\omega_{\mathbf{k}}}{2}(Q^2_{\mathbf{k}\sigma} + P^2_{\mathbf{k}\sigma})$ is the Hamiltonian for the mode labeled by $\mathbf{k}\sigma$.

We quantize this field by promoting the field quadratures to operators $\hat{Q}_{\mathbf{k}\sigma}$, $\hat{P}_{\mathbf{k}\sigma}$, and imposing on them the canonical commutation relations

$$[\hat{Q}_{\mathbf{k}\sigma}, \hat{P}_{\mathbf{k}'\sigma'}] = i\hbar\delta_{\mathbf{k}\mathbf{k}'}\delta_{\sigma\sigma'}, \quad [\hat{Q}_{\mathbf{k}\sigma}, \hat{Q}_{\mathbf{k}'\sigma'}] = [\hat{P}_{\mathbf{k}\sigma}, \hat{P}_{\mathbf{k}'\sigma'}] = 0. \tag{2.8}$$

Likewise the expansion coefficients $\alpha_{\mathbf{k}\sigma}$ and $\alpha^*_{\mathbf{k}\sigma}$ become operators $\hat{a}_{\mathbf{k}\sigma}$ and $\hat{a}^\dagger_{\mathbf{k}\sigma}$, respectively, such that

$$\hat{a}_{\mathbf{k}\sigma} = \frac{1}{\sqrt{2\hbar}}(\hat{Q}_{\mathbf{k}\sigma} + i\hat{P}_{\mathbf{k}\sigma}), \quad \hat{a}^\dagger_{\mathbf{k}\sigma} = \frac{1}{\sqrt{2\hbar}}(\hat{Q}_{\mathbf{k}\sigma} - i\hat{P}_{\mathbf{k}\sigma}). \tag{2.9}$$

These are the ladder operators for the quantum harmonic oscillator, and they obey the commutation relations

$$[\hat{a}_{\mathbf{k}\sigma}, \hat{a}^\dagger_{\mathbf{k}'\sigma'}] = \delta_{\mathbf{k}\mathbf{k}'}\delta_{\sigma\sigma'}, \quad [\hat{a}_{\mathbf{k}\sigma}, \hat{a}_{\mathbf{k}'\sigma'}] = [\hat{a}^\dagger_{\mathbf{k}\sigma}, \hat{a}^\dagger_{\mathbf{k}'\sigma'}] = 0. \tag{2.10}$$

Finally, the quantum Hamiltonian operator takes the form

$$\hat{H} = \sum_{\mathbf{k},\sigma} \frac{\hbar\omega_{\mathbf{k}}}{2}(\hat{a}_{\mathbf{k}\sigma}\hat{a}^{\dagger}_{\mathbf{k}\sigma} + \hat{a}^{\dagger}_{\mathbf{k}\sigma}\hat{a}_{\mathbf{k}\sigma}) = \sum_{\mathbf{k},\sigma} \hbar\omega_{\mathbf{k}} \left(\hat{a}^{\dagger}_{\mathbf{k}\sigma}\hat{a}_{\mathbf{k}\sigma} + \frac{1}{2}\right). \tag{2.11}$$

From this development it is evident that the free electromagnetic radiation field is equivalent to a set of decoupled quantum harmonic oscillators, each one corresponding to a mode labeled by $\mathbf{k}\sigma$ obeying the classical Maxwell's equations. The Hilbert space $\mathcal{H}$ associated with the radiation field is the tensor product of the Hilbert spaces $\mathcal{H}_\ell$ of each mode, where $\ell = \mathbf{k}, \sigma$ labels each mode. That is

$$\mathcal{H} = \otimes_{\ell}^{\infty} \mathcal{H}_\ell. \tag{2.12}$$

The operator $\hat{a}^{\dagger}_{\ell}\hat{a}_{\ell} = \hat{N}_\ell$ is known as the number operator: its eigenvalues are the natural numbers $n_\ell \in \mathbb{N}$, and its eigenvectors are the Fock states, $|n_\ell\rangle$. These form a basis for the Hilbert space $\mathcal{H}_\ell$ for the mode labeled by $\ell = \mathbf{k}, \sigma$. The state $|n_\ell\rangle$ is the state containing n photons in the mode ℓ, and the ground state for that mode is $|0_\ell\rangle$, containing zero photons. The ground state for the entire system is known as the vacuum state, $|\text{vac}\rangle$, where every mode is in the ground state

$$|\text{vac}\rangle = |0_1\rangle\,|0_2\rangle \ldots |0_\ell\rangle \ldots = |0_1; 0_2;\ \ldots 0_\ell;\ \ldots\rangle\,. \tag{2.13}$$

The creation operator $\hat{a}^{\dagger}_{\ell}$ acts on this state to create a single photon in the mode ℓ:

$$\hat{a}^{\dagger}_{\ell}\,|\text{vac}\rangle = |0_1; 0_2;\ \ldots 1_\ell;\ \ldots\rangle = |1_\ell\rangle\,. \tag{2.14}$$

More generally, the creation operator $\hat{a}^{\dagger}_{\ell}$ adds a photon to the mode ℓ, while the annihilation $\hat{a}_\ell$ operator removes a photon from the mode ℓ, according to

$$\begin{aligned}\hat{a}_\ell^\dagger \left|n_1; n_2; \ldots; n_\ell; \ldots\right\rangle &= \sqrt{n_\ell + 1}\left|n_1; n_2; \ldots; n_\ell + 1; \ldots\right\rangle, \\ \hat{a}_\ell \left|n_1; n_2; \ldots; n_\ell; \ldots\right\rangle &= \sqrt{n_\ell}\left|n_1; n_2; \ldots; n_\ell - 1; \ldots\right\rangle.\end{aligned} \tag{2.15}$$

2.1.1. Coherent states

Having quantized the field and constructed the Fock basis of states with definite photon number, it is worth mentioning another notable class of states. These are the coherent states, which are the closest in behavior to classical states of light. For a given mode of the light field, a coherent state $|\alpha\rangle$ is defined as an eigenstate of the annihilation operator with complex eigenvalue α:

$$\hat{a}\left|\alpha\right\rangle = \alpha\left|\alpha\right\rangle. \tag{2.16}$$

Solving this eigenvalue equation leads to the representation of a coherent state in terms of a vacuum state displaced by an amount α in the $\hat{X}, \hat{P}$ quadrature space:

$$\left|\alpha\right\rangle = \exp\left[\alpha\hat{a}^\dagger - \alpha^*\hat{a}\right]\left|\text{vac}\right\rangle. \tag{2.17}$$

In the Fock basis, the coherent state is represented by

$$\left|\alpha\right\rangle = e^{-|\alpha|^2/2}\sum_{n=0}^{\infty}\frac{\alpha^n}{\sqrt{n!}}\left|n\right\rangle. \tag{2.18}$$

The mean photon number is given by

$$\langle n\rangle = \langle\alpha|\hat{N}|\alpha\rangle = |\alpha|^2, \tag{2.19}$$

and the photon number distribution is Poissonian, given by

$$P(n) = |\langle n|\alpha\rangle|^2 = e^{-|\alpha|^2}\frac{|\alpha|^2}{n!}. \tag{2.20}$$

2.1.2. Wavepacket modes

The decomposition of the electromagnetic field into the plane-wave monochromatic modes, labeled by $\mathbf{k}\sigma$ is not unique. It was shown as far back as 1966 by Titulaer and Glauber that one could decompose the electromagnetic field in terms of wavepacket modes, defined by

$$\mathbf{v}_{m\sigma}(\mathbf{r}, t) = \int \frac{\mathrm{d}^3k}{(2\pi)^3} U_m^{\sigma}(\mathbf{k})\mathbf{u}_{\mathbf{k}\sigma}(\mathbf{r})e^{\imath\omega_{\mathbf{k}}t} \tag{2.21}$$

where $U_m^{\sigma}(\mathbf{k})$ is a unitary transformation satisfying

$$\int \frac{\mathrm{d}^3k}{(2\pi)^3} U_m^{\sigma *}(\mathbf{k})U_{m'}^{\sigma}(\mathbf{k}) = \delta_{mm'}, \tag{2.22}$$

and where we have defined $\mathbf{u}_{\mathbf{k}\sigma}(\mathbf{r}) = \mathbf{e}_{\sigma}u_{\mathbf{k}\sigma}(\mathbf{r})$.

Furthermore, it is possible to construct a new set of creation and annihilation operators, defined by

$$\hat{b}_{m\sigma} = \int \frac{\mathrm{d}^3k}{(2\pi)^3} U_m^{\sigma *}(\mathbf{k})\hat{a}_{\mathbf{k}\sigma}, \quad \hat{b}_{m\sigma}^{\dagger} = \int \frac{\mathrm{d}^3k}{(2\pi)^3} U_m^{\sigma}(\mathbf{k})\hat{a}_{\mathbf{k}\sigma}^{\dagger}, \tag{2.23}$$

which, because of the unitarity of the transformation $U_m^{\sigma}(\mathbf{k})$, also obey the bosonic commutation relations

$$[\hat{b}_{m\sigma}, \hat{b}_{m'\sigma'}^{\dagger}] = \delta_{mm'}\delta_{\sigma\sigma'}, \quad [\hat{b}_{m\sigma}, \hat{b}_{m'\sigma'}] = [\hat{b}_{m\sigma}^{\dagger}, \hat{b}_{m'\sigma'}^{\dagger}] = 0. \tag{2.24}$$

The operator $\hat{b}_m^{\dagger}$ ($\hat{b}_m$) creates (annihilates) a photon in wavepacket mode m.

2.2. Pulse-mode one-photon and two-photon states

In this dissertation, we are mainly concerned with quantum states of light in wavepacket modes defined over time and frequency, such as can be produced in pulsed laser systems. The broadband nature of these pulses, consisting of a superposition of frequencies, leads to a localization of the field amplitude in time. These wavepackets are localized in space as well, since they are produced by coherent laser fields which typically assume a Gaussian transverse profile. However, because the spatial degree of freedom is not as relevant to our work, and because we collect the light in single-mode fibers for interference and for detection, we can assume that the light occupies a single transverse spatial mode, and focus our attention on the temporal domain, as well as the spectral domain, which is its Fourier conjugate. Wavepacket modes defined in the time-frequency domain are commonly referred to as spectral-temporal modes, or temporal modes [35], in analogy with the spatial modes which result from boundary conditions imposed by waveguides and laser cavities.

We can now define a single-photon state in a temporal mode labeled by j as

$$|\psi_j\rangle = \int \mathrm{d}\omega \psi_j(\omega) \hat{a}^\dagger(\omega) \left|\mathrm{vac}\right\rangle, \tag{2.25}$$

where $\hat{a}^\dagger(\omega)$ creates a photon in a monochromatic mode with angular frequency ω. Here $\psi_j(\omega)$ is a complex mode function of angular frequency, normalized such that

$$\langle\psi_j|\psi_j\rangle = \int \mathrm{d}\omega \left|\psi_j(\omega)\right|^2 = 1. \tag{2.26}$$

By taking a Fourier transform to the time domain, we may equivalently express the same state in the time domain as

$$|\psi_j\rangle = \int \mathrm{d}t \tilde{\psi}_j(t)\hat{a}^\dagger(t)\,|\mathrm{vac}\rangle\,, \tag{2.27}$$

where

$$\hat{a}^\dagger(t) = \frac{1}{\sqrt{2\pi}} \int \mathrm{d}\omega \hat{a}^\dagger(\omega) e^{i\omega t}, \tag{2.28}$$

and

$$\tilde{\psi}_j(t) = \frac{1}{\sqrt{2\pi}} \int \mathrm{d}\omega \psi_j(\omega) e^{-i\omega t} \tag{2.29}$$

Henceforth we will exclusively represent states of light in the frequency domain, with the understanding that the time domain representations can always be obtained through Fourier transforms. This is because in the experimental work we discuss in this thesis, most of the measured quantities are functions of optical frequency, as the latter readily accessible in the laboratory using both stationary devices such as standard grating spectrometers, and time-of-flight spectroscopy methods as will be discussed in the experimental sections.

The temporal mode functions can be any set of functions which span the frequency and the time domains. For instance, they could be idealistic monochromatic modes, such that each mode has a frequency-domain representation that is a delta function of a single frequency, and a time-domain representation as a sinusoid of infinite extent. Often the temporal mode functions ψ_j of interest form an orthonormal basis, such as the Hermite-Gauss modes, of which we show the first three in Fig. 2.1. For such orthonormal mode functions, the inner product of two single-photon states gives

$$\langle \psi_j | \psi_k \rangle = \int \mathrm{d}\omega \psi_j^*(\omega)\psi_k(\omega) = \delta_{jk}. \tag{2.30}$$

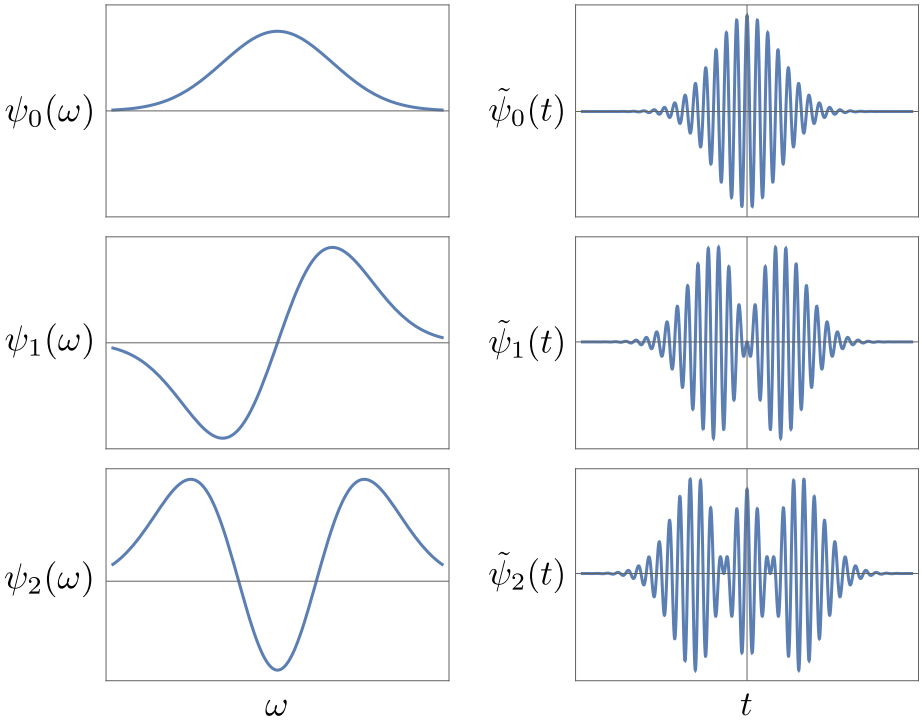

FIGURE 2.1. First three Hermite-Gauss modes in the frequency (left) and time (domain). The Hermite-Gauss modes form an orthonormal mode basis for frequency and time.

Furthermore, we can define creation (annihilation) operators $\hat{A}_j^\dagger$ ($\hat{A}_j$) as

$$\hat{A}_j^\dagger = \int \mathrm{d}\omega \psi_j(\omega)\hat{a}^\dagger(\omega) = \int \mathrm{d}t\tilde{\psi}_j(t)\hat{a}^\dagger(t), \tag{2.31}$$

and these obey the standard bosonic commutation relation

$$\left[\hat{A}_j, \hat{A}_k^\dagger\right] = \delta_{jk} \tag{2.32}$$

It is also possible to have a single-photon state in a temporal mode which is undetermined. As we shall see later, such a state can result when one photon from a pair of time-frequency entangled photons is detected without spectral resolution.

This situation corresponds to a mixed quantum state, represented as a convex combination of temporal-mode single-photon states

$$\hat{\rho} = \sum_j p_j \left|\psi_j\right\rangle \left\langle\psi_j\right|, \tag{2.33}$$

where p_j are weighting coefficients satisfying $\sum_j p_j = 1$. Expanding out the right hand side obtains

$$\hat{\rho} = \sum_j p_j \int \mathrm{d}\omega \mathrm{d}\omega' \psi_j(\omega)\psi_j^*(\omega')\hat{a}^\dagger(\omega)\left|\mathrm{vac}\right\rangle \left\langle\mathrm{vac}\right| \hat{a}(\omega'). \tag{2.34}$$

In this case it is convenient to define the single-photon spectral density matrix as

$$\rho(\omega,\omega') = \sum_j p_j \psi_j(\omega)\psi_j^*(\omega'). \tag{2.35}$$

This is the most general representation of a single-photon state in frequency space. For the special case of a pure state, only one term in the sum is populated, and the density matrix is factorable as $\rho(\omega,\omega') = \psi_j(\omega)\psi_j^*(\omega')$. Otherwise the state is mixed. We may define the *purity* of the state as

$$\mathcal{P}(\hat{\rho}) = \mathrm{Tr}(\hat{\rho}^2) = \int \mathrm{d}\omega \mathrm{d}\omega' \rho(\omega,\omega')\rho(\omega',\omega). \tag{2.36}$$

It follows that, in general, $0 \leq \mathcal{P}(\hat{\rho}) \leq 1$, where equality to 1 is achieved for a pure state, and to 0 for a maximally mixed state, one where there is complete lack of information about the spectral characteristics of the state.

2.3. Two-photon states and time-frequency entanglement

We now extend the discussion to include two-photon states of light, and study how entanglement, the non-classical correlations between distinct modes of the light field, can arise in such states. As we shall see shortly, two-photon entangled states, commonly known as entangled photon pairs, or EPP, are only a subset of the rich variety of entangled states of light that can be obtained in quantum optics. Indeed, because it is the modes, rather than the photons, that are the fundamental objects in quantum optics, the most fundamental understanding of entanglement must ultimately be framed in terms of the field quadratures of the harmonic oscillator modes. However, EPP are particularly well-studied due to their ease of generation and applications in various protocols, in addition to having a more intuitive interpretation as "objects". After all, it is the photons, rather than the modes, which are observable to our eyes.

We have already seen how a single-photon state can be generated from the vacuum by a single application of the creation operator: $|1_j\rangle = \hat{A}_j^\dagger |\text{vac}\rangle$. By repeated application of this operator, we can see that a normalized n-photon state of the mode j of the field can be represented as $|n_j\rangle = \frac{(A_j^\dagger)^n}{\sqrt{n!}} |\text{vac}\rangle$. In particular, a two-photon state in the mode j is given by

$$|2_j\rangle = \frac{(A_j^\dagger)^2}{\sqrt{2}} |\text{vac}\rangle . \tag{2.37}$$

Such a state is inherently a single-mode state of two photons. Because they are indistinguishable, there is no measurement in principle that could separate these photons deterministically. This single-mode two-photon state is interesting in its

own rights, but we only mention it here in passing for completeness. Things get more interesting when we consider a two-mode, two-photon state of the form

$$|\Psi\rangle = \hat{A}_j^\dagger \hat{A}_k^\dagger |\text{vac}\rangle \,. \tag{2.38}$$

In this case we have one photon in the mode j, and one in the mode k. Now there is a way in principle to distinguish these photons and separate them in a deterministic manner. If the modes j and k were labels of orthogonal polarization modes, then a polarizing beam splitter, such as we discuss in this work, would suffice for the task. In the present case of temporal modes, this can be done using a spectrometer for quasi-monochromatic modes, or more generally for arbitrary pulse-mode using a temporal-mode sorter [2, 45, 46], which relies on mode-selective frequency conversion to a register mode which can be subsequently detected. To generalize even further, the two photons could occupy distinguishable spatial or polarization modes, in addition to different temporal modes. We can distinguish this case by using a different letter for the creation operator, for instance,

$$|\Psi\rangle = \hat{A}_j^\dagger \hat{B}_k^\dagger |\text{vac}\rangle \tag{2.39}$$

Most generally, a two-photon state of light can be defined over a coherent superposition of modes,

$$|\Psi_{AB}\rangle = \sum_{j,k} \gamma_{jk} \hat{A}_j^\dagger \hat{B}_k^\dagger |\text{vac}\rangle \,, \tag{2.40}$$

where the γ_{jk} are complex coefficients satisfying the normalization condition $\sum_{j,k} |\gamma_{jk}|^2 = 1$. Written in terms of the expansions of $\hat{A}_j^\dagger = \int \mathrm{d}\omega \psi_j(\omega) \hat{a}^\dagger(\omega)$ and

$\hat{B}_k^\dagger = \int \mathrm{d}\omega' \psi_k(\omega')\hat{b}^\dagger(\omega')$ into their respective temporal mode functions, the state has the form

$$\begin{aligned} |\Psi\rangle &= \int \mathrm{d}\omega \mathrm{d}\omega' \sum_{j,k} \gamma_{jk}\psi_j(\omega)\psi_k(\omega')\ \hat{a}^\dagger(\omega)\hat{b}^\dagger(\omega')\,|\mathrm{vac}\rangle \\ &= \int \mathrm{d}\omega \mathrm{d}\omega' f(\omega,\omega')\hat{a}^\dagger(\omega)\hat{b}^\dagger(\omega')\,|\mathrm{vac}\rangle\,, \end{aligned} \tag{2.41}$$

where we have defined the *joint spectral amplitude* (JSA)

$$f(\omega,\omega') = \sum_{j,k} \gamma_{jk}\psi_j(\omega)\psi_k(\omega'). \tag{2.42}$$

The JSA can be thought of as a two-photon wavefunction in frequency space, and its modulus squared is the *joint spectral intensity* (JSI),

$$F(\omega,\omega') = |f(\omega,\omega')|^2, \tag{2.43}$$

normalized such that $\int \mathrm{d}\omega \mathrm{d}\omega' F(\omega,\omega') = 1$. This latter gives the probability density for detecting one photon at frequency ω and the other at frequency ω', and is readily measurable in the laboratory using spectrally correlated single-photon detection as we describe in this work.

A related quantity, obtainable by a double-Fourier transform of the JSA, is the joint-temporal amplitude,

$$\tilde{f}(t,t') = \frac{1}{2\pi}\int \mathrm{d}\omega \mathrm{d}\omega' f(\omega,\omega')e^{-i\omega t}e^{-i\omega' t'} = \sum_{j,k} \gamma_{jk}\tilde{\psi}_j(t)\tilde{\psi}_k(t'), \tag{2.44}$$

as well as it's modulus squared, the joint temporal intensity. Although the joint temporal amplitude (intensity) is in principle equivalent to the JSA (JSI), in the

regimes where we typically operate it is not as accessible due to the high timing precision required to resolve it using time-correlated measurements. Thus we will rarely refer to it throughout this text and mainly consider the spectral domain.

Entanglement in the time-frequency domain occurs when the JSA is not factorable into a product of functions of the form

$$f(\omega, \omega') = f_A(\omega) f_B(\omega'). \tag{2.45}$$

This is because, if the JSA is factorable, then it is possible to find a temporal-mode basis such that the state $|\Psi\rangle$ can be expressed as a product state. Equivalently, the two photon-state is entangled if γ_{jk} cannot be expressed as a product of the form $\alpha_j \beta_k$, otherwise it is a product state. At the end of this section we make some brief comments regarding entangled states of light, of which two-photon entangled states are only a subset. However, in what follows I focus solely on two-photon entanglement, showing how to describe entangled states uniquely using the Schmidt decomposition, and the relationship between two-photon entanglement and the purity of the constituent single photons.

2.3.1. Schmidt decomposition of a TF entangled state

For a given JSA $f(\omega, \omega') = \sum_{j,k} \gamma_{jk} \psi_j(\omega) \psi_k(\omega')$, it is possible to find a basis of modes such that it may be expressed uniquely as [52]

$$f(\omega, \omega') = \sum_i \sqrt{\lambda_i} \phi_i^A(\omega) \phi_i^B(\omega'), \tag{2.46}$$

where the complex functions $\phi_i^{A(B)}$, known as the Schmidt modes, form an orthonormal mode basis in the frequency space for photon $A(B)$, and where λ_i

are non-negative real coefficients, known as the Schmidt coefficients, and satisfy the normalization condition $\sum_i \lambda_i = 1$. This representation is known as the Schmidt decomposition, and it follows from the general result of the singular value decomposition of a complex matrix, in this case the matrix γ_{jk} [53]. Using this result, we can re-express the state in the Schmidt basis as

$$|\Psi\rangle = \sum_i \sqrt{\lambda_i}\, |\phi_i^A\rangle\, |\phi_i^B\rangle\,, \tag{2.47}$$

where

$$|\phi_i^A\rangle = \int \mathrm{d}\omega \phi_i^A(\omega) \hat{a}^\dagger(\omega)\, |\mathrm{vac}\rangle\,, \quad |\phi_i^B\rangle = \int \mathrm{d}\omega \phi_i^B(\omega') \hat{b}^\dagger(\omega')\, |\mathrm{vac}\rangle\,. \tag{2.48}$$

When expressed in the Schmidt basis, the state $|\Psi\rangle$ is a product state if it contains only one term, with $\lambda_0 = 1$ and $\lambda_i = 0$ for all other i. Otherwise the state is entangled. Furthermore, the Schmidt decomposition provides a way to quantify the amount of entanglement in the state, through the Schmidt number, or Schmidt rank, defined as [54]

$$K = \frac{1}{\sum_i \lambda_i^2}. \tag{2.49}$$

The Schmidt number essentially quantifies the number of populated mode pairs (ϕ_i^A, ϕ_i^B), and is equal to one for a product state, and tends to infinity for a maximally entangled state (one with an infinite amount of populated mode pairs).

2.3.2. The trade-off between purity and entanglement

Given a pure state of two photons $|\Psi_{AB}\rangle$, which may or may not be entangled, the state of either of the constituent photons, say photon A, is represented by the reduced density operator $\hat{\rho}_A$, given by

$$\hat{\rho}_A = \mathrm{Tr}_B(|\Psi_{AB}\rangle \langle\Psi_{AB}|) = \int \mathrm{d}\omega \, \langle \mathrm{vac}| \, \hat{b}(\omega) \, |\Psi_{AB}\rangle \, \langle\Psi_{AB}| \, \hat{b}^\dagger(\omega) \, |\mathrm{vac}\rangle \,, \tag{2.50}$$

where Tr_B denotes the trace over photon B's spectral degree of freedom. A straightforward calculation shows that

$$\hat{\rho}_A = \int \mathrm{d}\omega \mathrm{d}\omega' \rho_A(\omega, \omega') \hat{a}^\dagger(\omega) \, |\mathrm{vac}\rangle \, \langle \mathrm{vac}| \, \hat{a}(\omega'), \tag{2.51}$$

and that $\rho_A(\omega, \omega')$, photon A's spectral density matrix, is given in terms of the two-photon JSA as

$$\rho_A(\omega, \omega') = \int \mathrm{d}\Omega f(\omega, \Omega) f^*(\omega', \Omega). \tag{2.52}$$

From here it is evident that ρ_A is factorable if and only if the JSA f is factorable, such that if the two-photon state is entangled, the reduced state of photon A is necessarily mixed. Furthermore, if we express the JSA in the Schmidt basis, we obtain for the spectral density matrix

$$\rho_A(\omega, \omega') = \sum_i \lambda_i \phi_i^A(\omega) \phi_i^{A*}(\omega'). \tag{2.53}$$

Recalling the definition of the purity of a state as $\mathrm{Tr}(\hat{\rho}_A^2)$, we find

$$\mathcal{P}(\hat{\rho}_A) = \sum_i \lambda_i^2 = \frac{1}{K}. \tag{2.54}$$

Thus the purity of photon A tends to zero as the Schmidt number of the two-photon state increases. The same calculations can be done for the reduced state of photon B, given by $\hat{\rho}_B = \mathrm{Tr}_A(|\Psi_{AB}\rangle \langle\Psi_{AB}|)$, with the result that

$$\rho_B(\omega, \omega') = \sum_i \lambda_i \phi_i^B(\omega) \phi_i^{B*}(\omega') = \int \mathrm{d}\Omega f(\Omega, \omega) f^*(\Omega, \omega'), \tag{2.55}$$

and

$$\mathcal{P}(\hat{\rho}_B) = \frac{1}{K} = \mathcal{P}(\hat{\rho}_A). \tag{2.56}$$

We note, while these calculations have been done for photons entangled in their spectral degree of freedom, these results are general and hold for any pure bipartite quantum state.

Finally, we note that the mixedness of the reduced state provides a valid measure of entanglement of a pure bipartite state. More specifically, the entropy of entanglement of the state $|\Psi_{AB}\rangle$ is defined as the Von Neumann entropy S of either $\hat{\rho}_A$ or $\hat{\rho}_B$, given by

$$S(\hat{\rho}_{A(B)}) = -\mathrm{Tr}\left[\hat{\rho}_{A(B)} \log \hat{\rho}_{A(B)}\right] = -\sum_i \lambda_i \log \lambda_i. \tag{2.57}$$

2.3.3. Mixed-state entanglement

Just as with one photon, the most general quantum state for two photons is a mixed state, represented by a density operator which is a convex combination of pure states:

$$\hat{\rho}_{AB} = \sum_i p_i \left|\Psi^i_{AB}\right\rangle \left\langle\Psi^i_{AB}\right| . \tag{2.58}$$

We can express this state in terms of a two-photon spectral density matrix,

$$\hat{\rho}_{AB} = \int \mathrm{d}^4\omega \; \rho_{AB}(\omega_A, \omega'_A; \omega_B, \omega'_B) \hat{a}^\dagger(\omega_A)\hat{b}^\dagger(\omega_B) \left|\mathrm{vac}\right\rangle \left\langle\mathrm{vac}\right| \hat{a}(\omega'_A)\hat{b}(\omega'_B). \tag{2.59}$$

where $\rho_{AB}(\omega_A, \omega'_A; \omega_B, \omega'_B) = \sum_i p_i f_i(\omega_A, \omega_B) f_i^*(\omega'_A, \omega'_B)$, as for the one photon case. The state $\hat{\rho}_{AB}$ is a product state if it can be expressed as $\rho_{AB} = \rho_A \otimes \hat{\rho}_B$. However, now it is also possible for the state to exhibit classical correlations without being entangled. In general, such a state containing no entanglement is said to be *separable* if it can be expressed as

$$\hat{\rho}_{AB} = \sum_j w_j \hat{\rho}^j_A \otimes \hat{\rho}^j_B, \quad \sum_j w_j = 1, \tag{2.60}$$

otherwise it is entangled. Here we have used the w_j notation for the weighting coefficients simply to distinguish from the p_i.

Unlike for pure states, it is in general not straightforward to determine whether or not a mixed state is entangled. That is, given an arbitrary state $\hat{\rho}_{AB}$, it is not possible in general to show that it *cannot* be expressed in the form (2.60). However, there are numerous criteria in the literature that can test for mixed-state entanglement, usually in the form of necessary but not sufficient conditions for separability. Most notable among these is the Peres-Horodecki separability criterion [55]. In addition, there are quantities which serve as monotonic measures of entanglement. These include the concurrence [56], the entanglement of formation [57], and the negativity and logarithmic negativity [58]. In Chapter

IV, we show a test involving two-photon bunching which distinguished certain entangled states from all separable states, even in the mixed case.

2.3.4. A brief digression on entanglement

Entanglement is notoriously difficult to define in quantum physics and quantum information. Whether a quantum state is entangled or not often reduces to a question of the basis in which we choose to express the state. To give an example, consider a two-photon state consisting of a single photon in horizontal polarization H and on in the vertical polarization V. In this basis the state would be expressed as

$$|\psi\rangle = |1\rangle_H |1\rangle_V , \tag{2.61}$$

which is manifestly a factorable state. However, when expressed in the diagonal-antidiagonal basis, where

$$|1\rangle_D = \frac{|1\rangle_H + |1\rangle_V}{\sqrt{2}}, \quad |1\rangle_A = \frac{|1\rangle_H - |1\rangle_V}{\sqrt{2}}, \tag{2.62}$$

this same state becomes

$$|\psi\rangle = \frac{1}{\sqrt{2}}(|2\rangle_D |0\rangle_A - |0\rangle_D |2\rangle_A), \tag{2.63}$$

which exhibits number entanglement between the diagonal and antidiagonal polarization modes. Note that no physical changed ocurred to this state: we are simply reexpressing it in another basis. This fact crucially emphasizes the basis-dependence of entanglement. Entangled states of light need not even involve more

than a single photon. Indeed, the single-photon state $|1\rangle_D$ from Eq. (2.62), when written more explicitly as

$$|1\rangle_D |0\rangle_A = \frac{1}{\sqrt{2}}(|1\rangle_H |0\rangle_V + |0\rangle_H |1\rangle_V), \tag{2.64}$$

manifests number entanglement between polarization modes H and V. Far from being just a theoretical construct, this kind of modal entanglement is experimentally verifiable using homodyne measurement techniques [59].

When we refer to entanglement of photons, we usually refer to two photons that are spatially separated, that is, that occupy distinguishable spatial modes, and that exhibit entanglement in some additional degree of freedom. For instance, the two photons occupy distinct wavevectors, $\mathbf{k}_1$ and $\mathbf{k}_2$, and yet exhibit polarization entanglement. Such a state might look like

$$|\psi\rangle = \frac{1}{\sqrt{2}} \left(\hat{a}_H^\dagger(\mathbf{k}_1)\hat{a}_V^\dagger(\mathbf{k}_2) - \hat{a}_V^\dagger(\mathbf{k}_1)\hat{a}_H^\dagger(\mathbf{k}_2) \right) |\text{vac}\rangle , \tag{2.65}$$

which is a singlet state for polarization-entangled photons. Often it is convenient to represent such a state with a shorthand such as

$$|\psi\rangle = \frac{1}{\sqrt{2}} \left(|H\rangle_1 |V\rangle_2 - |V\rangle_1 |H\rangle_2 \right) , \tag{2.66}$$

where $|H\rangle_1 = \hat{a}_H^\dagger(\mathbf{k}_1)|\text{vac}\rangle$, for instance, and use expressions such as "photons 1 and 2 are polarization-entangled".

As a final example of an entangled quantum state of light which involves entangled modes but no entangled photons, consider the two-mode squeezed vacuum state, defined by

$$|\xi_{AB}\rangle = \exp(-\xi\hat{a}^\dagger\hat{b}^\dagger + \xi^*\hat{a}\hat{b})\,|\text{vac}\rangle\,, \tag{2.67}$$

where $\hat{a}$ and $\hat{b}$ are annihilation operators for two distinct modes A and B, respectively, and $\xi = r\ e^{i\phi}$ is known as the squeezing parameter. By expanding the exponential this state may be expressed as

$$|\xi_{AB}\rangle = \text{sech}(r)\sum_{n=0}^{\infty}[-e^{i\phi}\tanh(r)]^n\,|n_A; n_B\rangle\,. \tag{2.68}$$

This state exhibits non-classical photon number correlations between modes A and B, and this entanglement may be verified via balanced homodyne detection of the modes [60].

2.4. Parametric down conversion for the generation of EPP

Here we outline the theory of parametric down conversion (PDC), a nonlinear optical process that is the workhorse in quantum optics for generating entangled photon pairs (EPP). Over the past three decades, PDC has been well studied as a means of photon pair generation, and as a result it is now possible to tailor the process to deliver photons with a great amount of control over the modal characteristics and entanglement.

PDC is best described as an interaction involving three fields, the *pump* (p) field, which is provided by a bright laser source, and the *signal* (s) and *idler* (i) fields, which are taken to be in the vacuum state initially. The interaction occurs in a non-linear medium, typically a crystal exhibiting The interaction Hamiltonian for the three fields is given by

$$\hat{H}(t) = \chi \int \mathrm{d}^3 r \hat{E}_p^+(\mathbf{r},t)\hat{E}_s^-(\mathbf{r},t)\hat{E}_i^-(\mathbf{r},t) + \mathrm{H.c.}, \tag{2.69}$$

where χ is a complex coupling parameter associated with the medium, and H.c. denotes the Hermitian conjugate. In a thorough treatment of the theory, the fields are represented as vectors, and χ is a rank 3 tensor coupling the various combinations of field polarizations. However, for the scope of this work, we assume the three fields propagate in a collinear configuration, and we shall denote the relevance of the different polarizations as needed, so that it's sufficient to treat them as scalar quantities. The spatial integral is taken over the volume of the interaction medium, i.e. the crystal, taken to be of length L in the propagation direction.

We expand the fields in terms of their frequency components, giving

$$\begin{gathered}\hat{E}_j^+(\mathbf{r},t) = \int_0^\infty \mathrm{d}\omega_j A_j(\omega_j) \exp\left[i(\mathbf{k}_j(\omega_j)\cdot\mathbf{r} - \omega_j t)\right] \hat{a}_j^\dagger(\omega_j), \\ \hat{E}_j^-(\mathbf{r},t) = \left(\hat{E}_j^+(\mathbf{r},t)\right)^\dagger\end{gathered} \tag{2.70}$$

where $j = p, s, i$, and $A_j = \sqrt{\frac{\hbar\omega_j}{2\epsilon_0 V}}$ is slowly-varying so that it can be taken out of the integration. After absorbing the A_j into the interaction parameter χ, we obtain for the Hamiltonian

$$\begin{aligned}\hat{H}(t) = \chi \int \mathrm{d}^3 r \int \mathrm{d}^3\omega \exp\left[i(\mathbf{k}_p(\omega_p) - \mathbf{k}_s(\omega_s) - \mathbf{k}_i(\omega_i))\cdot\mathbf{r}\right] \\ \times \exp\left[-i(\omega_p - \omega_s - \omega_i)t\right] \hat{a}_p(\omega_p)\hat{a}_s^\dagger(\omega_s)\hat{a}_i^\dagger(\omega_i) + \mathrm{H.c.}.\end{aligned} \tag{2.71}$$

In a typical experimental setting the input state to the PDC process is a strong coherent pump field $|\alpha(\omega)\rangle_p$, with the signal and idler fields in the vacuum state,

so that we may replace the pump annihilation operator with the amplitude $\alpha(\omega)$. The output PDC state after a time t is given by Schrödinger evolution as

$$|\Psi_{\mathrm{PDC}}\rangle = \exp\left[-\frac{i}{\hbar}\int_0^t \mathrm{d}t'\hat{H}(t')\right]|\mathrm{vac}\rangle_{s,i} \approx \left(\hat{I} - \frac{i}{\hbar}\int_0^t \mathrm{d}t'\hat{H}(t')\right)|\mathrm{vac}\rangle_{s,i} \tag{2.72}$$

where the last approximation is valid in the weak interaction limit. Since the Hermitian conjugate part of the Hamiltonian annihilates the vacuum and gives 0, the output PDC state is

$$|\Psi_{\mathrm{PDC}}\rangle = \left(1 - \frac{i\chi}{\hbar}\int_0^t \mathrm{d}t' \int \mathrm{d}^3r \int \mathrm{d}^3\omega \exp\left[i(\Delta\mathbf{k}\cdot\mathbf{r} - \Delta\omega t')\right]\alpha(\omega_p)\hat{a}_s^\dagger(\omega_s)\hat{a}_i^\dagger(\omega_i)\right)|\mathrm{vac}\rangle_{s,i} \tag{2.73}$$

where we have defined $\Delta\mathbf{k} = \mathbf{k}_p(\omega_p) - \mathbf{k}_i(\omega_i) - \mathbf{k}_s(\omega_s)$ and $\Delta\omega = \omega_p - \omega_s - \omega_i$.

We take the pump field to be an ultrashort laser pulse, such that the interaction time is set by the pulse duration. This allows us to take the time integral to infinity, obtaining a delta function in frequency,

$$\int \mathrm{d}t' \exp\left[-i\Delta\omega t'\right] = 2\pi\delta(\Delta\omega).$$

This corresponds to energy conservation, since it imposes that $\omega_s + \omega_i = \omega_p$, and it allows us to also integrate over one of the frequencies. We choose ω_p, and replace all its occurrences with $\omega_s + \omega_i$.

As a further simplification, we take the spatial integral to infinity in the transverse spatial directions, x and y, by assuming that the transverse profiles interacting beams fit entirely within the crystal's cross-sectional area. Meanwhile,

the z integral is taken over the length L of the crystal. Thus for the spatial integral we have

$$\begin{aligned}\int \mathrm{d}^3 r \exp\left[i\Delta\mathbf{k}\cdot\mathbf{r}\right] &= \int \mathrm{d}x\ e^{i\Delta k_x x} \int \mathrm{d}y\ e^{i\Delta k_y y} \int_0^L \mathrm{d}z\ e^{i\Delta k_z z} \\ &= (2\pi)^2 \delta(\Delta k_x)\delta(\Delta k_y) \int_0^L \mathrm{d}z\ e^{i\Delta k_z z}.\end{aligned}$$

We assume a collinear configuration, where all the fields are copropagating along the z direction, so that $\Delta k_x = \Delta k_y = 0$. Then the spatial integral evaluates to

$$\int \mathrm{d}^3 r \exp\left[i\Delta\mathbf{k}\cdot\mathbf{r}\right] = (2\pi)^2 2L \exp\left[\frac{i\Delta k_z L}{2}\right] \mathrm{sinc}\left[\frac{\Delta k_z L}{2}\right].$$

Using these results, and absorbing all constant factors into χ (including $\hbar$), we may finally express the output state as

$$|\Psi_{\mathrm{PDC}}\rangle = |\mathrm{vac}\rangle_{s,i} - i\chi \int \mathrm{d}\omega_s \mathrm{d}\omega_i \alpha(\omega_s+\omega_i)\Phi(\omega_s,\omega_i)\hat{a}_s^\dagger(\omega_s)\hat{a}_i^\dagger(\omega_i)\,|\mathrm{vac}\rangle_{s,i}\,, \tag{2.74}$$

where we have introduced the *phasematching function* Φ, given by

$$\begin{aligned}\Phi(\omega_s,\omega_i) &= \exp\left[\frac{i\Delta k L}{2}\right] \mathrm{sinc}\left[\frac{i\Delta k L}{2}\right], \\ \Delta k &= k_p(\omega_s+\omega_i) - k_s(\omega_s) - k_i(\omega_i),\end{aligned} \tag{2.75}$$

with the z subscript omitted for clarity. This quantity corresponds to momentum conservation in the PDC process, and takes on its maximum value when $k_s + k_i = k_p$.

By inspection it can be seen that the product of the pump amplitude $\alpha(\omega_s + \omega_i)$ and the phasematching function $\Phi(\omega_s, \omega_i)$ constitutes a JSA for the two-photon PDC state:

$$f(\omega_s, \omega_i) = \alpha(\omega_s + \omega_i)\Phi(\omega_s, \omega_i). \tag{2.76}$$

By controlling these two quantities, it is possible to generate a rich variety of two-photon states with tailored spectral properties and time-frequency entanglement. The phasematching function is ultimately dependent on the dispersion properties of the nonlinear crystal. These may be calculated for a given crystal through the empirical Sellmeier equations[1]. Meanwhile the pump amplitude function may be controlled through laser source engineering and pulse-shaping techniques. Much progress has been made on both of these fronts in the last few decades, and a good review of the state of the art in two-photon spectral-temporal engineering may be found in Ref. [2]. Here we shall briefly outline a few important aspects of standard PDC sources in order to understand how they contribute to a variable amount of spectral-temporal entanglement.

2.4.1. Pump amplitude

The pump amplitude function is perhaps the easiest aspect to understand. It is a function of the sum frequency $\omega_s + \omega_i$ of the signal and idler photons, and, when derived from a pulsed laser system, it is adequately represented by a Gaussian profile:

[1]Since $k(\omega) = \omega n(\omega)/c$, where $n(\omega)$ is the index of refraction.

$$\alpha(\omega_s + \omega_i) = \alpha \exp\left[-\frac{(\omega_s + \omega_i - \omega_0)^2}{\sigma^2}\right] \exp\left[i\phi(\omega_s + \omega_i)\right], \tag{2.77}$$

where ω_0 is the carrier frequency, and $\phi(\omega_s + \omega_i)$ is some spectral phase, which is at most a linear function for a transform-limited pulse. In the limit of monochromatic pumping using a continuous wave (CW) laser,

$$\alpha(\omega_s + \omega_i) \to \delta(\omega_s + \omega_i - \omega_p).$$

The pump amplitude function can be plotted as a function of the signal and idler frequencies. Because it is a function of only the sum of these frequencies, it only varies along the diagonal direction in this plot. This behavior can be seen in the JSA plots in Fig. 2.2 below.

2.4.2. Birefringent phasematching

An important property of several crystals is birefringence, where there are two distinct indices of refraction for the two orthogonal polarizations of light propagating through the crystal. A detailed analysis of birefringence is beyond the scope of this work, and can be found, for example, in Fowles [61]. For our purposes it is sufficient to note that the anisotropy of the crystal lattice structure generally distinguishes two polarizations for an incident beam of light: one for which the index of refraction varies as a function of an angle θ between $\mathbf{k}_p$ and the crystal axis, known as the *extraordinary*, or e-, polarization, and one for which the index of refraction does not vary, known as the *ordinary*, or o-, polarization. The angle dependence of the e-polarization index of refraction is given by

$$n_e(\theta) = \left[\frac{\cos^2\theta}{n_o^2} + \frac{\sin^2\theta}{n_e^2} \right]^{-1/2}, \tag{2.78}$$

where n_o is the ordinary index, and n_e is the maximum value of the extraordinary index.

There are two configurations which make use of birefringent phasematching: type I, where the signal and idler fields share the same polarization, (say o-polarized), while the pump field is orthogonally polarized (e-polarized); and type II, where the signal and idler fields are orthogonally polarized (one e-polarized and one o-polarized), while the pump field is either e- or o-polarized[2].

To calculate the correct phasematching angle configuration for a given combination of pump, signal, and idler frequencies (or wavelengths), one can numerically solve the phasematching condition for θ, which corresponds to, for example,

$$k_e(\omega_s + \omega_i, \theta) = k_o(\omega_s) + k_o(\omega_i) \tag{2.79}$$

for type I, and

$$k_e(\omega_s + \omega_i, \theta) = k_e(\omega_s, \theta) + k_o(\omega_i) \tag{2.80}$$

for type II, using the fact that

$$k_o(\omega) = \frac{\omega n_o(\omega)}{c}, \quad k_e(\omega, \theta) = \frac{\omega n_e(\omega, \theta)}{c}. \tag{2.81}$$

[2]A convenient shorthand to denote these configurations is $e \to o+o$ or $o \to e+e$ for type I, and $e \to o+e$ or $o \to o+e$ for type II.

The dependence of n_o and n_e on ω is given by the dispersion relations obtained from the Sellmeier equations for a given crystal. In this work, we further restrict our consideration to degenerate phasematching, corresponding to an angle θ_D which solves the above equations with $\omega_s = \omega_i = \omega_0/2$.

In this case the most salient distinguishing feature of these two types of phasematching is the behavior of the phasematching function near the degenerate point (ω_0, ω_0) on the $\omega_s - \omega_i$ plane and the amount of entanglement it creates in the JSA. For type I, signal and idler experience the same dispersion. This results in the phasematching function being symmetric with respect to the two frequencies near the degenerate point, and running parallel to the pump amplitude function. This provides a high amount of overlap between the two functions and produces a JSA that is highly anti-correlated. In the type II case, since the signal and idler fields don't experience the same amount of dispersion, the phasematching function will not be symmetric near the degenerate point, and will be maximal at a direction that is generally oblique with respect to the pump amplitude function. This results in less entangled state, generally. In Peter Mosley's dissertation [62], it is shown how to take advantage of this configuration, and, by tuning the pump and phasematching bandwidths, create a two-photon state exhibiting close to no time-frequency correlations. In Fig. 2.2, we plot two typical JSA's obtainable through PDC, one via type 0 or I phasematching, and one via type II phasematching, showing a different degree of spectral correlations.

2.4.3. Quasi-phasematching through periodic poling

Another technique to achieve the phasematching condition is through periodic poling. This consists of applying a voltage to the crystal to reverse the

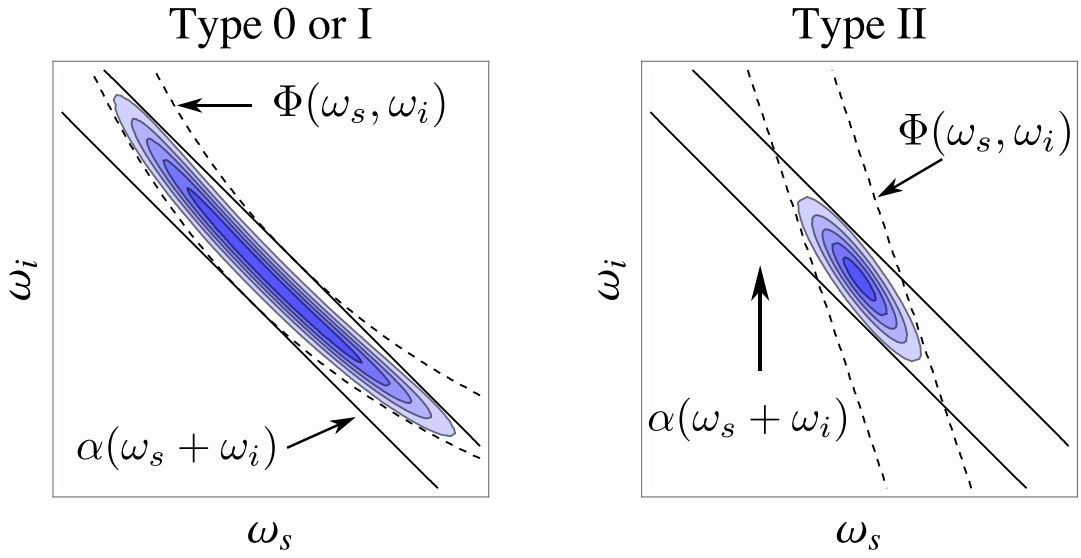

FIGURE 2.2. Two typical JSA's $f(\omega_s, \omega_i)$ (blue contour plots) obtainable through PDC. In both cases, the pump amplitude function α, here a Gaussian, is a symmetric function of ω_s, ω_i (solid contours). The phasematching function Φ is approximated as a Gaussian function here (dashed contours). For type 0 or I phasematching, Φ is symmetric where it crosses the $\omega_s = \omega_i$ line, and this typically leads to a high degree of frequency correlation in the JSA. Meanwhile, for type II phasematching, because the signal and idler fields experience different dispersion, there is no such symmetry.

domains of the crystal in a periodic fashion across its length. A treatment of the underlying physics can be found in Boyd, for example [63]. For our purposes, we can have an intuition for how this works by noticing that, for a small phase mismatch Δk, the spatial integral in the Hamiltonian (2.71) has the effect of cycling the energy periodically between the pump field and the signal and idler fields. The idea behind quasi-phasematching is to periodically reverse the direction of this cycling, such that the energy flow is towards the signal and idler fields. Thus the poling period Λ is chosen so that

$$\Delta k = \frac{2\pi}{\Lambda}, \tag{2.82}$$

and it is typically on the order of a few microns. Although quasi-phasematching can be, and is, combined with birefringent phasematching configurations, it is most useful for the case of type 0 phasematching, where the pump, signal, and idler fields are all co-polarized. In Reference [2], it is shown how quasi-phasematching is combined with type II phasematching, along with pump pulse shaping, to achieve two-photon states with a controllable number of Schmidt modes, as well as for the construction of highly versatile mode-selective quantum pulse gates.

2.5. Quantum measurement model of photon detection

In the laboratory, light can be detected at the single photon level using "click" detectors. These are detectors designed to give a macroscopic signal upon detection of a single photon. The most commonly available detectors of this kind are avalanche photodiodes (APDs), whereby a semiconducting detector is operated with a bias voltage, such that a single incident photon triggers an avalanche of photoelectrons, resulting in an electric pulse which can then be

detected using standard electronics. Another, more recent type of detector are the superconducting nanowire single-photon detectors (SNSPDs). These rely on a detection element in the form of a coiled wire cooled down just below the superconducting threshold temperature, such that there is no electrical resistance across the wire. The incidence of a single photon temporarily raises the temperature of the wire and induces a resistance, which is converted to an electrical pulse again to be detected electronically. Our laboratory uses both of these types of detectors, but in the current context, we shall abstract away from the physics and describe these click detections using the quantum measurement formalism. A proper description of the theory of photodetection can be found in standard quantum optics textbooks such as Mandel and Wolf [64].

2.5.1. Single-photon detection

The most rudimentary click detector for our purposes is one that clicks when it absorbs one or more photons, but does not distinguish between different photon numbers, or reveal any spectral-temporal information other than the arrival time to within a small finite integration time. This is a good approximation to the actual detectors in the laboratory. These detectors are fiber-coupled, so that we can neglect the spatial response and assume all the detected light is in a single spatial mode with annihilation operator $\hat{a}$. Further, we assume that the detector has uniform quantum efficiency η over the range of spectral modes of interest: given that a single photon in this spectral range is incident, the detector will click with probability η.

Using the positive operator-valued (POVM) formalism, we can express the POVM element for detecting no clicks as [65]

$$\hat{\Pi}_{\text{noclick}} = \sum_{n=0}^{\infty} (1-\eta)^n \hat{\Pi}_n, \tag{2.83}$$

and the one corresponding to obtaining a click as

$$\hat{\Pi}_{\text{click}} = \mathbb{1} - \sum_{n=0}^{\infty} (1-\eta)^n \hat{\Pi}_n \tag{2.84}$$

where $\mathbb{1}$ is the identity in the relevant Hilbert space. We define the $\hat{\Pi}_n$ as the POVM elements corresponding to detecting n photons in the field if the detector *could* resolve the photon number:

$$\hat{\Pi}_n = \begin{cases} |\text{vac}\rangle \langle \text{vac}| & n = 0 \\ \int \mathrm{d}\omega_1 \ldots \mathrm{d}\omega_n \; \hat{a}^\dagger(\omega_1) \ldots \hat{a}^\dagger(\omega_n) |\text{vac}\rangle \langle \text{vac}| \, \hat{a}(\omega_1) \ldots \hat{a}(\omega_n) & n \geq 1. \end{cases} \tag{2.85}$$

These definitions ensure that, given that the field is in some one-photon state $|\psi_j\rangle$ as defined in (2.25), the probabilty of obtaining a click or obtaining no click are, respectively

$$p_{\text{click}} = \langle \psi_j | \hat{\Pi}_{\text{click}} |\psi_j\rangle = \eta, \quad p_{\text{noclick}} = \langle \psi_j | \hat{\Pi}_{\text{noclick}} |\psi_j\rangle = 1 - \eta. \tag{2.86}$$

Finally, we note that although real detectors are susceptible to dark counts, where spurious counts are registered even in the presence of no photons, we neglect these in our model since their rates are typically very low, and in the coincidence detection schemes we employ, the error they contribute is negligible. For the

remainder of this section, we will assume that there is at most one photon incident on the detector during its integration time. This allows us to focus solely on

$$\hat{\Pi}_1 = \int \mathrm{d}\omega \hat{a}^\dagger(\omega) \left|\mathrm{vac}\right\rangle \left\langle\mathrm{vac}\right| \hat{a}(\omega), \tag{2.87}$$

as a representation of a single-photon detection, and show what kind of information can be gained about light given a click from such a detector, particularly in the context of entangled photons.

Consider the two-photon state $|\Psi_{AB}\rangle$ from (2.40), and suppose that we use a single photon detector to detect photon B, which indicates the presence of photon A (this is known as heralding). We represent this detection by the writing the POVM as

$$\hat{\Pi}^B = \int \mathrm{d}\omega \hat{b}^\dagger(\omega) \left|\mathrm{vac}\right\rangle \left\langle\mathrm{vac}\right| \hat{b}(\omega), \tag{2.88}$$

where we have dropped the 1 subscript for convenience.. After the detection, the state of photon A will be given by

$$\begin{aligned} \hat{\rho}^A &= \frac{\mathrm{Tr}_B(\hat{\Pi}_1^B \left|\Psi_{AB}\right\rangle \left\langle\Psi_{AB}\right|)}{\mathrm{Tr}(\hat{\Pi}_1^B \left|\Psi_{AB}\right\rangle \left\langle\Psi_{AB}\right|)} \\ &= \int \mathrm{d}\omega \mathrm{d}\omega' \rho^A(\omega,\omega') \hat{a}^\dagger(\omega) \left|\mathrm{vac}\right\rangle \left\langle\mathrm{vac}\right| \hat{a}(\omega'), \end{aligned} \tag{2.89}$$

with $\rho^A(\omega,\omega')$ given by (2.52). Since the detector does not resolve frequency, the only information we gain is the presence of photon A, and any spectral entanglement between the two photons will result in a corresponding mixedness of the heralded photon.

We now consider restricting the detector's spectral range by placing a frequency bandpass filter in front of it, which we model using a complex

transmission amplitude function $\mathcal{T}_j(\omega)$[3], whose support is restricted around some frequency ω_j with a finite bandwidth [66]. This results in a measurement operator given by

$$\hat{\Pi}_j^B = \int \mathrm{d}\omega \; |\mathcal{T}_j(\omega)|^2 \; \hat{b}^\dagger(\omega) \, |\mathrm{vac}\rangle \, \langle \mathrm{vac}| \, \hat{b}(\omega), \tag{2.90}$$

and the heralded state of photon A is given

$$\hat{\rho}_j^A = \int \mathrm{d}\omega \mathrm{d}\omega' \rho_j^A(\omega, \omega') \hat{a}^\dagger(\omega) \, |\mathrm{vac}\rangle \, \langle \mathrm{vac}| \, \hat{a}(\omega'), \tag{2.91}$$

where

$$\rho_j^A(\omega, \omega') = \frac{\int \mathrm{d}\Omega |\mathcal{T}_j(\Omega)|^2 f(\omega, \Omega) f^*(\omega', \Omega)}{\int \mathrm{d}\Omega \mathrm{d}\Omega' |\mathcal{T}_j(\Omega)|^2 |f(\Omega', \Omega)|^2}. \tag{2.92}$$

where the integration range is now narrowed down by the filter function, thus reducing the mixedness of the state.

In the limit that $\mathcal{T}_j(\omega) \; \rightarrow \; \delta(\omega - \omega_j)$ the measurement becomes an ideal spectrally resolved measurement

$$\hat{\Pi}_j^B \rightarrow \hat{\Pi}^B(\omega_j) = \hat{b}^\dagger(\omega_j) \, |\mathrm{vac}\rangle \, \langle \mathrm{vac}| \, \hat{b}(\omega_j). \tag{2.93}$$

In this limit, the heralded photon A now has a spectral density matrix given by

$$\rho_j^A(\omega, \omega') = \frac{f(\omega, \omega_j) f^*(\omega', \omega_j)}{\int \mathrm{d}\Omega |f(\Omega, \omega_j)|^2}. \tag{2.94}$$

[3]A filter can be modeled as a frequency-dependent beamsplitter, with transmission and reflection amplitudes $\mathcal{T}_j(\omega)$ and $\mathcal{R}_j(\omega)$, obeying the unitarity relation $|\mathcal{T}_j(\omega)|^2 + |\mathcal{R}_j(\omega)|^2 = 1$.

Closer inspection shows that this is just a pure single-photon state, which we may express as

$$|\phi_j^A\rangle = \int \mathrm{d}\omega \phi_j^A(\omega)\hat{a}^\dagger(\omega)\,|\mathrm{vac}\rangle\,, \quad \phi_j^A(\omega) = \frac{f(\omega,\omega_j)}{\sqrt{\rho^B(\omega_j,\omega_j)}}, \tag{2.95}$$

where ρ^B is the spectral density matrix for photon B as defined in (2.55). Although this limit is unphysical, it provides a good understanding of some our main results in this dissertation, and the definitions ensure that the pure states are normalizable and have an intuitive physical interpretation.

2.5.2. Two-photon detection

Next we consider the joint detection of single photons using two detectors. The most general measurement operator would be a tensor product of POVM elements for each of modes A and B,

$$\hat{\Pi}^{AB}_{\mathrm{click}} = \hat{\Pi}^{A}_{\mathrm{click}} \otimes \hat{\Pi}^{B}_{\mathrm{click}}. \tag{2.96}$$

However, in the present case, we will restrict our consideration to only the one photon term from each element. Again omitting the 1 subscript for clarity, we have

$$\hat{\Pi}^{AB} = \int \mathrm{d}\omega \mathrm{d}\omega' \hat{a}^\dagger(\omega)\hat{b}^\dagger(\omega')\,|\mathrm{vac}\rangle\,\langle\mathrm{vac}|\,\hat{a}(\omega)\hat{b}(\omega'). \tag{2.97}$$

The extensions to the filtered coincidence detection

$$\hat{\Pi}^{AB}_{jk} = \int \mathrm{d}\omega \mathrm{d}\omega'\ |\mathcal{T}_j(\omega)|^2\ |\mathcal{T}_k(\omega')|^2\ \hat{a}^\dagger(\omega)\hat{b}^\dagger(\omega')\,|\mathrm{vac}\rangle\,\langle\mathrm{vac}|\,\hat{a}(\omega)\hat{b}(\omega'), \tag{2.98}$$

and to the spectrally-resolved coincidence detection

$$\hat{\Pi}^{AB}(\omega_j, \omega_k) = \hat{a}^\dagger(\omega_j)\hat{b}^\dagger(\omega_k) \left|\text{vac}\right\rangle \left\langle\text{vac}\right| \hat{a}(\omega_j)\hat{b}(\omega_k), \tag{2.99}$$

are readily obtained. The spectrally-resolved detection gives a direct measure of the JSI of the two-photon state, since the probability of a coincidence is

$$P(\omega_j, \omega_k) = \left\langle\Psi_{AB}\right| \hat{\Pi}^{AB}(\omega_j, \omega_k) \left|\Psi_{AB}\right\rangle = |f(\omega_j, \omega_k)|^2 = F(\omega_j, \omega_k). \tag{2.100}$$

2.5.3. Bell state measurements on two-photon states

A crucial feature of measurements in quantum mechanics is that they affect the post-measurement state. This is widely recognized by students of quantum mechanics in the famous Stern-Gerlach experiment, where a measurement of an electron's spin along the z-axis ensures that subsequent measurements along that same axis are bound to give the same result (always spin up, for instance), while causing measurements along the other two axes (x and y) to give either result (spin up or down) randomly. In the language of quantum mechanics, this is because a measurement of spin in the z basis projects the spin state onto an eigenstate of the spin-z operator, which is not an eigenstate of the spin-x or spin-y operators [67].

This projective property of quantum measurements is not as obvious in the case of photon detection, because a photon cannot be measured again once it has been detected. However, it becomes easier to appreciate when we consider detection of entangled photons. We have already seen how detecting photon B from the frequency-entangled state $\left|\Psi_{AB}\right\rangle$ without resolving its frequency results

in photon A being described by a mixed state $\hat{\rho}^A$. Meanwhile, choosing instead to resolve the frequency of photon B, and obtaining the result ω_j, projects photon A onto a pure state $|\phi^A\rangle$. As another example, consider the two-mode squeezed vacuum state $|\xi_{AB}\rangle$ from Eq. (2.68). Without applying any detection to mode B, the reduced state of mode A is completely mixed state, known as thermal state, with an exponential photon number distribution. However, detecting n photons in mode B projects mode A into a Fock state with n photons. In fact, the most complete description of the PDC state is an ensemble of two-mode squeezed vacua exhibiting pairwise photon number correlations, and the example just described is precisely what happens when we produce heralded single (or n) photon states.

Of particular importance in many quantum protocols is the Bell state measurement (BSM), which is a projective measurement onto one or more of the Bell states, the maximally entangled states for a bipartite system. For a system of two qubits with basis states $\{|0\rangle_{A(B)}, |1\rangle_{A(B)}\}$, the four Bell states are

$$\begin{aligned} |\Phi^{\pm}\rangle &= \frac{1}{\sqrt{2}}(|0\rangle_A |0\rangle_B \pm |1\rangle_A |1\rangle_B), \\ |\Psi^{\pm}\rangle &= \frac{1}{\sqrt{2}}(|0\rangle_A |1\rangle_B \pm |1\rangle_A |0\rangle_B). \end{aligned} \tag{2.101}$$

It is known that, using linear optics and coincidence photon detection, it is possible to implement a BSM. However, such a linear-optics BSM can only project onto a two-qubit Bell-state of the form above, and furthermore, it is an incomplete BSM, in that it can at most distinguish three out of these four Bell states [51]. For many quantum protocols, it suffices to implement an incomplete BSM which projects onto one of the Bell states, namely $|\Psi^-\rangle$, and in our work, the two qubits are two photons occupying two distinct frequency modes.

The BSM is achieved as follows: Two single photons are incident on the opposite input modes $\hat{a}$ and $\hat{b}$ of a 50-50 beam splitter, which transmits half and reflects half of each input mode. The output modes $\hat{c}$ and $\hat{d}$ are given in terms of the input modes as

$$\hat{c}(\omega) = \frac{\hat{a}(\omega) + \hat{b}(\omega)}{\sqrt{2}}, \quad \hat{d}(\omega) = \frac{\hat{a}(\omega) - \hat{b}(\omega)}{\sqrt{2}}, \tag{2.102}$$

which amounts to a unitary basis transformation. Now consider placing a frequency-resolved single-photon detector at each output mode, such that a coincidence detection is given by

$$\hat{\Pi}^{CD}(\omega_j, \omega_k) = \hat{c}^\dagger(\omega_j)\hat{d}^\dagger(\omega_k) \left|\text{vac}\right\rangle \left\langle\text{vac}\right| \hat{c}(\omega_j)\hat{d}(\omega_k). \tag{2.103}$$

When expressed in the basis of the input modes, this becomes

$$\begin{aligned}\hat{\Pi}^{CD}(\omega_j, \omega_k) = \frac{1}{2}\left(\hat{a}^\dagger(\omega_j)\hat{a}^\dagger(\omega_k) - \hat{a}^\dagger(\omega_j)\hat{b}^\dagger(\omega_k) + \hat{b}^\dagger(\omega_j)\hat{a}^\dagger(\omega_k) - \hat{b}^\dagger(\omega_j)\hat{b}^\dagger(\omega_k)\right)\left|\text{vac}\right\rangle \\ \times \left\langle\text{vac}\right| \frac{1}{2}\left(\hat{a}(\omega_j)\hat{a}(\omega_k) - \hat{a}(\omega_j)\hat{b}(\omega_k) + \hat{b}(\omega_j)\hat{a}(\omega_k) - \hat{b}(\omega_j)\hat{b}(\omega_k)\right).\end{aligned} \tag{2.104}$$

Considering that there is only one input photon in each of the modes $\hat{a}$ and $\hat{b}$, the terms containing a product of two $\hat{a}$'s or two $\hat{b}$'s do not contribute to the detection, and a successful coincidence detection projects onto a two-photon, two-frequency Bell state

$$\hat{\Pi}^{CD}(\omega_j, \omega_k) = \left|\Psi_{jk}\right\rangle \left\langle\Psi_{jk}\right|, \tag{2.105}$$

with

$$|\Psi^{-}_{jk}\rangle = \frac{1}{\sqrt{2}}\left(\hat{a}^{\dagger}(\omega_j)\hat{b}^{\dagger}(\omega_k) - \hat{a}^{\dagger}(\omega_k)\hat{b}^{\dagger}(\omega_j)\right)|\text{vac}\rangle\,. \tag{2.106}$$

It is important to point out that the input state need not have been in this Bell state before the measurement, and it need not have been entangled at all, in order to obtain a successful detection with non-zero probability. All that is required is that it had some non-zero overlap (in the inner product sense) with the Bell state. Indeed, this is the power of the BSM, in the case of a complete BSM, in that it can project any input state onto a Bell state, since the Bell states form a basis for the bipartite Hilbert space over which they are defined.

BSM's of the kind we just described, using a beam splitter and projecting onto Bell states of various degrees of freedom of light, are a key ingredient in the implementation of several quantum protocols, including quantum teleportation [28], superdense coding [68], and entanglement swapping [34], and the reader is encouraged to review these references for a detailed analysis.

2.5.4. Bridge

Having developed a basic understanding of multimode quantum optics and two-photon entanglement in the time-frequency domain, in the next chapter, we will describe a striking demonstration of the power BSM's on spectrally-entangled photons. We will demonstrate an entanglement swapping scheme, which takes two pairs of multimode entangled photons, and using linear optics and spectral resolution, transforms that entanglement into several, mutually orthogonal, frequency-encoded Bell states. This is an important step towards implementing entangled measurements that utilize the multimode nature of time-frequency entanglement.

CHAPTER III

SPECTRAL ENTANGLEMENT SWAPPING VIA MULTIMODE BELL STATE MEASUREMENTS

This Chapter includes material that was published in: Merkouche, S., Thiel, V., and Smith, B. J. "Spectrally resolved four-photon interference of time-frequency-entangled photons", *Phys. Rev. A* **105**, 023708 (2022). Reprinted with permission from the authors. I developed the theory and conceived the experiment. VT and I performed the experiment and data analysis, and wrote the paper. BJS was the principal investigator for this work.

3.1. Introduction

With the advent of the quantum information age, it is well-established by now that the encoding of quantum information into the degrees of freedom of light is the key component of quantum communication networks [14]. Whereas polarization and spatial-mode encoding benefit from ease of implementation, they are prone to scrambling from environmental noise and optical-fiber transmission, which undermines their suitability for long-distance communication. Meanwhile, the time-frequency (TF) degree of freedom is more robust in this regard (frequency-channel crosstalk does not occur in optical fiber), and TF-encoding has now been established as a complete toolkit for quantum-information processing [35], opening an active venue of research into the generation, manipulation, and measurement of TF-encoded quantum states of light.

In the quantum regime, entanglement plays a key role in many protocols for computation [69] and communication [23, 70]. Furthermore, entanglement of

photons has recently been of great interest to the metrology and spectroscopy communities due to its promise of enhancements in sensitivity beyond what is attainable in the classical domain [71]. It comes as no surprise, then, that the generation of photon pairs in well-defined TF-entangled states is a widely-researched area of quantum optics, and great strides have been made over this terrain in the past two decades [2]. In addition to state generation, harnessing the full capabilities of quantum entanglement also requires the ability to perform projective measurements onto entangled states. Indeed, entangled measurements [31], of which the Bell-state measurement is the prototype, are nearly as ubiquitous in quantum protocols as entangled states, most notably in quantum teleportation [28] and entanglement swapping [34].

In this work, we describe theoretically, and demonstrate experimentally, an entanglement swapping scheme that relies on the multimode nature of TF-entanglement in pairs of photons. The central component of the setup is a multimode, frequency-resolved Bell-state measurement (BSM), performed on idler photons from two independent TF-entangled pairs generated from spontaneous parametric down conversion (SPDC). The BSM heralds the signal photons onto a pulsed Bell state whose central frequencies depend on the result of the BSM. In this way we are able to herald multiple orthogonal Bell pairs and verify entanglement in each pair, all derived from the same source state and within the measurement scheme. This aspect of our work can be viewed as a generalization of pulse-mode entanglement swapping, such as that reported in Ref. [50], to utilizing the high-dimensional TF entanglement that is available in standard of-the-shelf SPDC sources. In section 3.2 we outline the theory underlying our work. In section 3.3 we describe the experimental setup. Then, in section 3.4 we

describe our results, which show remarkable agreement with a simple and intuitive Gaussian model using pure quantum states, before concluding in section 3.5. Finally, in the Appendix we cover the more technical details of our work which would otherwise encumber the account of our main results.

3.2. Theory

3.2.1. Four photon state

The entanglement swapping protocol we realize is depicted conceptually in Fig. 3.1. The protocol consists of two independent spontaneous parametric down conversion (SPDC) sources. Each source generates pairs of photons into paths labeled by the bosonic operators $\hat{a}_n$ for the signal and $\hat{b}_n$ for the idler, where $n \in \{1, 2\}$ labels the two sources. Here we consider pulsed collinear type II SPDC sources, where the signal and idler modes are distinguished by their orthogonal polarization. Furthermore, all the light is collected into single-mode optical fibers, so that only the time-frequency degree of freedom is relevant.

In Appendix A.1, we derive the general four-photon quantum state of SPDC in the context of Fig. 3.1. Generally, this state is a coherent superposition containing terms corresponding to either source generating two pairs of photons, as well as a term corresponding to each source generating exactly one pair of photons. This last term is the one of interest throughout this work, and in Appendix A.1 we outline the assumptions that allow us to consider solely this term. Under the assumptions that both sources are identical, the four photon state arising from this

term is given by

$$|\psi\rangle = \int \mathrm{d}^4\omega \; f(\omega_\mathrm{S}, \omega_\mathrm{I}) f(\omega'_\mathrm{S}, \omega'_\mathrm{I}) \; \hat{a}_1^\dagger(\omega_\mathrm{S}) \hat{b}_1^\dagger(\omega_\mathrm{I}) \hat{a}_2^\dagger(\omega'_\mathrm{S}) \hat{b}_2^\dagger(\omega'_\mathrm{I}) \, |\mathrm{vac}\rangle \,, \tag{3.1}$$

where $f(\omega_\mathrm{S}, \omega_\mathrm{I})$ is the joint spectral amplitude (JSA) associated with either source. The modulus squared of the JSA, known as the joint spectral intensity (JSI), corresponds to the probability density function for creating a pair of photons, called signal and idler, at optical frequencies ω_S and ω_I, respectively. The two-photon state from either source contains spectral entanglement when the JSA cannot be factored into a product of the form $f(\omega_\mathrm{S}, \omega_\mathrm{I}) = f_\mathrm{S}(\omega_\mathrm{S}) f_\mathrm{I}(\omega_\mathrm{I})$.

Most of the experiments in this chapter rely on performing a spectrally-resolved BSM on the idler photons. Although the spectral resolution of this BSM is finite, we model the results in the limit of narrow spectral resolution. This limit has the benefit of providing a simple and intuitive model with which to understand the physics in terms of pure quantum states. A more complete model taking into account the finite spectral resolution of the BSM and the resulting states is then easily constructed from this pure-state approximation, which is done in Appendix A.2. As we shall see, the pure-state approximation is sufficient to account for the majority of the results of our experiment.

3.2.2. Heralded state and JSI

A Bell-state measurement is performed on the idler photons by resolving their frequencies at the output of a 50:50 beam splitter, with a small path difference at the input giving a relative time delay τ_I as depicted in Fig. 3.1. The

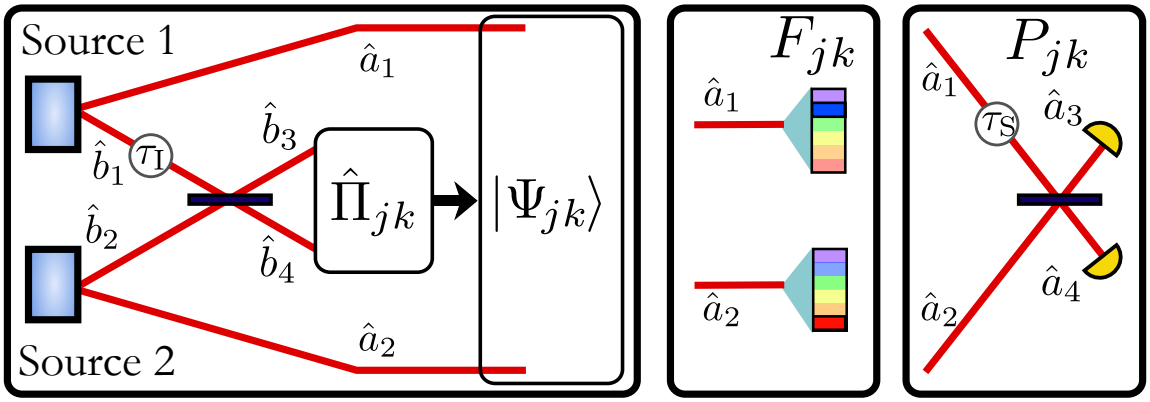

FIGURE 3.1. Conceptual scheme of the experiment. Two sources, 1 and 2, emit photon pairs into the modes labelled $\hat{a}$ and $\hat{b}$ for signal and idler, respectively. The BSM $\hat{\Pi}_{jk}$ on the idler photons projects the signal photons onto the state $|\Psi_{jk}\rangle$. This state in the signal modes is characterized by measuring its JSI F_{jk}, as well as the two-photon interference signal P_{jk}. The time delays τ_I and τ_S serve to balance the interferometer.

beam splitter transforms the input field operators $\hat{b}_1^\dagger$, $\hat{b}_2^\dagger$ into

$$\begin{aligned}\hat{b}_3^\dagger(\Omega) &= \frac{e^{i\Omega\tau_\mathrm{I}}\hat{b}_1^\dagger(\Omega) + \hat{b}_2^\dagger(\Omega)}{\sqrt{2}},\\ \hat{b}_4^\dagger(\Omega') &= \frac{e^{i\Omega'\tau_\mathrm{I}}\hat{b}_1^\dagger(\Omega') - \hat{b}_2^\dagger(\Omega')}{\sqrt{2}},\end{aligned} \tag{3.2}$$

and coincidences are detected between $\hat{b}_3$ and $\hat{b}_4$. For clarity, we will label the optical frequencies of the idlers as Ω and those of the signals as ω. Because we use the pure state approximation, we can consider that this spectral measurement is achieved with perfect resolution, whereby the measurement operator is given by

$$\hat{\Pi}_{jk} = \hat{b}_3^\dagger(\Omega_j)\hat{b}_4^\dagger(\Omega_k)\,|\mathrm{vac}\rangle\,\langle\mathrm{vac}|\,\hat{b}_3(\Omega_j)\hat{b}_4(\Omega_k) \tag{3.3}$$

which is a projector onto single photon states with monochromatic frequencies Ω_j and Ω_k. Although this limit of frequency-resolved detection corresponds to projective measurements, it is important to recognize that a more realistic

model of the measurement with finite resolution should incorporate a positive operator-valued measure (POVM) element defined over a frequency band, as we outline in Appendix A.2. Furthermore, since the POVM formalism describes the most general quantum measurements, projectors such as $\hat{\Pi}_{jk}$ are indeed POVM elements, and for consistency throughout the text, we refer to all our measurement operators as POVM elements. We define

$$|\Omega_j, \Omega_k\rangle_{34} = \hat{b}_3^\dagger(\Omega_j)\hat{b}_4^\dagger(\Omega_k)\,|\text{vac}\rangle\,,$$

and we compute the heralded signal state, $|\Psi_{jk}\rangle_{12}$, defined by

$$|\Psi_{jk}\rangle_{12} \otimes |\Omega_j, \Omega_k\rangle_{34} = \frac{\hat{\Pi}_{jk}\,|\psi\rangle}{\sqrt{p_{jk}}}, \tag{3.4}$$

with the norm p_{jk} given by

$$p_{jk} = \langle\psi|\,\hat{\Pi}_{jk}\,|\psi\rangle\,. \tag{3.5}$$

Since our original state $|\psi\rangle$ only contains a single photon in each of paths $\hat{b}_1^\dagger$ or $\hat{b}_2^\dagger$, applying $\hat{\Pi}_{jk}$ acts as an effective Bell-state measurement on these modes. Henceforth, we will drop the 12-index in $|\Psi_{jk}\rangle_{12}$ for convenience.

To compute the form of $|\Psi_{jk}\rangle$, we will introduce, for convenience, the reduced density matrices for the states of the signal and idler photons, given respectively by,

$$\begin{aligned}\rho_{\text{S}}(\omega,\omega') &= \int \mathrm{d}\Omega f(\omega,\Omega) f^*(\omega',\Omega),\\ \rho_{\text{I}}(\Omega,\Omega') &= \int \mathrm{d}\omega f(\omega,\Omega) f^*(\omega,\Omega'),\end{aligned} \tag{3.6}$$

both of which obey the relation $\rho(\omega,\omega') = \rho^*(\omega',\omega)$. Using these, along with the assumption of identical sources, it is straightforward to show that

$$p_{jk} = \frac{1}{2}\Big[\rho_{\mathrm{I}}(\Omega_j,\Omega_j)\rho_{\mathrm{I}}(\Omega_k,\Omega_k) - |\rho_{\mathrm{I}}(\Omega_j,\Omega_k)|^2\cos\theta_{jk}\Big], \tag{3.7}$$

with

$$\theta_{jk} = (\Omega_j - \Omega_k)\tau_{\mathrm{I}} = \Delta\Omega_{jk}\tau_{\mathrm{I}}, \tag{3.8}$$

where we defined $\Delta\Omega_{jk}$ as the difference between the heralding frequencies. Eq. (3.7) is the probability distribution for a coincidence between the idler photons at (Ω_j,Ω_k), or equivalently, the JSI of the idler photons at the output of the beam splitter.

Most importantly, the heralded signal Bell-state has the simple form

$$|\Psi_{jk}\rangle = \frac{|\phi_j\rangle_1 |\phi_k\rangle_2 - e^{i\theta_{jk}}|\phi_k\rangle_1 |\phi_j\rangle_2}{\sqrt{2\mathcal{C}_{jk}}}, \tag{3.9}$$

where $|\phi_j\rangle_n$ is a pulse-mode normalized single photon state [72] given by

$$|\phi_j\rangle_n = \int \mathrm{d}\omega\, \phi_j(\omega)\hat{a}_n^\dagger(\omega)\,|\mathrm{vac}\rangle\,, \tag{3.10}$$

with

$$\phi_j(\omega) = \frac{f(\omega,\Omega_j)}{\sqrt{N_j}}, \tag{3.11}$$

where $N_j = \rho_{\mathrm{I}}(\Omega_j,\Omega_j)$, as described in Appendix A.10, and $n \in \{1,2\}$. Essentially, $|\phi_j\rangle_n$ is the state that the signal photon is projected onto, when its corresponding idler photon is detected at frequency Ω_j. Finally the normalization constant $\mathcal{C}_{jk}$ is

given by

$$\mathcal{C}_{jk} = 1 - |\langle\phi_j|\phi_k\rangle|^2 \cos\theta_{jk}, \tag{3.12}$$

where the inner product $\langle\phi_j|\phi_k\rangle$ is taken either in mode 1 or in mode 2, but we have dropped the index for better readability. The functions ϕ_j are defined from the JSA and several identities are shown in Appendix A.10. While normalized, they are not necessarily orthogonal, hence the dependence on the modal overlap in the normalization from Eq. (3.12). In Sec.3.4, we will use a Gaussian approximation that gives a simple expression for those functions.

Since nearly all of our measurements are conditioned upon the BSM on the idler photons, we will use the state $|\Psi_{jk}\rangle$ to calculate our quantities of interest. In addition, we also consider the case of a non-resolving BSM, given by

$$\hat{\Pi} = \sum_{j,k} \hat{\Pi}_{jk} = \iint \mathrm{d}\Omega_j \mathrm{d}\Omega_k \, |\Omega_j, \Omega_k\rangle \langle\Omega_j, \Omega_k| \,, \tag{3.13}$$

which, upon taking $\mathrm{Tr}\Big(\hat{\Pi} \, |\psi\rangle \langle\psi| \Big)$, heralds the mixed state

$$\hat{\rho} = \frac{\sum_{jk} p_{jk} \, |\Psi_{jk}\rangle \langle\Psi_{jk}|}{\sum_{jk} p_{jk}}. \tag{3.14}$$

This state is normalized by $\sum_{jk} p_{jk}$, which is not equal to unity in general, but this fact is inconsequential to our measurements, as only the relative probabilities p_{jk} are physically relevant. At this point we note that we are using the sum $\sum_{jk}$ in place of the integral $\int \mathrm{d}\Omega_j \mathrm{d}\Omega_k$. This summation serves as a reminder that the pure state description of $|\Psi_{jk}\rangle$ is itself an approximation stemming from the infinite spectral resolution limit. In Appendix A.2 we justify the validity of this

approximation, which gives similar results as the model taking into account the finite resolution of the BSM and the resultant impurity of the heralded state.

3.2.3. State characterization and entanglement verification

We characterize the heralded state $|\Psi_{jk}\rangle$ first by measuring its joint spectral intensity (JSI). This measurement is defined by the POVM element

$$\hat{\Pi}^{\mathrm{JSI}} = |\omega_1, \omega_2\rangle \langle\omega_1, \omega_2| , \tag{3.15}$$

with

$$|\omega_1, \omega_2\rangle = \hat{a}_1^\dagger(\omega_1)\hat{a}_2^\dagger(\omega_2) |\mathrm{vac}\rangle ,$$

and we calculate the resultant JSI as

$$F_{jk}(\omega_1, \omega_2) = \langle\Psi_{jk}| \hat{\Pi}^{\mathrm{JSI}} |\Psi_{jk}\rangle . \tag{3.16}$$

Using (3.9), we then obtain

$$F_{jk}(\omega_1, \omega_2) = \frac{1}{2\mathcal{C}_{jk}} \left| \phi_j(\omega_1)\phi_k(\omega_2) - e^{i\theta_{jk}} \phi_j(\omega_2)\phi_k(\omega_1) \right|^2 . \tag{3.17}$$

In the absence of spectral resolution in the BSM, the heralded state is $\hat{\rho}$ from Eq.(3.14), and the measured JSI is given by

$$F(\omega_1, \omega_2) = \sum_{jk} p_{jk} F_{jk}(\omega_1, \omega_2). \tag{3.18}$$

In terms of previously defined quantities, this function takes the general form

$$F(\omega_1,\omega_2) = \frac{1}{2}\left[\rho_{\mathrm{S}}(\omega_1,\omega_1)\rho_{\mathrm{S}}(\omega_2,\omega_2) - \left|\int \mathrm{d}\Omega f(\omega_1,\Omega) f^*(\omega_2,\Omega) e^{i\Omega\tau_{\mathrm{I}}}\right|^2\right]. \tag{3.19}$$

To verify that the heralded state $|\Psi_{jk}\rangle$ is indeed entangled, beyond classical correlation, two-photon interference is used in a manner analogous to Refs. [50, 73]. In our verification protocol, the signal photons are combined at a 50:50 beam splitter while scanning a relative delay between the input modes ($\hat{a}_1$ and $\hat{a}_2$) denoted by τ_{S} and monitoring coincidences at the output modes ($\hat{a}_3$ and $\hat{a}_4$) as depicted in Fig. 3.1. These modes transform as

$$\begin{aligned}\hat{a}_3^\dagger(\omega) &= \frac{e^{i\omega\tau_{\mathrm{S}}}\hat{a}_1^\dagger(\omega) + \hat{a}_2^\dagger(\omega)}{\sqrt{2}},\\ \hat{a}_4^\dagger(\omega') &= \frac{e^{i\omega'\tau_{\mathrm{S}}}\hat{a}_1^\dagger(\omega') - \hat{a}_2^\dagger(\omega')}{\sqrt{2}}.\end{aligned} \tag{3.20}$$

The POVM element associated with such a coincidence detection is defined as

$$\hat{\Pi}_{\mathrm{verif}} = \iint \mathrm{d}\omega\mathrm{d}\omega' \left|\omega,\omega'\right\rangle \left\langle\omega,\omega'\right|, \tag{3.21}$$

with

$$\left|\omega,\omega'\right\rangle = \hat{a}_3^\dagger(\omega)\hat{a}_4^\dagger(\omega')\left|\mathrm{vac}\right\rangle, \tag{3.22}$$

where we will again consider only the terms that contain both $\hat{a}_1^\dagger$ and $\hat{a}_2^\dagger$. The probability of detecting a coincidence heralded for the input state $|\Psi_{jk}\rangle$ is given by

$$P_{jk}(\tau_{\mathrm{S}}) = \left\langle \Psi_{jk}\right| \hat{\Pi}_{\mathrm{verif}} \left|\Psi_{jk}\right\rangle = \iint \mathrm{d}\omega\mathrm{d}\omega' \left|\left\langle\omega,\omega'|\Psi_{jk}\right\rangle\right|^2. \tag{3.23}$$

Evaluating this using Eq. (3.9), we obtain

$$P_{jk}(\tau_{\mathrm{S}}) = \frac{1}{2\mathcal{C}_{jk}}\Big(1 + \Phi_j(\tau_{\mathrm{S}})\Phi_k(\tau_{\mathrm{S}})\cos\left[(\omega_j - \omega_k)\tau_{\mathrm{S}} - \theta_{jk}\right] - \mathcal{O}(|\langle\phi_j|\phi_k\rangle|^2)\Big). \quad (3.24)$$

where $\Phi_j(\tau_{\mathrm{S}})$ is the modulus of the Fourier transform of $|\phi_j(\omega)|^2$, ω_j is the center frequency of ϕ_j, and finally,

$$\mathcal{O}(|\langle\phi_j|\phi_k\rangle|^2) = \left|\int \mathrm{d}\omega \phi_j^*(\omega)\phi_k(\omega)e^{i\omega\tau_{\mathrm{S}}}\right|^2 + |\langle\phi_j|\phi_k\rangle|^2\cos\theta_{jk} \quad (3.25)$$

are terms that depend on the overlap of ϕ_j and ϕ_k and are negligible except for when $\Omega_j \approx \Omega_k$, which is the regime where $p_{jk} \approx 0$. The main feature of $P_{jk}(\tau_{\mathrm{S}})$ is the interference due to the oscillating term at the difference frequency $(\omega_j - \omega_k)$. This interference is a signature of frequency-bin entanglement [73, 74], as it arises due to the coherence between the two terms in the state $|\Psi_{jk}\rangle$. It is important to note that $P_{jk}(\tau_{\mathrm{S}})$ also depends on τ_{I} implicitly through θ_{jk}, and we will sometimes write $P_{jk}(\tau_{\mathrm{S}}, \tau_{\mathrm{I}})$ when showing this dependence explicitly.

In the absence of frequency resolution of the BSM, we can consider the interference signal associated with the mixed state $\hat{\rho}$, and obtain

$$P(\tau_{\mathrm{S}}, \tau_{\mathrm{I}}) = \sum_{jk} p_{jk}P_{jk}(\tau_{\mathrm{S}}, \tau_{\mathrm{I}}). \quad (3.26)$$

In terms of the previously defined quantities, we have

$$P(\tau_{\mathrm{S}}, \tau_{\mathrm{I}}) = \frac{1}{4}\Bigg(1 + \left|\iint \mathrm{d}\omega\mathrm{d}\Omega\ |f(\omega,\Omega)|^2\, e^{i(\omega\tau_{\mathrm{S}} + \Omega\tau_{\mathrm{I}})}\right|^2 - \iint \mathrm{d}^2\Omega\ |\rho_{\mathrm{I}}(\Omega,\Omega')|^2\, e^{i(\Omega-\Omega')\tau_{\mathrm{I}}} - \iint \mathrm{d}^2\omega\ |\rho_{\mathrm{S}}(\omega,\omega')|^2\, e^{i(\omega-\omega')\tau_{\mathrm{S}}}\Bigg). \quad (3.27)$$

In both Eqs. (3.18) and (3.26), we see that the quantities F and P are obtained by taking a weighted sum over the individual quantities F_{jk} and P_{jk}, with the weights given by p_{jk}. The results are equivalent to replacing the spectrometers with "bucket" (non-resolving) detectors. This weighted sum may also be interpreted in terms of probabilities, where the probability of obtaining a four fold coincidence is the product of the probability of a heralding event from a coincidence between the idler photons, and the probability of a coincidence between the signal photons conditional on the heralding event. This concept of weighting the average is analogous to other experiments that utilize multi-pixel detection in the spatial [75] or spectral [76, 77] domains.

3.3. Experiment

3.3.1. Description

The experimental setup shown in Fig. 3.2(a) consists of a single 2.5mm-long bulk BiBO crystal, double-passed by a pump laser to generate two pairs of SPDC photons in a type-II configuration, where signal and idler are orthogonally polarized. By convention we label the first-pass SPDC process as source 1, and the second-pass process as source 2. The pump for this process is obtained by second harmonic generation (SHG) of a commercial Ti:Sapph laser (Spectra-Physics Tsunami) delivering 100 fs-long pulses at a repetition rate of 80 MHz centered at a wavelength of 830 nm. A part of the Ti:Sapph beam is directed to a fast photodiode to generate a clock for the experiment. The SHG is realized in a 1mm-long type I BiBO crystal and the output consist of another train of pulse centered at 415 nm with a bandwidth of 2.3 nm at full width at half-maximum (FWHM). The SHG efficiency is over 30%, with an average output power of over 300 mW at

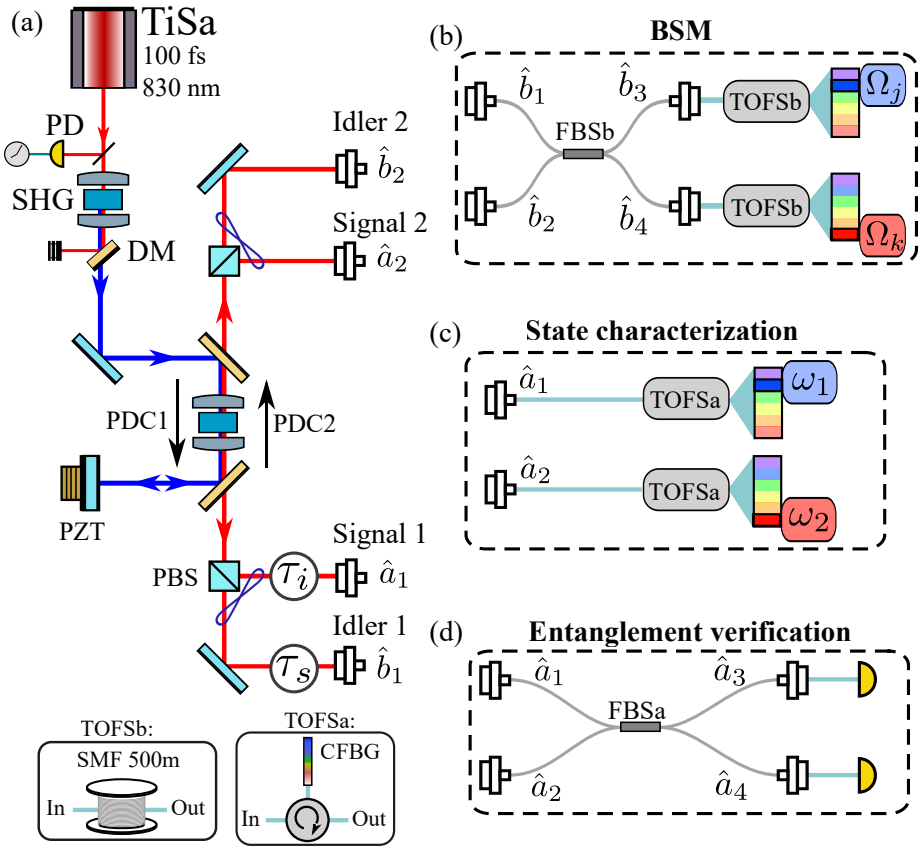

FIGURE 3.2. a) Experimental setup; PD: photodiode; SHG: second harmonic generation; DM: dichroic mirror; PDC: parametric down conversion; PZT: piezoelectric actuator; PBS: polarizing beamsplitter; TOFS: time of flight spectrometer; SMF: single mode fiber; CFBG: chirped fiber Bragg grating; FBS: fiber beam splitter. b) Bell state measurement: the idler photons interferences are spectrally-resolved and used as a herald. c-d) different configuration of the measurement on the signal photons depending on the experiment.

415 nm. To ensure better quality of the spatial mode of the SPDC photons, the pump beam is spatially filtered by a pinhole, transmitting about 60% of the power. This filtering has been shown to greatly optimize the heralding efficiency of SPDC sources when the photons are collected by single-mode fibers.

The double-pass configuration consists of reflecting the pump beam back into the crystal, while transmitting the SPDC single photons from the first source (first pass) through the dichroic mirrors used to steer the pump beam. This

configuration ensures spectral overlap of the two sources. The back mirror for the second source (second pass) is mounted on a piezo actuator (PZT) with a 10 μm travel to finely adjust the phase between the two sources. The SPDC photon pairs are separated by polarization with polarizing beam splitter (PBS) as signal (V polarization, 10 nm FWHM) and idler (H polarization, 16 nm FWHM) and injected into single mode polarization-maintaining fibers. Motorized delay lines are introduced into both signal and idler of source 1 to match their time of arrival with the other photons from the second source.

The BSM is achieved by interfering the idler photons from each source on a fiber beamsplitter prior to the heralding spectral measurement. Spectral resolution is then obtained by utilizing frequency-to-time conversion at the output of the beamsplitter, thus heralding the frequency bins Ω_j and Ω_k, see Fig. 3.2(b). Finally, the heralded JSI and verification is done respectively by routing the signal photons through the setup described in Fig. 3.2(c), (d).

3.3.2. Detection

The single photons are detected utilizing superconducting nanowire single photon detectors (SNSPDs) from IDQuantique (ID281) which can detect the arrival time of photons with a resolution of 20 ps. This temporal resolution is translated into spectral resolution using time-of-flight spectrometers (TOFS), thanks to frequency-to-time conversion [78, 79]. For coarse spectral resolution, we used two spools of 500 m-long HP780 fiber (see Fig. 3.2(a)). These imprint a dispersion of approximately 50 ps per nm of bandwidth at 830 nm, with losses of less than 1 dB per spool. For fine resolution, we used two chirped fiber Bragg gratings (CFBG from Teraxion) with a dispersion of $\sim$ 1000 ps/nm [80] (see

Fig. 3.2(a)). This extra resolution comes at the expense of an overall signal attenuation of over 10 dB due to coupling losses and to a finite spectral window of 10 nm. The photocurrent coming out of the detectors is registered with a time-to-digital converter (TDC, ID900 from IDQuantique). The time reference is provided by the optical clock, thus ensuring that each time tag is taken with respect to a stable signal for each pulse.

When the photons are detected at the SNSPDs, their time of arrival is recorded with an adjustable precision. Throughout this work, this resolution was set to 100 ps unless stated otherwise, which corresponds to a spectral resolution that depends on which dispersive medium is used. Using the calibration data shown in Fig. A.4 in Appendix A.4, this spectral resolution is 0.1 nm for the CFBG and 2 nm for the fiber spools. These resolutions define the minimal bin size in which the frequency of any event is recorded. Therefore, when doing any type of four-fold coincidence measurement, the time of arrival of every event may be binned with that resolution in a histogram, thus resulting in spectral bins, or pixels, as depicted in Fig. 3.3, which can be analyzed in post processing.

For instance, for experiments that only require spectral resolution on the herald (such as the verification P_{jk}), time tags corresponding to heralding frequencies Ω_j, Ω_k are acquired and subsequently binned at the resolution of the spectrometer, corresponding to the probability of getting spectral coincidences in every possible combination of frequency bins. When all four spectrometers are needed (for instance to measure the JSI F_{jk} heralded by a BSM at frequencies Ω_j and Ω_k), the measurement then consists of four sets of time tags that can be binned into a four-dimensional histogram, such as shown in Fig. 3.6. For more readability, we label those heralding bins by integers j and k, such that index 0

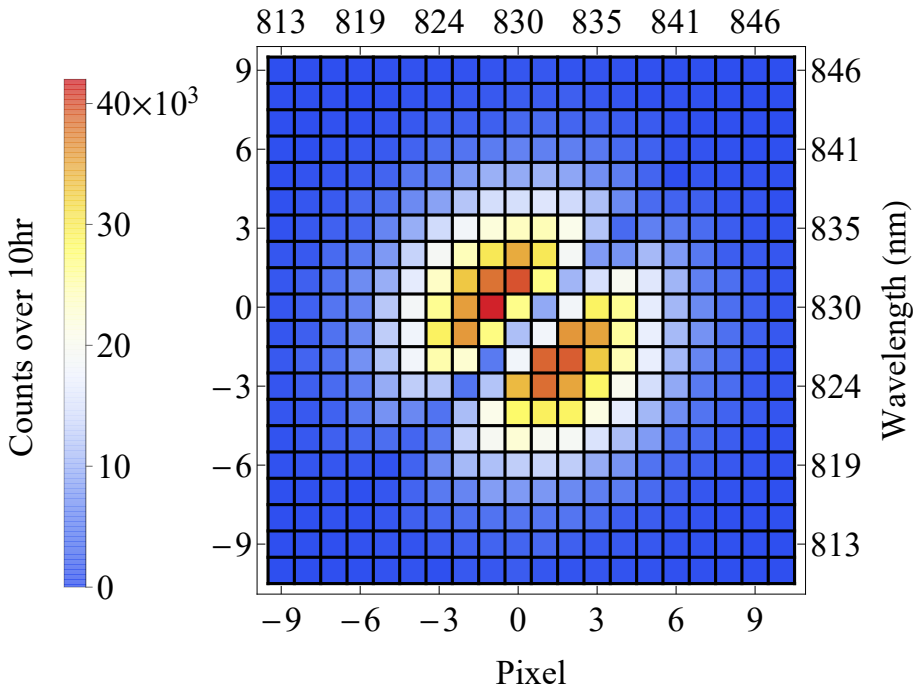

FIGURE 3.3. Acquisiton of the heralded JSI p_{jk} of the idler photons showing the calibration and indexing convention of the frequency bins.

corresponds to Ω_0, the central wavelength of the idler spectrum. The axes in Fig. 3.3 give the index-to-wavelength mapping.

3.3.3. Source distinguishability

This experiment relies on the indinstinguishability of the two sources as noted in the previous section. This has to be achieved on every degree of freedom. Since the polarization and the spatial degree of freedom are constrained by polarization-maintaining fibers, there remains to match the sources in frequency and in time.

The spectral indistinguishability can be estimated by measuring the joint spectral intensity of both sources. We obtained such JSI measurements by using the two 500m fiber spools (TOFSb) to detect signal and idler photons from

each source in coincidence, while operating the time tagger at its maximum resolution of 13 ps, such that the spectral resolution is only limited by the timing jitter of the SNSPDs. These measurements are shown in Fig. 3.4. It can be seen that both sources are very similar thanks to the dual-pass configuration of the pump. A Gaussian fit to this experimental JSI is used throughout this chapter to define the parameters of the JSA $f(\omega, \Omega)$ that are used in our mathematical model, as described in Sec.3.4.1. Note that there can be an additional cause of distinguishability due to spectral phase mismatch between both sources which cannot be determined with an intensity measurement. Therefore, the dispersion was mostly matched in every path of the interferometer by ensuring that every fiber element had the same length.

Temporal mode matching is achieved by scanning both delays τ_{S} and τ_{I} while monitoring the coincidences between ports $\hat{b}_3$ and $\hat{b}_4$ for the idlers (at FBSb) and $\hat{a}_3$ and $\hat{a}_4$ for the signals (at FBSa), which do not share photon number correlations. This results in an unheralded Hong-Ou-Mandel (HOM) dip with a poor visibility (less than 10%), which is still sufficient to coarsely match the time of arrival of the photons. We also measured a higher-visibility HOM interference in a heralded manner by detecting fourfold coincidences between ports $\hat{b}_1$, $\hat{b}_2$, $\hat{a}_3$ and $\hat{a}_4$. In Appendix A.7, we show how such a measurement with and without spectral resolution can give a lower bound on the purity of the heralded state.

Finally, another convenient method [81] to match both sources can be applied. With the configuration from Fig.3.1, we can monitor the two-fold coincidences between combinations of one output from each beamsplitter, for instance $\hat{b}_3$ and $\hat{a}_3$. When both delays are matched, i.e. $\tau_{\mathrm{S}} = \tau_{\mathrm{I}} = 0$, then these coincidences oscillate at the optical frequency. This interference is phase-

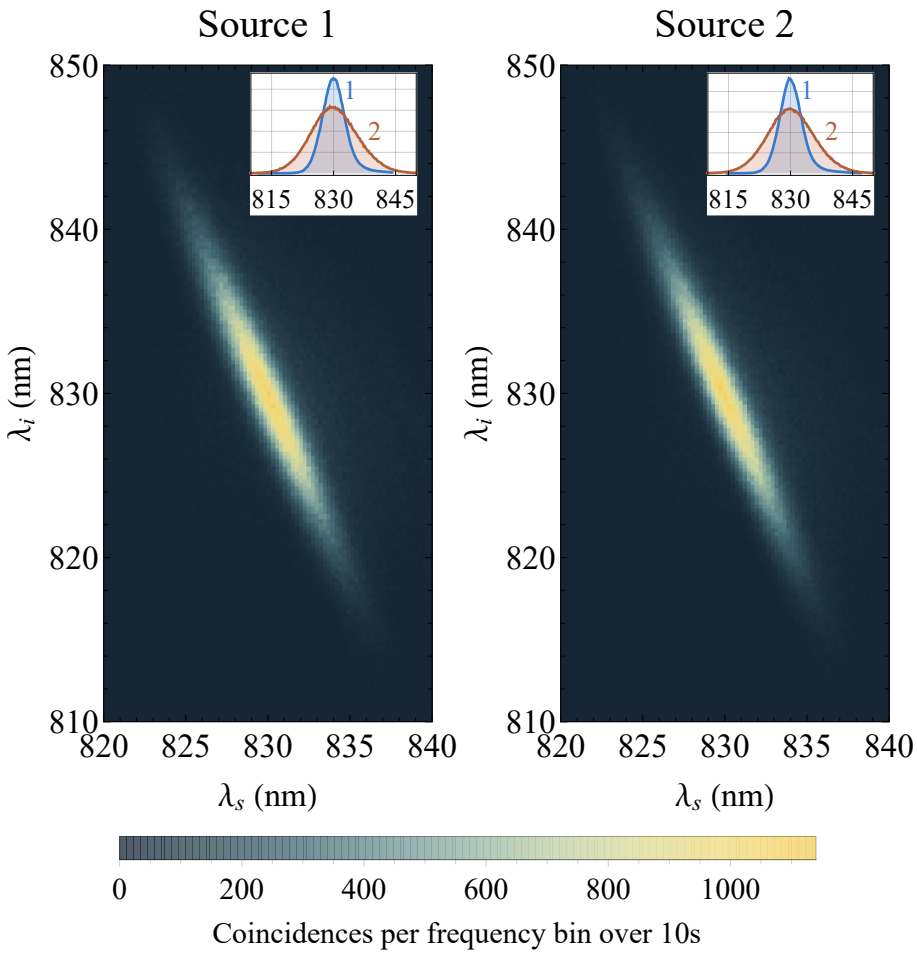

FIGURE 3.4. Experimental joint spectral intensity of both sources. Insets: marginal spectra.

sensitive, and analogous to classical first-order interference, except that it is observed in the coincidences. In Appendix A.6, we show that the visibility of this interference provides a direct measurement of the overlap between both sources, taking into account any phase effects. This method proved essential to accurately match delays before every experiment, while it also provided a bound to quantify indistinguishability, with a maximum measured contrast of 80%.

3.4. Simulations and results

In this section, we further model the experiment with a Gaussian approximation of the JSA to derive analytical expressions from the quantities defined in Sec. 3.2. This allows for a better understanding of the dependence of the interferences on the experimental parameters, notably on the delay between the idler photons in the BSM. We then compare our experimental results to the theory using this approximation.

3.4.1. Gaussian model

It is convenient to write the JSA $f(\omega_\mathrm{S}, \omega_\mathrm{I})$ as a Gaussian distribution by approximating the sinc function with a Gaussian of the same width :

$$f(\omega_\mathrm{S}, \omega_\mathrm{I}) = C \exp\left[-\left(\frac{\omega_\mathrm{S} - \omega_0}{2\sigma_\mathrm{S}}\right)^2 - \left(\frac{\omega_\mathrm{I} - \omega_0}{2\sigma_\mathrm{I}}\right)^2 - \alpha(\omega_\mathrm{S} - \omega_0)(\omega_\mathrm{I} - \omega_0)\right], \quad (3.28)$$

where σ_s (σ_I) is the cross-sectional width of the JSI in the ω_S- (ω_I-) direction evaluated at ω_I (ω_S), ω_0 is the center frequency, α quantifies the amount of spectral entanglement, and $C = \left(\int \mathrm{d}^2\omega \, |f(\omega, \omega')|^2\right)^{-1/2}$ is a normalization constant. Fitting the experimental JSI from Fig. 3.4 to this function, we obtain the following parameters: $\sigma_\mathrm{S} = 2.39$ THz, $\sigma_\mathrm{I} = 5.24$ THz and $\alpha = 37.5 \cdot 10^3$ fs^2. These provide all the values necessary to simulate the experiment in the Gaussian model that is presented here. Note that the center frequency ω_0 is adjusted to the experimental data, so it is a free parameter.

Using the form of Eq. (3.28) for the JSA, the density matrices ρ_{S} and ρ_{I} are given by

$$\rho_{\mathrm{S}}(\omega,\omega') = C^2\sqrt{2\pi}\sigma_{\mathrm{I}}\exp\left[-\frac{(\omega-\omega_0)^2+(\omega'-\omega_0)^2}{4\sigma_{\mathrm{S}}^2}+\frac{1}{2}\alpha^2\sigma_{\mathrm{I}}^2(\omega+\omega'-2\omega_0)^2\right], \tag{3.29}$$

$$\rho_{\mathrm{I}}(\Omega,\Omega') = C^2\sqrt{2\pi}\sigma_{\mathrm{S}}\exp\left[-\frac{(\Omega-\omega_0)^2+(\Omega'-\omega_0)^2}{4\sigma_{\mathrm{I}}^2}+\frac{1}{2}\alpha^2\sigma_{\mathrm{S}}^2(\Omega+\Omega'-2\omega_0)^2\right]. \tag{3.30}$$

Meanwhile, the ϕ_j functions are given by

$$\phi_j(\omega) = \frac{1}{\sqrt{\sigma_{\mathrm{S}}\sqrt{2\pi}}}\exp[-(\omega-\omega_j)^2/4\sigma_{\mathrm{S}}^2], \tag{3.31}$$

which are Gaussians with a width equal to that of the signal's cross-sectional width and a central frequency given by

$$\omega_j-\omega_0 = -2\alpha\ \sigma_{\mathrm{S}}^2\ (\Omega_j-\omega_0). \tag{3.32}$$

Finally, the normalization constant $\mathcal{C}_{jk}$ is given by

$$\mathcal{C}_{jk} = 1-\exp\left[-\Delta\omega_{jk}^2/4\sigma_{\mathrm{S}}^2\right]\cos\left[\Delta\Omega_{jk}\tau_{\mathrm{I}}\right], \tag{3.33}$$

where $\Delta\omega_{jk} = \omega_j-\omega_k$ is the difference between the central frequencies of the heralded modes, and follows the relation $\Delta\omega_{jk} = -2\alpha\sigma_s^2\Delta\Omega_{jk}$. Note that, for most of our data, $(\omega_j-\omega_k)^2 \gg \sigma_{\mathrm{S}}^2$, so that $\mathcal{C}_{jk}\simeq 1$. In Fig. 3.5, we used the experimental JSI to plot the measured $\left|\phi_{j(k)}(\omega)\right|^2$ in the limit of infinite spectral resolution at the BSM.

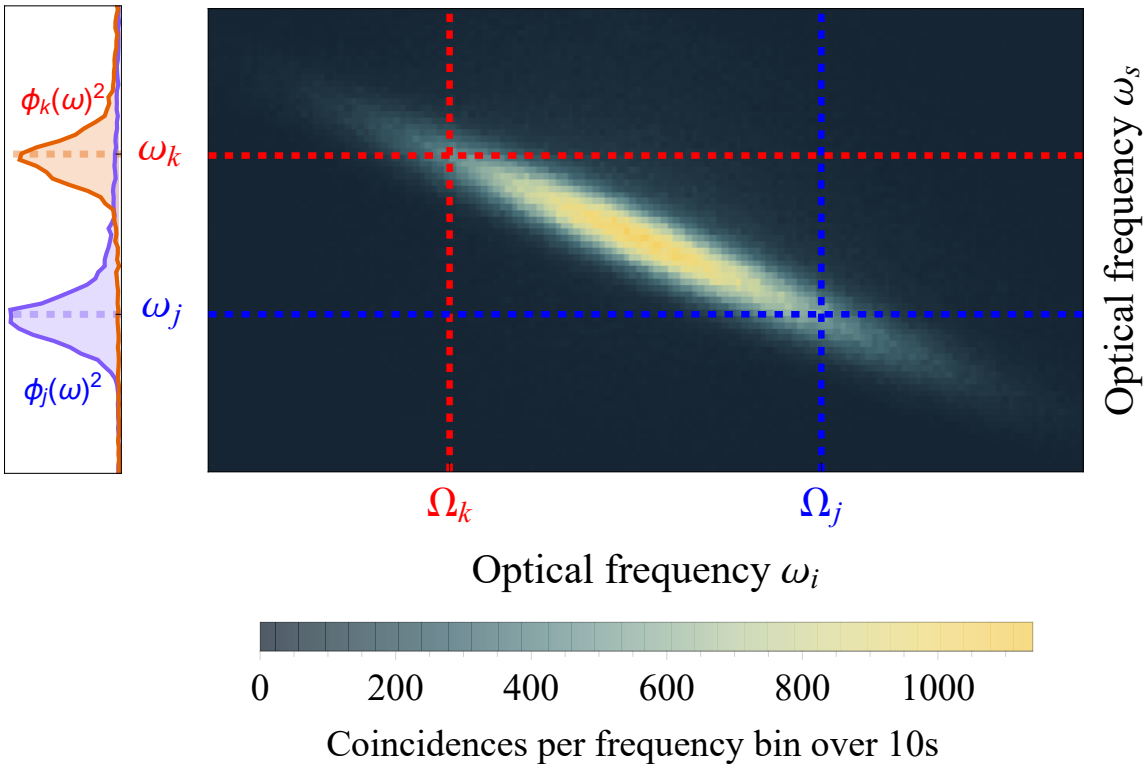

FIGURE 3.5. Gaussian approximation of the spectral heralding: a detection at frequency $\Omega_{j(k)}$ projects the signal photon onto the mode $\phi_{j(k)}$, centered at $\omega_{j(k)}$, shown on the left (dashed). The pure state model assumes that the idler photon is detected with perfect resolution onto a mode with infinitesimal spectral support (top, dashed). A more accurate development is shown in Appendix A.2, which considers integration over a finite spectral window for the herald.

In the following, we first consider the case of a perfect BSM with $\tau_{\mathrm{I}} = 0$, and then explore the effect of minor distinguishability in the BSM with $\tau_{\mathrm{I}} \neq 0$. The latter, more general, case, not only describes the four photon interference effect more comprehensively, but also allows for the heralding of the generalized Bell states given by Eq. (3.9).

3.4.2. Case of $\tau_{\mathrm{I}} = 0$ $(\theta_{jk} = 0)$

We first study the case where the idler paths are exactly matched, setting $\tau_{\mathrm{I}} = 0 (\theta_{jk} = 0)$, which yields the results that we report on in [1]. Under this

constraint, and using the Gaussian model in Eq. (3.28), we proceed to obtain analytic forms for our measured quantities. First, the probability p_{jk} of performing a BSM at frequencies Ω_j and Ω_k and heralding the state $|\Psi_{jk}\rangle$ is given by Eq. (3.7) with $\theta_{jk} = 0$

$$p_{jk} = \frac{1}{2}\Big[\rho_{\mathrm{I}}(\Omega_j, \Omega_j)\rho_{\mathrm{I}}(\Omega_k, \Omega_k) - |\rho_{\mathrm{I}}(\Omega_j, \Omega_k)|^2\Big]. \tag{3.34}$$

The distribution p_{jk} in fact corresponds to the joint probability of detecting two photons at the output of a beam splitter, when they are in a separable state at the input, with each photon described by a density matrix ρ_{I}. Notably, the indistinguishability of the photons manifests as a dip along the degenerate $\Omega_j = \Omega_k$ frequencies as $p_{j=k} = 0$. This implies that the probability of measuring any quantities is zero in this case. An experimental measurement of p_{jk} is shown in Fig. 3.3, showing the bimodal structure of this distribution. It also shows our labelling convention for $\Omega_{j(k)}$ where we set $j(k) = 0$ to correspond to Ω_0 which is the center frequency of the degenerate SPDC light.

Next we compute the JSI F_{jk} associated with the state $|\Psi_{jk}\rangle$ from Eq. (3.17)

$$F_{jk}(\omega_1, \omega_2) = \frac{|\phi_j(\omega_1)\phi_k(\omega_2) - \phi_j(\omega_2)\phi_k(\omega_1)|^2}{2\mathcal{C}_{jk}}, \tag{3.35}$$

which can be approximated for $|\Omega_j - \Omega_k| \gg 0$, *i.e.* for distant heralding frequencies, as

$$F_{jk}(\omega_1, \omega_2) \simeq \frac{|\phi_j(\omega_1)\phi_k(\omega_2)|^2 + |\phi_j(\omega_2)\phi_k(\omega_1)|^2}{2}, \tag{3.36}$$

FIGURE 3.6. (a) Simulation of the heralded JSI F_{jk} for pure states, from Eq. (3.35), using experimental parameters derived from the sources' JSI measurement. (b) Experimental result from [1] obtained by acquiring 30000 spectral coincidences over 10 hours and binning the JSI into frequency bins, labelled according to Fig. 3.3.

(a)

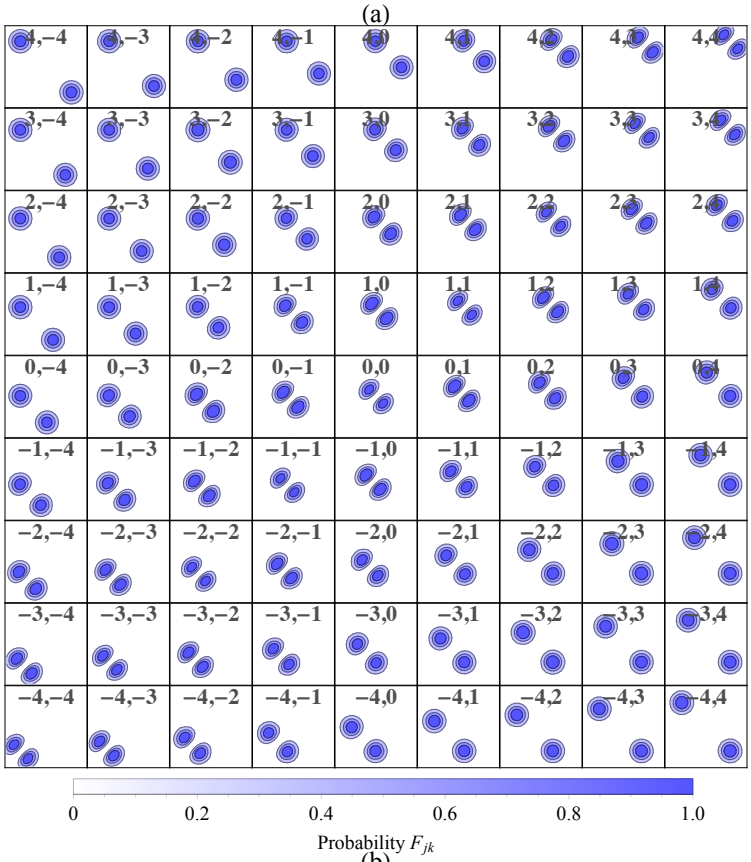
4,−4 4,−3 4,−2 4,−1 4,0 4,1 4,2 4,3 4,4
3,−4 3,−3 3,−2 3,−1 3,0 3,1 3,2 3,3 3,4
2,−4 2,−3 2,−2 2,−1 2,0 2,1 2,2 2,3 2,4
1,−4 1,−3 1,−2 1,−1 1,0 1,1 1,2 1,3 1,4
0,−4 0,−3 0,−2 0,−1 0,0 0,1 0,2 0,3 0,4
−1,−4 −1,−3 −1,−2 −1,−1 −1,0 −1,1 −1,2 −1,3 −1,4
−2,−4 −2,−3 −2,−2 −2,−1 −2,0 −2,1 −2,2 −2,3 −2,4
−3,−4 −3,−3 −3,−2 −3,−1 −3,0 −3,1 −3,2 −3,3 −3,4
−4,−4 −4,−3 −4,−2 −4,−1 −4,0 −4,1 −4,2 −4,3 −4,4
0 0.2 0.4 0.6 0.8 1.0
Probability F_{jk}

(b)

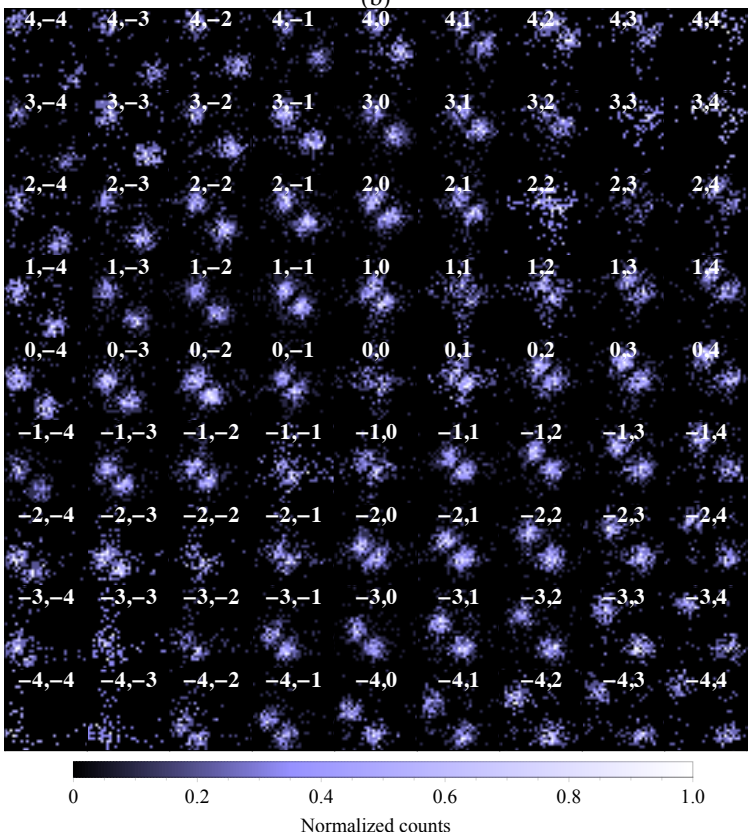
4,−4 4,−3 4,−2 4,−1 4,0 4,1 4,2 4,3 4,4
3,−4 3,−3 3,−2 3,−1 3,0 3,1 3,2 3,3 3,4
2,−4 2,−3 2,−2 2,−1 2,0 2,1 2,2 2,3 2,4
1,−4 1,−3 1,−2 1,−1 1,0 1,1 1,2 1,3 1,4
0,−4 0,−3 0,−2 0,−1 0,0 0,1 0,2 0,3 0,4
−1,−4 −1,−3 −1,−2 −1,−1 −1,0 −1,1 −1,2 −1,3 −1,4
−2,−4 −2,−3 −2,−2 −2,−1 −2,0 −2,1 −2,2 −2,3 −2,4
−3,−4 −3,−3 −3,−2 −3,−1 −3,0 −3,1 −3,2 −3,3 −3,4
−4,−4 −4,−3 −4,−2 −4,−1 −4,0 −4,1 −4,2 −4,3 −4,4
0 0.2 0.4 0.6 0.8 1.0
Normalized counts

which corresponds to two Gaussian spots centered at (ω_j, ω_k) and (ω_k, ω_j), mirror-symmetric about the $\omega_1 = \omega_2$ axis. For exactly degenerate heralding events $\Omega_j = \Omega_k$, the heralded JSI vanishes as the probability of obtaining a BSM result is null in this case.

In the intermediate case where $\Omega_j \simeq \Omega_k$, the two Gaussian spots of the heralded JSI begin to overlap. However, the cross terms obtained by expanding Eq. (3.35) manifest in the JSI as a dip along the degenerate $\omega_1 = \omega_2$ frequencies, akin to Eq. (3.34). The heralded JSI is simulated in Fig. 3.6(a) for the pure state approximation and using values of (Ω_j, Ω_k) that are determined experimentally, showing the aforementioned behavior. To retrieve the same quantity experimentally, we set up the experiment for the characterization procedure (Fig. 3.2(c)) and measure spectral coincidences at the output of FBSa heralded by a BSM at frequencies (Ω_j,Ω_k) (Fig. 3.2(b)). The result is shown in Fig. 3.6(b) where the frequency bins are labelled according to Fig. 3.3. Note that both color maps are normalized, such that the amount of energy per bin has to be multiplied by the probability of realizing this measurement, given by p_{jk} in Fig. 3.3. Therefore, when computing the total number of four fold coincidences per pixel in Fig. 3.6(b), we obtain exactly the distribution depicted in Fig. 3.3.

We assess the validity of our theoretical model by comparing it with the experimental data. For each measured F_{jk}, the counts are distributed into two clusters. We calculate the center of mass of each of the two clusters for a given experimental F_{jk}, and, by taking the difference of the centers of mass, obtain an experimental measure of $\Delta\omega_{jk}$ for that JSI. We compute the relative error with respect to the theoretical value of each $\Delta\omega_{jk}$ from the Gaussian model as given by Eq. (3.32). Over the whole set presented in Fig. 3.6(b), the relative error is

25%, which is mostly dominated by the statistical noise due to the low number of events close to the degenerate heralding frequencies ($j = k$). For the F_{jk} with a high number of total counts (corresponding to a high probability of a coincidence between the heralding photons, see Fig. 3.3), the relative error is lower than 10%. This simple comparison shows that the pure state approximation used in our model is adequate for describing our results.

Taking a weighted sum over $F_{jk}(\omega_1, \omega_2)$ from Eq. (3.35), with the weights given by p_{jk} according to Eq. (3.18), we obtain the mixed-state JSI $F(\omega_1, \omega_2)$ from Eq. (3.19) with $\tau_{\mathrm{I}} = 0$, which simplifies to

$$F(\omega_1, \omega_2) = \frac{1}{2}\left[\rho_{\mathrm{S}}(\omega_1, \omega_1)\rho_{\mathrm{S}}(\omega_2, \omega_2) - |\rho_{\mathrm{S}}(\omega_1, \omega_2)|^2\right]. \tag{3.37}$$

First we note that the distribution $F(\omega_1, \omega_2)$ for the signal photons is analogous to the distribution p_{jk} from Eq. (3.34) for the idler photons. Indeed, this is the joint spectral distribution that would be obtained were the beam splitter placed in the signal paths rather than the idler paths, and the fact that such a distribution is measured without the presence of a beam splitter is evidence of the non-local nature of this fourfold measurement. In Fig. 3.7(a), we simulate $F(\omega_1, \omega_2)$ using the values obtained from the source JSI's, where it can be seen the bimodal structure persists in the summation.

By summing our experimental data from Fig. 3.6(b) over all heralded bins, we obtain the histogram shown in Fig. 3.7(b), which closely matches the simulation. We note that the JSI is indeed zero for degenerate frequencies, which is a consequence of HOM interference. The measurement of the heralded JSI shows the validity of the pure state approximation for the resolution of the heralding TOFS, which is sufficiently narrow.

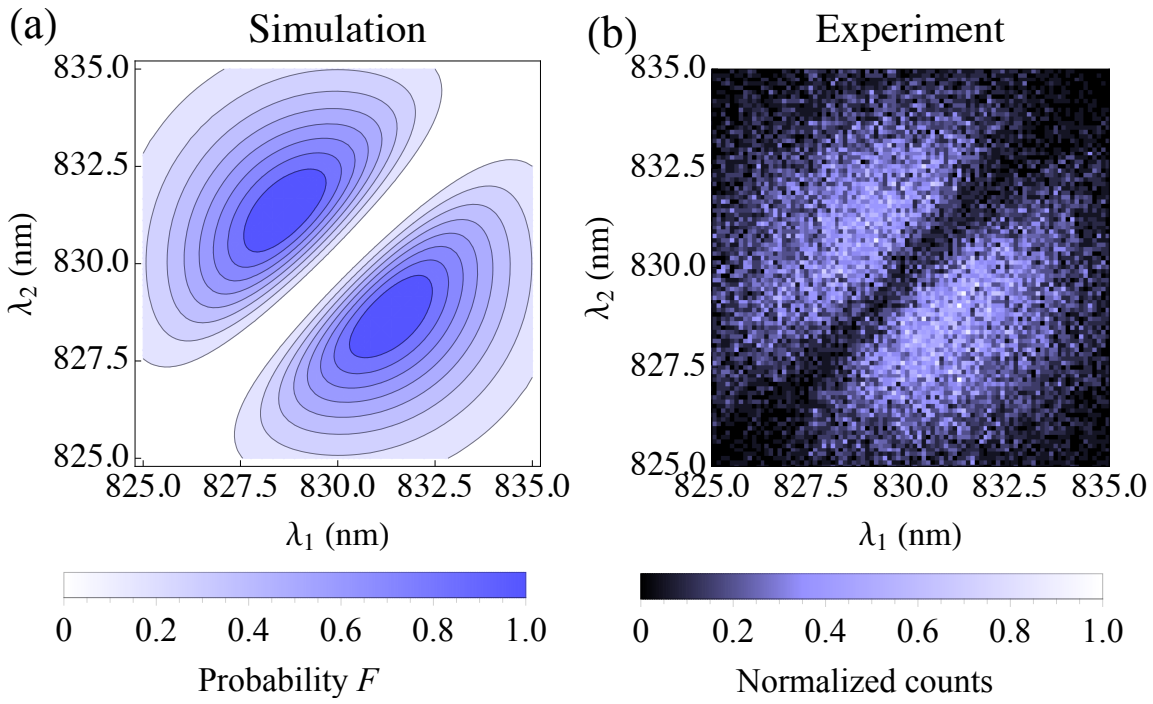

FIGURE 3.7. (a) Simulation of the full heralded JSI F defined by the sum of Eq. (3.18) over all j, k. (b) Experimental result obtained by summing the acquisitions from Fig. 3.6(b) over all bins.

We now proceed to evaluate the entanglement verification signal $P_{jk}(\tau_{\mathrm{S}})$ from Eq. (3.24), for this case of $\theta_{jk} = 0$. We find that $\Phi_j(\tau_{\mathrm{S}}) = \Phi_k(\tau_{\mathrm{S}})$ since the Gaussians $\phi_{j(k)}$ only differ in their first moment $\omega_{j(k)}$ (see Eqs. (3.31) and (3.32)), such that we have:

$$P_{jk}(\tau_{\mathrm{S}}) = \frac{1}{2\mathcal{C}_{jk}}\Big\{1 + e^{-\sigma_{\mathrm{S}}^2\tau_{\mathrm{S}}^2}\cos\left[\Delta\omega_{jk}\tau_{\mathrm{S}}\right] - |\,\langle\phi_j|\phi_k\rangle\,|^2(1 + e^{-\sigma_{\mathrm{S}}^2\tau_{\mathrm{S}}^2})\Big\}. \tag{3.38}$$

Similar to the heralded JSI, we analyzing this function depending on the spectral distance between Ω_j and Ω_k. We find that for $|\Omega_j - \Omega_k| \gg 1/\alpha\sigma_S$, $\langle\phi_j|\phi_k\rangle \to 0$ such that the verification signal reduces to

$$P_{jk}(\tau_{\mathrm{S}}) = \frac{1 + e^{-\sigma_{\mathrm{S}}^2\tau_{\mathrm{S}}^2}\cos\left[\Delta\omega_{jk}\tau_{\mathrm{S}}\right]}{2}. \tag{3.39}$$

The constant term corresponds to a background probability of 1/2 of getting a coincidence event between uncorrelated, heralded single photons after the balanced beam splitter. The other term is a Gaussian envelope with the transform-limited temporal width of the signal photon, analogous to what is obtained in classical cross-correlation between ultrafast pulses. This envelope is modulated by fringes at the difference of the heralded frequencies $\omega_j - \omega_k$. Note that the fringes vanish when setting $\alpha = 0$ in Eq. (3.32), consistent with the notion that the observed fringes are a result of discrete frequency entanglement. Additionally, for the case of $\tau_{\mathrm{I}} = 0$ and $\theta_{jk} = 0$, these fringes have no phase offset and always a maximum at $\tau_{\mathrm{S}} = 0$.

In the pure state model, the probability p_{jk} of obtaining a coincidence detection event after the balanced beam splitter at degenerate frequencies $\Omega_j = \Omega_k$ is null, and the verification signal Eq. (3.38) is not defined. However, we find that

it has the following limit

$$P_{j\to k}(\tau_{\mathrm{S}}) \to \frac{1}{2} - \frac{1}{2}\left(2\sigma_{\mathrm{S}}^2\tau_{\mathrm{S}}^2 - 1\right) e^{-\sigma_{\mathrm{S}}^2\tau_{\mathrm{S}}^2}, \tag{3.40}$$

which can be easily demonstrated by noticing that $\langle\phi_j|\phi_k\rangle$ is a Gaussian function of the variable $\Delta\omega_{jk}$ under the Gaussian approximation (see for instance Eq. (3.33)). The expression is similar to that reported in [50] that utilizes an engineered non-linear interaction to obtain spectral Bell states.

In Fig. 3.8(a), we plotted the simulated P_{jk} using our approximated model and parameters obtained experimentally. This plot shows the previously described behavior, showing oscillations at the difference frequency which merge into a single peak in the near degenerate case. The background color map for these plots represent the probability of measuring these events, *i.e.* p_{jk} from Eq. (3.34).

In Fig. 3.8(b), we show the experimental counterpart, with the colored background representing the experimental p_{jk} obtained by computing the total number of counts in each bin. Using a fit to the Gaussian model (shown as a solid red curve in the experimental plot), we again assess the validity of the model. The fitted parameters $\Delta\omega_{jk}$ are within 15% of the value predicted by the model when averaged over all bins, while for several bins that contain faster oscillations (such as $(3, -3)$ and its immediate neighbors), the relative error is lower than 5%. It is also worth noting that the fitted values agree within the same margins with the retrieved values from the experimental JSI in Fig.3.6(b). Additionally, we find that the visibility of the interference fringes is between 70 and 80%. While the visibility should in theory be unity, in practice it is limited by the indistinguishability of the two source JSA's. In App. A.6, we demonstrate this relationship and we experimentally estimate the indistinguishability to be on the order of 80%, and

FIGURE 3.8. (a) simulation of the entanglement verification signal P_{jk} for pure states, see Eq. (3.38). (b) experimental result from [1], obtained by binning the verification signal acquired over 15 hours. These results are fitted to the approximated model from (3.39). The frequency bins are labelled according to Fig. 3.3. The colormap in the background represents the probability p_{jk} of an heralding event, theoretical (left) and experimental (right).

(a)

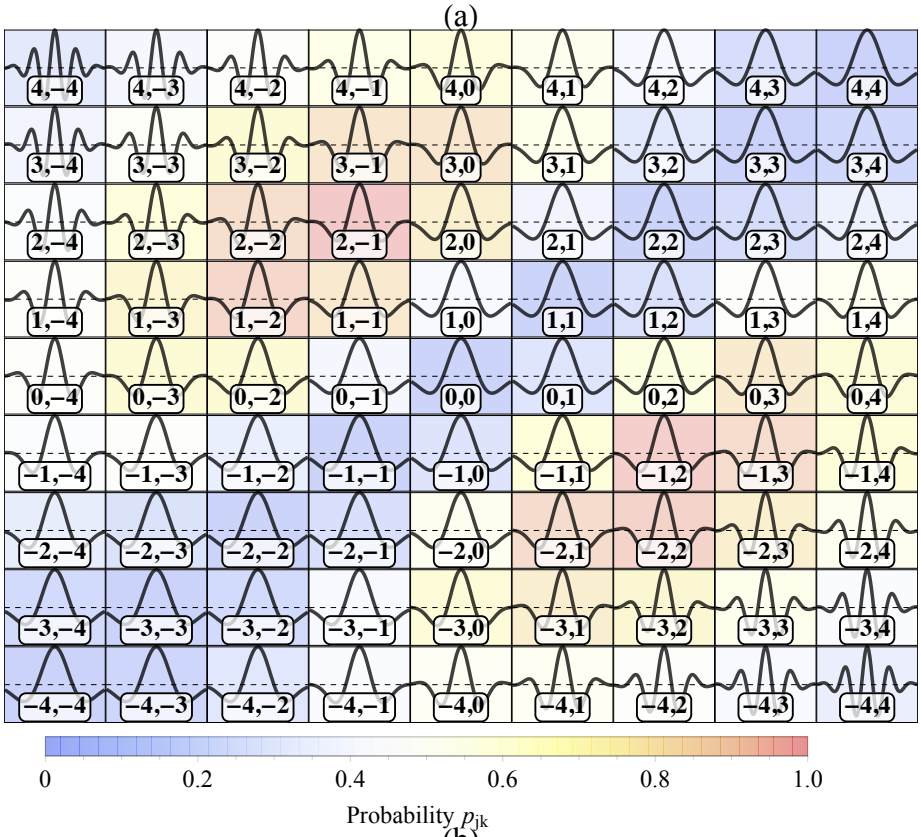
4,−4 4,−3 4,−2 4,−1 4,0 4,1 4,2 4,3 4,4
3,−4 3,−3 3,−2 3,−1 3,0 3,1 3,2 3,3 3,4
2,−4 2,−3 2,−2 2,−1 2,0 2,1 2,2 2,3 2,4
1,−4 1,−3 1,−2 1,−1 1,0 1,1 1,2 1,3 1,4
0,−4 0,−3 0,−2 0,−1 0,0 0,1 0,2 0,3 0,4
−1,−4 −1,−3 −1,−2 −1,−1 −1,0 −1,1 −1,2 −1,3 −1,4
−2,−4 −2,−3 −2,−2 −2,−1 −2,0 −2,1 −2,2 −2,3 −2,4
−3,−4 −3,−3 −3,−2 −3,−1 −3,0 −3,1 −3,2 −3,3 −3,4
−4,−4 −4,−3 −4,−2 −4,−1 −4,0 −4,1 −4,2 −4,3 −4,4
0 0.2 0.4 0.6 0.8 1.0
Probability p_{jk}

(b)

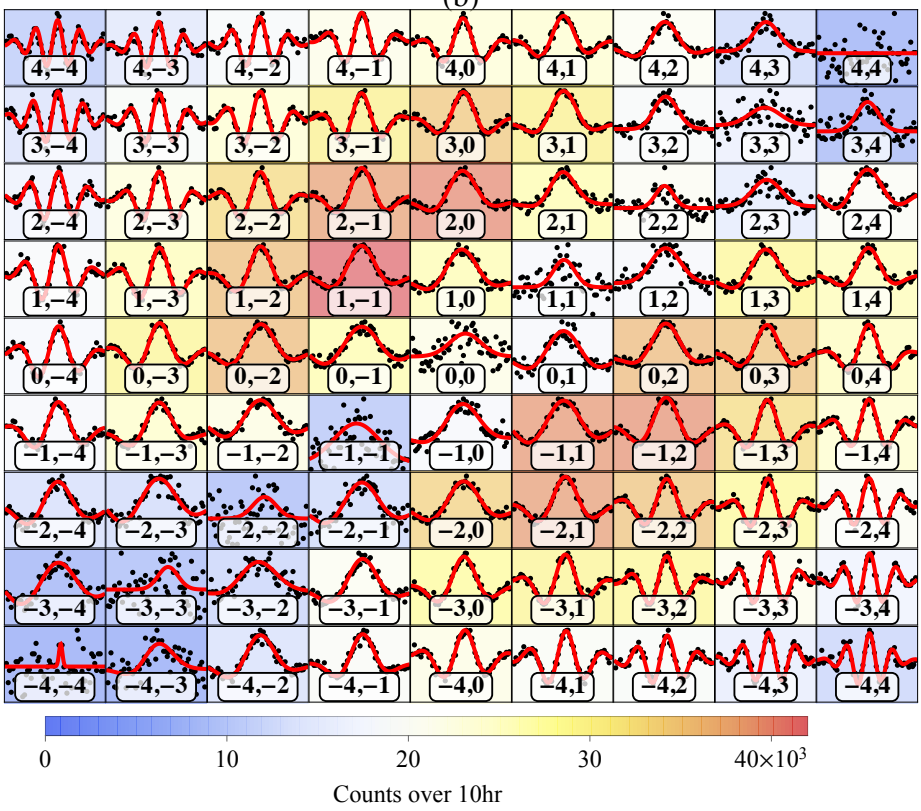
4,−4 4,−3 4,−2 4,−1 4,0 4,1 4,2 4,3 4,4
3,−4 3,−3 3,−2 3,−1 3,0 3,1 3,2 3,3 3,4
2,−4 2,−3 2,−2 2,−1 2,0 2,1 2,2 2,3 2,4
1,−4 1,−3 1,−2 1,−1 1,0 1,1 1,2 1,3 1,4
0,−4 0,−3 0,−2 0,−1 0,0 0,1 0,2 0,3 0,4
−1,−4 −1,−3 −1,−2 −1,−1 −1,0 −1,1 −1,2 −1,3 −1,4
−2,−4 −2,−3 −2,−2 −2,−1 −2,0 −2,1 −2,2 −2,3 −2,4
−3,−4 −3,−3 −3,−2 −3,−1 −3,0 −3,1 −3,2 −3,3 −3,4
−4,−4 −4,−3 −4,−2 −4,−1 −4,0 −4,1 −4,2 −4,3 −4,4
0 10 20 30 40×10^3
Counts over 10hr

thus the visibility of the fringes shown in Fig. 3.8(b) is in good agreement with the theory (a).

Finally we evaluate the verification signal $P(\tau_{\mathrm{S}})$ with $\theta_{jk} = 0$ for the non-spectrally-resolved case, given by Eq. (3.26). We find that it contains four terms:

$$P(\tau_{\mathrm{S}}) = \frac{1}{4}\Bigg[1 + \left|\iint \mathrm{d}\omega\mathrm{d}\Omega\ |f(\omega,\Omega)|^2\, e^{i\omega\tau_{\mathrm{S}}}\right|^2 - \iint \mathrm{d}^2\Omega\ |\rho_{\mathrm{I}}(\Omega,\Omega')|^2 - \iint \mathrm{d}^2\omega\ |\rho_{\mathrm{S}}(\omega,\omega')|^2\, e^{i(\omega-\omega')\tau_{\mathrm{S}}}\Bigg]. \tag{3.41}$$

The first term is simply a background probability, while the second term corresponds to the overlap between the two sources with a relative delay τ_{S} between the signal photons. Evaluating this term reveals a Gaussian along τ_{S} whose width depends on the joint temporal distribution of the sources. This is quite similar to the cross-correlation between two classical pulses, except that in the present case, the phase of the fringes is constant, implying that the P_{jk} sum coherently to a single peak at $\tau_{\mathrm{S}} = 0$. We will see in the next section how that phase can be offset by introducing an additional time delay in the BSM.

The last two terms of Eq. (3.41) correspond respectively to the overlap integrals between the idler and the signal density matrices of each source. The former evaluates to a constant, which is unity when the sources are perfectly matched. The latter describes an unheralded HOM dip between the signal photons. Hence, the full verification signal can be summarized as a Gaussian peak centered in a HOM dip which is similar in form to Eq. (3.40). In Fig. 3.9(a), we plot a simulation of the full signal $P(\tau_{\mathrm{S}})$ showing this behavior. In Fig. 3.9(b), we show the experimental result obtained without binning the data from Fig. 3.8(b), where the red curve is not a fit, but rather the sum of the fits to the individual

P_{jk} signals. Most remarkably, the visibility of the HOM peak is not limited by the purity of the incident quantum state, suggesting that antibunching can reveal entanglement even for a certain class of mixed states.

We stress that the presence of oscillating fringes in $P_{jk}(\tau_{\mathrm{S}})$ or a peak in $P(\tau_{\mathrm{S}})$, where the coincidence probability goes above the baseline of 1/2, is a witness of an entangled state (see, for example, [74]). Our setup is therefore capable of performing entanglement swapping between a large number of frequency Bell states. As we show in [1], not all of the heralded states shown in Fig. 3.6(b) are mutually orthogonal, but it is possible to select multiple subsets which form a set of mutually orthogonal Bell states. In Appendix A.9, we show how to post-select an orthogonal set of states by running an algorithm that isolates sets of quasi-orthogonal modes, all of which satisfy the verification procedure for our entanglement swapping protocol.

3.4.3. Case of $\tau_{\mathrm{I}} \neq 0$ ($\theta_{jk} \neq 0$)

We now study the case when there is a temporal delay τ_{I} between the idler photons at the output of FBSb. Note that when this delay becomes too large compared to the temporal width $\sigma_{\mathrm{I}}^{-1} \approx 300$ fs of the idler photons, they become distinguishable at the output of the beam splitter, effectively reducing the entanglement in the heralded Bell state. Therefore, in the scope of the chapter, we take τ_{I} to be smaller than this value, such that the state $|\Psi_{jk}\rangle$ retains some entanglement. One limitation of the pure state model arises because the idler BSM from Eq. (3.3) assumes perfect spectral resolution, leading to infinite temporal support of the quantities defined in Sec. 3.2 over τ_{I} whereas they should necessarily be bounded by an envelope whose width is inversely proportional to the

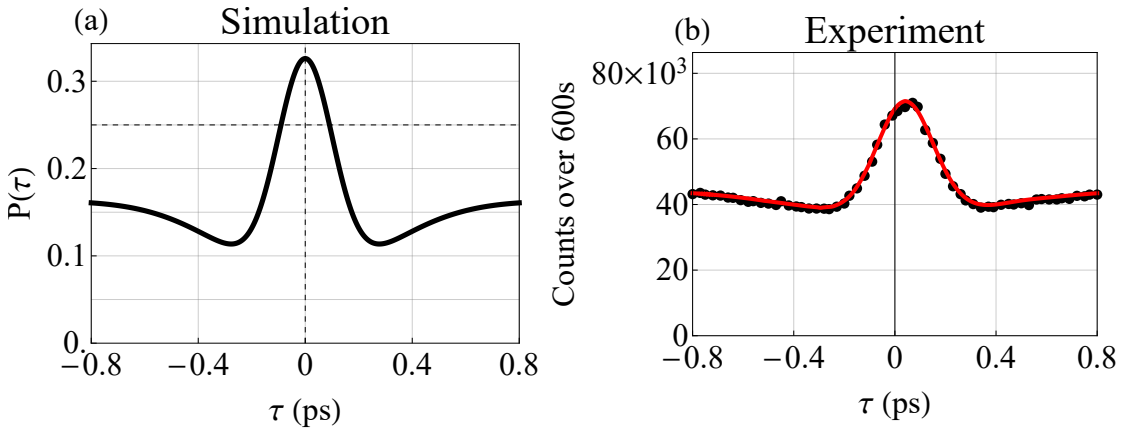

FIGURE 3.9. Probability $P(\tau_{\mathrm{S}})$ of a coincidence heralded by a BSM without spectral resolution. Left: simulation from Eq. (3.41); Right: experimental result presented in [1] obtained by summing the individual P_{jk} that are depicted in Fig. 3.8(b). The solid red curve is a sum of the individual fits on the experimental Gaussian model from Eq. (3.39).

spectral resolution. The derivation for the mixed state case, corresponding to finite spectral resolution, is shown in Appendix A.2. Nevertheless, the pure state model accurately predicts our results and is therefore sufficient to describe the effects of slight distinguishability in the BSM.

The heralded state in the Gaussian model is given by Eq.(3.9) and shows a phase offset between the two states that depends on τ_{I}. The heralded JSI from Eq. (3.17) evaluates to

$$F_{jk}(\omega_1,\omega_2)=\frac{1}{2\mathcal{C}_{jk}}\Big[\,|\phi_j(\omega_1)\phi_k(\omega_2)|^2+|\phi_k(\omega_1)\phi_j(\omega_2)|^2-2\gamma_{jk}(\omega_1,\omega_2)\cos\left(\Delta\Omega_{jk}\tau_{\mathrm{I}}\right)\Big], \tag{3.42}$$

where $\gamma(\omega_1,\omega_2)=\phi_j(\omega_1)\phi_k(\omega_2)\phi_j(\omega_2)\phi_k(\omega_1)$ for real modes $\phi_{j(k)}$, for simplicity. The last term is responsible for the HOM dip along the degenerate frequencies $\omega_1=\omega_2$, marking indistinguishability. As previously, $\gamma_{jk}\to 0$ when heralding distant bins $|\Omega_j-\Omega_k|\gg 0$ so the delay between the idlers photons has no

influence. However, for degenerate bins $\Omega_j \to \Omega_k$ and for $\tau_\mathrm{I} < \sigma_\mathrm{I}^{-1}$, $\gamma_{jk} \times \cos\theta_{jk} \to 0$ which causes the two Gaussian spots to merge.

Putting these limits together, we find that a small delay between the idler photons results in a heralded JSI similar to Fig. 3.6(a) where the JSI in the bins close to the $j \to k$ diagonal are more or less merged depending on τ_I. For spectral bins that are spaced further, the JSI is unchanged since the distinguishability is marked by a relative phase between the Gaussian spots.

The full JSI is obtained by summing F_{jk} according to Eq.(3.18):

$$F(\omega_1, \omega_2) = \frac{\rho_\mathrm{S}(\omega_1, \omega_1)\rho_\mathrm{S}(\omega_2, \omega_2) - \Gamma(\omega_1, \omega_2; \tau_\mathrm{I})}{2}, \tag{3.43}$$

where Γ is a function that depends on the overlap of the signal density matrices as a function of the idler delay (see Appendix A.10). Similar to the previous case, the overlap between ϕ_j and ϕ_k depends on the indistinguishably in time of the idlers.

We next consider the entanglement verification signal from Eq. (3.24), which depends on both τ_S and τ_I. Evaluating it with the Gaussian model, we obtain

$$P_{jk}(\tau_\mathrm{S}, \tau_\mathrm{I}) = \frac{1}{2\mathcal{C}_{jk}}\left(1 + e^{-\sigma_\mathrm{S}^2\tau_\mathrm{S}^2}\cos\left[\Delta\omega_{jk}\tau_\mathrm{S} - \theta_{jk}\right] - |\,\langle\phi_j|\phi_k\rangle\,|^2(e^{-\sigma_\mathrm{S}^2\tau_\mathrm{S}^2} + \cos\theta_{jk})\right). \tag{3.44}$$

We perform yet another asymptotic behavior analysis. For distant heralding frequencies, we find that the limit is similar to Eq. (3.39) with an additional phase shift

$$P_{jk}(\tau_\mathrm{S}, \tau_\mathrm{I}) = \frac{1 + e^{-\sigma_\mathrm{S}^2\tau_\mathrm{S}^2}\cos\left[\Delta\omega_{jk}(\tau_\mathrm{S} - \tau_\mathrm{I}')\right]}{2}, \tag{3.45}$$

where we used Eq. (3.32) to factorize by the difference of heralded frequencies and we defined $\tau_{\mathrm{I}}' = \tau_{\mathrm{I}}/2\alpha\sigma_{\mathrm{S}}^2$. We can see that the value of τ_{I} has a more noticeable effect compared to the heralded JSI. The fringes are no longer synchronized to the envelope and a phase shift occurs when the delay between the idlers photons is nonzero. This effect is quite important in our case since a delay as small as 100 fs between the idler photons is sufficient to cause a phase shift of π due to the relatively large spectral bandwidth of the JSA.

Note that using the more realistic mixed state model, the envelope of the fringes is also affected by this delay and causes a reduction in visibility. In the pure state approximation, the envelope in the idler direction is infinite, but it is sufficient to show the most noticeable effect of the phase shift. Note also that it is possible to find a value for both delays such that $\tau_{\mathrm{S}} = \tau_{\mathrm{I}}'$, in which case the phase shift cancels, but the visibility of the fringes would be decreased. This is illustrated in Fig. 3.10 which compares a simulation (left) that uses the approximated model with the same parameters as the experimental results (right). The entanglement verification utilizes the previous experimental protocol for 7 different values of τ_{I}. While we see good qualitative good agreement between the experimental and simulated fringes, the envelope in the model has no dependence on τ_{I} whereas it is clearly the case experimentally.

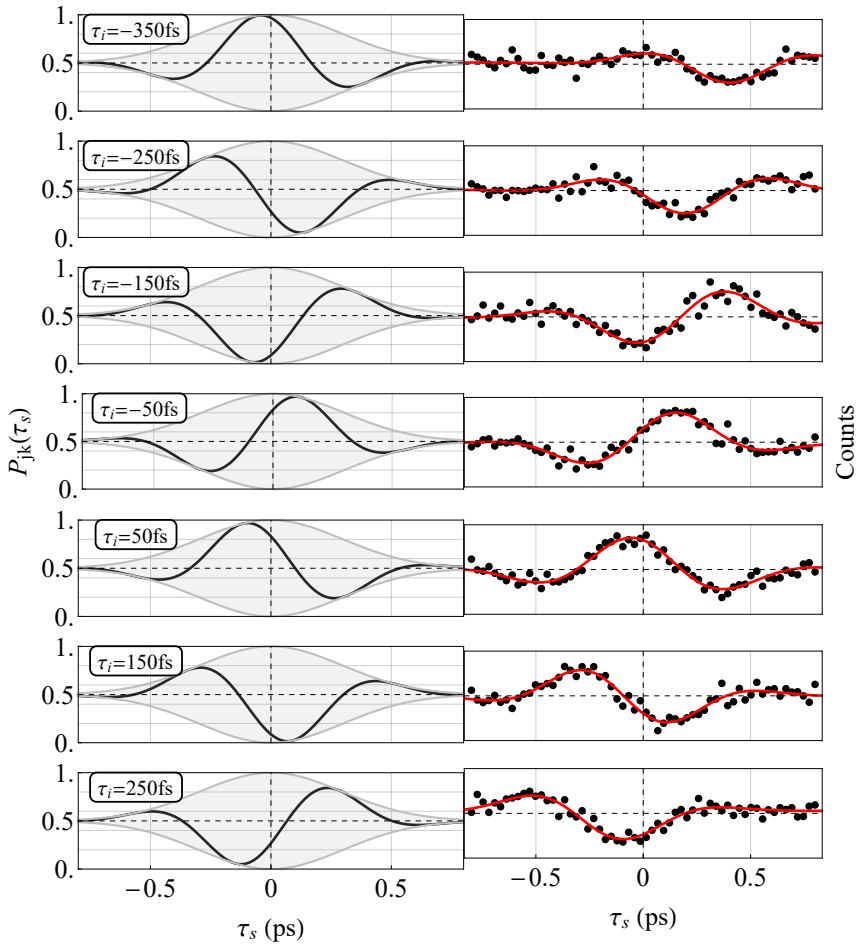

FIGURE 3.10. Simulated (left) and experimental (right) probability to get a coincidence at FBSa between $\hat{a}_3$ and $\hat{a}_4$ heralded by a BSM at frequencies Ω_j and Ω_k for $(j,k) = (2,-2)$. The simulation utilizes the Gaussian, pure state approximation from Eq. (3.45) with the same parameters as in the experimental case. The experimental plots are acquired over 900s for different positions of the idler stage (on the right). The heralding frequencies are separated by 8nm (or about 10 THz). The red curve represents a fit to the theoretical model. This is a different representation of the data shown in Fig. 3.11 in the bin labelled $(2,-2)$.

For near-degenerate heralding frequencies, we have the following limit

$$P_{j\to k}(\tau_{\mathrm{S}},\tau_{\mathrm{I}}) = \frac{1}{2} - \frac{1}{2}\cdot\frac{2\sigma_{\mathrm{S}}^2(\tau_{\mathrm{S}}-\tau_{\mathrm{I}}')^2-1}{1+4(\tau_{\mathrm{I}}')^2}e^{-\sigma_{\mathrm{S}}^2\tau_{\mathrm{S}}^2}. \tag{3.46}$$

which is equal to Eq. (3.40) when setting $\tau_{\mathrm{I}} = 0$. Putting both limits together, we find that a scan over τ_{S} and τ_{I} of the verification signal P_{jk} from Eq. (3.44) look very similar to Fig. 3.8(a), except that the fringes will be offset as a function of τ_{I} while the peak close to the diagonal remains centered. In both cases, the visibility is decreased. This effect was very useful experimentally to verify that the delay at both beam splitters was as close to zero as possible. Moreover, the decrease in contrast for non-zero values of τ_{I} is yet another proof that the visibility of the oscillations in P_{jk} is a marker of entanglement.

In Fig. 3.11 we show an experimental waterfall plot representing each P_{jk} for values of τ_{I} ranging from -300 to +300 fs which originates from the same dataset as Fig. 3.10. In this measurement, the spectrally resolved heralding is done at half the resolution than used earlier (shown in Fig. 3.3) to have sufficient data statistics. These plots show that the fringes have a phase shift as a function of τ_{I} for distant (j,k) frequency bins as predicted by Eq. (3.45), while in the degenerate $j = k$ case, the fringes collapse to a single peak as described by Eq. (3.46). The phase shift is defined by the proportionality factor between τ_{I} and τ_{I}', which depends on the amount of entanglement and on the spectral bandwidth of the signal photons. This data shows that entanglement swapping is still achieved for this specific range of delay mismatch in the BSM, even though this mismatch introduces some distinguishability.

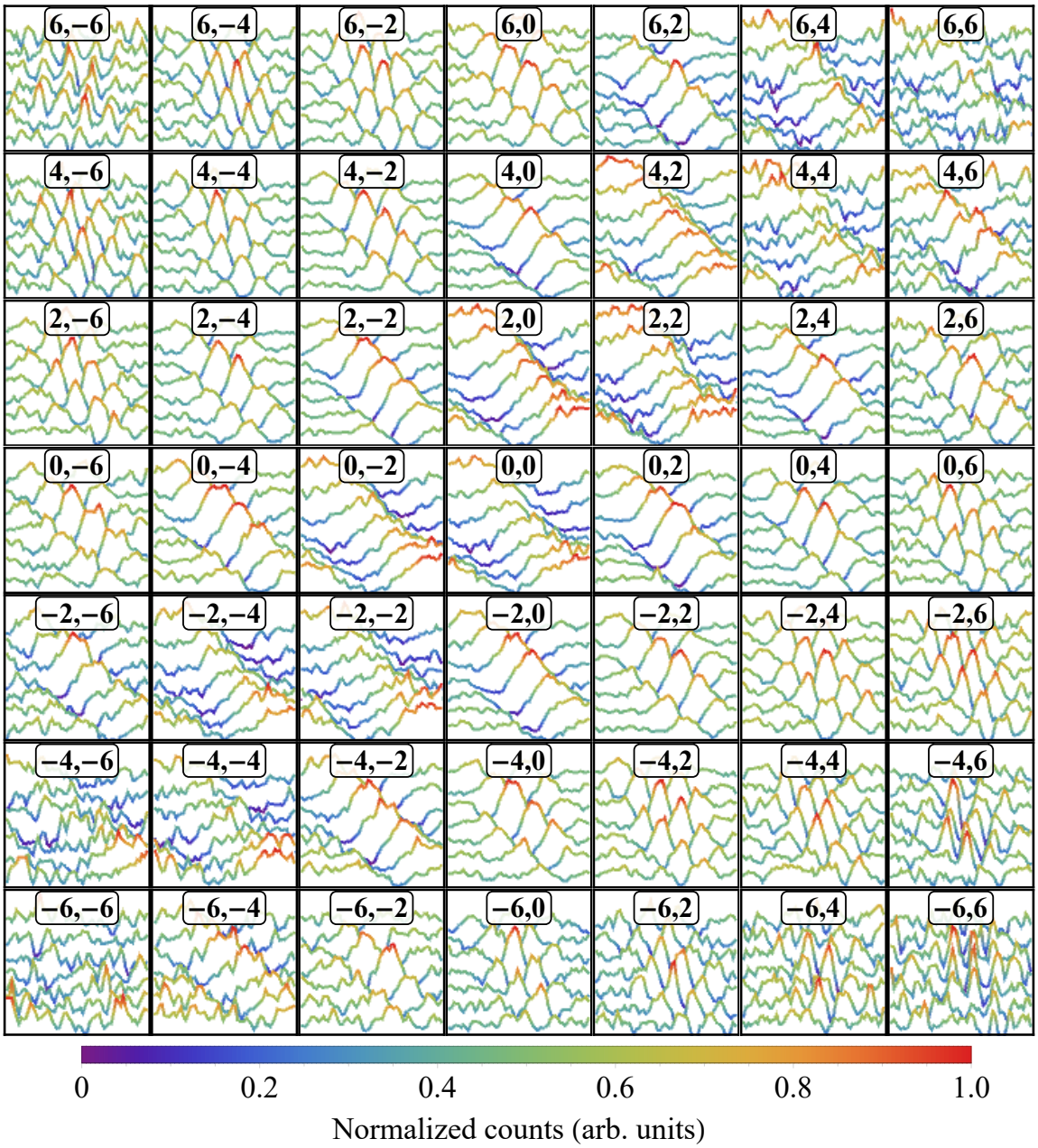

FIGURE 3.11. Waterfall plot of P_{jk} plotted against τ_{S} (horizontal) for different values of τ_{I} (vertical) where each plot represents a frequency bin Ω_j, Ω_k labelled by j and k. The plot range and units for τ_{S} and τ_{I} are the same as shown in Fig. 3.10. For each j, k subplot, the color gradient spans the entire range for that subplot, such that the color is representative of the amount of data collected.

Finally, by repeating the same experiment either without spectral resolution of the BSM or by summing the individual P_{jk} according to Eq. (3.26), we find that the expression of the verification signal is then given by

$$P(\tau_{\mathrm{S}},\tau_{\mathrm{I}}) = \frac{1}{4}\Bigg(1 + \left|\iint \mathrm{d}\omega\mathrm{d}\Omega\ |f(\omega,\Omega)|^2\, e^{i(\omega\tau_{\mathrm{S}}+\Omega\tau_{\mathrm{I}})}\right|^2 - \iint \mathrm{d}^2\Omega\ |\rho_{\mathrm{I}}(\Omega,\Omega')|^2\, e^{i(\Omega-\Omega')\tau_{\mathrm{I}}} - \iint \mathrm{d}^2\omega\ |\rho_{\mathrm{S}}(\omega,\omega')|^2\, e^{i(\omega-\omega')\tau_{\mathrm{S}}}\Bigg), \tag{3.47}$$

which is similar to Eq.(3.41) with an additional dependence on τ_{I}. We simulated this expression using the Gaussian model in Fig. 3.12 and show the corresponding experimental result. It is straightforward to identify the three nonconstant terms as familiar quantities. The second term is the cross-correlation between both JSA as a function of both delays. It can be written as the product of Fourier transform of the joint spectrum with respect to ω and Ω, thus reducing to the product of envelope functions centered at τ_{S} and τ_{I}. This term is responsible for the slanted peak in Fig. 3.12. The last two terms correspond respectively to the overlap integrals between the density matrices of the idlers and of the signals. They show the effect of interferences between uncorrelated photons and hence are visible as HOM dips along either τ_{S} or τ_{I}, as shown again in Fig. 3.12. This figure allows us to identify more clearly the range over which entanglement swapping can be verified, which is essentially the area over which the slanted peak appears, since the HOM dips correspond only to quantum interferences between unentangled single-photon states.

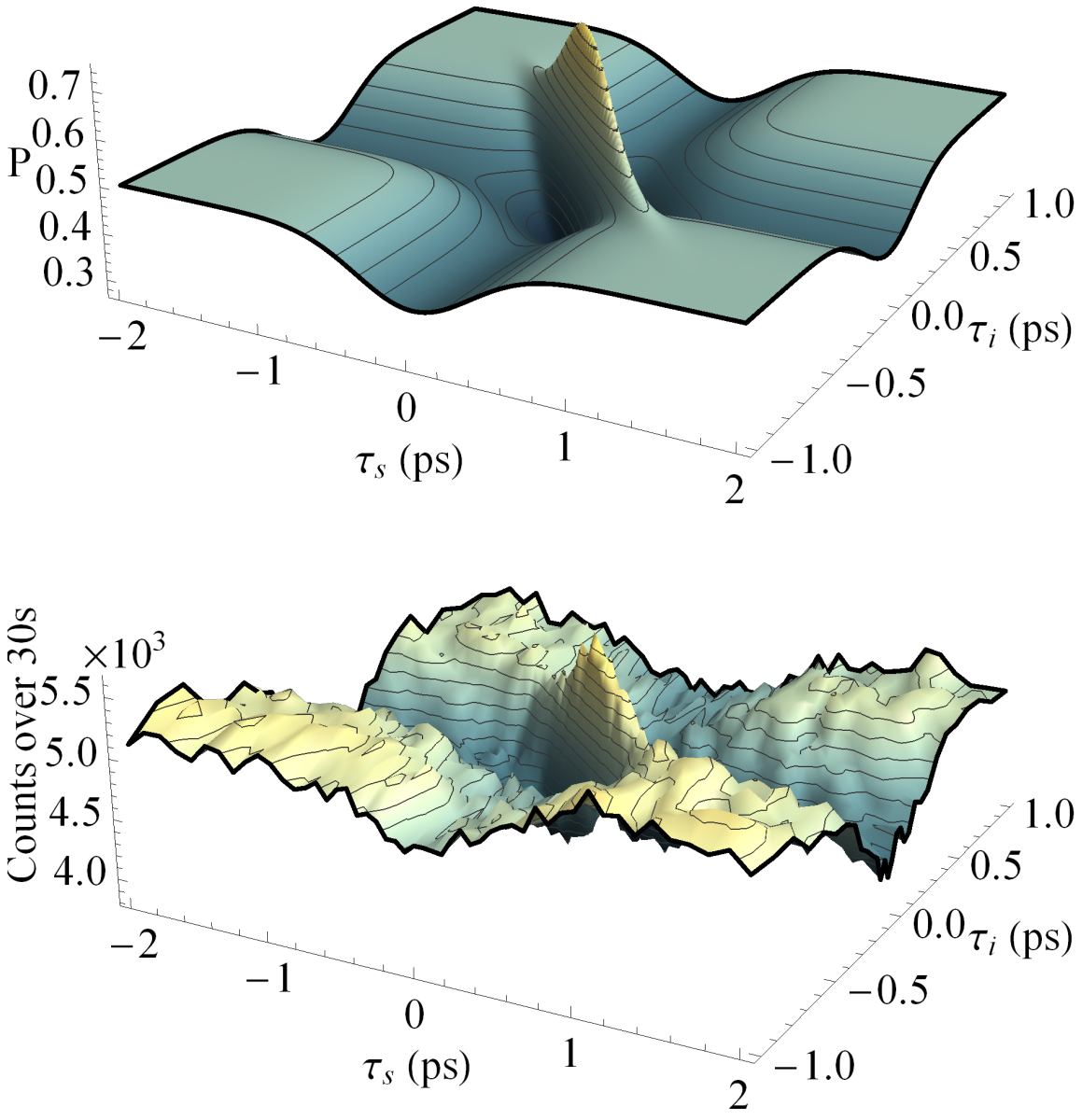

FIGURE 3.12. Top: Simulation of Eq. (3.47) with experimental parameters. Bottom: experimental acquisition obtained by monitoring four-fold coincidences over 15 hours while scanning both τ_{S} and τ_{I} without spectral resolution of the herald.

By exploring the range of both time delays in this configuration, we explicitly see the ultimate equivalence between signals and the idlers in what is effectively a four-photon interferometer. As such, it is adequate to consider $P_{jk}(\tau_{\mathrm{S}}, \tau_{\mathrm{I}})$ and $P(\tau_{\mathrm{S}}, \tau_{\mathrm{I}})$ as the most general representation of the phase-insensitive part of four-photon interference where TF entanglement is present.

3.5. Conclusion

In this work, we have undertaken a more thorough and more general analysis of the results we report on in Ref. [1]. In summary, we demonstrated and analyzed a novel scheme for TF entanglement swapping, using a multimode, spectrally-resolved Bell-state measurement as the heralding mechanism. The most salient feature of our method is the heralding of several, mutually-orthogonal Bell states derived from identical multimode entangled photon pairs. We further generalized our result to consider the case of non-zero time delay in the heralding Bell-state measurement, giving rise to Bell states with a varying amount of phase. Our setup is the first known to the authors to incorporate four simultaneous time-of-flight spectrometers, and thus points towards a promising venue of study of TF entangled four-photon interferometry.

As a proof-of-concept experiment, our work paves a way towards utilizing the high-dimensionality of the TF entanglement available in SPDC sources for distributed quantum information. It is straightforward to scale this protocol to herald a large number of orthogonal entangled states, which is in principle limited by the bandwidth, and thus the amount of the entanglement, of the SPDC sources. Our measurement scheme could further be extended to high-dimensional quantum teleportation and entanglement swapping, whereby ancillary photons

and multiport beam splitters are used to implement a high-dimensional Bell state measurements, as has been recently demonstrated for path [82, 83] and orbital angular momentum [84] entanglement. Alternately, it is possible in principle to use sum-frequency generation to implement projective measurements onto high-dimensional TF-entangled states for the same purpose [85]. Finally, if used in combination with deterministic sources of entangled photon pairs [86] and with quantum memories [87], multimode quantum repeaters of the kind that our protocol allows could prove to be a scalable solution for multiplexed quantum networks.

CHAPTER IV

CHARACTERIZATION OF SPECTRALLY-ENTANGLED PHOTONS

4.1. Spectrally-resolved interference and entanglement

It is well-known that two-photon interference of the Hong-Ou-Mandel type can be used to characterize the modal properties of the incoming light fields. For example, interference of an input single photon with a reference single photon [88] or highly attenuated coherent state [89] can be used to reconstruct the density matrix of the input photon. Similarly, HOM interference of two photons can reveal the extent of their indistinguishability and their symmetry properties [74, 90].

In this section we will analyze how spectrally-resolved two-photon HOM interference type can reveal spectral entanglement in certain two-photon states which may even be mixed states. The measurement we consider is that of a JSI at the output of a HOM interferometer, where there is a fixed relative time delay τ between the arrival times of the input photons. We will call this measurement a "HOM-JSI" for convenience, and the configuration for making such a measurement is depicted in Fig. 4.1. It consists of a two photon state which may or may not be pure, and may or may not be spectrally entangled, where each photon is incident at one of the input modes of a beam splitter, with a fixed relative time delay τ between them. At the output, spectrally-resolved coincidence measurements are made on the two photons.

Following the developments in Chapter III, we can write down the POVM element corresponding to a coincidence detection at frequencies (Ω, Ω') in the basis of the input modes, as

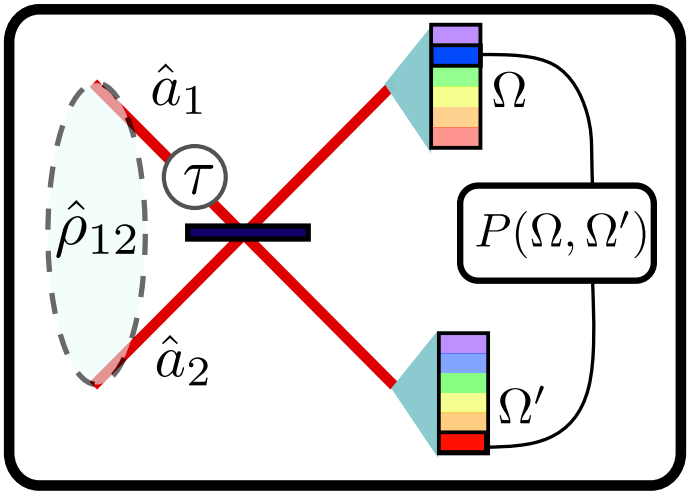

FIGURE 4.1. Spectrally-resolved interference for measuring HOM-JSI: a two-photon state is incident on a balanced beam splitter, where the photons each occupy mode $\hat{a}_1$ and $\hat{a}_2$, but otherwise may be in a pure or mixed state and may or may not be spectrally entangled. A joint detection is made at the output at frequencies Ω and Ω' with probability $P(\Omega, \Omega'; \tau)$.

$$\hat{\Pi}(\Omega, \Omega'; \tau) = \frac{\hat{a}_1^\dagger(\Omega)\hat{a}_2^\dagger(\Omega') - e^{i\Delta\Omega\tau}\hat{a}_1^\dagger(\Omega')\hat{a}_2^\dagger(\Omega)}{2} |\text{vac}\rangle \langle\text{vac}| \frac{\hat{a}_1(\Omega)\hat{a}_2(\Omega') - e^{-i\Delta\Omega\tau}\hat{a}_1(\Omega')\hat{a}_2(\Omega)}{2}, \tag{4.1}$$

where $\Delta\Omega = \Omega - \Omega'$. Note the factor of $1/2$, which is related to the fact that we have dropped terms corresponding to two-photons in the same input mode, since we are assuming that the two photons are in opposite input modes.

We consider the most general two-photon state in this configuration, given by

$$\hat{\rho}_{12} = \int \mathrm{d}^2\omega_1 \mathrm{d}^2\omega_2 \rho_{12}(\omega_1, \omega_1'; \omega_2, \omega_2') \hat{a}_1^\dagger(\omega_1)\hat{a}_2^\dagger(\omega_2) |\text{vac}\rangle \langle\text{vac}| \hat{a}_1(\omega_1')\hat{a}_2(\omega_2'), \tag{4.2}$$

where $\rho_{12}(\omega_1, \omega_1'; \omega_2, \omega_2')$ is the spectral density matrix for the two photons. If the two-photon state is separable, the spectral density matrix can be expressed as follows:

$$\rho_{12}(\omega_1, \omega_1'; \omega_2, \omega_2') = \sum_i \; p_i \; \rho_1^{(i)}(\omega_1, \omega_1')\rho_2^{(i)}(\omega_2, \omega_2'), \qquad \sum_i p_i = 1. \tag{4.3}$$

Consider performing a spectrally-resolved HOM interference measurement on these photons, such that they are detected at frequencies (Ω, Ω') at the output of a 50-50 beamsplitter. The probability for such a coincidence, and hence the measured HOM-JSI, is given by

$$\begin{aligned} P(\Omega, \Omega'; \tau) = \frac{1}{4}\Big(&\rho_{12}(\Omega, \Omega; \Omega', \Omega') + \rho_{12}(\Omega', \Omega'; \Omega, \Omega) \\ -&\rho_{12}(\Omega, \Omega'; \Omega', \Omega)\exp[i(\Omega - \Omega')\tau] - \rho_{12}(\Omega', \Omega; \Omega, \Omega')\exp[-i(\Omega - \Omega')\tau]\Big). \end{aligned} \tag{4.4}$$

The first two terms do not show any interference, and we shall refer to them as the constant terms, because they show no τ-dependence. Meanwhile, we refer to the second two terms, which do depend on τ, as the interference terms. We now proceed to analyze this HOM-JSI for a few special cases, which help guide us to a conjecture about how the HOM-JSI can reveal spectral entanglement.

4.1.1. Case 1: Pure product states

The simplest case to begin with is one where the photons are separable and each is in a pure spectral state. The form for ρ_{12} in is:

$$\rho_{12}(\omega_1, \omega_1'; \omega_2, \omega_2') = \phi_1^*(\omega_1)\phi_1(\omega_1')\phi_2^*(\omega_2)\phi_2(\omega_2'). \tag{4.5}$$

In this case, the HOM-JSI reduces to:

$$\begin{aligned} P(\Omega, \Omega'; \tau) = \frac{1}{4}\Big(&|\phi_1(\Omega)|^2|\phi_2(\Omega')|^2 + |\phi_1(\Omega')|^2|\phi_2(\Omega)|^2 \\ &-\phi_1^*(\Omega)\phi_2(\Omega)\phi_2^*(\Omega')\phi_1(\Omega')\exp\left[i(\Omega - \Omega')\tau\right] - \text{c.c.}\Big) \end{aligned} \tag{4.6}$$

There are two limiting cases of interest for this expression. The first is when the two photons are identical, $\phi_1(\omega) = \phi_2(\omega) = \phi(\omega)$. In that case, the expression for $P(\Omega, \Omega'; \tau)$ reduces to

$$P(\Omega, \Omega'; \tau) = \frac{1}{2}\left[|\phi(\Omega)|^2|\phi(\Omega')|^2\left(1 - \cos(\Omega - \Omega')\tau\right)\right]. \tag{4.7}$$

This corresponds to interference fringes everywhere in the JSI. Furthermore, note that $\tau = 0$ corresponds to no coincidences, as is expected from HOM interference. We simulate this case in Fig. 4.2 (a), where take both photons to have Gaussian spectral amplitudes centered at 830 nm with a FWHM bandwidth of 5 nm, and set the relative time delay τ to 1 ps.

The other limiting case is where there is no spectral overlap between the photons, such that $\phi_1^*(\omega)\phi_2(\omega) \approx 0,\ \forall\omega$. Then the interference term vanishes, and we obtain

$$P(\Omega, \Omega'; \tau) = \frac{1}{4}\left(|\phi_1(\Omega)|^2|\phi_2(\Omega')|^2 + |\phi_1(\Omega')|^2|\phi_2(\Omega)|^2\right). \tag{4.8}$$

This corresponds to two factorable JSI's located symmetrically about the $\Omega = \Omega'$ axis. This case is simulated in Fig 4.2 (b), where we have centered the photons at 825 nm and 835 nm while keeping the other parameters the same.

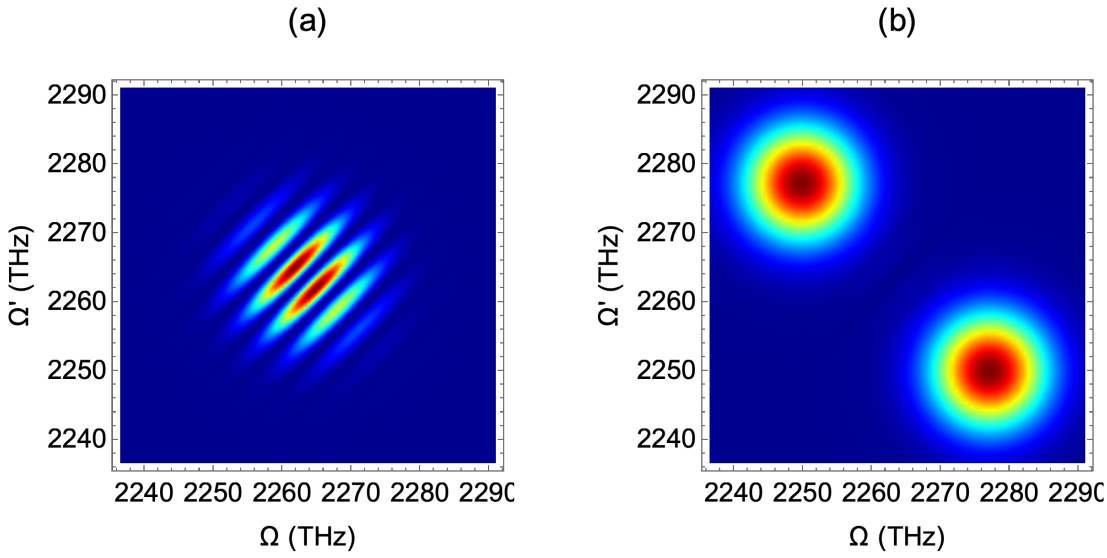

FIGURE 4.2. HOM-JSI's for two photons in pure factorable states. (a) Identical photons centered at 830 nm with 5 nm FWHM bandwidth, and $\tau = 1ps$. (b) Distinguishable photons, where photon 1 is centered at 825 nm and photon 2 is centered at 835 nm, with all other parameters kept the same.

4.1.2. Case 2: Separable mixed states

We can now generalize further to the case of mixed separable states, ones of the form (4.3). In this case the coincidence probability takes the form

$$P(\Omega,\Omega';\tau) = \frac{1}{4}\sum_i p_i \Big[\rho_1^i(\Omega,\Omega)\rho_2^i(\Omega',\Omega') + \rho_1^i(\Omega',\Omega')\rho_2^i(\Omega,\Omega) \\ -\rho_1^i(\Omega,\Omega')\rho_2^i(\Omega',\Omega)\exp\left[i(\Omega-\Omega')\tau\right] - \text{c.c.}\Big]. \tag{4.9}$$

We can treat each term individually without loss of generality, so we'll consider the i-th term and omit the index for simplicity.

Again we consider two limiting cases. The first case is where the two photons are identical, with $\rho_1(\omega,\omega') = \rho_2(\omega,\omega') = \rho(\omega,\omega')$. Then we obtain

$$P(\Omega,\Omega';\tau)=\frac{1}{2}\left[\rho(\Omega,\Omega)\rho(\Omega',\Omega')-\left|\rho(\Omega,\Omega')\right|^2\cos(\Omega-\Omega')\tau\right]. \tag{4.10}$$

Here the constant term consists of the product of the two marginal spectra, just as in the pure case. However, the amplitude of interference term is just the modulus squared of the density matrix. In the limit of a maximally mixed state, this amplitude is only non-zero in the diagonal region where $\Omega \approx \Omega'$, while in the pure state limit, we recover the result of Eq. (4.8), where the constant term and the interference term are identical. In Fig. 4.3 (a), we plot the HOM-JSI for

The second limit is again when there is no spectral overlap between the photons, such that $\rho_1(\omega,\omega')\rho_2(\omega',\omega) \approx 0,\ \forall\omega,\omega'$. The interference term vanishes again, and we are left with

$$P(\Omega,\Omega';\tau)=\frac{1}{4}\left[\rho_1(\Omega,\Omega)\rho_2(\Omega',\Omega')+\rho_1(\Omega',\Omega')\rho_2(\Omega,\Omega)\right], \tag{4.11}$$

In this limit the HOM-JSI is identical to that of the pure distinguishable states, and no information is revealed about the coherence properties of the state.

4.1.3. Case 3: Bell states and other symmetric states

For the case of a frequency-encoded Bell state, such as those resulting from the entanglement swapping experiment of Ch. III, we have a drastically different situation. As we shall see, interference occurs even where we have no spectral overlap between photons 1 and 2. In particular we will study the case of the frequency anti-correlated Bell states, with JSA's of the form

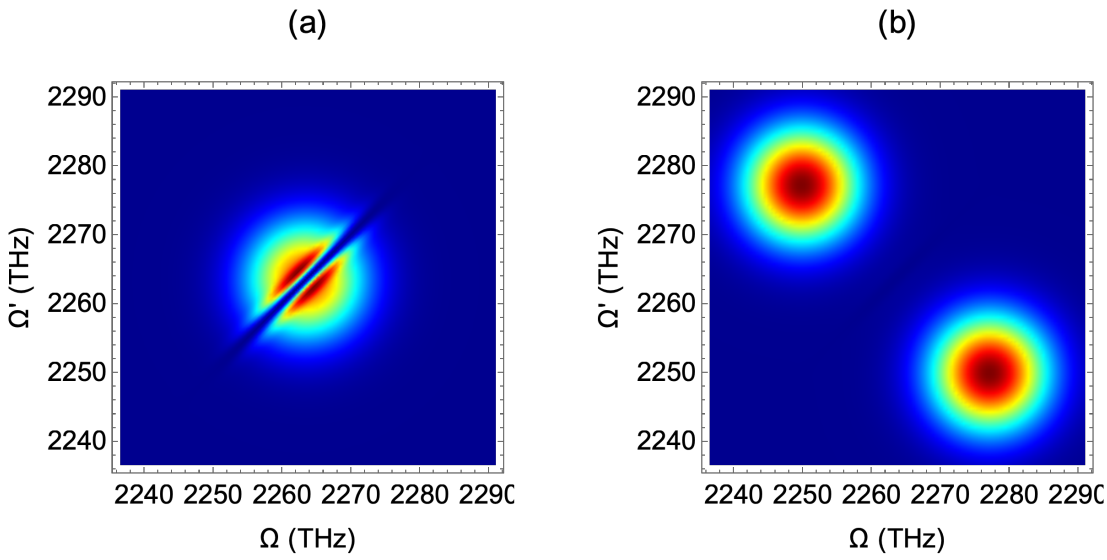

FIGURE 4.3. HOM-JSI's for two photons in mixed separable states. (a) Identical photons centered at 830 nm with 5 nm FWHM bandwidth, and $\tau = 1$ ps, and a spectral coherence linewidth of 1 nm. (b) Distinguishable photons, where photon 1 is centered at 825 nm and photon 2 is centered at 835 nm, with all other parameters kept the same.

$$\Psi^{\pm}_{jk}(\omega_1,\omega_2) = \frac{1}{\sqrt{2}}\left(\phi_j(\omega_1)\phi_k(\omega_2) \pm \phi_k(\omega_1)\phi_j(\omega_2)\right), \tag{4.12}$$

and where we assume no spectral overlap between the mode function, that is, $\phi_j(\omega)\phi^*_k(\omega) = 0\ \forall\omega$. These are the states that we herald in Ch.III, and they exhibit (anti)symmetry under exchange of mode labels:

$$\Psi^{\pm}_{jk}(\omega_1,\omega_2) = \pm\ \Psi^{\pm}_{jk}(\omega_2,\omega_1). \tag{4.13}$$

Due to these symmetry properties of these states, we find that, for $\rho^{\pm}_{jk}(\omega_1,\omega_1';\omega_2,\omega_2') = \Psi^{\pm}_{jk}(\omega_1,\omega_2)\left(\Psi^{\pm}_{jk}(\omega_1',\omega_2')\right)^*$,

$$\rho^{\pm}_{jk}(\Omega,\Omega;\Omega',\Omega') = \rho^{\pm}_{jk}(\Omega',\Omega';\Omega,\Omega) = \pm\ \rho^{\pm}_{jk}(\Omega,\Omega';\Omega',\Omega). \tag{4.14}$$

Because of this, we have the result that the constant term and the interference term in the HOM-JSI are identical, up to a sign, yielding a HOM-JSI of the form:

$$P_{jk}(\Omega,\Omega';\tau) = \frac{1}{2}\rho^{\pm}_{jk}(\Omega,\Omega;\Omega',\Omega')\left(1 \mp \cos(\Omega-\Omega')\tau\right). \tag{4.15}$$

To appreciate the significance of the interference term in this case, we shall contrast it with the classically correlated state

$$\rho^{\mathrm{cl}}_{jk}(\omega_1,\omega_1';\omega_2,\omega_2') = \frac{1}{2}\left(\phi_j(\omega_1)\phi_k(\omega_2)\phi_j^*(\omega_1')\phi_k^*(\omega_2') + \phi_j(\omega_2)\phi_k(\omega_1)\phi_j^*(\omega_2')\phi_k^*(\omega_1')\right). \tag{4.16}$$

In this case the HOM-JSI is identical to that of Eq. (**??**), exhibiting no interference. Thus in this case the interference fringes, in combination with the correlated nature of the JSI and the HOM-JSI, are a signature of entanglement. In Fig. 4.4 we show the HOM-JSI for both (a) Ψ^+ and (b) Ψ^-, simulated with the same parameters used before. Note the interference fringes are out of phase with each other between these two states, as expected from the sign difference.

We now arrive at an even more notable result. Consider mixtures of Bell states of the form

$$\rho^{\pm}(\omega_1,\omega_1';\omega_2,\omega_2') = \sum_{jk} p_{jk}\rho^{\pm}_{jk}(\omega_1,\omega_1';\omega_2,\omega_2'). \tag{4.17}$$

These are the mixed states we herald in the entanglement-swapping experiment when we do not resolve the BSM, and they retain the symmetry properties of their constituent Bell states, such that

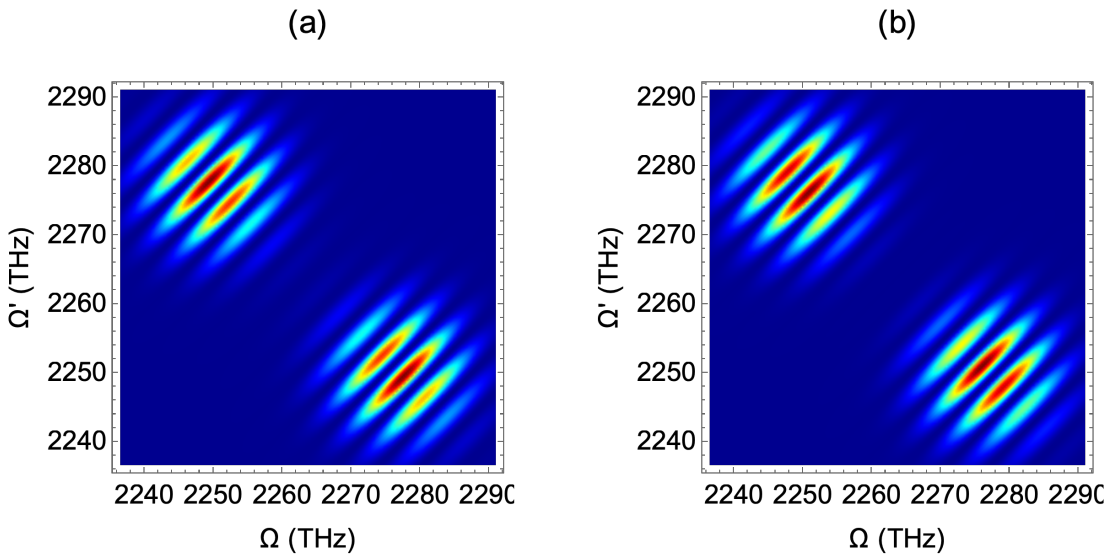

FIGURE 4.4. HOM-JSI's for two photons in a Bell state $|\Psi^+_{jk}\rangle$ (a) or $|\Psi^-_{jk}\rangle$ (b). Note the out-of-phase interference fringes due to the sign difference between the states.

$$\rho^{\pm}(\Omega,\Omega;\Omega',\Omega') = \rho^{\pm}(\Omega',\Omega';\Omega,\Omega) = \pm\,\rho^{\pm}(\Omega,\Omega';\Omega',\Omega). \tag{4.18}$$

Thus for these mixed states, the HOM-JSI still contains identical constant and interference terms:

$$P(\Omega,\Omega';\tau) = \frac{1}{2}\rho^{\pm}(\Omega,\Omega;\Omega',\Omega')\,(1 \mp \cos(\Omega-\Omega')\tau)\,, \tag{4.19}$$

and still display interference fringes across the full spectrum. In Fig. 4.5 we show the HOM-JSI simulated for the mixed state $\hat{\rho}$ from the entanglement swapping experiment, with a delay of $\tau = 1$ ps.

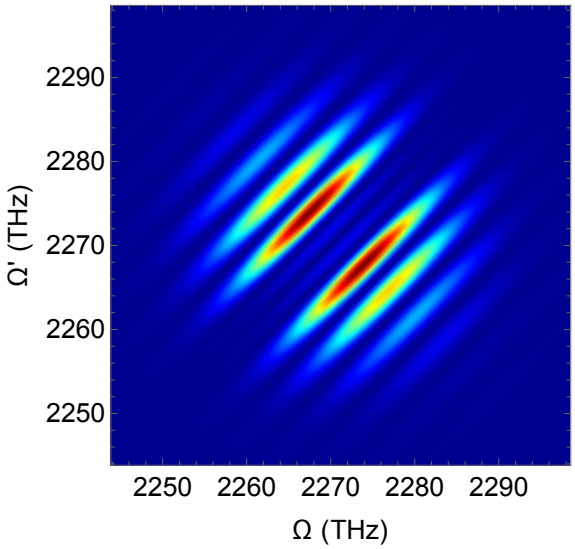

FIGURE 4.5. HOM-JSI simulated for the mixed state $\hat{\rho}$ from the entanglement swapping experiment. The interference fringes persist because of the full antisymmetry of the state.

4.1.4. When spectrally-resolved interference can verify entanglement

Having studied these cases of spectrally resolved HOM interference, we can arrive at a conjecture as to when the HOM-JSI reveals spectral entanglement of a two-photon state. We first observe that the interference fringes are observed over the entire HOM-JSI only for the states where the constant term and the interference term are identical (up to a sign). This condition, as we have seen, holds for at least two classes of two-photon states: pure factorable identical states, and states that, although mixed, exhibit (anti)symmetry with respect to exchange of the frequencies. Furthermore, we saw how, for states that contain only classical correlations, there will be no spectral fringes except along the diagonal $\Omega = \Omega'$. This leads to the intuition that if the JSI[1] of the two-photon state is not factorable, and if the HOM-JSI exhibits interference fringes throughout the

[1]We indeed mean the JSI (not the HOM-JSI), which can be measured directly without using a beam splitter.

spectrum, then we can conclude the two-photon state is entangled. We can make the notion more precise by examining the converse:

If a two-photon state is not entangled, then it falls into either Case 1 or Case 2 that we studied above. In these cases, the symmetry condition

$$\rho_{12}(\Omega,\Omega;\Omega',\Omega') = \rho_{12}(\Omega',\Omega';\Omega,\Omega) = \pm\,\rho_{12}(\Omega,\Omega';\Omega',\Omega) \tag{4.20}$$

is only obtained for Case 1, in the limit that the two single-photon states are identical, for which the JSI is factorable. Therefore, if the JSI is not factorable, and the condition (4.20) holds, such that the constant and the interference terms in the JSI are identical, then the state is entangled. If the JSI is factorable, or if the symmetry condition fails, then no conclusion can be made with regards to the entanglement.

4.1.5. Experimental verification of entanglement using HOM-JSI

We are able to experimentally investigate this conjecture by using the heralded Bell states $|\Psi_{jk}\rangle$ and $\hat{\rho} = \sum_{jk} p_{jk} |\Psi_{jk}\rangle \langle\Psi_{jk}|$ from the experiment in Chapter III. As we indicated in Chapter III Appendix A.2, because of the pulsed nature of our photon states, we lose entanglement whenever τ_{I} is much greater than the pulse duration, since this introduces distinguishability in the heralded states. Thus by changing this parameter we are able to test the HOM-JSI for both the entangled and the classically correlated case.

The setup for this experiment is identical to that for measuring the $F_{jk}(\omega_1,\omega_2)$, except that we introduce the beamsplitter before the JSI measurement. We set the delay τ_{S} at a constant value of 3 ps, in order to introduce spectral fringes, and then we measured $P_{jk}(\Omega,\Omega';\tau)$ for both the entangled case, where

$\tau_{\mathrm{I}} = 0$ps, and the non-entangled case, where we set $\tau_{\mathrm{I}} = 1$ps. We determined that this delay was sufficient to destroy the entanglement based on the two-dimensional peak we measured in the entanglement-swapping experiment. We collected the data for each case over a period of 16 hours.

In Fig. 4.6, we show the results of the entangled case, with $\tau_{\mathrm{I}} = 0$ps. Note the spectral interference fringes that are present in every HOM-JSI for each state $|\Psi_{jk}\rangle^2$, even for the states in the regions away from the diagonal line. The presence of the fringes over the full spectrum suggest that the states satisfy the symmetry condition (4.20). We also look at the aggregate HOM-JSI due to the mixed state $\hat{\rho}$, and observe that these same interference fringes persist over the entire spectrum (Fig. 4.7).

We take a double Fourier transform of the data to isolate the constant and the interference terms. We plot the Fourier-domain data in Fig. 4.8 (a), where we see a peak in the center corresponding to the constant term, and two peaks offset along the diagonal at 3 ps away from the center, which correspond to the interference term and agree with the delay τ_{S} that we set. We isolate the constant and the interference terms and, by taking an inverse Fourier transform, we can plot their respective amplitudes (Fig. 4.8 (b) and (c)), and see that the interference term extends over the entire spectrum.

[2]In this data, we have binned the (j, k) components at twice the native resolution of the time-tagger. This is because it allows us to observe four times as much data in each bin and better resolve the spectral fringes. Ultimately the count rate of this measurement is half of that of the F_{jk} due to the addition of a second beamsplitter.

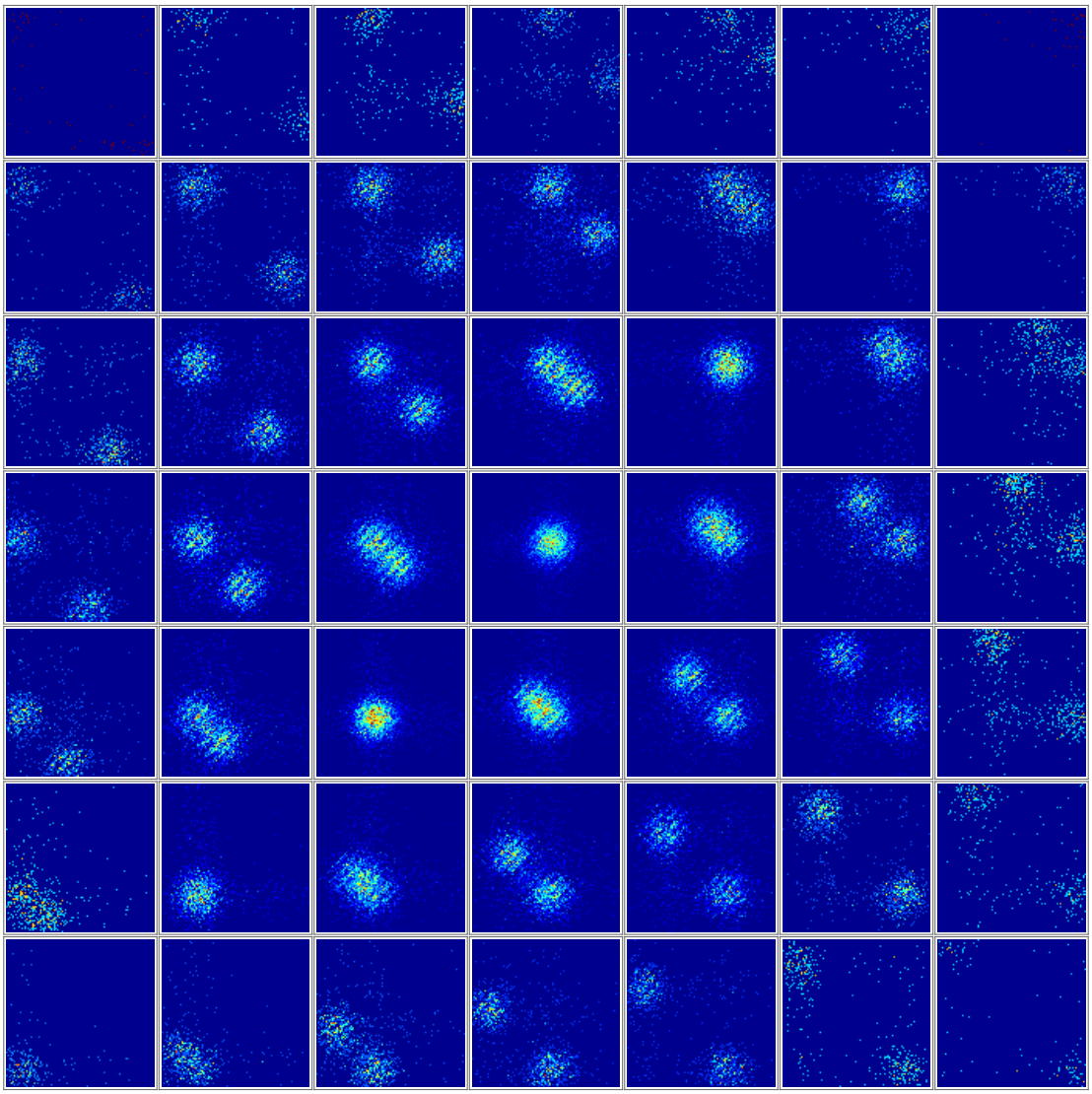

FIGURE 4.6. Experimental HOM-JSI's measured for the $|\Psi_{jk}\rangle$ heralded in the entanglement swapping experiment, with $\tau_{\mathrm{I}} = 0$ ps. Here the data was binned at twice the native resolution so that there are more counts per bin, making the fringes more visible.

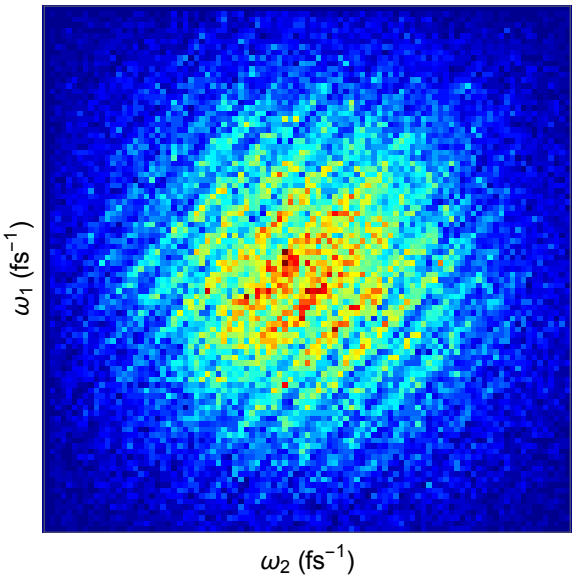

FIGURE 4.7. Aggregate HOM-JSI for the state $\hat{\rho}$ from the entanglement swapping experiment. The antisymmetry of the Bell pairs persists in the mixed state, and interference fringes can be seen on the spectrum.

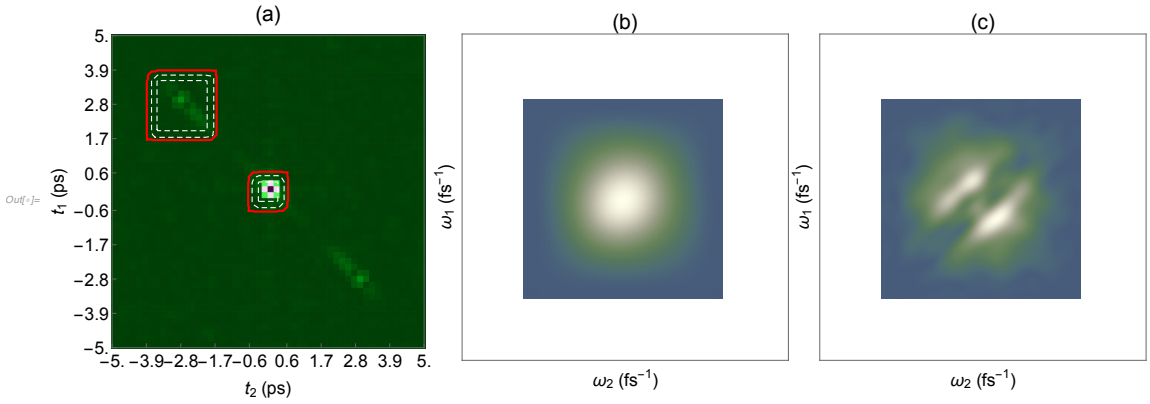

FIGURE 4.8. (a) Fourier-domain representation of the data from Fig. 4.7. We apply filters (shown in red) in the Fourier domain to isolate the constant and interference terms, and, by taking an inverse Fourier transform, plot their amplitudes in the spectral domain. The amplitudes of the constant (b) term and the interference (c) term can be seen to have their support over the same region, which is consistent with the symmetry condition.

We contrast the entangled case with the non-entangled case, which we obtain by setting $\tau_{\mathrm{I}} = 1$ ps for the heralded states. This is sufficient to introduce distinguishability between the heralding photons, and result in a classically correlated state. This destruction of coherence results in the erasure of interference fringes in the HOM-JSI, and this can be observed in Fig. 4.9, where fringes are only observed along the diagonal where $|\rho(\Omega, \Omega')|^2$ is nonzero. We again take a double Fourier transform and isolate the constant and interference terms. By transforming back to the frequency domain, we see that the interference term only has support along the diagonal (Fig. 4.11 (c)).

These results are consistent with our theoretical prediction that the symmetry condition (4.20) is a sufficient test for entanglement in the case of states with a symmetric JSI exhibiting frequency anti-correlations. That is, given a two-photon JSI $F(\omega_1, \omega_2)$ which exhibits frequency anti-correlations symmetric about the diagonal $\omega_1 = \omega_2$, it is possible to test for whether these anti-correlations

are classical or quantum in nature by measuring the HOM-JSI. The presence of interference fringes in the HOM-JSI can confirm the quantum nature of the correlations, whereas the absence of fringes is inconclusive. This test surprisingly verifies entanglement even for the class of fully mixed states which happen to satisfy the symmetry condition.

4.2. Antibunching of photons in mixed entangled states

In Reference [74], it was shown by Fedrizzi *et al* that antibunching of two photons at a beam splitter in the HOM configuration is indicative of a state that is antisymmetric upon exchange of the input mode labels. In other words, this kind of antibunching is indicative of entanglement in some degree of freedom. In the case of that article, and in the case we study in this thesis, the entanglement is in frequency. Here we generalized this result to show that this test of antibunching can reveal entanglement even in mixed states.

Consider the HOM coincidence probability from the previous section, with $\tau = 0$, but instead of spectrally resolving the detections, we simply detect all of the coincidences. The coincidence probability is now given by

$$P(\tau = 0) = \int \mathrm{d}\Omega \mathrm{d}\Omega' P(\Omega, \Omega'; 0) = \frac{1}{2} \int \mathrm{d}\Omega \mathrm{d}\Omega' \Big(\rho_{12}(\Omega, \Omega; \Omega', \Omega') - \rho_{12}(\Omega, \Omega'; \Omega', \Omega) \Big). \tag{4.21}$$

For a separable state of the form (4.3), this probability evaluates to

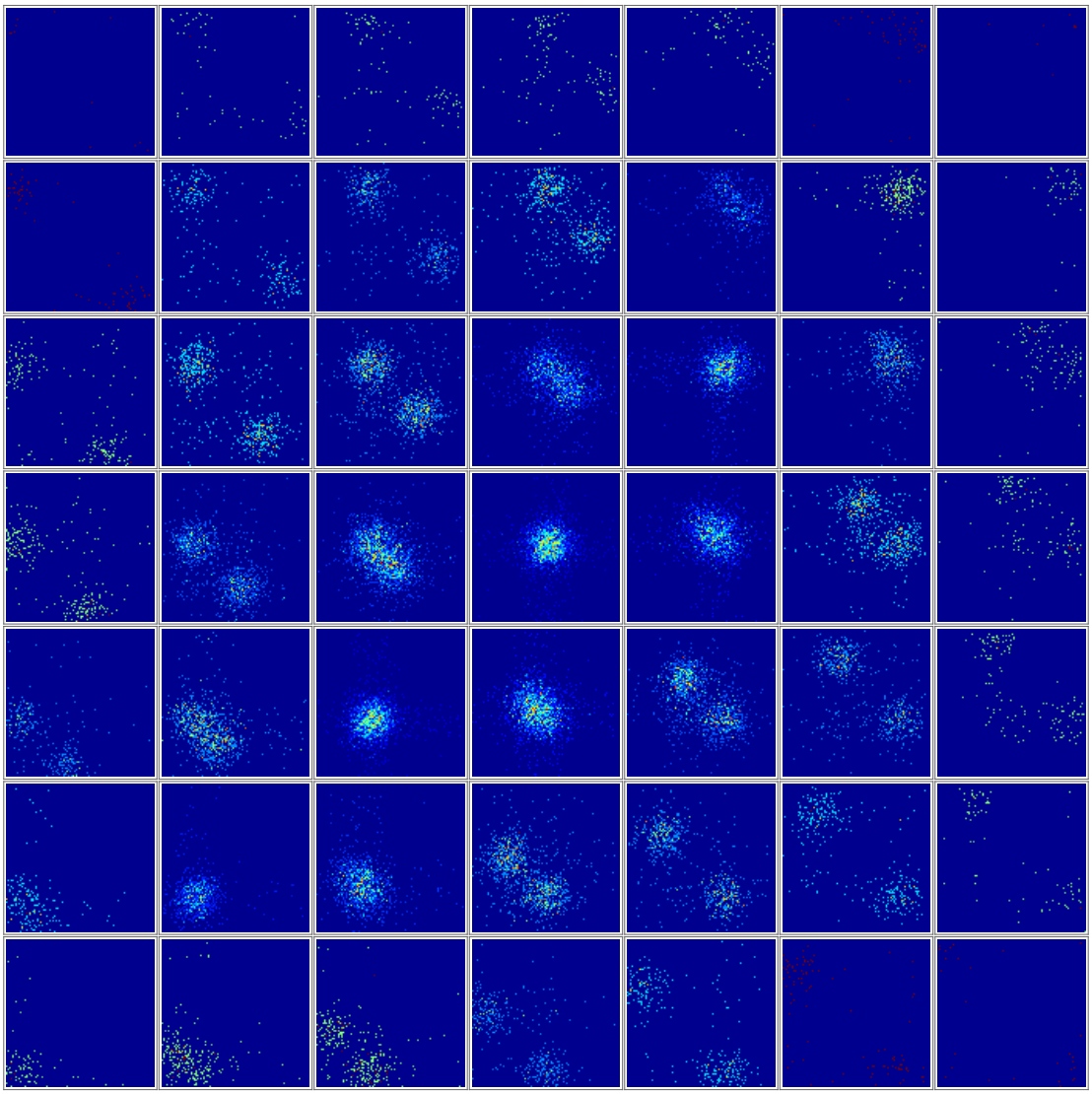

FIGURE 4.9. Experimental HOM-JSI's measured for the $\hat{\rho}_{jk}$ heralded in the entanglement swapping experiment, with $\tau_{\mathrm{I}} = 1$ ps, introducing distinguishability and erasing coherence between the two terms in the Bell state. Note the absence of interference fringes now.

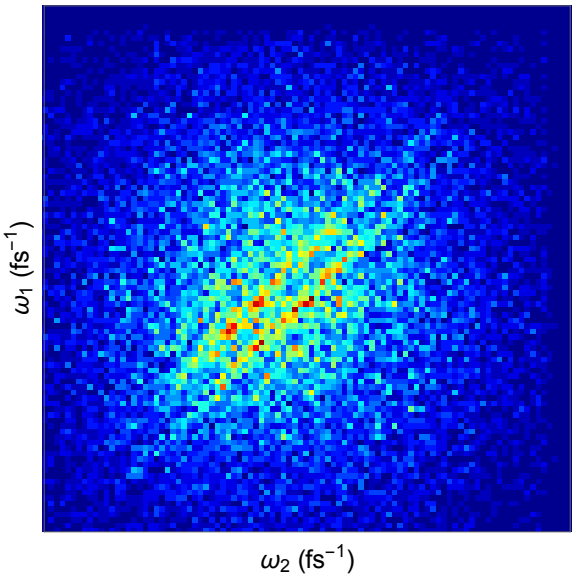

FIGURE 4.10. Aggregate HOM-JSI for the state $\hat{\rho}$ from the entanglement swapping experiment. Because of the distinguishability introduced by the time delay $\tau_{\mathrm{I}} = 1$ ps, the interference fringes are erased and only survive in the diagonal region where there $\rho(\Omega, \Omega')$ is nonzero.

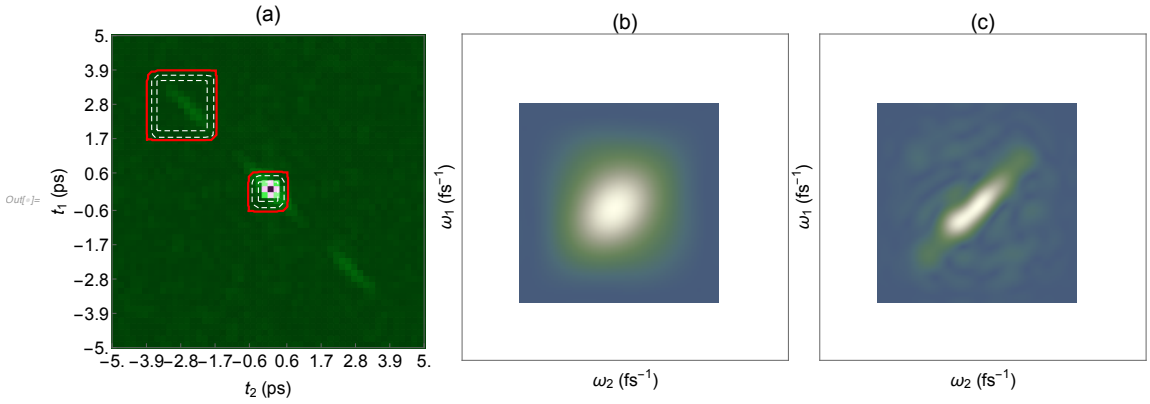

FIGURE 4.11. (a) Fourier-domain representation of the data from Fig. 4.10. We apply filters (shown in red) in the Fourier domain to isolate the constant and interference terms, and, by taking an inverse Fourier transform, plot their amplitudes in the spectral domain. The amplitude of the interference term (c) is now restricted to the diagonal region, as compared with the amplitude of the constant term (b).

$$P(0) = \frac{1}{2}\sum_i p_i \left(\int \mathrm{d}\Omega \rho_1^{(i)}(\Omega,\Omega) \int \mathrm{d}\Omega' \rho_2^{(i)}(\Omega',\Omega') - \int \mathrm{d}\Omega \mathrm{d}\Omega' \rho_1^{(i)}(\Omega,\Omega')\rho_2^{(i)}(\Omega',\Omega) \right)$$
$$= \frac{1}{2}\sum_i p_i \left(1 - \mathrm{Tr}(\hat{\rho}_1^{(i)}\hat{\rho}_2^{(i)})\right). \tag{4.22}$$

The quantity $\mathrm{Tr}(\hat{\rho}_1^{(i)}\hat{\rho}_2^{(i)})$ is a measure of the overlap of the the two states $\hat{\rho}_1^{(i)}$ and $\hat{\rho}_2^{(i)}$, and satisfies (see, for example [62])

$$0 \leq \mathrm{Tr}(\hat{\rho}_1^{(i)}\hat{\rho}_2^{(i)}) \leq 1. \tag{4.23}$$

Therefore, for all separable states (pure or mixed), we have

$$0 \leq P(0) \leq \frac{1}{2}. \tag{4.24}$$

Thus, whenever $P(0) > \frac{1}{2}$, that is, whenever a HOM peak, rather than a dip, is observed, we can conclude that the two-photon input state is not separable, and therefore entangled. This is indeed the case for the state responsible for the peak in Chapter III, Fig. 3.9, which retains the antisymmetry of the constituent states $|\Psi_{jk}\rangle \langle\Psi_{jk}|$.

We may equivalently express this result in terms of the POVM element corresponding to the HOM detection, which, as we saw in the previous chapter, is a sum over the Bell-state measurements $\hat{\Pi}_{jk}$,

$$\hat{\Pi}_{\mathrm{HOM}} = \sum_{jk} \hat{\Pi}_{jk}. \tag{4.25}$$

Now the inequality (4.24) may be expressed as

$$\mathrm{Tr}(\hat{\rho}\hat{\Pi}_{\mathrm{HOM}}) \leq \frac{1}{2}, \quad \text{for all separable states } \hat{\rho}. \tag{4.26}$$

Thus observing $\mathrm{Tr}(\hat{\rho}\hat{\Pi}_{\mathrm{HOM}}) > \frac{1}{2}$ indicates that $\hat{\rho}$ is non-separable, and this quantity is an entanglement witness [91].

4.3. Bridge

We have developed theoretically and experimentally a spectrally multiplexed method of implementing entangled measurements on two-photon states, and demonstrated entanglement swapping of multimode time-frequency entangled states. Our methods rely on the standard linear optics Bell state measurement, coupled with high spectral resolution to enable both the heralding and verification of multimode entangled states. Perhaps one obvious question that arises is, given that it is possible to generate high-dimensional entanglement in two photon states,

is it equally possible to perform two-photon entangled measurements that project onto correspondingly high-dimensional entanglement? In the next chapter, we answer this question in the affirmative, by showing how to exploit a non-linear optical process that is the reverse of parametric down-conversion: sum-frequency generation. In this process, two photons interact in a non-linear medium to produce one photon. We show using the POVM formalism how the subsequent detection of that photon amounts to a joint measurement on the two input photons, and describe several properties associated with the two-photon POVM, including entanglement. We believe this formalism paves the way towards having a general framework for multimode entangled measurements which can be applied towards understanding two-photon processes and informing implementations of quantum protocols.

CHAPTER V

POSITIVE OPERATOR-VALUED MEASURE FOR TWO-PHOTON DETECTION VIA SUM-FREQUENCY GENERATION

This Chapter includes material that was published in: Merkouche, S., Thiel, V., and Smith, B. J. "Positive operator-valued measure for two-photon detection via sum-frequency generation", *Phys. Rev. A* **103**, 043711 (2021). Reprinted with permission from the authors. I developed the theory and wrote the paper, and VT edited the paper. BJS was the principal investigator for this work.

5.1. Introduction

Entangled photon pairs are an extremely useful system for studying both the fundamentals [92] and applications of quantum mechanics, and are the workhorse of experimental quantum optics. This is mainly due to their ease of generation in the laboratory through spontaneous parametric downconversion (PDC), whereby a nonlinear medium such as a crystal is pumped with a bright laser beam and mediates the probabilistic splitting of one pump photon into a pair of photons, subject to energy and momentum conservation. Over the past three decades, much progress has been made in the generation of PDC photon pairs with well-engineered polarization, spectral-temporal, and spatial structure, exhibiting varying degrees of correlation in all of these degrees of freedom. Particular attention has been given recently to encoding quantum information in the spectral-temporal degree of freedom of light. This is because time-frequency modes of light, generally referred to as *temporal modes*, can encode a large amount of information, are particularly well-suited to integrated optics technology, and are robust to

communication channel noise [35]. In addition, time-frequency entangled photons are useful for applications such as large-alphabet quantum key distribution [93], quantum-enhanced spectroscopy [71, 94, 95], and quantum-enhanced sensing [96].

Complementary to two-photon state generation is two-photon joint detection, which is an example of the more general concept of a joint quantum measurement on two systems. It is known that joint quantum measurements on separately prepared systems can inherently reveal more information than accessible through separate measurements relying on local operations and classical communication [97]. In addition *entangled measurements*, joint measurements whose eigenstates are entangled states, are as crucial a resource as entangled states in quantum protocols such as quantum teleportation [28], remote state preparation [98], entanglement swapping [99**?**], superdense coding, and quantum illumination [**?**]. In fact, the equal footing that entangled states and entangled measurements have in quantum protocols such as teleportation has only recently been given due attention [29].

One way to implement a two-photon joint measurement is to use the complement of PDC, sum-frequency generation (SFG). Here two photons interact in a nonlinear medium and are upconverted to a single photon, conserving energy and momentum. Two-photon measurement via SFG has been explored theoretically [95] and experimentally [100]. In addition, it has been pointed out that the theory of two-photon detection by SFG closely parallels that of two-photon absorption in a molecule, and a unified framework describing both of these processes can be found in reference [95].

In this work we construct and analyze the positive operator valued measure (POVM) associated with joint two-photon measurements relying on SFG followed

by mode-selective detection of the upconverted photon in the time-frequency domain. Our development of the two-photon POVM closely parallels that of the POVM for a single photon detected after a filter, as described in reference [66]. We then give some figures of merit for such measurements that are relevant to some of the aforementioned protocols, namely the projectivity, orthogonality, and entanglement of the measurement operators. We illustrate the role of entanglement in measurements with a model of the spectral quantum teleportation scenario. We conclude by highlighting some questions and possible future directions left open by this work.

5.2. Framework

5.2.1. The three-wave mixing interaction

We begin by writing down the transformation describing three-wave mixing, which includes both parametric down-conversion and sum-frequency generation, in the interaction picture. We assume a given polarization configuration and assume that all the interacting fields occupy a single transverse spatial mode, so that only the time-frequency degrees of freedom of the field are relevant. Under these conditions the transformation may be expressed as

$$\begin{aligned} \hat{H} &= \hat{H}_{PDC} + \hat{H}_{SFG}, \\ \hat{H}_{PDC} &= \chi \int \mathrm{d}\omega_s \mathrm{d}\omega_i \Phi(\omega_s, \omega_i)\ \hat{a}_p(\omega_s + \omega_i)\hat{a}_s^\dagger(\omega_s)\hat{a}_i^\dagger(\omega_i), \\ \hat{H}_{SFG} &= (\hat{H}_{PDC})^\dagger, \end{aligned} \tag{5.1}$$

where $\hat{a}_j^{(\dagger)}(\omega_j)$ is the annihilation (creation) operator for a single photon at monochromatic mode j with frequency ω_j, and $j = p, s, i$ label the pump, signal,

and idler frequencies; $\chi \ll 1$ is a parameter characterizing the efficiency of the process, describing the second-order nonlinearity and containing all the parameters that are constant or slowly-varying over the integration; and $\Phi(\omega_s, \omega_i)$ is the *phase-matching function*, which has the form

$$\Phi(\omega_s, \omega_i) \propto \mathrm{sinc}\left(\frac{\Delta\mathbf{k}\cdot\mathbf{L}}{2}\right), \tag{5.2}$$

where $\mathbf{L}$ is the vector quantifying the length of the interaction medium, and $\Delta\mathbf{k} = \mathbf{k}_p(\omega_s + \omega_i) - \mathbf{k}_s(\omega_s) - \mathbf{k}_i(\omega_i)$ is the wavevector mismatch for the three fields. Φ takes on its maximum value when $\Delta\mathbf{k} = \mathbf{0}$, and thus corresponds to momentum conservation in the process. Finally, we have separated the transformation explicitly into $\hat{H}_{PDC}$, the term responsible for PDC, and its Hermitian conjugate, $\hat{H}_{SFG}$, responsible for SFG.

The interacting fields evolve unitarily under this transformation, and for our analysis, we will consider only the weak-interaction limit, so that, for an input state $|\Psi_{\mathrm{in}}\rangle$, the output state is given by

$$|\Psi_{\mathrm{out}}\rangle = \exp\left[-i\hat{H}\right]|\Psi_{\mathrm{in}}\rangle \approx \left(1 - i\hat{H}\right)|\Psi_{\mathrm{in}}\rangle\,. \tag{5.3}$$

Note that, in a slight abuse of notation, we are using $\hat{H}$ to reflect the fact that this transformation is derived from the interaction Hamiltonian for three-wave mixing, although the latter is a time-dependent quantity with a different dimensionality (see Appendix B.1).

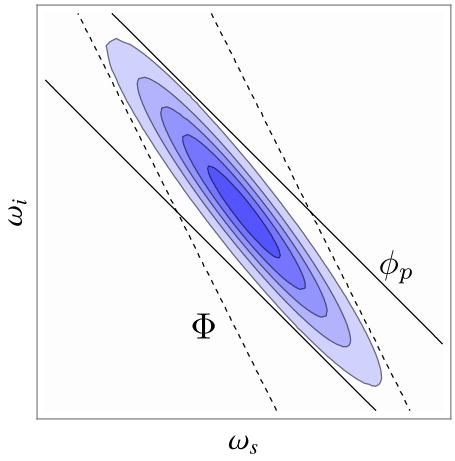

FIGURE 5.1. Two-dimensional plot of the magnitude of a typical JSA. The solid lines contour a Gaussian pump mode $\phi_p(\omega_s + \omega_i)$, and the dashed lines contour the phasematching function $\Phi(\omega_s, \omega_i)$. This shows how spectral correlations arise in the JSA. Frequencies are in arbitrary units.

5.2.2. PDC photon pairs and the joint spectral amplitude

It is instructive to briefly review the spectral-temporal structure of photon pairs generated by PDC, governed by the $\hat{H}_{PDC}$ term. In most applications PDC is pumped by a strong coherent state occupying a spectral mode function $\phi_p(\omega)$, which can be treated as a classical field amplitude $E_p(\omega) = E_0\phi_p(\omega)$, where E_0 quantifies the field strength, and $\phi_p(\omega)$ is normalized as $\int \mathrm{d}\omega \, |\phi_p(\omega)|^2 = 1$. However, since we are working in the perturbative limit, it is equivalent to consider a single-photon pump in the state

$$|\Psi_{\mathrm{in}}\rangle = |\phi_p\rangle = \int \mathrm{d}\omega \phi_p(\omega)\hat{a}_p^\dagger(\omega)\,|\mathrm{vac}\rangle\,. \tag{5.4}$$

After this state undergoes unitary evolution according to equation (5.3), we obtain the output state

$$|\Psi_{\mathrm{out}}\rangle = |\phi_p\rangle - i\sqrt{w}\,|\Psi_{\mathrm{PDC}}\rangle\,, \tag{5.5}$$

where

$$|\Psi_{\mathrm{PDC}}\rangle = \frac{\chi}{\sqrt{w}} \int \mathrm{d}\omega_s \mathrm{d}\omega_i \phi_p(\omega_s + \omega_i)\Phi(\omega_s, \omega_i)\hat{a}_s^\dagger(\omega_s)\hat{a}_i^\dagger(\omega_i)\,|\mathrm{vac}\rangle \tag{5.6}$$

is a normalized two-photon state, and where

$$w = \int \mathrm{d}\omega_s \mathrm{d}\omega_i |\chi\ \phi_p(\omega_s + \omega_i)\Phi(\omega_s, \omega_i)|^2 \tag{5.7}$$

is a normalization factor.

It is convenient here to define the *joint spectral amplitude* (JSA)

$$f(\omega_s, \omega_i) = \frac{\chi}{\sqrt{w}}\phi_p(\omega_s + \omega_i)\Phi(\omega_s, \omega_i), \tag{5.8}$$

so that

$$|\Psi_{\mathrm{PDC}}\rangle = \int \mathrm{d}\omega_s \mathrm{d}\omega_i f(\omega_s, \omega_i)\hat{a}_s^\dagger(\omega_s)\hat{a}_i^\dagger(\omega_i)\,|\mathrm{vac}\rangle \tag{5.9}$$

The JSA can be viewed as a two-photon wavefunction, and its modulus squared, $|f(\omega_s, \omega_i)|^2$, is the probability density function for the photon pair in frequency space, normalized as $\int \mathrm{d}\omega_s \mathrm{d}\omega_i |f(\omega_s, \omega_i)|^2 = 1$. Considerable progress has been made in engineering the temporal-mode structure of PDC photon pairs, which is completely characterized by the JSA, and this is done by shaping of the pump spectral amplitude $\phi_p(\omega_s + \omega_i)$ and engineering of the phasematching $\Phi(\omega_s, \omega_i)$ in the nonlinear medium. We plot schematically in Fig. 5.1 a typical JSA configuration showing its dependence on the pump amplitude and the phasematching function. A thorough review of the state-of-the-art in two-photon state engineering in the time-frequency domain can be found in reference [2].

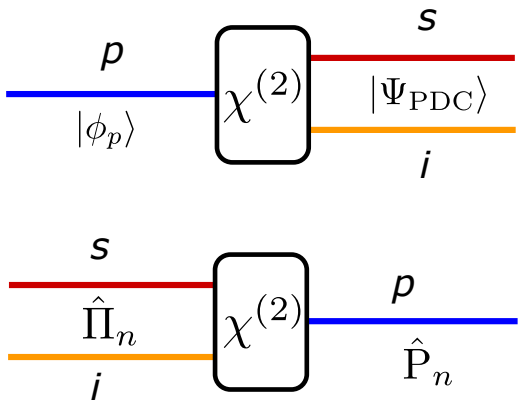

FIGURE 5.2. PDC uses a $\chi^{(2)}$ interaction medium to convert a single-photon state $|1_\phi\rangle$ in the mode p to a pair of photons in modes s and i, described by the state $|\psi_{\mathrm{PDC}}\rangle$ given in the text. In the time-reverse picture, a projective measurement $\hat{\mathrm{P}}_n$ of a single photon produced by SFG implements measurement with POVM element $\hat{\Pi}_n$ on the two input photons.

5.2.3. Two-photon SFG and the two-photon POVM

We now turn our attention to the SFG term in equation (5.1), explicitly given by

$$\hat{H}_{SFG} = \chi^* \int \mathrm{d}\omega_s \mathrm{d}\omega_i \Phi^*(\omega_s, \omega_i) \hat{a}_p^\dagger(\omega_s + \omega_i) \hat{a}_s(\omega_s) \hat{a}_i(\omega_i) \tag{5.10}$$

and consider the upconversion of an arbitrary pure two photon state given by

$$|\Psi_{\mathrm{in}}\rangle = |\psi_g\rangle = \int \mathrm{d}\omega_s \mathrm{d}\omega_i g(\omega_s, \omega_i) \hat{a}_s^\dagger(\omega_s) \hat{a}_i^\dagger(\omega_i) \, |\mathrm{vac}\rangle \,, \tag{5.11}$$

where $g(\omega_s, \omega_i)$ is a two-photon JSA. The output state will then be

$$|\Psi_{\mathrm{out}}\rangle = |\psi_g\rangle - i\chi^* \, |\sigma\rangle \,, \tag{5.12}$$

where

$$|\sigma\rangle = \int d\nu \sigma(\nu) \hat{a}_p^\dagger(\nu) \left|\text{vac}\right\rangle, \tag{5.13}$$

with the (unnormalized) spectral amplitude function

$$\sigma(\nu) = -\frac{1}{2} \int d\nu' \; \tilde{\Phi}^* \left(\nu, \nu'\right) \tilde{g} \left(\nu, \nu'\right). \tag{5.14}$$

We obtain this last equation by changing variables to the sum and difference frequencies $\nu = \omega_s + \omega_i$ and $\nu' = \omega_s - \omega_i$, and defining $\tilde{\Phi}^*(\nu, \nu') = \Phi^* \left(\frac{\nu+\nu'}{2}, \frac{\nu-\nu'}{2}\right)$ (and likewise for $\tilde{g}(\nu, \nu')$).

We are now equipped to develop the two-photon POVM corresponding to a detection of the upconverted single-photon state $|\sigma\rangle$, which closely mirrors the one-photon, pre-filter POVM described in reference [66]. Consider performing an ideal, projective measurement of the upconverted photon onto an orthonormal set of temporal mode single photon states $\{(\hat{\mathrm{P}}_n = |\phi_n\rangle \langle\phi_n|)_{n=1}^{\infty}\}$ with

$$|\phi_n\rangle = \int \mathrm{d}\omega \phi_n(\omega) \hat{a}_p^\dagger(\omega) \left|\text{vac}\right\rangle, \tag{5.15}$$

satisfying

$$\langle\phi_n|\phi_m\rangle = \int \mathrm{d}\omega \; \phi_n^*(\omega) \phi_m(\omega) = \delta_{nm}. \tag{5.16}$$

Such a measurement can in principle be realized using a quantum pulse gate, recently described and demonstrated in references [46, 101], whereby a strong pump field in a particular temporal mode selects out that same mode from an input signal field and upconverts it through SFG to a register mode which can be

easily detected with a spectrometer. The probability for a successful detection for this measurement will be given by

$$\begin{aligned} p_n &= |\chi^* \langle \phi_n | \sigma \rangle|^2 \\ &= \left| -\frac{\chi^*}{2} \int \mathrm{d}\nu \mathrm{d}\nu' \; \phi_n^*(\nu) \tilde{\Phi}^* (\nu, \nu') \, \tilde{g} (\nu, \nu') \right|^2 \\ &= \left| \chi^* \int \mathrm{d}\omega_s \mathrm{d}\omega_i \phi_n^*(\omega_s + \omega_i) \Phi^*(\omega_s, \omega_i) g(\omega_s, \omega_i) \right|^2 \end{aligned} \tag{5.17}$$

However, this same probability can be obtained by applying the Born rule to the input state $\hat{\rho}_{\mathrm{in}} = |\Psi_{\mathrm{in}}\rangle \langle \Psi_{\mathrm{in}}|$ in the two-photon space:

$$p_n = \mathrm{Tr}(\hat{\rho}_{\mathrm{in}} \hat{\Pi}_n), \tag{5.18}$$

if we define a POVM element

$$\hat{\Pi}_n = w_n \, |\Psi_n\rangle \langle \Psi_n| \, , \tag{5.19}$$

where

$$|\Psi_n\rangle = \frac{\chi}{\sqrt{w_n}} \int \mathrm{d}\omega \mathrm{d}\omega' \phi_n(\omega + \omega') \Phi(\omega, \omega') \hat{a}_s^\dagger(\omega) \hat{a}_i^\dagger(\omega') \, |\mathrm{vac}\rangle \, , \tag{5.20}$$

and

$$w_n = \int \mathrm{d}\omega \mathrm{d}\omega' |\chi \; \phi_n(\omega + \omega') \Phi(\omega, \omega')|^2. \tag{5.21}$$

We immediately recognize $|\Psi_n\rangle$ as the normalized two-photon state that would result from PDC with a pump photon in the state $|\phi_n\rangle$. That is, a projective measurement of an upconverted photon with projector $\hat{\mathrm{P}}_n = |\phi_n\rangle \langle \phi_n|$

implements a generalized measurement of the two input photons with POVM element $\hat{\Pi}_n$. This is schematically shown in Fig. 5.2. Furthermore, the properties of $\hat{\Pi}_n$ follow immediately from the properties of the PDC state $|\Psi_n\rangle$, as we will see in the following section. It is convenient to associate with the POVM element $\hat{\Pi}_n$ a *measurement* JSA

$$f_n(\omega + \omega') = \frac{\chi}{\sqrt{w_n}} \phi_n(\omega + \omega') \Phi(\omega, \omega'). \tag{5.22}$$

To complete the POVM, we note that we are considering an ideal detector in the SFG mode, such that any upconverted photon is detected with certainty. We are thus justified in defining an element corresponding to no detection as

$$\hat{\Pi}_{\text{null}} = \mathbb{1} - \sum_{n=1}^{\infty} \hat{\Pi}_n, \tag{5.23}$$

where $\mathbb{1}$ denotes the identity operator in the relevant two-photon subspace. Using the fact that the ϕ_n mode functions form a complete orthonormal set, such that

$$\sum_{n=1}^{\infty} \phi_n(\omega + \omega') \phi_n(\tilde{\omega} + \tilde{\omega}') = \delta(\omega + \omega' - \tilde{\omega} - \tilde{\omega}'), \tag{5.24}$$

we can evaluate

$$\sum_{n=1}^{\infty} \hat{\Pi}_n = |\chi|^2 \int \mathrm{d}\omega \mathrm{d}\omega' \Phi(\omega, \omega') \Phi^*(\tilde{\omega}, \omega + \omega' - \tilde{\omega}) \left|\omega, \omega'\right\rangle \left\langle \tilde{\omega}, \omega + \omega' - \tilde{\omega}\right|, \tag{5.25}$$

where $|\omega, \omega'\rangle = \hat{a}_s^\dagger(\omega) \hat{a}_i^\dagger(\omega_i) |\text{vac}\rangle$. Using the completeness relation of POVMs, we can express $\hat{\Pi}_{\text{null}}$ explicitly as

$$\hat{\Pi}_{\text{null}} = \mathbb{1} - |\chi|^2 \int \mathrm{d}\omega \mathrm{d}\omega' \mathrm{d}\tilde{\omega} \Phi(\omega, \omega') \Phi^*(\tilde{\omega}, \omega + \omega' - \tilde{\omega}) \left|\omega, \omega'\right\rangle \left\langle \tilde{\omega}, \omega + \omega' - \tilde{\omega}\right| . \quad (5.26)$$

Thus the complete two-photon POVM is

$$\left\{ (\hat{\Pi}_n)_{n=1}^{\infty}, \hat{\Pi}_{\text{null}} \right\}, \quad (5.27)$$

satisfying

$$\sum_{n=1}^{\infty} \hat{\Pi}_n + \hat{\Pi}_{\text{null}} = \mathbb{1}. \quad (5.28)$$

5.3. Properties of the measurement operator

5.3.1. Projectivity

We will now take advantage of the well-studied properties of the two-photon PDC state $|\Psi_n\rangle$ to analyze some of the useful properties of the POVM element $\hat{\Pi}_n$. We begin by defining the retrodicted two-photon state [25], corresponding to an outcome n, as

$$\hat{\rho}_n = \frac{\hat{\Pi}_n}{\mathrm{Tr}(\hat{\Pi}_n)} = \left|\Psi_n\right\rangle \left\langle \Psi_n\right| . \quad (5.29)$$

We consider the measurement *projective*, if $\hat{\rho}_n$ is a pure state, satisfying $\mathrm{Tr}(\hat{\rho}_n^2) = 1$, which is indeed the case for equation (5.29).

In general, however, single-photon detectors are not perfectly resolving. In the case of the quantum pulse gate, a detector click may not correspond to single pulse mode, but rather an incoherent mixture of a few modes. In the case of a

non-ideal spectrally resolving detection, one either uses a filter of finite bandwidth, or a spectrometer with finite resolution. In all of these cases, it is more accurate to describe a non-ideally resolving, that is, non-projective, single-photon measurement by

$$\hat{\mathrm{P}}_q = \sum_n q_n \hat{\mathrm{P}}_n \tag{5.30}$$

where $0 \leq q_n \leq 1$ are weighting coefficients. This leads to a two-photon POVM element

$$\hat{\Pi}_q = \sum_n q_n \hat{\Pi}_n, \tag{5.31}$$

and a retrodicted state

$$\hat{\rho}_q = \frac{\hat{\Pi}_q}{\mathrm{Tr}(\hat{\Pi}_q)}, \tag{5.32}$$

which has $\mathrm{Tr}(\hat{\rho}_q^2) \leq 1$ and is not in general a pure state. Evidently, the two-photon POVM elements are projective if and only if the single-photon measurement operators are projective.

Projective two-photon measurements are of particular importance in quantum teleportation and remote-state preparation, and entanglement swapping, because in these schemes the measurement acts as a herald to a single photon state or a two-photon entangled state, respectively. Ideally the heralded states should be pure to be useful for quantum information processing. And the purity of the heralded state is limited by both the purity of the input states and the purity (projectivity) of the heralding measurement [25].

5.3.2. Orthogonality

Orthogonal measurements are measurements which project onto orthogonal states, and thus satisfy

$$\hat{\Pi}_n \hat{\Pi}_m \propto \delta_{nm} \hat{\Pi}_n. \tag{5.33}$$

We note here that orthogonal measurements of the SFG photon do not correspond to orthogonal two-photon POVM elements in general. This is analogous to the fact that PDC pumped with orthogonal pulse modes does not produce orthogonal PDC states in general. The non-orthogonality of the two-photon states can be seen by taking

$$\begin{gathered} \langle \Psi_n | \Psi_m \rangle = \\ \frac{|\chi|^2}{\sqrt{w_n w_m}} \int \mathrm{d}\omega \mathrm{d}\omega' \phi_n^*(\omega + \omega') \phi_m(\omega + \omega') |\Phi(\omega, \omega')|^2 \neq \delta_{nm}. \end{gathered} \tag{5.34}$$

This is due to the filtering induced by the phasematching function. This is indeed analogous to what happens when two orthogonal modes are subjected to linear filtering (see reference [66] on this point): in general the transmitted modes considered alone are not orthogonal, even though filtering is a unitary process. The orthogonality is preserved only when considering all of the modes involved in the transformation, whereas here we are only considering the signal and idler modes and not the pump.

An obvious question that arises then is, in what cases do the POVM elements, in fact, correspond to orthogonal measurements? The answer to this question becomes obvious when we rewrite equation (5.34) in terms of the sum and difference frequencies ν and ν',

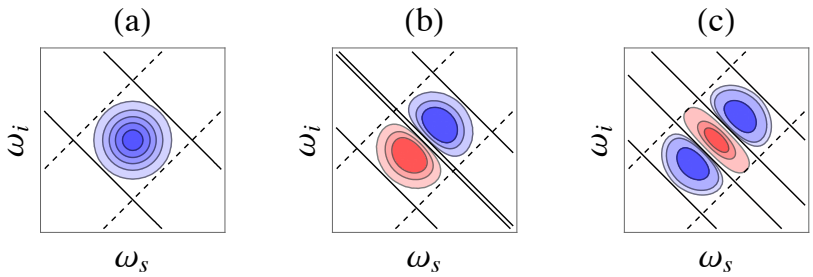

FIGURE 5.3. JSA's for the configuration described in the text where the phasematching function is engineered through group-velocity matching makes an angle $\theta = 45^{\circ}$ with respect to the ω_s-axis. Then it becomes independent of the sum frequency $\nu = \omega_s + \omega_i$, and thus orthogonal measurements of the SFG photon correspond to orthogonal two-photon POVM elements. Blue (red) indicates positive (negative) amplitudes. In the case of PDC, the amount of correlations in the JSA can be controlled by shaping of the pump pulse, as described in reference [2]. Here we plot the JSA's obtained by shaping the pump into the (a) zeroth-, (b) first-, and (c) second-order Hermite-Gauss modes, resulting into mutually-orthogonal two-photon states. Frequencies are in arbitrary units.

$$\langle \Psi_n | \Psi_m \rangle = \frac{|\chi|^2}{4\sqrt{w_n w_m}} \int \mathrm{d}\nu \mathrm{d}\nu' \phi_n^*(\nu)\phi_m(\nu) \left| \tilde{\Phi}\left(\nu, \nu'\right) \right|^2 . \tag{5.35}$$

Clearly, only when the phasematching function does not depend on the sum-frequency ν, that is, $\Phi = \Phi(\nu')$, then do we obtain

$$\langle \Psi_n | \Psi_m \rangle = \delta_{nm}, \tag{5.36}$$

and the $\hat{\Pi}_n$ then satisfy

$$\hat{\Pi}_n \hat{\Pi}_m = \delta_{nm} w_n \hat{\Pi}_n. \tag{5.37}$$

Orthogonality of the two-photon POVM elements is of interest, for example, in the quantum illumination scheme as originally described by Lloyd [**?**]. Here an entangled two-photon state $|\Psi_n\rangle$ is prepared and one of the photons sent

to reflect off a possibly present target, while the other photon is kept in the lab. The two photons are then to be jointly measured, whereupon a successful projection onto the initial state $|\Psi_n\rangle$ indicates the presence of the target. If one is to implement this scheme using SFG as the two-photon measurement, non-orthogonal measurements would suffer from the possibility that the desired state $|\Psi_n\rangle$ could give a positive outcome corresponding to the "wrong" measurement associated with a non-orthogonal state $|\Psi_m\rangle$.

In general, the orthogonality condition (5.36) can be approximately satisfied as long as the phase-matching function varies slowly enough in the ν direction, in comparison to the support of the detection mode function. This happens, for example, in a sufficiently short interaction medium. However, there are two limiting cases that are of note. The first is the spectrally resolved detection limit, which corresponds to simply measuring the output with an ideal spectrometer. In this limit, the detection mode can be approximated by a delta function,

$$\phi_n(\omega) \to \delta(\omega - \omega_n), \tag{5.38}$$

and

$$f_n(\omega, \omega') \propto \delta(\omega + \omega' - \omega_n), \tag{5.39}$$

where ω_n is the measured frequency at the spectrometer. This is the analogue of pumping a PDC source with monochromatic, or continuous-wave (cw), light. In both of these cases, orthogonal pump (or measurement modes) with frequencies ω_n and ω_m correspond to orthogonal two-photon states (or measurements) with sum frequencies ω_n and ω_m.

The second case of interest is achieved by extended phase-matching techniques, as described in reference [2]. For certain nonlinear materials and field configurations, it is possible, using group-velocity matching, to make the phase-matching function approximately constant in the ν direction over some range of interest. More precisely, the phase-matching function can be engineered to make an angle $\theta = 45^{\circ}$ in the ω_s-ω_i plane, perpendicular to the angle that the pump function makes. This configuration has been used by Ansari *et al* to generate PDC states with a controllable temporal-mode structure and degree of entanglement through pump pulse-shaping [101]. This concept is illustrated schematically in Fig. 5.3. More recently, similarly exotic two-photon states have been obtained through phasematching shaped by the periodic poling of the nonlinear crystal, rather than pulse-shaping of the pump [50].

An interesting result that follows from the limit where Φ is independent of ν is the possibility of downconverting an arbitrary pulse shape in a nonlinear medium into an entangled photon pair, and recovering the pump pulse shape by upconverting the photon pair in an identical medium. This can be seen by taking $\tilde{g}(\nu, \nu') = \phi(\nu)\tilde{\Phi}(\nu')$ in equation (5.14), and obtaining

$$\sigma(\nu) = \phi(\nu) \int d\nu' |\tilde{\Phi}(\nu')|^2, \tag{5.40}$$

which is evidently proportional to the input $\phi(\nu)$. The spatial analogue of this result, whereby a pump beam shaped in a specific transverse spatial mode is downconverted, and the photon resulting from the upconversion of the PDC pair is shown to recover the transverse spatial mode, has recently been experimentally demonstrated by Jimenez *et al* [102].

5.3.3. Entanglement

We now turn to perhaps a more interesting question regarding the two-photon measurement operator: when is the POVM element $\hat{\Pi}_n$ a projector onto an entangled two-photon state, and thus can be said to enact an *entangled measurement* on the input photons? [31, 103] We can answer this question readily: $\hat{\Pi}_n$ is an entangled measurement, if the retrodicted state ρ_n is an entangled state. Entangled measurements play a central role in quantum teleportation, superdense coding, and quantum illumination, among many other protocols, and recently the role of entanglement in joint measurements has been recognized to be equally important to the role of entanglement of states as a shared resource [29].

To illustrate the role of entangled measurements in a quantum protocol, we will investigate briefly the spectral quantum teleportation scenario, described by Molotkov [104] and by Humble [3] (and whose spatial analogue was described by Walborn *et al* [105]). In this protocol, Alice and Bob share a two-photon entangled state described by a JSA $f_s(\omega_a, \omega_b)$, and Alice is to teleport a single photon state with spectral amplitude $\psi_c(\omega_c)$ by performing an SFG measurement on this photon and her half of the entangled state, and communicating the measurement result to Bob.

Reference [104] considers only the case of a maximally-correlated pair of entangled photons shared between Alice and Bob, while reference [3] generalizes this result to the case of a Gaussian JSA, which is a good approximation to what can be produced using pulsed lasers as a pump. In both references however, Alice's joint measurement is a spectrally-resolved measurement of the SFG photon. Here we use our formalism to generalize further to a pulse-mode resolved measurement of the SFG photon, as can be realized with a quantum pulse gate, by considering

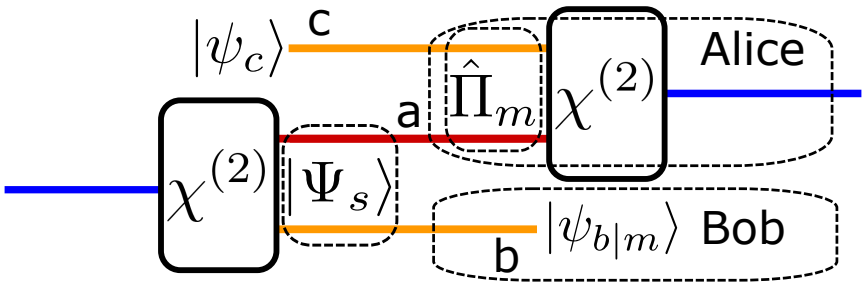

FIGURE 5.4. Spectral teleportation scenario considered in the text. Alice and Bob share entangled photons a and b in the state $|\Psi_s\rangle$. Alice performs a two-photon SFG measurement $\hat{\Pi}_m$ on her photon a and photon c, in the state $|\psi_c\rangle$, and communicates the result of her measurement to Bob, whereupon Bob reconstructs the state $|\psi_{b|m}\rangle$.

a generalized measurement JSA $f_m(\omega_a, \omega_c)$. It was first pointed out in the original proposal of quantum teleportation [28] that in addition to the maximally-entangled state (generalized Bell-state) shared by Alice and Bob, quantum teleportation with unit fidelity is achieved when Alice's joint measurement projects onto a maximally-entangled state. Here we show behavior that is consistent with this result by quantifying the teleportation fidelity as a function of the entanglement of *both* the shared state *and* the joint measurement. It is worth clarifying that our current goal is not to *demonstrate* that the POVM element is entangled, but rather, it is to show that our POVM formalism is sufficient to describe quantum teleportation in the time-frequency domain, provided we stipulate entanglement as a property of the measurement. This is in keeping with the more familiar case of the Bell-state measurement's role in qubit teleportation.

The teleportation scenario we consider is shown schematically in Fig. 5.4. Alice and Bob share entangled photons a and b, respectively, described by a Gaussian JSA similar to the one in reference [3]:

$$
\begin{aligned}
|\Psi_s\rangle &= \int \mathrm{d}\omega_a \; \mathrm{d}\omega_b \; f_s(\omega_a, \omega_b)\hat{a}_a^\dagger(\omega_a)\hat{a}_b^\dagger(\omega_b)\,|\mathrm{vac}\rangle \\
f_s(\omega_a, \omega_b) &= N_s \mathrm{Exp}\left[-\frac{1}{\gamma_s^2(1-\alpha^2)}\left(\frac{\omega_a^2}{2} + \frac{\omega_b^2}{2} + \alpha\omega_a\omega_b\right)\right]
\end{aligned}
\tag{5.41}
$$

where $\alpha \in [-1, 1]$ is the correlation between the the photon frequencies, with $\alpha = 1$ corresponding to maximal frequency anticorrelation, such as would be obtained from a cw pump; γ_s is the characteristic bandwidth of the PDC photons, and N_s is the normalization constant. Alice provides a single photon c to be teleported, described by the state

$$
|\psi_c\rangle = \int \mathrm{d}\omega_c \psi_c(\omega_c)\hat{a}_c^\dagger(\omega_c)\,|\mathrm{vac}\rangle \tag{5.42}
$$

where $\psi_c(\omega_c)$ is an arbitrary spectral amplitude function. Alice initiates the teleportation by performing an SFG measurement on photons a and c, represented by an operator $\hat{\Pi}_m = w_m\,|\Psi_m\rangle\,\langle\Psi_m|$, with

$$
\begin{aligned}
|\Psi_m\rangle &= \int \mathrm{d}\omega_a \; \mathrm{d}\omega_c \; f_m(\omega_a, \omega_c)\hat{a}_a^\dagger(\omega_a)\hat{a}_c^\dagger(\omega_c)\,|\mathrm{vac}\rangle \\
f_m(\omega_a, \omega_c) &= N_m \mathrm{Exp}\left[-\frac{1}{\gamma_m^2(1-\beta^2)}\left(\frac{\omega_a^2}{2} + \frac{\omega_c^2}{2} + \beta\omega_a\omega_c\right)\right]
\end{aligned}
\tag{5.43}
$$

with parameters defined similarly to $|\Psi_s\rangle$.

We point out here that we have centered both f_s and f_m at 0 in frequency space, without loss of generality. This is because, in the protocol described in reference [3], Alice communicates her obtained frequency $\omega_a + \omega_c$ to Bob, whereupon he performs the appropriate frequency translation to his photon b to recover the state that would have resulted, had Alice obtained $\omega_a + \omega_b$ in her measurement. Further note that we are using the parameters α and β to quantify the entanglement of the shared state and the joint measurement, respectively,

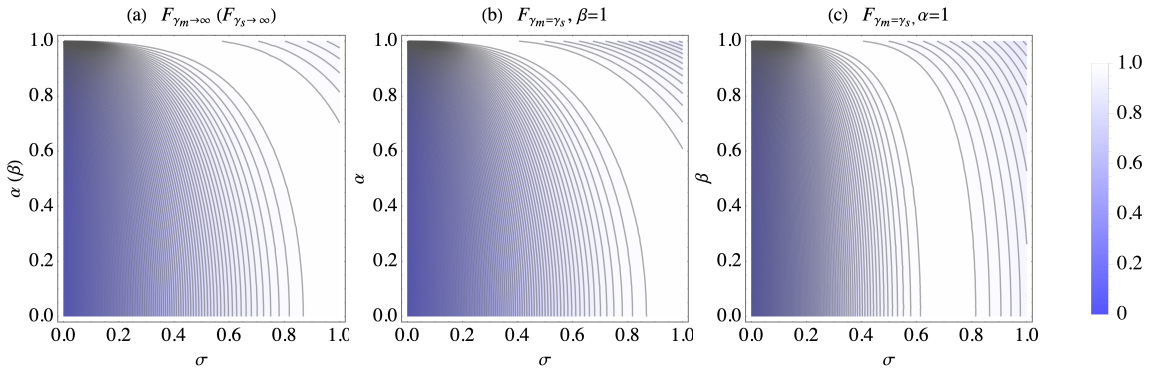

FIGURE 5.5. Behavior of the teleportation fidelity for the different cases described in the text. Plot (a) shows the behavior with α, the state entanglement, and $\sigma = \gamma_c/\gamma_s$, for the ideal SFG measurement, with $\beta = 1$ and $\gamma_m \to \infty$, as considered in Ref [3]. The same plot describes the fidelity as a function of β and $\sigma = \gamma_c/\gamma_m$ for the case of a maximally entangled state with $\alpha = 1$ and $\gamma_s \to \infty$. Plots (b) and (c) illustrate the behavior of the fidelity when the entangled state and the entangled measurement have comparable bandwidths (here $\gamma_s = \gamma_m = 1$). Here the fidelity behaves differently with α and with β, because f_s and f_m are not in general interchangeable in the expression for $\psi_{b|m}$. All quantities are dimensionless.

rather than a more familiar measure of entanglement for pure states, such as the Schmidt number [106]. We have made this choice because, although the Schmidt number K bears a simple relationship with our parameter α (or β), satisfying $K = \frac{1}{\sqrt{1-\alpha^2}}$ (see Appendix B.2), the latter has the convenient feature of being bounded by the interval $[-1, 1]$, whereas the Schmidt number diverges for maximal entanglement.

With all of this in consideration, Alice's joint measurement on photons a and c heralds Bob's photon b in the teleported state

$$\begin{aligned} |\psi_{b|m}\rangle &= \int \mathrm{d}\omega_b \psi_{b|m}(\omega_b)\hat{a}_b^\dagger(\omega_b)\,|\mathrm{vac}\rangle\,, \\ \psi_{b|m}(\omega_b) &= N_{b|m}\int \mathrm{d}\omega_a \mathrm{d}\omega_c f_m^*(\omega_a,\omega_c) f_s(\omega_a,\omega_b)\psi_c(\omega_c). \end{aligned} \tag{5.44}$$

where $N_{b|m}$ is the appropriate normalization constant. The teleportation fidelity is then given by the modulus squared of the overlap,

$$F = \left|\langle\psi_c|\psi_{b|m}\rangle\right|^2 = \left|\int \mathrm{d}\omega \psi_c^*(\omega)\psi_{b|m}(\omega)\right|^2 \tag{5.45}$$

For this analysis, we let ψ_c be a Gaussian function with characteristic width γ_c,

$$\psi_c(\omega) = \frac{1}{\sqrt{\gamma_c\sqrt{\pi}}} e^{-\omega^2/2\gamma_c^2}. \tag{5.46}$$

Using this form for the states and measurements, we obtain an algebraic expression for the fidelity which depends on five parameters, $F = F(\alpha, \beta, \gamma_s, \gamma_m, \gamma_c)$. The full expression is unwieldy and not very instructive to display here. We shall verify that our formalism reproduces the result of reference [3] in the appropriate limits. That reference studies the behavior of the fidelity as a function of α and $\sigma = \gamma_c/\gamma_s$ for a uniformly phasematched SFG process followed by an ideally-resolved frequency detection. This corresponds to taking the limit $\gamma_m \to \infty$ and $\beta = 1$. In these limits, our formalism exactly recovers the fidelity

$$F_{\gamma_m\to\infty} = \sqrt{\frac{4\sigma^2(\sigma^2+1)(\sigma^2+1-\alpha^2)}{((\sigma^2+1)^2-\alpha^2)^2}}, \tag{5.47}$$

which is displayed in Fig. 5.5 (a). In that reference, an interesting feature of this behavior of the fidelity was noted. That is, although the fidelity increases monotonically with the source entanglement α for $\sigma \ll 1$, this is no longer true for when γ_c is comparable to γ_s. In particular, the fidelity is equal to one along the curve $\alpha^2 = 1 - \sigma^4$, and is equal to $\sqrt{8/9}$ at the upper-right hand corner of the plot, where $\alpha = 1$ and $\sigma = 1$. In the language of our formalism, given the ideal entangled measurement, with infinite SFG bandwidth and ideal spectral resolution,

there is a trade-off between spectral bandwidth and spectral entanglement of the sources.

Our result allows us to generalize further, however, and also consider the case of the Gaussian SFG measurement with finite bandwidth. First we consider the reverse scenario to the one above, where the source is perfectly entangled, with $\gamma_s \to \infty$ and $\alpha = 1$, and look at the dependence of the fidelity on β and σ. In this case we find that the fidelity exhibits the same dependence, that is,

$$F_{\gamma_s \to \infty} = \sqrt{\frac{4\sigma^2(\sigma^2+1)(\sigma^2+1-\beta^2)}{((\sigma^2+1)^2-\beta^2)^2}}, \tag{5.48}$$

and we can conclude that, given an ideal entangled state between Alice and Bob, there is a trade off between spectral bandwidth and spectral entanglement of the measurement.

Finally, we arrive at the most realistic case, where both the entangled source and the measurement have finite bandwidths, corresponding to finite phasematching in the PDC and SHG processes. Here we set them equal, taking $\gamma_s = \gamma_m = 1$, and obtain

$$F_{\gamma_m=\gamma_s} = \sqrt{\frac{4\sigma^2(\beta^2-2(1+\sigma^2))(\beta^2-(2-\alpha^2)(1+\sigma^2))}{(1+\sigma^2)^2(\alpha^2+\beta^2-2(1+\sigma^2))^2}}. \tag{5.49}$$

In this case we find the interesting and counterintuitive result that the behaviors of the fidelity with the source entanglement α and with the measurement entanglement β are no longer equivalent. We show this by plotting the behavior of the limiting cases of $F_\gamma(\alpha, 1, \sigma)$ (spectral resolution of the SFG) and $F_\gamma(1, \beta, \sigma)$ (monochromatic pumping of the PDC) in Fig. 5.5 (b) and (c), respectively. In the case of $\beta = 1$, the fidelity is maximized along the curve $\alpha^2 = \frac{1+\sigma^2-2\sigma^4}{1+\sigma^2}$ and has

similar limiting behaviors to the ideal case considered in reference [3]. The case of $\alpha = 1$ exhibits a starker contrast, taking its maximum value along the curve $\beta^2 = \frac{-1+\sigma^2+2\sigma^4}{-1+\sigma^2}$. Unlike any of the previous cases, the fidelity is no longer equal to unity in the bottom right-hand corner, for $\sigma = 1$, $\beta = 0$, but instead it is equal to $\sqrt{8/9}$.

We emphasize that $\beta < 1$ does not represent a non-ideal spectral resolution of the upconverted photon, since we are only considering projective measurements, but instead corresponds to a coherent broadband measurement, as could be obtained using a quantum pulse gate. What this last result suggests is that, for finite bandwidths of the entangled source and the entangled measurement, it is not generally the case that spectral resolution maximizes the teleportation fidelity. Further, the asymmetry between the behaviors of entangled state and the entangled measurement can be understood from the fact that the state JSA f_s and the measurement JSA f_m are not interchangeable in the expression for $\psi_{b|m}$, with f_m having both of its arguments integrated over. Most notably, we have shown that, by treating two-photon measurements more generally and on equal footing with the two-photon states, it is possible not only to recover previously-obtained results in the limit of ideal measurements, but also to uncover which states and measurements are optimal for a given task (in this case spectral teleportation), under more realistic constraints (in this case, finite PDC and SFG bandwidths).

This brief analysis leaves open the question of how to generalize to a more realistic, non-ideally resolved SFG measurement. For a mixed bipartite state $\hat{\rho}$, a convenient measure of entanglement is the *negativity* [58]. The negativity essentially counts the negative eigenvalues of $\hat{\rho}$ partially transposed with respect to one of its subsystems, and it sets an upper bound on the teleportation capacity

of the state. This suggests that we may define a negativity associated with a non-projective POVM element $\hat{\Pi}_q$ as the negativity of its mixed retrodicted state $\hat{\rho}_q$. The role of finite spectral resolution in SFG detection has been investigated numerically for entanglement swapping in reference [107]. However, it could be more elegant to frame this relationship in terms of the negativities both of the input states and the measurements in scenarios such as quantum teleportation and entanglement swapping, and this remains to be explored in future work.

5.4. Conclusion

We have demonstrated how to construct the POVM associated with two-photon detection by SFG followed by temporal-mode-selective single-photon detection. We have shown that this POVM is proportional to the two-photon state created in the time-reverse PDC process pumped with a field in the detected mode. This allowed us to characterize several aspects of the POVM relevant to its adequacy for quantum information protocols. In particular, we have shown that a projective measurement of the SFG photon corresponds to a projective two-photon POVM element. We have pointed out the special case where orthogonal SFG single-photon measurements correspond to orthogonal two-photon measurements. And finally, we have shown the correspondence between the two-photon entanglement retrodicted by the SFG measurement and the two-photon entanglement produced by the time-reversed PDC process. These results could have implications for quantum information experiments relying on PDC and SFG in terms of exploring the interplay between entangled states and entangled measurements. Additionally, it remains an open question how best to *certify* the entanglement of the SFG measurement [33], or even to perform quantum

tomography of the process. Finally, given recent interest in using quantum light for two-photon absorption [94] [108], our results open the question of whether it's possible to have a combined framework of two-photon processes in terms of quantum measurement theory.

CHAPTER VI

IMPLICATIONS OF THE POVM MODEL OF TWO-PHOTON SFG

The POVM model for two-photon detection via mode-resolved sum-frequency generation (SFG) developed in the previous chapter opens the question of whether, and how, it is possible to experimentally test some of the predictions of the model. Just as a quantum state can be characterized through a set of measurements in various bases, it is possible to characterize a quantum measurement by preparing a judicious set of quantum states and deducing the properties of the measurement from the resulting statistics. This is the basis of quantum measurement tomography. In general this is difficult to perform for an arbitrarily large Hilbert space, since a tomographically complete set of states tends to scale as the square of the dimensionality [109]. However, it can still be worthwhile to verify the basic assumptions of the model by following through some of its implications. To that end, in this chapter we carry out the calculation for the POVM corresponding to an SFG measurement where the upconverted mode is simply detected without resolution. We show that even in this limit, entanglement of the input two photon state can enhance the SFG process. We then propose an experimental design to verify quantitatively the enhancement due to entanglement. In our setup, the SFG signal generated was not sufficient to allow for following through with the experiment, but we suggest some possible improvements that would achieve this goal.

6.1. Theoretical model

Having constructed the POVM for two-photon detection by SFG followed by a mode-resolved single-photon detection in Chapter V, we can make quantitative predictions about how entanglement enhances the process. We begin by considering the case of a single-photon detector which does not resolve the SFG photon, but simply detects its presence. This corresponds to summing over all the POVM elements corresponding to a detection:

$$\hat{\Pi}_{\mathrm{SFG}} = \sum_{n=1}^{\infty} \hat{\Pi}_n. \tag{6.1}$$

The fact that the ϕ_n SFG detection modes form an orthonormal basis, as noted in Section 5.2, we obtain the result

$$\sum_{n=1}^{\infty} \phi_n(\omega+\omega')\phi_n^*(\tilde{\omega}+\tilde{\omega}') = \delta(\omega+\omega-\tilde{\omega}-\tilde{\omega}'). \tag{6.2}$$

This in turn leads to expressing $\hat{\Pi}_{\mathrm{SFG}}$ as

$$\hat{\Pi}_{\mathrm{SFG}} = |\chi|^2 \int \mathrm{d}\omega \mathrm{d}\omega' \mathrm{d}\tilde{\omega}\ \Phi(\omega,\omega')\Phi^*(\tilde{\omega},\omega+\omega'-\tilde{\omega})\ \left|\omega,\omega'\right\rangle \left\langle\tilde{\omega},\omega+\omega'-\tilde{\omega}\right|. \tag{6.3}$$

For a given two-photon input state $|\Psi_{\mathrm{in}}\rangle = \int \mathrm{d}\omega \mathrm{d}\omega' f_s(\omega,\omega') \left|\omega,\omega'\right\rangle$, we can calculate the total probability of SFG detection by

$$\begin{aligned} P_{\mathrm{SFG}} &= \left\langle\Psi_{\mathrm{in}}\right| \hat{\Pi}_{\mathrm{SFG}} \left|\Psi_{\mathrm{in}}\right\rangle \\ &= |\chi|^2 \int \mathrm{d}\omega \mathrm{d}\omega' \mathrm{d}\tilde{\omega} f^*(\omega,\omega')\Phi(\omega,\omega') f(\tilde{\omega},\omega+\omega'-\tilde{\omega}')\Phi^*(\tilde{\omega},\omega+\omega'-\tilde{\omega}) \end{aligned} \tag{6.4}$$

The last equality shows that the detection probability is simply given by the norm of the upconverted single-photon state, which we recall we never normalized. By changing to the sum and difference frequency variables again, $\nu = \omega + \omega'$, $\nu' = \omega - \omega'$, we find that this probability reduces to

$$P_{\mathrm{SFG}} = |\chi|^2 \int \mathrm{d}\nu \, |\sigma(\nu)|^2 = |\chi|^2 \langle \sigma | \sigma \rangle \,, \tag{6.5}$$

where

$$\sigma(\nu) = -\frac{1}{2} \int d\nu' \; \Phi^* \left(\nu, \nu'\right) f_s \left(\nu, \nu'\right) \tag{6.6}$$

is the spectral amplitude function of the upconverted signal from Eq. (5.14), which we recall is not normalized. In terms of the JSA and the phasematching function, this probability has the form

$$P_{\mathrm{SFG}} = \frac{|\chi|^2}{4} \int \mathrm{d}\nu \left| \int \mathrm{d}\nu' \Phi^*(\nu, \nu') f_s(\nu, \nu') \right|^2 . \tag{6.7}$$

This expression of the detection probability in terms of the SFG phasematching function and the two-photon JSA allows to construct a simple model that tests directly when and how the SFG conversion efficiency depends on the two-photon entanglement. We note that although it has been shown that the upconversion of broadband EPP is dependent on the spectral phase across the JSA [**?**], the efficiency has not been quantified in terms of the amount of spectral entanglement.

6.1.1. Gaussian model

In order to make some quantitative estimates regarding the effect of entanglement on SFG, it is useful to adopt a simple model for both the JSA of

the two input photons and the SFG phasematching function. We assume a type-0 or type-I PDC process for creating the EPP, and the same type of process for the SFG. This allows us again to make use of the bivariate Gaussian from Chapter V, Eq. (5.41). This time, we express it in terms of the broad bandwidth γ_s and a narrow, correlation bandwidth, σ_s,

$$f_s(\omega_a, \omega_b) = \sqrt{\frac{2}{\pi\gamma_s\sigma_s}} \exp\left[-\frac{(\omega_a - \omega_b)^2}{2\gamma_s^2} - \frac{(\omega_a + \omega_b)^2}{2\sigma_s^2}\right] \tag{6.8}$$

Direct comparison with (5.41) shows that the normalization constant N_s is given by

$$N_s = \sqrt{\frac{2}{\pi\gamma_s\sigma_s}}, \tag{6.9}$$

and the correlation parameter α is given by

$$\alpha = \frac{\gamma_s^2 - \sigma_s^2}{\gamma_s^2 + \sigma_s^2}. \tag{6.10}$$

Recall that in Chapter V we noted that $\alpha \in [-1, 1]$, with $\alpha \to 1$ corresponding to a maximally anticorrelated JSA. This is consistent with (6.10).

In terms of the sum and difference frequencies $\nu = \omega_a + \omega_b$ and $\nu' = \omega_a - \omega_b$ the JSA is

$$f_s(\nu, \nu') = \sqrt{\frac{2}{\pi\gamma_s\sigma_s}} \exp\left[-\frac{\nu'^2}{2\gamma_s^2} - \frac{\nu^2}{2\sigma_s^2}\right]. \tag{6.11}$$

Upon inspection we can see that this JSA is separable into functions of ν and ν' (see [108]), $f(\nu, \nu') = f_N(\nu) f_B(\nu')$, if we define

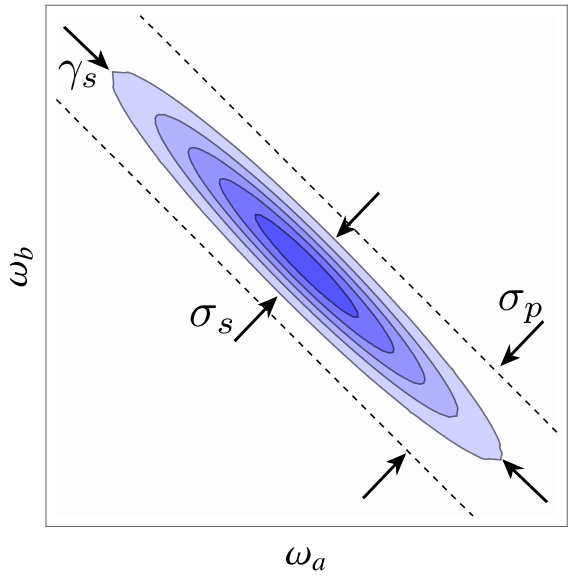

FIGURE 6.1. Plot of the Gaussian model used for two-photon SFG, showing the relevant state bandwidths γ_s and σ_s, and the phasematching bandwidth σ_p. The two-photon JSA is shown in blue, and the contour of the phasematching function is shown in dotted lines.

$$f_N(\nu) = \sqrt{\frac{\sqrt{2}}{\sqrt{\pi}\sigma_s}} \exp\left[-\frac{\nu'^2}{2\sigma_s^2}\right], \quad f_B(\nu') = \sqrt{\frac{\sqrt{2}}{\sqrt{\pi}\gamma_s}} \exp\left[-\frac{\nu'^2}{2\gamma_s^2}\right]. \tag{6.12}$$

Likewise for the case of type-0 or type-I phasematching it is reasonable to take the function $\Phi(\omega_a, \omega_b)$ to be symmetric in the frequencies, and approximate the sinc function with a Gaussian of the form

$$\Phi(\omega_a, \omega_b) = \Phi(\omega_a + \omega_b) = \exp\left[-\frac{(\omega_a + \omega_b)^2}{2\sigma_p^2}\right] = \exp\left[-\frac{\nu^2}{2\sigma_p^2}\right], \tag{6.13}$$

where σ_p is the phasematching bandwidth. The relevant parameters are shown in Fig. 6.1.

Using these approximations, we arrive at a closed form for the SFG probability, given by

$$P_{\mathrm{SFG}} = \frac{|\chi|^2}{4} \int \mathrm{d}\nu \, |\Phi(\nu)|^2 \, |f_N(\nu)|^2 \left| \int \mathrm{d}\nu' f_B(\nu') \right|^2 . \tag{6.14}$$

The insight gained from this approximation is that the phasematching function simply acts as a frequency filter in the ν ("narrow") direction, where phase effects do not contribute since we are using incoherent detection on the SFG mode. This is in contrast to the ν' ("broad") direction, spectral phase effects are significant, as we shall see when we examine the effect of dispersion.

6.1.2. The effect of dispersion

This model correctly predicts the effect of quadratic phase, or dispersion, on the SFG efficiency. We assume that the input photon pair propagates in a collinear configuration, so that both photons experience the same amount of dispersion. In our model, the JSA picks up a quadratic phase with the group-delay dispersion (GDD) parameter β, such that the JSA after dispersion is given by

$$\tilde{f}(\omega_a, \omega_b) = f(\omega_a, \omega_b) \exp\left[i\beta(\omega_a^2 + \omega_b^2)\right] = f(\nu, \nu') \exp\left[i\frac{\beta}{2}(\nu^2 + \nu'^2)\right] . \tag{6.15}$$

We can already see from the form of Eq. (6.14) that we do not expect the quadratic phase to have an effect on the ν-dependent part. This is confirmed by direct calculation: by computing the SFG probability with and without dispersion, we can take the ratio of these two probabilities and obtain a closed form for the effect of dispersion,

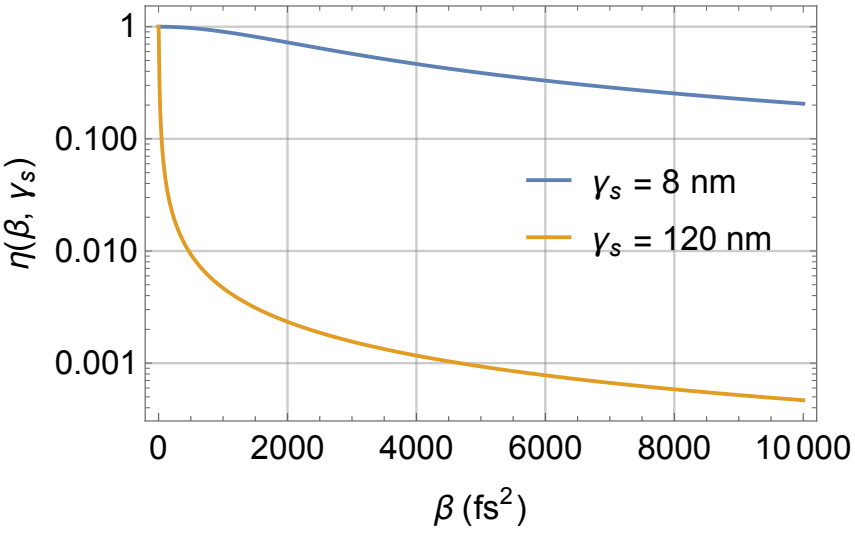

FIGURE 6.2. Plot of the reduction of the SFG signal, $\eta(\beta, \gamma_s)$, for two different values of bandwidth γ_s at a central wavelength of 830 nm, as a function of the dispersion parameter β.

$$\eta(\beta, \gamma_s) = \frac{\int \mathrm{d}\nu \left| \int \mathrm{d}\nu' \Phi^*(\nu) \tilde{f}_s(\nu, \nu') \right|^2}{\int \mathrm{d}\nu \left| \int \mathrm{d}\nu' \Phi^*(\nu) f_s(\nu, \nu') \right|^2} = \frac{1}{\sqrt{1 + \beta^2 \gamma_s^4}}. \tag{6.16}$$

As expected, the SFG signal is reduced for large β, and this effect is greater the larger the bandwidth γ_s. This is in agreement with calculations for the effect of dispersion on two-photon processes using broadband EPP [108]. The reduction of efficiency due to dispersion β for two different bandwidths γ_s is plotted in Fig. 6.2.

6.1.3. The effect of the entanglement parameter α

We can evaluate the effect of the entanglement parameter α on the SFG probability if we express P_{SFG} in closed form in terms of the parameters for the Gaussian model. We carry out this calculation and obtain

$$P_{\mathrm{SFG}} = |\chi|^2 \frac{\gamma_s}{\sigma_s} \sqrt{\frac{\pi}{1/\sigma_s^2 + 1/\sigma_p^2}}. \tag{6.17}$$

For a given SFG phasematching bandwidth σ_p and two-photon correlation bandwidth σ_s, we see that the probability depends on the state bandwidth ratio $\frac{\gamma_s}{\sigma_s}$. We can use (6.10) to express this bandwidth ratio in terms of α as

$$\frac{\gamma_s}{\sigma_s} = \sqrt{\frac{1+\alpha}{1-\alpha}}. \tag{6.18}$$

Evidently $\alpha \rightarrow 1$ maximizes P_{SFG}, which also corresponds to $\frac{\gamma_s}{\sigma_s} \rightarrow \infty$. While obviously unphysical, this model gives a good intuition for the role that entanglement plays in SFG at the two-photon level, and is in good agreement with the models recently developed for two-photon absorption in molecules [108].

6.2. Experimental setup

The aim of the following experiment was to characterize the role of time-frequency (TF) entanglement in the two-photon process of SFG. The main experimental goal is to use spontaneous parametric down conversion in a crystal to create entangled photon pairs (EPP) exhibiting a high degree of TF entanglement, to use pulse compression and pulse shaping techniques to manipulate the amount of TF entanglement, and subsequently quantify how the efficiency of the SFG process depends on the amount of entanglement. As such, there were several desirable parameters as well as technical constraints which influenced the experimental design. Perhaps the most crucial constraint is the low cross-section for SFG in the low-flux regime of two-photon states. The SFG efficiency in this regime is on the order of $10^{-9} - 10^{-7}$, which, considering the laser repetition rate of 80 MHz and the regime of one photon pair per laser pulse, dictates a success rate on the order of 1 Hz. This low-flux regime in turn requires optimization of the process, namely through compensation of the dispersion experienced by the

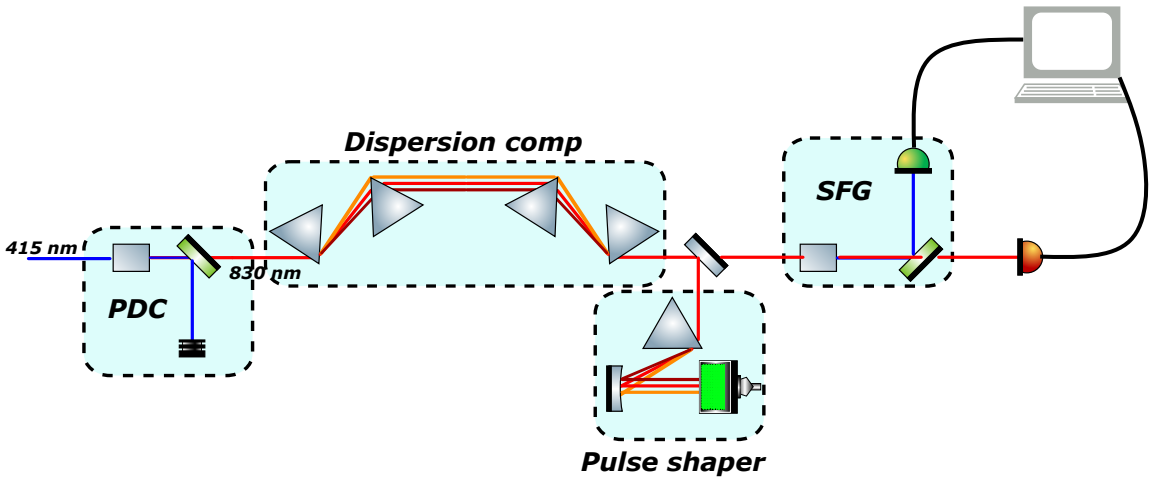

FIGURE 6.3. Experimental setup for charactering the effect of two-photon entanglement on SFG. Broadband EPP are generated using PDC at a nonlinear crystal. Subsequently

EPP due to their broadband nature, which is expected to attenuate the signal by about two to three orders of magnitude. In the end it proved very difficult to obtain a practical SFG signal, and we suspect this was due to the extremely broad bandwidth (120 nm) of the EPP, coupled with their large spatial extent. In the Results subsection we discuss some suggestions to improve this experiment. The experimental design is outlined in Fig. 6.3, and described in detail in the following subsections.

6.2.1. PDC stage

The pump beam was generated by frequency-doubling the Ti:Sapph pulses in a 1 mm-long BiBO, producing pulses at 415 nm with about 2.3 nm of FWHM bandwidth via type I SHG. This is the same pump beam as was used for the entanglement-swapping experiment. The spatial filter was removed to provide maximum power to the PDC crystal. This beam is focused onto the ppKTP using

a f = 200mm achromatic plano-convex focusing lens. The PDC beam is collected and collimated using a f=100 mm B-coated achromatic lens.

The EPP source for the experiment is a 10 mm-long, periodically-poled potassium titanyl phosphate (ppKTP) crystal from Raicol. The crystal is poled for type-0 phasematching for degenerate PDC from 415 nm to 830 nm, and the poling period is quoted to be 3.45 μm. It was found through second-harmonic generation (SHG) measurements that 20°C (293 K) was not optimal for phasematching at 830 nm, but that the optimal temperature for this wavelength was 50°C (323 K). The crystal temperature control is achieved by placing the crystal in a machined copper oven, heated by a resistance heating element. The oven is passively cooled, meaning that it cannot be operated below room temperature. Thus it is possible to operate in one of two configurations, either by heating the crystal to 323 K, or by operating at the phasematching wavelength for 293 K, which was 828.2 nm, which can be achieved by wavelength-tuning the laser.

6.2.2. SFG stage

The SFG crystal is identical to the one used for PDC, another 10 mm-long ppKTP, with a poling period of 3.45 μm. The PDC beam is focused onto this crystal using a f = 100 mm, in a configuration symmetrical to the PDC collimation. The SFG was aligned using the classical tracer beam, which was overlapped with the pump beam to ensure that it takes the same path as the PDC beam.

To further ensure overlap of the tracer beam with the pump beam, we introduced a free-space delay line to achieve temporal overlap between the two pulses. We verified this temporal overlap by observing difference-frequency

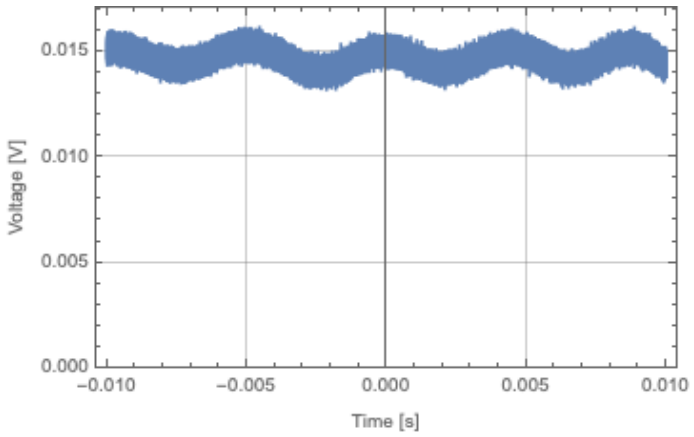

FIGURE 6.4. Oscilloscope trace of the tracer beam detected at a photodiode, showing phase-sensitive amplification and deamplification due to overlap with the pump field.

generation (DFG) at the PDC crystal. Because of the degeneracy of the process, the tracer beam field at 830 nm experiences amplification and deamplification as a function of the relative phase between itself and the pump field at 415 nm (see, for example, [110] and [111]). Thus the overlap was verified by collecting the tracer field into a photodiode and measured at an oscilloscope, and varying the relative delay between tracer and pump until phase-sensitive fringes are observed on the oscilloscope. The oscilloscope trace showing these fringes is shown in Fig. 6.4.

Once the overlap of the pump and tracer beam was insured, the SFG efficiency was benchmarked using second-harmonic generation (SHG) from the classical tracer beam, obtaining 140 μW of SHG when pumping with 5 mW of Ti:Sapph pulses. The SHG from the classical tracer beam was collimated using a f=75 mm A-coated lens, and coupled into a multimode fiber (MMF) for detection. The tracer beam is attenuated down to the 10-100 nW range using neutral density filters, and then the MMF is connected to a single-photon counting detector (LASER COMPONENTS COUNT BLUE). The detector has a quantum efficiency of around 55% at 415 nm, a dark count rate under 10 Hz, and a timing jitter of

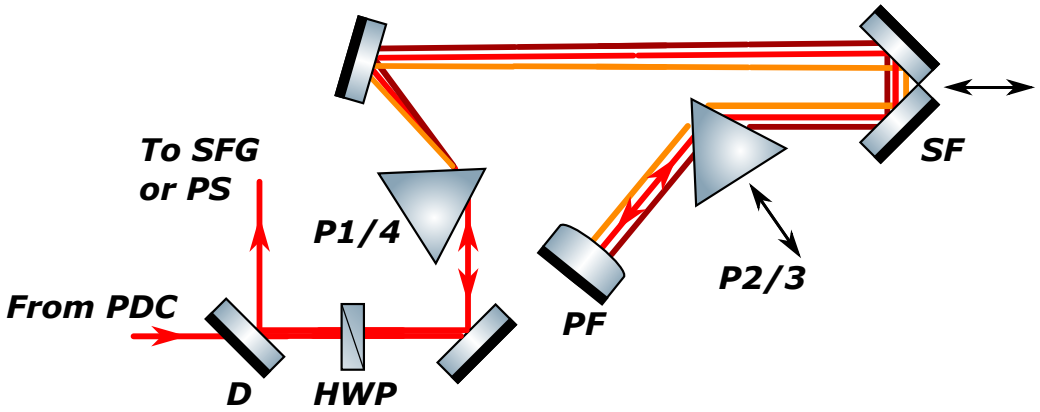

FIGURE 6.5. Prism compressor for dispersion compensation in a folded configuration. D: D-shaped mirror. HWP: achromatic half-wave plate at 830 nm. P 1, 2, 3, 4: SF11 prisms in the order in which they are traversed. PF: primary fold. SF: secondary fold.

around 2 ns. In order to reject background noise and dark counts, we temporally resolve the signal by using the ID900 time tagger with the 80 MHz laser pick off as a reference. This has the same effect as temporally gating the detector.

6.2.3. Dispersion-compensation module

The broadband nature of the PDC leads to a significant impact on the SFG signal due to dispersion. The dispersion-compensation module is a prism compressor, which consists of two dispersive SF11 glass prisms and an adjustable inter-prism distance. The geometry of the setup is such that it causes the red end of the spectrum to travel throug a longer path through glass than does the blue end, thereby compensating for any common-path dispersion induced elsewhere in the setup. The setup is shown in Fig. 6.5, which makes clear how the red part of the spectrum travels through more glass.

Direct measurement of the amount of dispersion in the setup would required ultrafast pulse duration measurement using autocorrelation techniques [112].

Instead a rough estimate is obtained by accounting for the optical elements that the EPP encounter, which include the PDC and SFG crystals and the focusing and collimating lenses. The group velocity dispersion (GVD) of KTP at 830 nm is about 177 fs^2/mm[1], so for a total of 20 mm of KTP we expect to acquire about 3540 fs^2 of group delay dispersion (GDD). The two achromatic doublets that we use for collimating and focusing the PDC beam (Thorlabs AC254-100-AB) each consist of a LAK22 element that is 8 mm thick (GVD = 65 fs^2/mm) and a SF10 element that is 4 mm thick (GVD = 150 fs^2/mm). All together, the GDD acquired through both lenses is estimated to be 2240 fs^2. Thus the GDD in the entire set up is on the order of 5780 fs^2.

Using software to calculate a reasonable prism insertion and separation to compensate for this dispersion, it is found that an insertion of 3 mm for each prism and a separation of 400 mm is sufficient. Thus we built the prism compressor to be able to explore a range that encompasses these values. In practice we found that an insertion of 3 mm for each prism and about 600 mm of prism separation was capable of nearly doubling the SHG signal due to the classical tracer beam which has a bandwidth of around 8 nm, which is somewhat consistent with our estimates. By comparing with Fig. 6.2, we expect about 2-3 orders of magnitude of reduction in the SFG signal from the PDC beam, which has a bandwidth of around 120 nm.

6.2.4. Pulse-shaping module

In addition to dispersion compensation, it is desirable to have arbitrary control over the spectral amplitude and phase of the PDC. To this end we constructed a prism-based 4-f pulse shaper [113]. This pulse shaper was not used

[1]This value, along with the subsequent GVD values, were obtained from refractiveindex.info.

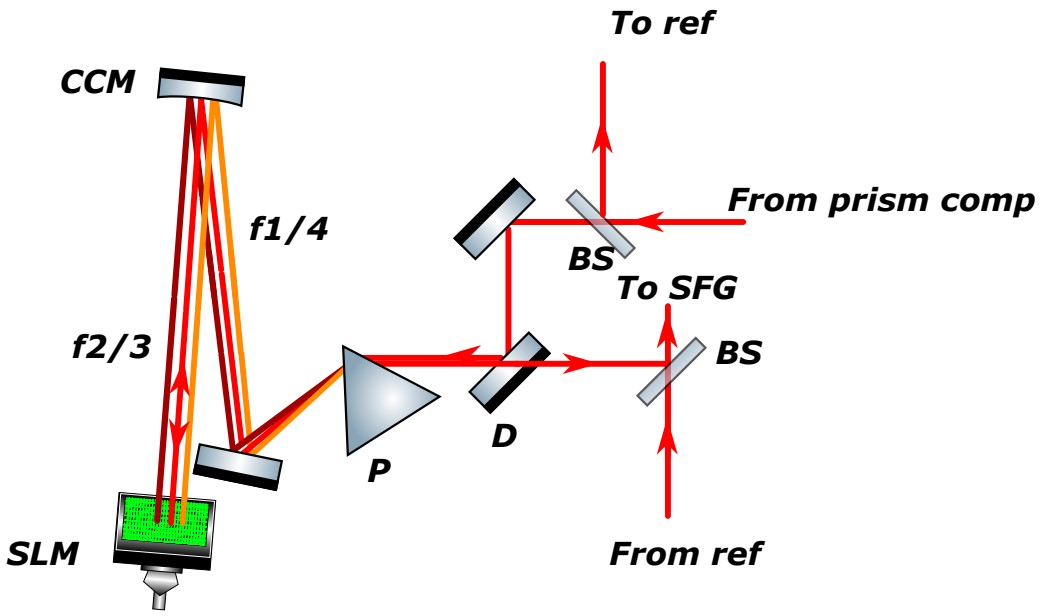

FIGURE 6.6. Pulse shaper for arbitrary amplitude and phase modulation of the PDC spectrum. D: D-shaped mirror. BS: beam splitters used to pick off a reference line for pulse shaper calibration. P: SF11 prism. CCM: cylindrical concave mirror, f = 400mm. f 1, 2, 3, 4: the four f = 400 mm focal lengths constituting the 4-f line. When not in calibration mode, the upper BS is removed, and the lower BS is replaced with a mirror.

in the experiment since we did not obtain a practical SFG signal from the PDC photons, and due to the difficulty of managing the PDC beam spatially over large path lengths, but nonetheless we describe the pulse shaper here for completeness. The pulse-shaper consists of an SF11 equilateral prism, which disperses the PDC spectrum, followed by an f = 400mm cylindrical concave mirror to focus the light onto a reflective spatial light modulator (SLM) (Hamamatsu X13139-02). The configuration is shown in Fig. 6.6.

The pulse shaper was not used in the experiment as of yet, as there was difficulty obtaining enough SFG signal in the first place using the unshaped PDC light. However, after being constructed, the pulse was roughly pre-calibrated by using the classical tracer beam. The beam is split with a 50-50 beam splitter,

and half of it is sent to through a reference line with an adjustable delay. The other half is sent through the pulse shaper, before the two are recombined and the spectrum is measured with a standard spectrometer (Ocean Optics Flame). When there is an a relative time delay τ between the two pulses, and a spectral phase $\phi(\omega)$ imparted by the SLM, one expects to see spectral fringes such that the spectrum $I(\omega)$ is modified to give a term of the form $I(\omega)(1 + \cos(\omega\tau + \phi(\omega)))$. An exemplary spectral interferogram and its Fourier transform are shown in Fig. 6.7.

6.2.5. Results and discussion

In Fig. 6.8 we show the best-case SFG signal obtained when pumping the crystal with 200 mW of 414 nm blue, with all the crystals operated at room temperature, and while bypassing the prism compressor and pulse shaper. The data was collected over one hour. Subsequently the SFG crystal was removed from the beam path and data was collected for another hour to obtain the background counts. Integrating the area under the SFG curve gives a count rate of about 2.9 Hz. We note that 200 mW is above the estimated damage threshold of the ppKTP (around 30 mW), so that this configuration would be unsustainable for continued operation.

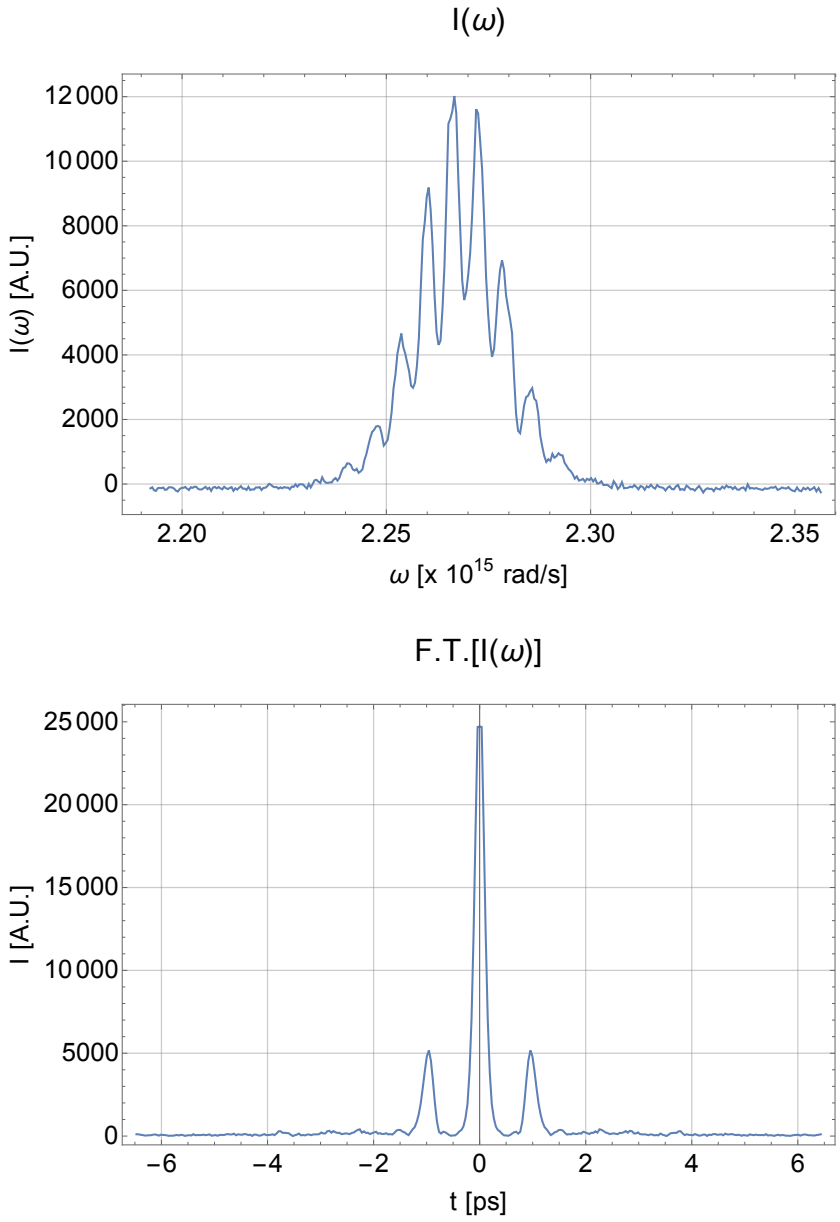

FIGURE 6.7. Spectral interference for calibrating the pulse shaper. Top: spectral interferogram showing fringes due to interference between the a pulse going through the pulse shaper and a reference pulse. Bottom: Modulus of the Fourier transform of the interferogram, where the sidebands correspond to a relative time delay between the pulses of about 1 ps. In general, calibration of the pulse shaper can be obtained by extracting the phase from the interferogram.

It proved very difficult in this experiment to obtain a consistent SFG signal from the PDC photons. Although we obtained a peak PDC power of around 12 nW when pumping with 200 mW of blue, this PDC flux proved insufficient to generate a practical signal to optimize on. We conclude that this is due to the very large bandwidth of the PDC, coupled with the large transverse spatial profile of the PDC beam, which was on the order of 1 cm in diameter. Although it was possible to collect the entire beam at the SFG crystal when bypassing the prism compressor, the dispersion acquired through the setup in this configuration likely caused 2-3 orders of magnitude of reduction of the signal. Meanwhile, significant clipping of the beam occurred when going through the prism compressor, resulting in only 1 to 2 nW of PDC arriving at the SFG crystal. The most straightforward improvement to the setup would be to replace the components of the prism compressor with 2-inch optics to reduce the amount of clipping.

Finally, we note that, alternately, it was possible to use a 2 mm long ppKTP to generate the blue pump at 414 nm. This gave an estimated pump bandwidth of 0.4 nm, and reduced the PDC bandwidth significantly to around 60 nm. For completeness we show the PDC marginal spectrum acquired with this configuration, and compare it with the one obtained with the 2.3 nm bandwidth pump, in Fig. 6.9, along with their simulations, calculated using the Sellmeier equations for KTP. Both of these spectra were obtained with a single-photon sensitive spectrometer (Horiba iHR320). The spectral bandwidth of 60 nm is more practical to operate with, since the effects of dispersion are less prohibitive than they are for 120 nm of bandwidth. However, in this configuration it was not possible to generate a significant amount of blue pump (under 40 mW), and thus PDC (around 1-2 nW), without damaging the 2 mm long ppKTP, and so again

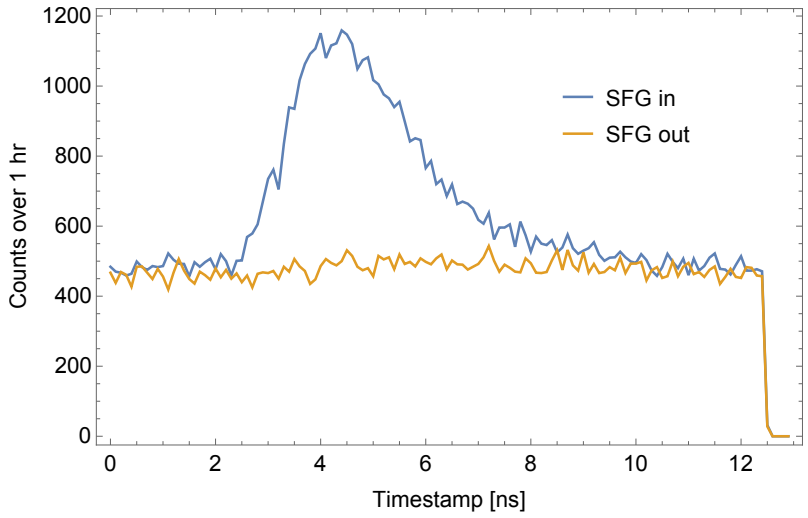

FIGURE 6.8. SFG signal obtained in the best case scenario, showing counts measured over the period of one hour, while pumping the PDC crystal with 200 mW of blue (above damage threshold, yielding 12 nW of PDC incident at the SFG crystal. The blue curve shows counts obtained with the SFG crystal in the beam path, while the yellow curve shows the counts obtained with the crystal out of the beam path. In both cases the counts are time-resolved by triggering on a reference pulse from the Ti:Sapph laser, so that it's easier to reject background counts. Integrating the area between these curves in the region under the peak gives a count rate of about 2.9 Hz.

this was not practical. In principle the experiment could be improved overall by operating with a narrowband blue pump with sufficient power.

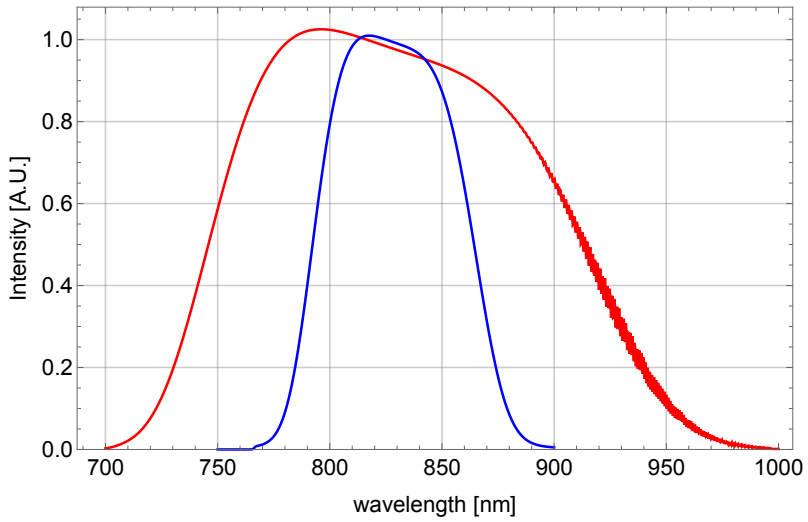

(a)

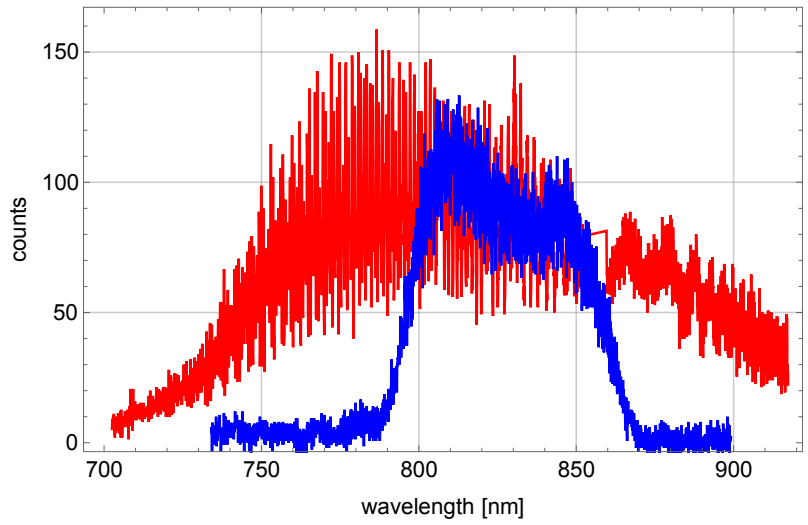

(b)

FIGURE 6.9. Comparison of marginal spectra of PDC when pumped with a 2.3 nm-bandwidth pump (red), and a 0.4 nm-bandwidth pump (blue). (a) Simulation obtained from Sellmeier equations for KTP. (b) Measured spectra using a single-photon sensitive spectrometer.

CHAPTER VII

CONCLUDING REMARKS AND FUTURE DIRECTIONS

Entanglement is a fundamental feature of quantum theory, and it is the aspect of this theory which provides for the most striking departures from classical physics. Still, quantum entanglement of physical systems is a subtle phenomenon that hides in plain sight, requiring the most careful experimental efforts to tease out its implications, and, like its cousin, quantum coherence, is easily destroyed by interaction with the environment. Even more subtle still is the entanglement of measurements, a seemingly esoteric and purely theoretical construct which turns out to have very real, measurable physical consequences.

In this thesis we have explored both kinds of entanglement, as well as the interplay between them, using light as the physical system of interest. In particular we aimed to take advantage of the high dimensionality, and thus high information capacity, offered by photons entangled in their spectral-temporal properties, and to extend standard quantum protocols into this regime. First, we experimentally demonstrated how to perform entanglement swapping using time-frequency entangled photons, in a way that utilizes the multimode nature of the entanglement by making spectrally multiplexed two dimensional Bell-state measurements on highly-entangled photon pairs available from standard parametric down conversion sources. This work represents the first demonstration of multiplexed entanglement swapping producing distinct, heralded Bell states in an optical fiber based setting.

Next we showed how spectrally multiplexed Bell state measurements can reveal time-frequency entanglement even for certain mixed states, ones that are

mixtures of antisymmetric Bell states. This is a somewhat surprising result given that mixed states of Bell states are typically less entangled than their constituent components. Because the mixed two-photon states we consider retain the full antisymmetry properties of their mutually orthogonal constituent Bell states, the photons exhibit antibunching at a beam splitter, showing quantum interference whose visibility does not decrease even in the limit of maximally mixed states. This allows us to construct an entanglement witness in the form of an inequality that is satisfied by all separable states, but conclusively violated by certain entangled states.

Finally, we addressed the question of how to perform joint measurements on two photons that project onto arbitrary multimode two-photon states, analogous to parametric down conversion. We showed that such measurement can be realized using sum frequency generation, a process that is the reverse of parametric down conversion, and showed how to describe this measurement in a theoretically consistent way using the language of POVMs. Although two-photon SFG has been previously demonstrated and suggested as a tool for spectral quantum teleportation and entanglement swapping, we believe that our framing of it as a two-photon measurement which can exhibit entanglement in analogy with the entanglement of two-photon states provides more insight into understanding this process as well as other similar two-photon processes such as two-photon absorption.

We proposed and constructed an experiment to test some of the quantitative of the entangled POVM model of two-photon SFG, namely the role of two-photon entanglement in the process. In particular, we expect the SFG to increase linearly with the amount of entanglement, quantified by a correlation parameter

α which can be directly related to the Schmidt number. While ambitious, this experiment in its current configuration suffers from low count rates, due to the low cross section for observing SFG at the low, isolated photon pair flux regime, compounded with the deleterious effects of dispersion on the highly broadband two-photon states we use. Thus the main improvements we suggest for this particular experiment are twofold. The first is to reduce the bandwidth of the entangled photon pair by using a narrower-bandwidth pump, which would make the effects of dispersion less detrimental to the efficiency of the setup. The second is to use a PDC crystal with a higher damage threshold that allows for using a blue pump power on the order of 200 mW. Both of these can be satisfied by a pump and crystal configuration such as the one we used in Ref. [114].

Given that the experiment conducted in Chapter VI produces viable SFG count rates, it lends itself to being easily adaptable for various proof-of-principle experiments. One is a test of quantum illumination as originally proposed by Lloyd in Ref. [16]. For instance the pulse-shaper module could perform double duty by being used to simulate a target that is to be detected by one of the photons in the entangled pair, while simultaneously varying the amount of two-photon entanglement. Another possible direction to take is towards more extensively characterizing the SFG process as a two-photon measurement. In particular, it could be possible to construct a set of two-photon states using pulse shaping techniques that could test whether two-photon SFG is indeed an entangled measurement as we claim, in manner similar to the experiment in Ref. [33].

In this thesis we have made the case that two-photon measurements are an interesting object of study in their own right, on par with two-photon states. This is particularly true when it comes to the rather mysterious role of entanglement

in such measurements, especially because entanglement is typically understood in terms the nonlocal behavior of bipartite and multipartite systems that are spatially separated to disallow communication. We have shown that there are measurable physical quantities that can be directly related to the POVM describing the two-photon measurement as a projector onto a particular two-photon state, both theoretically in the context of Chapter V, and experimentally in the context of Chapter III. We hope that our results help guide future research towards more completely characterizing measurements of this kind, which we expect will prove to be increasingly important towards quantum networks relying on distributed entanglement, in addition to their significance for understanding the fundamental nature of measurement inherent in the quantum mechanical worldview.

APPENDIX A

ENTANGLEMENT SWAPPING SUPPLEMENTAL

A.1. Deriving the four-photon state

In the low gain regime, the output state of the n^{th} SPDC source, where $n \in \{1, 2\}$, is given by

$$|\psi_n\rangle = \sum_{p=0}^{\infty} \frac{\sqrt{\eta_n}^p}{p!} \left(\iint \mathrm{d}\omega_{\mathrm{S}} \mathrm{d}\omega_{\mathrm{I}} f_n(\omega_{\mathrm{S}}, \omega_{\mathrm{I}}) \hat{a}_n^\dagger(\omega_{\mathrm{S}}) \hat{b}_n^\dagger(\omega_{\mathrm{I}}) \right)^p |\mathrm{vac}\rangle \,. \tag{A.1}$$

The function $f_n(\omega_{\mathrm{S}}, \omega_{\mathrm{I}})$ is the joint spectral amplitude (JSA), given by

$$f_n(\omega_{\mathrm{S}}, \omega_{\mathrm{I}}) = u_n(\omega_{\mathrm{S}} + \omega_{\mathrm{I}}) \mathrm{sinc} \left[\frac{\Delta k_n(\omega_{\mathrm{S}}, \omega_{\mathrm{I}}) L}{2} \right], \tag{A.2}$$

where u_n represents the spectral mode function of the pump, Δk_n is the wave-vector mismatch between the pump, signal and idler modes, and L is the length of the interaction medium. Finally, η_n is the gain of the parametric process, which depends on the length L, the non-linear strength of the material and the number of photons in the pump beam.

The SPDC state due to the two independent sources can be written as a tensor product $|\psi_1\rangle \otimes |\psi_2\rangle$. We expand this and keep only terms of order η, which are responsible for the four-photon contribution, obtaining the following state after normalization

$$|\psi_\eta\rangle = \frac{\left(\sqrt{\eta_1 \eta_2} \, |\psi_{12}\rangle + \frac{\eta_1}{2} \, |\psi_{11}\rangle + \frac{\eta_2}{2} \, |\psi_{22}\rangle\right)}{\sqrt{\eta_1 \eta_2 + \eta_1^2/4 + \eta_2^2/4}}, \tag{A.3}$$

where

$$|\psi_{nm}\rangle = \int \mathrm{d}^4\omega \; f_n(\omega_\mathrm{S}, \omega_\mathrm{I}) f_m(\omega'_\mathrm{S}, \omega'_\mathrm{I}) \times \\ \hat{a}^\dagger_n(\omega_\mathrm{S}) \hat{a}^\dagger_m(\omega'_\mathrm{S}) \hat{b}^\dagger_n(\omega_\mathrm{I}) \hat{b}^\dagger_m(\omega'_\mathrm{I}) \, |\mathrm{vac}\rangle \, . \tag{A.4}$$

is the four-photon state arising from either a photon pair from each source, or two pairs from one source and none from the other.

To facilitate the discussion of our results, we made a few simplifying assumptions in the main text, which we will now enumerate in the context of Eq. (A.3). First, we assumed that both sources are identical, such that $f_1(\omega_\mathrm{S}, \omega_\mathrm{I}) = f_2(\omega_\mathrm{S}, \omega_\mathrm{I}) = f(\omega_\mathrm{S}, \omega_\mathrm{I})$ and $\eta_1 = \eta_2 = \eta$. This is because in the experiment, the two sources are derived from double-pumping the same crystal as in Ref. [47], and are matched to a great degree as discussed in the experimental section. Further, any source mismatch does not reduce the quality of the entanglement in the swapped state, just the visibility of quantum interference in the method we use to verify entanglement.

Second, we assumed that the relative phases between the three terms in Eq. (A.3) are random. This implies that these terms are not mutually coherent and therefore do not contribute to any quantum interference. In reality there is such a coherence, which is due to the phase of the pump, and we observe this in both two- and four-photon interference, as we show in Appendix A.6. However, this phase drifts over the course of the interference measurements we will describe, which are several hours long, and thus $|\psi_{11}\rangle$ and $|\psi_{22}\rangle$ contribute to a constant background in these measurements.

Finally, in the main text we focused our attention solely on the $|\psi_{12}\rangle$ term of Eq. (A.3), which corresponds to each source producing a pair of entangled photons, which is rewritten as $|\psi\rangle$ for better readability. In most entanglement swapping and quantum teleportation experiments relying on SPDC sources, the other two terms (the double-pair terms), though present, do not contribute when the four photons are detected in coincidence, so that heralded states are *post-selected* [115]. Similarly, the double-pair terms only contribute in our setup in the aforementioned interference measurement, where they constitute a constant background, which we measure and subtract in Appendix A.8.

A.2. Mixed state model

In the realistic case, the BSM on the idler photons is not performed with perfect resolution, but rather within a finite spectral window. In our case, this is due to the resolution of the time-of-flight spectrometer, which is a convolution of multiple response functions in the frequency-to-time conversion. It is dominated by the timing jitter ($\simeq$ 20 ps) of the superconducting nanowires.When this resolution is not perfect, then we can show that the signal photons are heralded into a mixed state. The effect of this finite resolution on the heralded spectral distributions is shown graphically in Fig. A.1.

We begin by redefining the BSM operator as:

$$\begin{aligned}\hat{\Pi}_{lm}^{\mathrm{BSM}} &= \iint \mathrm{d}\Omega_j \mathrm{d}\Omega_k |t_l(\Omega_j)|^2 |t_m(\Omega_k)|^2 \; \hat{\Pi}_{jk}^{\mathrm{BSM}} \\ &= \iint \mathrm{d}\Omega_j \mathrm{d}\Omega_k |t_l(\Omega_j)|^2 |t_m(\Omega_k)|^2 \, |\Omega_j, \Omega_k\rangle \langle \Omega_j, \Omega_k| \,, \\ |\Omega_j, \Omega_k\rangle &= \hat{c}^\dagger(\Omega_j) \hat{d}^\dagger(\Omega_k) \, |\mathrm{vac}\rangle \,,\end{aligned} \tag{A.5}$$

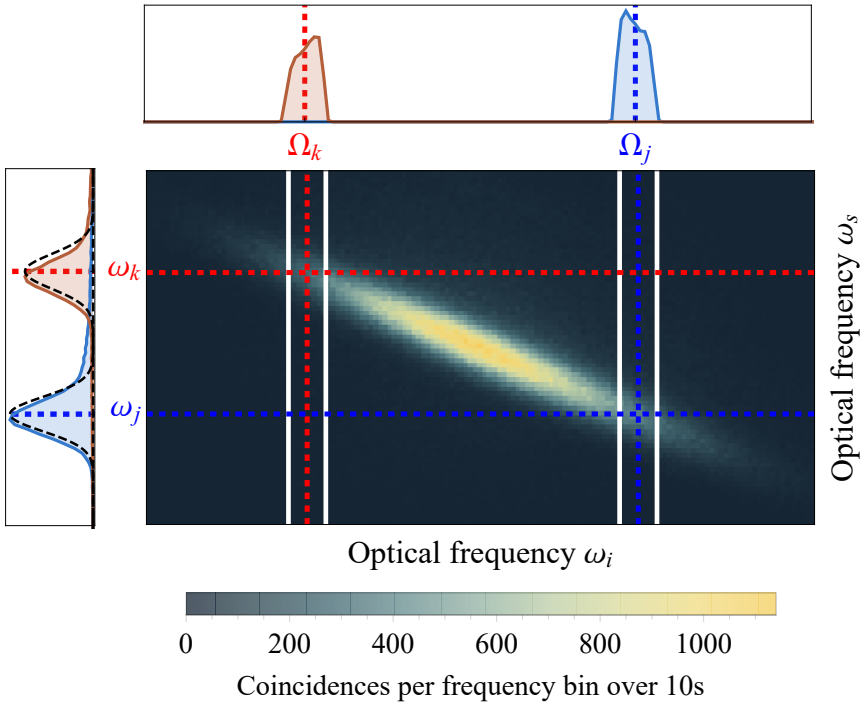

FIGURE A.1. Representation of the effect of finite resolution on the heralding. The finite bandwidth (white vertical lines) implies that a detection at frequencies (Ω_j, Ω_k) (vertical dashed lines) is integrated over the filtered modes, shown in the top plots. The heralded modes are represented on the left, where the black dashed line represent $|\phi_j|^2$ and $|\phi_k|^2$ from the pure state model.

where $t_{l(m)}(\Omega_{j(k)})$ are transmission amplitudes centered at $\Omega_{l(m)}$, and satisfy $\sum_{lm} |t_l(\Omega_j)|^2 |t_m(\Omega_k)|^2 = 1$. We have introduced new indices l, m, so that we may incorporate the j,k-dependent quantities from the main text into our analysis. Moreover, it is straightforward to show that the POVM element (3.3) is obtained by setting $t_{l(m)}(\Omega) \to \delta(\Omega - \Omega_{l(m)})$. To simplify our notation henceforth, we will use the following shorthand

$$\iint_{lm} \mathrm{d}\Omega_j \mathrm{d}\Omega_k := \iint \mathrm{d}\Omega_j \mathrm{d}\Omega_k |t_l(\Omega_j)|^2 |t_m(\Omega_k)|^2. \tag{A.6}$$

It can be seen from Fig.3.5 that the finite resolution of the idler detection bin reduces the purity of the heralded signal state, due to the entanglement of the two-

photon state. Because of this, the POVM element (A.5) requires that we describe the heralded state as a mixed state

$$\hat{\rho}_{lm} = \frac{\mathrm{Tr}_{\hat{b}}\left[\hat{\Pi}_{lm}^{\mathrm{BSM}} \left|\psi_{12}\right\rangle \left\langle\psi_{12}\right|\right]}{p_{lm}}, \tag{A.7}$$

where $\mathrm{Tr}_{\hat{b}}$ is the partial trace over the subspace defined by operators $\hat{b}_1$ and $\hat{b}_2$. Analogously to the pure state case, the probability p_{lm} are defined as

$$\begin{aligned} p_{lm} &= \mathrm{Tr}\left[\hat{\Pi}_{lm}^{\mathrm{BSM}} \left|\psi_{12}\right\rangle \left\langle\psi_{12}\right|\right] \\ &= \iint_{lm} \mathrm{d}\Omega_j \mathrm{d}\Omega_k \; p_{jk}. \end{aligned} \tag{A.8}$$

where the idler density matrix is defined as Eq.(3.6), and we again obtain Eq.(3.7) by setting the filters $t_{l(m)}$ as δ functions.

We may now compute the heralded state density matrix:

$$\hat{\rho}_{lm} = \frac{1}{p_{lm}} \iint_{lm} \mathrm{d}\Omega_j \mathrm{d}\Omega_k \; p_{jk} \; \left|\Psi_{jk}\right\rangle \left\langle\Psi_{jk}\right| \tag{A.9}$$

while recalling the definition of $\phi_{j(k)}(\omega)$ in $\left|\Psi_{jk}\right\rangle$ as

$$\phi_{j(k)}(\omega) = \frac{f(\omega, \Omega_{j(k)})}{\sqrt{\rho_{\mathrm{I}}(\Omega_{j(k)}, \Omega_{j(k)})}}. \tag{A.10}$$

This has the intuitive interpretation of a mixed state as an incoherent sum of pure states over the detection bandwidth of $t_{l(m)}$. All of the measured quantities follow in a straightforward manner. In the absence of frequency resolution, we herald again the mixed state

$$\hat{\rho} = \sum_{lm} \; p_{lm} \; \hat{\rho}_{lm}, \tag{A.11}$$

just as with the pure state model.

The heralded JSI is given by:

$$F_{lm}(\omega_1, \omega_2) = \langle \omega_1, \omega_2 | \, \hat{\rho}_{lm} \, | \omega_1, \omega_2 \rangle \, , \tag{A.12}$$

which can be expressed in terms of F_{jk} as

$$F_{lm}(\omega_1, \omega_2) = \frac{1}{p_{lm}} \iint_{lm} \mathrm{d}\Omega_j \mathrm{d}\Omega_k \; p_{jk} \; F_{jk}(\omega_1, \omega_2). \tag{A.13}$$

The integrated JSI corresponding to the state $\hat{\rho}$ is again given by

$$F(\omega_1, \omega_2) = \sum_{lm} p_{lm} F_{lm}(\omega_1, \omega_2). \tag{A.14}$$

When the signal photons in the state $\hat{\rho}_{lm}$ are incident on a 50:50 beamsplitter, the coincidence fringes at the output are given by

$$P_{lm}(\tau_\mathrm{S}, \tau_\mathrm{I}) = \mathrm{Tr}\left(\hat{\Pi}_{\mathrm{verif}} \, \hat{\rho}_{lm}\right) = \iint \mathrm{d}^2\omega \, \langle \omega, \omega' | \, \hat{\rho}_{lm} \, | \omega, \omega' \rangle \, , \tag{A.15}$$

where $|\omega, \omega'\rangle = \hat{a}_3^\dagger(\omega)\hat{a}_4^\dagger(\omega') \, |\mathrm{vac}\rangle$ as before. Evaluating this in terms of P_{jk}, we

$$P_{lm}(\tau_\mathrm{S}, \tau_\mathrm{I}) = \frac{1}{p_{lm}} \iint_{lm} \mathrm{d}\Omega_j \mathrm{d}\Omega_k \; p_{jk} \; P_{jk}(\tau_\mathrm{S}, \tau_\mathrm{I}). \tag{A.16}$$

Finally the integrated interference peak for the state $\hat{\rho}$ is recovered by taking

$$P(\tau_\mathrm{S}, \tau_\mathrm{I}) = \sum_{lm} \; p_{lm} \; P_{lm}(\tau_\mathrm{S}, \tau_\mathrm{I}). \tag{A.17}$$

We will make a few comments regarding the most interesting feature of comparing this model with the pure state model. To this end, we shall represent the pure state $|\Psi_{jk}\rangle\langle\Psi_{jk}|$ as a density matrix in the $\{|\phi_j\rangle|\phi_k\rangle, |\phi_k\rangle|\phi_j\rangle\}$ basis as follows:

$$|\Psi_{jk}\rangle\langle\Psi_{jk}| = \frac{1}{2\mathcal{C}_{jk}} \begin{pmatrix} 1 & e^{i\theta_{jk}} \\ -e^{-i\theta_{jk}} & 1 \end{pmatrix}. \tag{A.18}$$

Meanwhile, the mixed state $\hat{\rho}_{lm}$ has the representation:

$$\hat{\rho}_{lm} = \frac{1}{p_{lm}} \iint_{lm} \mathrm{d}\Omega_j \mathrm{d}\Omega_k \, \frac{p_{jk}}{2\mathcal{C}_{jk}} \begin{pmatrix} 1 & e^{i\theta_{jk}} \\ -e^{-i\theta_{jk}} & 1 \end{pmatrix}. \tag{A.19}$$

Notably, the off-diagonal terms $e^{\pm i\theta_{jk}} = e^{\pm i(\Omega_j - \Omega_k)\tau_\mathrm{I}}$, the coherence terms, are the hallmark of the bipartite entanglement in these states, and are responsible for the interference we observe in P_{jk}. It seems reasonable then to ask if, and to what extent, the averaging over the l, m bands in the mixed state is expected to reduce the entanglement. Take first the special case of $\tau_\mathrm{I} = 0$. In this case, $\theta_{jk} = 0 \; \forall \; j, k$, and the off-diagonal terms are equal to unity, and hence, no phase-averaging occurs for the mixed state $\hat{\rho}_{lm}$. Indeed, the off-diagonals survive even for the fully-averaged state $\hat{\rho}$, and one can interpret this as the reason why the interference peak survives at full visibility for $\tau_\mathrm{I} = 0$.

More generally, however, for $\tau_\mathrm{I} \neq 0$, the disagreement between the two models becomes more salient. The pure-state model assumes that the idler photons are detected at monochromatic frequency modes at (Ω_j, Ω_k), which are necessarily infinite in extent in the time domain. This means that the idler photons remain indistinguishable at the output of the BSM beamsplitter, even for arbitrary τ_I delays at the input. On the other hand, taking into account the averaging over

the l, m bands introduces distinguishability, and the BSM is no longer ideal in this case. Furthermore, this averaging introduces more distinguishability the larger τ_{I} is, since the argument of the phase factor $(\Omega_j - \Omega_k)\tau_{\mathrm{I}}$ is proportional to this time delay. This phase-averaging results in a reduction of the off-diagonal terms, and of the visibility of the P_{lm} interference for large enough τ_{I}. This behavior is most clearly seen in the profile of the fully-integrated two-dimensional peak in Fig. 3.12, which results from averaging over all phases with a weight p_{jk}. The peak vanishes in the τ_{I} direction over a delay timescale comparable to the inverse bandwidth of the idler photons. The intuitive interpretation is that the idler photons become distinguishable at the output of the beamsplitter when the relative delay is at least as long as their pulse durations.

A.3. Experimental details (ADDENDUM)

It is convenient to conceive of the experiment as composed of three main elements: the pump module, the PDC sources, and the detection apparatus. In this section we will describe some of the more technical details of each of these elements, along with some detailed schematics and alignment procedures.

A.3.1. Pump module

The laser source for the experiment is a wavelength-tunable pulsed Tsunami titanium sapphire oscillator (Ti:Sapph) from Spectra Physics, pumped by a Millenia eV (also from Spectra Physics) 532 nm continuous-wave (CW) diode-pumped solid-state laser. The Millenia eV is operated at 10 W to generate from the Tsunami with an average power of 1.5 W, centered at 830 nm, with approximately 8 nm of full-width at half-maximum (FWHM) bandwidth, and a

repetition rate of 80 MHz. The 830 nm beam is filtered through a quarter-wave plate (QWP) and a half-wave plate (HWP) followed by Glan-Thompson polarizer, which generates a clean linear polarization while allowing for external optical power control. For this experiment we set the HWP to operate at a power of 1.1 W.

The remainder of the pump module is shown in Fig. A.2. The 830 nm (IR) pulses are then frequency-doubled via type-I second-harmonic generation (SHG) in a 1.5 mm-long bismuth triborate (BiBO) crystal, generating a 415 nm pulse train (blue) with a FWHM bandwidth of 2.7 nm. The IR beam is focused onto the BiBO using an f = 50 mm plano-convex lens, and the blue beam is collimated using another f = 75 mm plano-convex lens. A dichroic mirror is used to reflect the blue beam, through which the IR beam is transmitted and dumped onto a beam block. We use a blue glass filter to further reject any residual IR light. After the blue glass filter, the blue power was measured to be about 300 mW, corresponding to an SHG efficiency of about 30%.

Finally we use an f = 50 mm lens to focus the blue beam onto a 25 μm-diameter pinhole to filter the spatial mode in the Fourier plane. This selects a nearly Gaussian mode of the blue pump beam, which is otherwise astigmatic due to the walk-off inherent in birefringent phasematching [62], which is found to improve the heralding efficiencies of the photon pairs. After the spatial filter, the blue pump power was measured to be about 190-200 mW. The filtered blue pump beam is then collimated using another f = 50 mm lens and sent to the PDC sources.

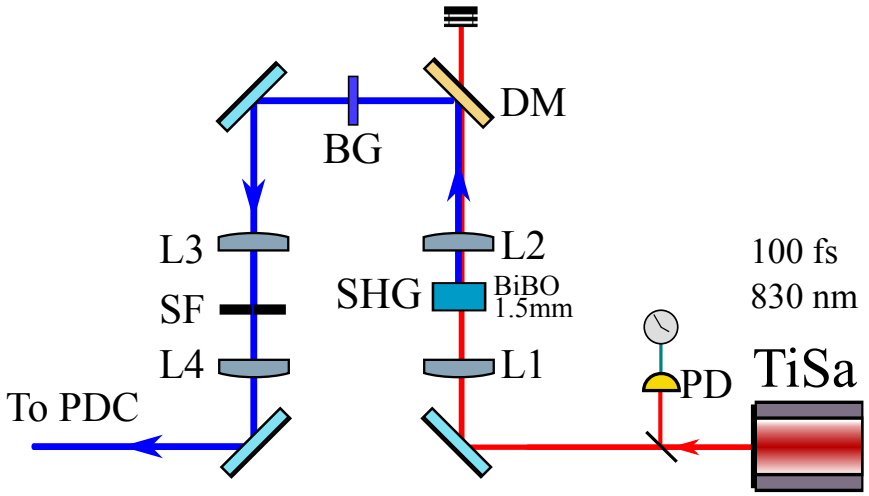

FIGURE A.2. Components of the pump module. L1: f=75 mm lens. L2, L3, L4: f=50mm lenses. DM: dichroic mirror. SF: spatial filter with a 25 μm pinhole.

A.3.2. PDC sources

The PDC sources for the two pairs of photons used for entanglement swapping are depicted in Fig. A.3. The two PDC sources are derived from the same 2.5 mm-long type-II phasematched BiBO crystal, which is double-passed by the pump to generate a pair of PDC photons on each pass. For the first pass the blue pump is directed into the crystal using a dichroic mirror (DM1), and focused into the crystal using an f = 250 mm lens which precedes DM1. This creates the PDC photon pair for source 1. After the crystal the blue pump is reflected through a second dichroic mirror (DM2), through which the PDC photon pair is transmitted and collimated using an achromatic f = 125 mm lens, as well as going through a red glass filter for further pump rejection. The signal and idler photons are then separated using a polarizing beam splitter (PBS), where the H-polarized idler photon is transmitted while the V-polarized signal photon is reflected. Each photon is routed through a delay line consisting of a motorized stage controlled by a Kinesis module from Thorlabs, and finally coupled into polarization maintaining

(PM) single-mode fibers. The delay lines are labeled τ_S for signal 1 and τ_I for idler 1. These delays allow for temporal matching with the PDC photons from source 2.

After being reflected at DM2, the blue pump beam is collimated using an f = 150 mm lens, and retro-reflected on a mirror mounted on a piezo-electric transducer stack (PZT), where the 75 mm-lens serves to refocus the pump beam onto the BiBO crystal in a second pass, counterpropagating with respect to the first pass. This second pass creates the PDC photon pair for source 2. The blue pump is reflected at DM1, where the photon pair is transmitted, filtered through a red glass filter and collimated using an achromatic f = 125 mm lens, just as with the photon pair from source 1. The signal and idler from source 2 are split using another PBS, before being coupled into another pair of PM fibers. A motorized delay line was placed into the beam path of the source 2 idler photon to allow for balancing all four beam paths, but this configuration was not necessary or used for this experiment.

Because of the collinear nature of the PDC process we use, the procedure for aligning the collection PMF fibers was relatively straightforward. We back-injected each fiber using a pick-off from the IR beam from the Ti:Sapph, and directed the output towards the BiBO crystal for use as a tracer beam. Removing the red glass filters allowed the blue pump beam to counterpropagate with this IR beam for some distance, which enabled the overlapping of the two beams at two points. This was found to be sufficient for detecting single-photon counts at each fiber, and detecting coincidences at a rate higher than the accidental coincidence rate for uncorrelated photon counts (see A.3.4). From that point it is straightforward to align by optimizing both the single-photon count rates and the coincidence count rates. At the optimum, we obtained raw single photon count rates of 1.8

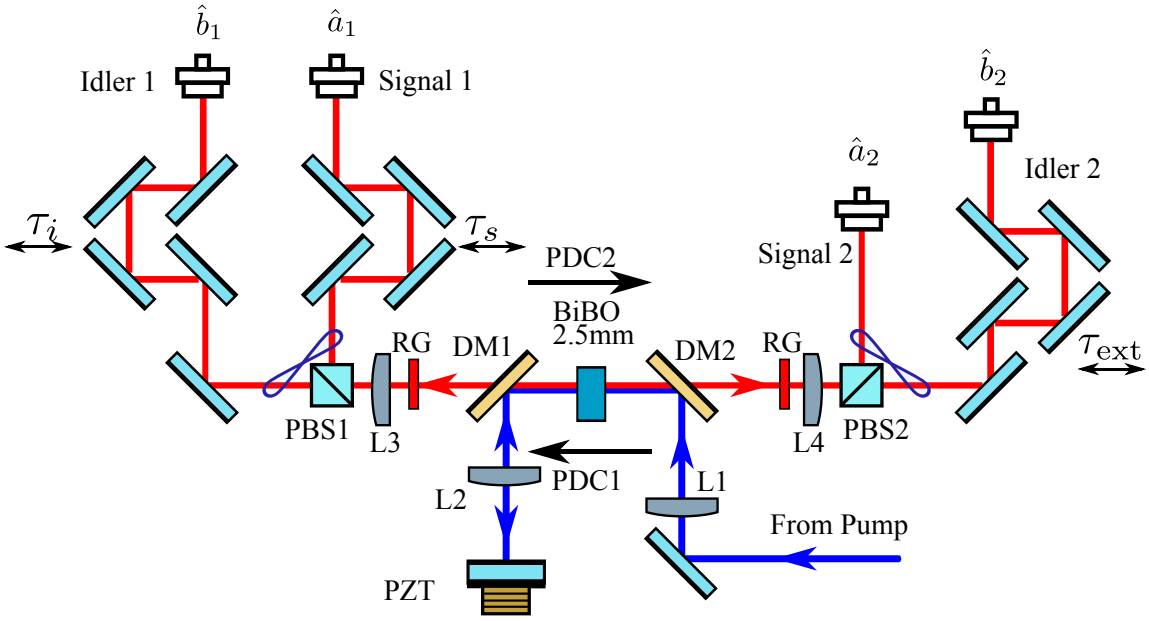

FIGURE A.3. Schematic for the PDC sources. L1: f = 250 mm lens. L2: f = 150 mm lens. L3, L4: f = 125 mm achromatic lenses. PBS1, PBS2: polarizing beam splitters to separate signal and idler. RG: red glass filter. τ_{ext} is a delay line to allow matching of all four paths, not used in this experiment.

MHz for each signal and idler, coincidence rates of 300 kHz for each source, and fourfold coincidence rates of 1 kHz, all measured directly with the superconducting nanowire single-photon detectors (SNSPDs).

To match the photon paths temporally, we inject either idler 1 and idler 2 or signal 1 and signal 2 through a 50-50 PM fiber beamsplitter (from Oz Optics), and scan either τ_{I} (for the idlers) or τ_{S} for the signals, until we observe a Hong-Ou-Mandel (HOM) interference dip in the coincidences. For this measurement and the rest of the experiment, it is important to use a half-wave plate (HWP) before each injected fiber to optimize polarization matching. Since these measured coincidences are accidental, arising from events from independent sources, the visibility of the HOM dip is limited not only by the spectral purity of each photon (as described in A.7), but also by the spurious two-photon events arising from

double-pair emissions from each source. As a result, the HOM dip visibility in these measurements is around 10%. Nevertheless, it is sufficient to allow path-length matching to within $\sim$ 100 fs. Finally, with both fiber beam splitters in place, it is possible to check the visibility of the path interference effect described in A.6 to further optimize the temporal as well as spectral matching. At the optimum, we obtained a path interference visibility of 80%.

A.3.3. Detection apparatus

Once the alignment is optimized and the PDC photon pairs are matched temporally and spectrally, as well as in polarization, the remainder of the experiment is all fiber-based, consisting of dispersive elements for time-of-flight spectrometry, SNSPD's for efficient single-photon detection, and time-taggers for recording the timestamps of correlated photon detection events. In section A.4 we detail how the time-of-flight spectrometers are calibrated, and in section A.5 we outline the algorithms for obtaining the correlated timestamps. Here we simply describe the different detection configurations and what each is used for.

In the `default` detection configuration, the four photons, each coupled into its collection fiber, are routed directly to four SNSPD's. From there, the photodetection events are converted to electrical signals, amplified, and sent as inputs to the ID900 time-tagger. The time-tagger then directly computes the desired coincidences onboard and outputs the time stamps to a computer. In this configuration the time stamps do not contain information about the spectral-temporal structure of the light, but are simply used to record the count rates. Optimization of the optical alignment is always done in the `default` configuration.

In the `JSI` configuration, signal 1 and idler 1 (or signal 2 or idler 2) are each routed through a 500 m-long fiber spool to impart dispersion and measure the JSI of source 1 (or source 2). The output of each fiber spool is then routed to the SNSPD's, and the remainder of the setup is the same as in the `default` configuration. In this case the time stamps of the photodetection events impart information about the wavelength of the incoming light, and in section A.5 we describe how they are used to calculated the JSI's.

In the `heralded JSI` configuration, each idler photon is coupled to the input of a 50-50 FBS, and the outputs are each routed through one of the dispersive fiber spools. Meanwhile, the signal photons are each routed through one of the CFBGs. The outputs of the fiber spools and the CFBGs are each coupled to an SNSPD, and the remainder of the setup is the same as the previous configurations. In order to ensure that a near-ideal BSM is performed on the idlers, before any measurement run, τ_{I} is scanned until the center of the idler HOM dip is found, and the translation stage is set at this center position. In section A.5 we describe how the time-tagger is used to calculate the heralded JSI's $F_{jk}(\omega_1, \omega_2)$ in this configuration.

In the `HOM` configuration, the idler photons are coupled to the FBS and then to the dispersive fiber spools, just as in the `heralded JSI` configuration. In this case, the signal photons are also coupled to the inputs of another 50-50 FBS. The outputs of the latter are then routed directly to the SNSPDs. The remainder of the setup is the same as in the previous configuration. Before any measurement run, both τ_{I} and τ_{S} are independently scanned to find the centers of the idler and signal HOM dips, and further fine adjustment of the delays is made to optimize the interference fringes observed in Fig. A.7. In section A.5 we describe how

the time-tagger is used to calculate the interference fringes $P_{jk}(\tau_{\mathrm{S}}, \tau_{\mathrm{I}})$ in this configuration.

A.3.4. Normalizing coincidence counts

The figure of merit for assessing how the measured coincidence rate R_{AB} at two detectors A and B differs from the expected accidental coincidence rate R_{acc} is the coincidence-to-accidental ratio, or CAR, given simply by R_{AB}/R_{acc}. It is equal to unity for uncorrelated photon counts, and is greater than unity for correlated counts. For uncorrelated photon counts, the probability $P_{acc} = R_{acc}/R_L$ (where R_L is the laser repetition rate) of detecting an accidental coincidence between two detectors A and B is given by

$$P_{acc} = P_A P_B, \tag{A.20}$$

where P_A and P_B are the probabilities of obtaining a single detection event at detector A and B, respectively. In terms of count rates, this can be expressed as

$$\frac{R_{acc}}{R_L} = \frac{R_A}{R_L}\frac{R_B}{R_L}. \tag{A.21}$$

Using this last expression, the CAR is calculated as

$$\mathrm{CAR} = \frac{R_{AB}}{R_{acc}} = \frac{R_{AB}R_L}{R_A R_B}. \tag{A.22}$$

Because the motion of the translation stages used for the τ_{S} and τ_{I} delays induces some steering of the PDC photon beams, there is always some variation of the fiber coupling, and thus the detected count rates, whenever the translation stages are scanned. This variation must be taken into account in order to faithfully

quantify the HOM and P_{jk} interference visibilities, and so we normalize the interference counts in a manner similar to the CAR calculation. For the standard, unheralded HOM interference, measured in terms of coincidences at detectors A and B at the output of a 50-50 beam splitter, the normalized coincidence probability is given as a function of input delay τ as

$$P_{AB}(\tau) = \frac{R_{AB}(\tau)R_L}{R_A(\tau)R_B(\tau)}. \tag{A.23}$$

This takes into account the fact R_A and R_B can vary as a function of τ as the translation stage is scanned.

We follow the same reasoning to normalize the four fold coincidence counts for $P_{jk}(\tau)$. This fourfold configuration can be thought of as the same as the HOM configuration just discussed, but this time conditioned on a coincidence detection at two other detectors, C and D. The probability of obtaining an accidental coincidence at detectors A and B, *given* a coincidence at detectors C and D, is given by

$$P_{AB|CD} = P_{A|CD}P_{B|CD}. \tag{A.24}$$

In terms of count rates, this is expressed as

$$\frac{R_{ABCD}}{R_{CD}} = \frac{R_{ACD}}{R_{CD}}\frac{R_{BCD}}{R_{CD}}. \tag{A.25}$$

Thus, just as with the unheralded HOM case, as we scan τ, the normalized probability of measuring four-fold coincidences is given by

$$P_{ABCD}(\tau) = \frac{R_{ABCD}(\tau)R_{CD}}{R_{ACD}(\tau)R_{BCD}(\tau)}. \tag{A.26}$$

A.4. Time-of-flight spectrometer calibration

To ensure that our TOFS are accurate, it is necessary to calibrate them. While it is usually sufficient to use a rough estimate of the dispersion imprinted by the fiber spool or by the CFBG, this doesn't take into account waveguide dispersion or other sources of dispersion in the setup. Therefore, we opted for an in-situ calibration utilizing the single photons from the SPDC.

We used a pulse shaper based on a spatial light modulator (SLM) placed at the midpoint of a 4-f line [40], enabling us to address both the amplitude and phase of the mode-function of single photons over a 30 nm range with a resolution of 0.02 nm. By scanning a narrow interference filter of 1 nm FWHM over the SLM mask while recording the resulting time tags, we obtain a calibration curve between the recorded time tags and the wavelength of the filter set on the pulse shaper. Over our wavelength range, this function is mostly linear and its slope is the dispersion parameter of the TOFS. The results are shown in Fig. A.4. With the two CFBG-based spectrometers, we obtained a dispersion of 944 ± 4 ps/nm and 946 ± 2 ps/nm. With the fiber spools, we measured an equal dispersion of -54 ± 1 ps/nm. With the calibration in hand, it is straightforward to convert time stamps to wavelength for any detection event after a TOFS, see for example Fig.3.3.

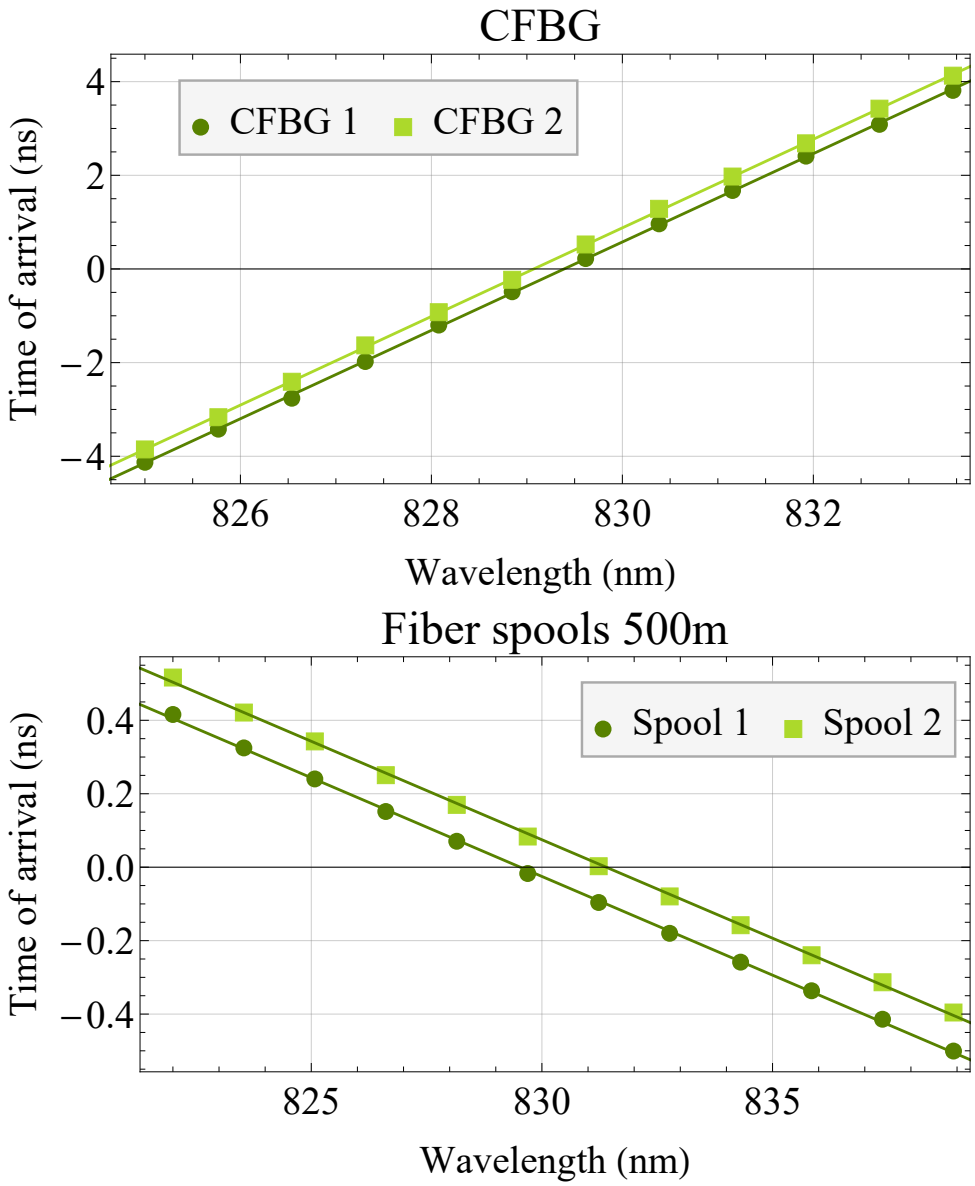

FIGURE A.4. Calibration of each TOFS. The curves have been offset vertically for better visibility.

A.5. Two- and four-fold time-correlated measurements (ADDENDUM)

In order to obtain the various joint spectral measurements that we measure, in addition to the well-calibrated CFBG's and fiber spools, we make use of various time correlation algorithms that rely on the ID900 time tagger software. Here we describe these algorithms to some extent. The main configurations we employ are: (I) the two-fold coincidence configuration using the fiber spools for JSI measurements of the sources; (II) the fourfold coincidence configuration for $F_{jk}(\omega_1, \omega_2)$ using the the fiber spools for the idler photon BSM and the CFBG's for the signal photon heralded JSI's; and (III) the fourfold coincidence configuration for $P_{jk}(\tau)$ using the fiber spools for the idler photon BSM, and direct detection of the signal photons as a function of scanning the delay τ_{S}.

While it is relatively straightforward to simply record The ID900 time tagger has two operation modes: `HI-SPEED`, or high speed, mode and `HI-RES`, or high resolution, mode. `HI-SPEED` mode enables the use of a dedicated `START` input channel, which can receive up to 100 MHz input signal, in addition to the four standard input channels, which are limited to a 25 MHz signal. In this mode the maximum obtainable timing resolution is 100 ps per time bin. `HI-RES` mode allows a higher resolution of 13 ps per time bin, but it is not compatible with use of the `START` channel, so that only the four standard inputs can be used. We make use of both of these modes in our measurements, as necessary.

A.5.1. I. Source JSI's

The simplest measurement to obtain is the JSI for each source, since it only involves two-photon coincidence counting, in addition to the reference. Because the CFBG spectral window is only about 10 nm around 830 nm, the source JSI's

FIGURE A.5. The ID900 time-tagger used for the experiment (top). Note the `START` port, in addition to the four standard input ports. The second time tagger (bottom) is identical and also used in our laboratory for other experiments.

large bandwidth would cause it to be cropped. Therefore we opted to use the fiber spools, along with `HI-RES` mode of the time tagger, to obtain the JSI. This is the `JSI` configuration from section A.3. In order to obtain a clock signal suitable for use with the standard inputs, we attenuate a pickoff from the ti:sapphire beam until it produces a single-photon count rate of under 25 MHz, and detect it with one of the SNSPD's, thus generating a stochastic clock signal (input 3). The signal and idler photons are each routed through one of the fiber spools, before being detected at two other SNPSD's and two other time-tagger inputs (inputs 1 and 2). The stochastic clock cuts down our overall rates by about a factor of four, since we

only observe about one out of four clock pulses, but this is not too consequential since the coincidence rates are high enough to obtain a JSI in a matter of seconds.

The algorithm for computing the time correlated coincidences is conceptually simple. First the appropriate electronic delays are set to ensure that the signal and idler photons from the same clock cycle are identified, which is easily achieved by observing the coincidence rate. If we had been using a deterministic clock signal at 80 MHz, this would automatically reset the clock every 12.5 ns at the arrival of each pulse. But since we are attenuating this signal optically and detecting it with an SNSPD, the FPGA logic in the time tagger is instead programmed to generate a 12.5 ns time window whenever input 3 receives a signal. The FPGA then performs the following operations within that 12.5 ns window: if input 1 is received first, record the timestamp of input 2 with respect to input 1 and with respect to input 3, whereas if input 2 is received first, record the timestamp of input 1 with respect to input 2 and with respect to input 3. Thus in each case we have a relative timestamp and an absolute timestamp, from which we can determine the timestamps of the two photons.

A.5.2. II. Heralded JSI's

The algorithm for obtaining the heralded JSI's $F_{jk}(\omega_1, \omega_2)$ is necessarily more involved, being a fourfold time-correlated measurement. Here the idler photons are each routed through one of the fiber spools at the output of the fiber beam splitter, while the signal photons are each routed directly through the one of the CFBG's, before all four photons are detected with SNSPD's. This is the `heralded JSI` configuration in section A.3. The clock signal in this case is deterministic, and is an analog signal generated from detecting the ti:sapph pickoff directly with a

fast photodiode with a timing jitter of $\sim$ 15 ps, which is fed to the `START` input of the time tagger. Thus the time tagger is used in `HI-SPEED` mode, yielding a timing resolution of 100 ps per time bin. The idler photon events are routed to inputs 1 and 3 of the time tagger, and the signal photon events are routed to inputs 2 and 4.

Electronic delay matching is achieved by observing coincidences between each signal photon channel with each of the two idler photon channels. In this case the physical time delay incurred by the idler photons with respect to the signal photons from traveling through 500 m of fiber must be accounted for. Once all channels are synchronized, a configuration is achieved such that idler photon timing distributions, which span about 1.5 ns each, occur at the beginning (input 1) and at the end (input 3) of each clock cycle. Meanwhile the signal photon timing distributions (inputs 2 and 4), which span about 9 ns each, overlap in the middle of the clock cycle. This configuration is shown schematically in Fig. A.6, and allows for removing ambiguities when it comes to calculating the relative timestamps, as described in the following.

The algorithm for computing the time-correlated fourfold coincidences is as follows:

- Generate a 12.5 ns pulse from each of `input 2` and `input 4`.
- Perform a logical `AND` operation between these pulses, generating a pulse `2AND4`.
- Use `input1` and the next `START` to filter `2AND4`, generating a pulse `1AND2AND4`.

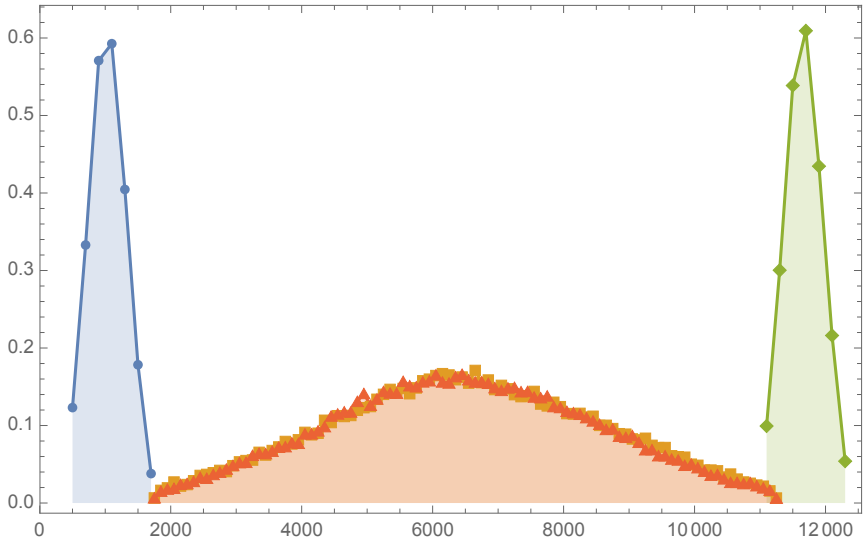

FIGURE A.6. Exemplary distribution of timetags used for fourfold spectral coincidences. Input 1 is in blue, inputs 2 and 4 are in orange, and input 3 is in green.

– Add 12.5 ns to `1AND2AND4` and use this pulse to filter `input 3`, which is the last pulse to arrive.

This algorithm allows us to generate the arrival time of `input 3` with respect to `START`, `input 1`, `input 2`, and `input 4`, conditional on a fourfold coincidence between the four standard inputs. From these values we can compute the timestamps of the four inputs with respect to `START` in post-processing.

A.5.3. III. Heralded two-photon interference

The time tagger configuration to obtain $P_{jk}(\tau_S, \tau_I)$ is nearly identical to that for measuring the heralded JSI's $F_{jk}(\omega_1, \omega_2)$, with the following exceptions. The first is that we route the signal photons through a second 50-50 fiber beam splitter, and bypass the CFBG's since we are not measuring the spectra for these photons. This is the `HOM` configuration in section A.3. The removal of the fiber spools results in sharper distributions for the time stamps of `input 2` and `input 4`, such that

they contain no spectral information. Thus even though we collect four time stamps as before, only the idler time stamps contain relevant information, and we simply aggregate the idler time stamps.

The other exception is that now we are interested in the behavior of these fourfold coincidences as a function of the physical delays τ_{S} and τ_{I}. Therefore we scan the positions of the each stage, and at each position we collect the fourfold time-correlated data and generate a separate file of timestamps. By associating each file with a stage position we can generate an interferogram for each j and k in post-processing. Finally it should be noted that while we collect data in this configuration, we jitter the PZT that back-reflects the blue pump so that we average the interference over any pump optical phase.

A.6. Source distinguishability

The entanglement verification protocol we use, that is, the two-photon interference of the state $|\Psi_{jk}\rangle$, ultimately relies on the indistinguishability of the two source states. To see this, we relabel the source JSA's as $f_1(\omega, \Omega)$ and $f_2(\omega, \Omega)$, and for simplicity, we assume that they are identical up to a translation in frequency space. Note now that this leads to a heralded state

$$|\Psi_{jk}\rangle \propto |\phi_j^1\rangle_1 |\phi_k^2\rangle_2 - |\phi_k^1\rangle_1 |\phi_j^2\rangle_2 , \tag{A.27}$$

where

$$|\phi_{j(k)}^{1(2)}\rangle = \int \mathrm{d}\omega \phi_{j(k)}^{1(2)}(\omega) \hat{a}_{1(2)}^{\dagger}(\omega) |\mathrm{vac}\rangle , \tag{A.28}$$

and

$$\phi^{1(2)}_{j(k)}(\omega) = \frac{f_{1(2)}(\omega, \Omega_{j(k)})}{\rho_{1(2)}(\Omega_{j(k)}, \Omega_{j(k)})}. \tag{A.29}$$

Although this state is still entangled, the verification method using coincidence fringes in $P_{jk}(\tau_{\rm S})$ will suffer from a reduction in visibility due to the distinguishability of f_1 and f_2. To see this, we recalculate $P_{jk}(\tau_{\rm S})$ in its approximate form (3.45), and find

$$P_{jk}(\tau_S) \approx \frac{1}{2}\left(1 - V_{jk}\, e^{\sigma_{\rm S}^2 \tau_S^2} \cos\left[\left(\frac{\omega_j^1 + \omega_j^2}{2} - \frac{\omega_k^1 + \omega_k^2}{2}\right)\tau_S\right]\right) \tag{A.30}$$

where the visibility V_{jk} is given by

$$V_{jk} = \left(\int \mathrm{d}\omega \phi_j^{1*}(\omega)\phi_j^2(\omega)\right)\left(\int \mathrm{d}\omega \phi_k^{1*}(\omega)\phi_k^2(\omega)\right). \tag{A.31}$$

We can maximize this visibility by maximizing the overlap f_1 and f_2. We see that this latter provides a lower bound on V_{jk} by writing

$$\begin{aligned}\int \mathrm{d}\omega \phi_j^{1*}(\omega)\phi_j^2(\omega) &= \frac{\int \mathrm{d}\omega f_1^*(\omega, \Omega_j) f_2(\omega, \Omega_j)}{\sqrt{\rho_1(\Omega_j, \Omega_j)\rho_2(\Omega_j, \Omega_j)}} \\ &\geq \int \mathrm{d}\omega \mathrm{d}\Omega f_1^*(\omega, \Omega) f_2(\omega, \Omega),\end{aligned} \tag{A.32}$$

and likewise for k.

It is relatively straightforward to maximize the quantity on the left by tuning experimental parameters, namely pump wavelength, phasematching angle, and transverse optical fiber position (due to residual spatial chirp), and observing two-fold coincidences resulting from first order interference of the sources. Because both sources are pumped with the same pulse, the two-photon term of the state is given by

$$|\psi\rangle \propto \int \mathrm{d}\omega \mathrm{d}\Omega \Big(f_1(\omega,\Omega)\hat{a}_1^\dagger(\omega)\hat{b}_1^\dagger(\Omega) + f_2(\omega,\Omega)\hat{a}_2^\dagger(\omega)\hat{b}_2^\dagger(\Omega) \Big) |\mathrm{vac}\rangle \,. \tag{A.33}$$

A straightforward calculation shows that the probability of a two-fold coincidence between ports $\hat{b}_3$ (or $\hat{b}_4$) and $\hat{a}_3$ (or $\hat{a}_4$) is given by

$$\begin{aligned} P_{cc} &= \frac{1}{4}\int \mathrm{d}^2\omega \Big| f_1(\omega,\Omega) \pm f_2(\omega,\Omega) \Big|^2 \\ &= \frac{1}{2}\Big(1 \pm \mathrm{Re} \int \mathrm{d}^2\omega f_1^*(\omega,\Omega) f_2(\omega,\Omega) \Big) \end{aligned} \tag{A.34}$$

In the following, we will outline additional measurements to quantify the source indistinguishability. In our case, our dual-pass geometry implies that we need to match the JSI of both sources, which is achieved when both signals and idlers from both sources have maximum overlap. We opted for a bulk crystal source in Type II to enable pumping in both directions while being able to separate our four photons into different paths. We used a BiBO crystal due to its relatively high non linearity.

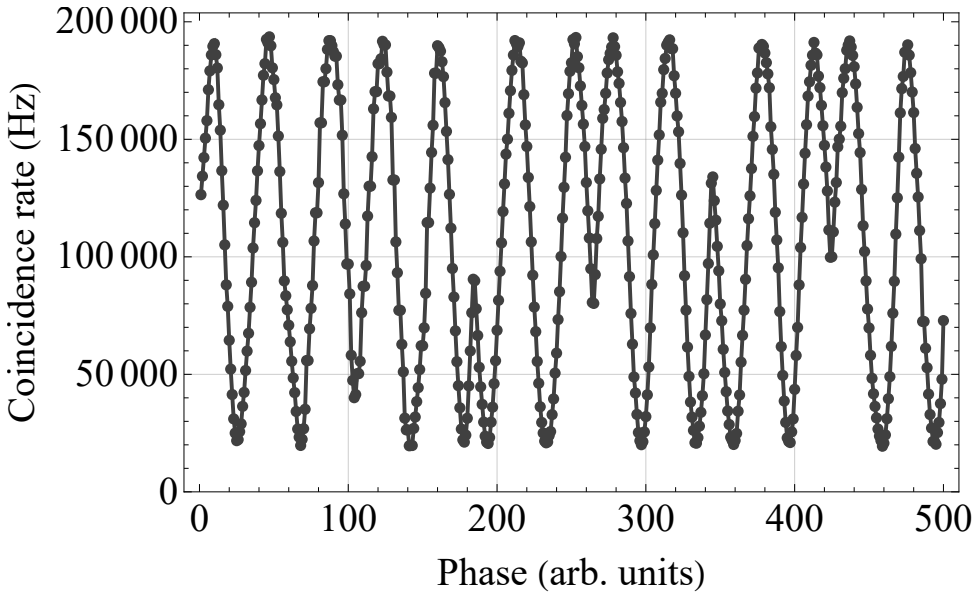

FIGURE A.7. Measured coincidence fringes $P_{cc}(\tau)$ with a contrast of 80%.

First, we measured the JSI by directing the two photons from either source into the fiber spools, since their large spectral bandwidth would be cropped with the CFBG. The JSI from each source is depicted in Fig3.4. They show that both sources are nearly indistinguishable; a singular value decomposition yields a Schmidt number of $K_1 = 2.9 \pm .1$ and $K_2 = 2.9 \pm .1$. These values are lower than the theoretical expectation ($K \sim 5$) because of the timing jitter of our detectors that result in a broader distribution. This was confirmed by measuring the JSI with the CFBG's, which have a better resolution but are limited in range. The correlation width was found to be lower and therefore the Schmidt number can be expected to be at least $K = 4$.

Note that this method is insensitive to any spectral phase difference, such as dispersion from the pump (which is equivalent to setting $\alpha \in \mathbb{C}$ in the JSA (3.28)), since the second pump is slightly more dispersed than the first due to propagation. This has been shown to increase the entanglement and the Schmidt number

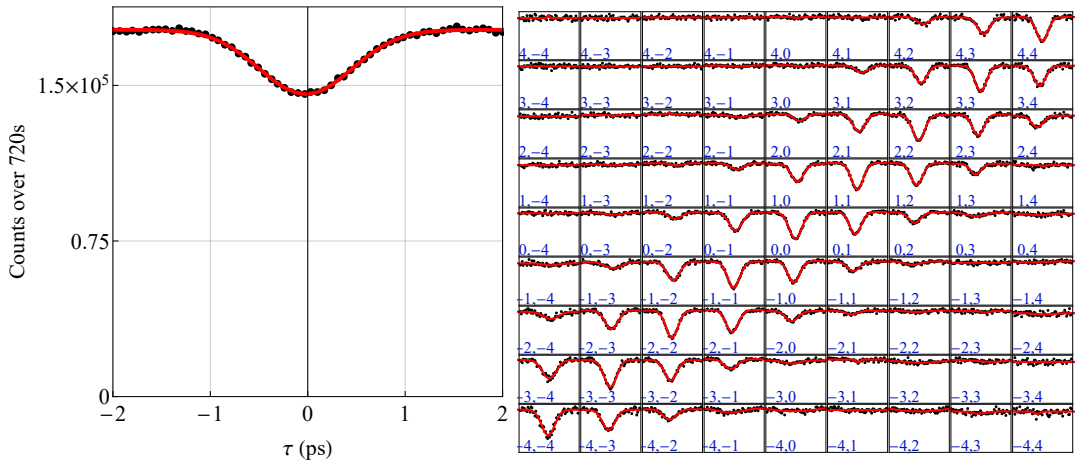

FIGURE A.8. Left: HOM dip between the signal photons heralded by a coincidence between the idler photons. Right: same measurement but with spectral resolution of the heralding photons, labelled j, k for Ω_k, Ω_k, where index $j, k = 0$ corresponds to the center frequency ω_0. The labelling convention is described in Fig. 3.3.

[2, 116]. However, this difference should be negligible, and the method presented that relies on Eq.(A.34) allows for a more accurate estimation of the overlap. Nevertheless, the JSI measurement showed near-perfect correspondence between the intensity of the two sources which is a critical step to ensure indistinguishably between the uncorrelated photon pairs.

To further characterize the indistinguishability of the sources, we measure their heralded $g^{(2)}$ by splitting their signal photon into a beamsplitter. This yields a value of $g_1^{(2)} = 0.16 \pm 0.003$ and $g_2^{(2)} = 0.14 \pm 0.003$. These values are consistent with the relatively high optical power that is utilized to pump the sources in order to maximize the probability of four-fold coincidences. The lower value of $g^{(2)}$ for source 2 is consistent with the fact that it also has a higher heralding efficiency than source 1. The reason is not entirely clear, but it is likely that the previous interaction with the PDC crystal on the first pass results in an additional filtering on the pump as well as a slight reduction in optical power because of absorption.

Finally, in Fig. A.7 we measured the coincidences between ports $\hat{b}_3$ and $\hat{a}_3$ (see Fig3.1) while scanning the relative phase between the two pump fields with a piezoelectric stack, which is related to the probability from Eq.(A.34). We scanned using a slow voltage ramp resulting in a few micrometers of displacement over a few seconds. The visibility of those fringes is 80%, which is a direct measurement of the overlap between the two sources, and therefore a quantification of distinguishability.

A.7. Purity of the heralded states

Since the state $|\psi_{12}\rangle$ from the sources is assumed to be a pure state, the purity of the heralded states $|\Psi_{jk}\rangle$ is ultimately dependent on the amount of spectral filtering in the heralding BSM. To assess this purity, we measure HOM interference between the heralded signal photons when there is no beamsplitter in the idler arms. In this case, upon a coincidence detection of the idler photons at (Ω_j, Ω_k), the reduced state of the signal photons is separable, and given by

$$\hat{\rho}_j \otimes \hat{\rho}_k = \left(\int \mathrm{d}^2\omega \rho_j(\omega,\omega')\right)\left(\int \mathrm{d}^2\tilde{\omega}\rho_k(\tilde{\omega},\tilde{\omega}')\right) \hat{a}_1^\dagger(\omega)\hat{a}_2^\dagger(\tilde{\omega})\left|\mathrm{vac}\right\rangle\left\langle\mathrm{vac}\right|\hat{a}_1(\omega')\hat{a}_2(\tilde{\omega}'), \tag{A.35}$$

where

$$\rho_{j(k)}(\omega,\omega') = \int \mathrm{d}\Omega |t_{j(k)}(\Omega)|^2 f(\omega,\Omega) f^*(\omega',\Omega). \tag{A.36}$$

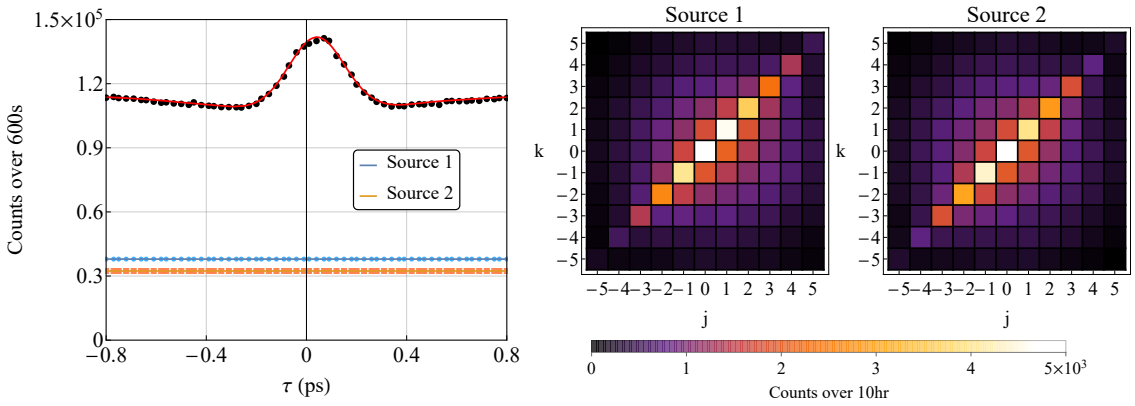

FIGURE A.9. Left: $P(\tau_S)$ without removing the constant two photon contribution from source 1 (dot) and source 2 (square). $P(\tau_S)$ resembles Eq.(3.41) and the fit is obtained by summing the individual fits of P_{jk} as given by (3.26). Right: distribution of these background terms as a function of the heralding frequencies Ω_j, Ω_k

When the signal photons in this state are incident on a 50:50 beamsplitter, the expected visibility of the HOM interference is given by [38]

$$V = \mathrm{Tr}(\hat{\rho}_j \hat{\rho}_k), \tag{A.37}$$

and when the idlers are detected in identical frequency bins ($j = k$), this becomes

$$V = \mathrm{Tr}(\hat{\rho}^2_{j(k)}) = \mathcal{P}(\hat{\rho}_{j(k)}), \tag{A.38}$$

where $\mathcal{P}(\cdot)$ denotes the purity of a state. Thus, for ($j = k$) the visibility of the HOM dip gives a lower bound on the purity of the state $\hat{\rho}_{j(k)}$, and by extension, the state $\hat{\rho}_{jk}$. Our measurements, shown in Fig. A.8, indicate that purity of the heralded states is *at least* 70%, as evidenced by the HOM visibility along the $j = k$ line. By comparison, a direct calculation of the expected purity using our

experimental parameters gives $\sim 78\%$. The purity of our heralded state seems to be dominated by the spectral resolution of our spectrometer. Without spectral resolution, the purity of the heralded state is about 20% as shown in Fig. A.8. We note that at the time of writing, an experiment has been reported using spectral-to-spatial spectrally-multiplexed HOM interference scheme, showing a similar decrease in HOM visibility as a function of distance between frequency bins [117].

A.8. Background signal

As shown by Eq.(A.3), the full four photon state in the interferometer (see Fig. 3.1) contains a contribution from photon pairs emitted by individual sources due to the stochastic nature of parametric down conversion. These terms contribute to $P(\tau_S)$ in the form of interferences that get averaged over the course of a measurement. It is therefore possible to remove that contribution from the signal subsequently to the measurement by blocking a source and recording the rate of four-fold coincidences.

We therefore repeated the measurement of $P_{jk}(\tau_S)$ with either source blocked to obtain the constant background signal for each j, k frequencies, as shown in Fig. A.9. This shown that the background terms are similar between both sources, therefore the two sources are similar. Summing over all the bins, we can plot on the same scale the contribution of all term in Fig. A.9. The peak corresponds to interferences from $|\psi_{12}\rangle$ while the flat terms represent $|\psi_{11}\rangle$ and $|\psi_{22}\rangle$. As expected from the theory, both source contribute to 1/4 of the full signal. Removing those backgrounds at Ω_j, Ω_k from P_{jk}, we obtain the fringes from Chapter III with optimal visibility.

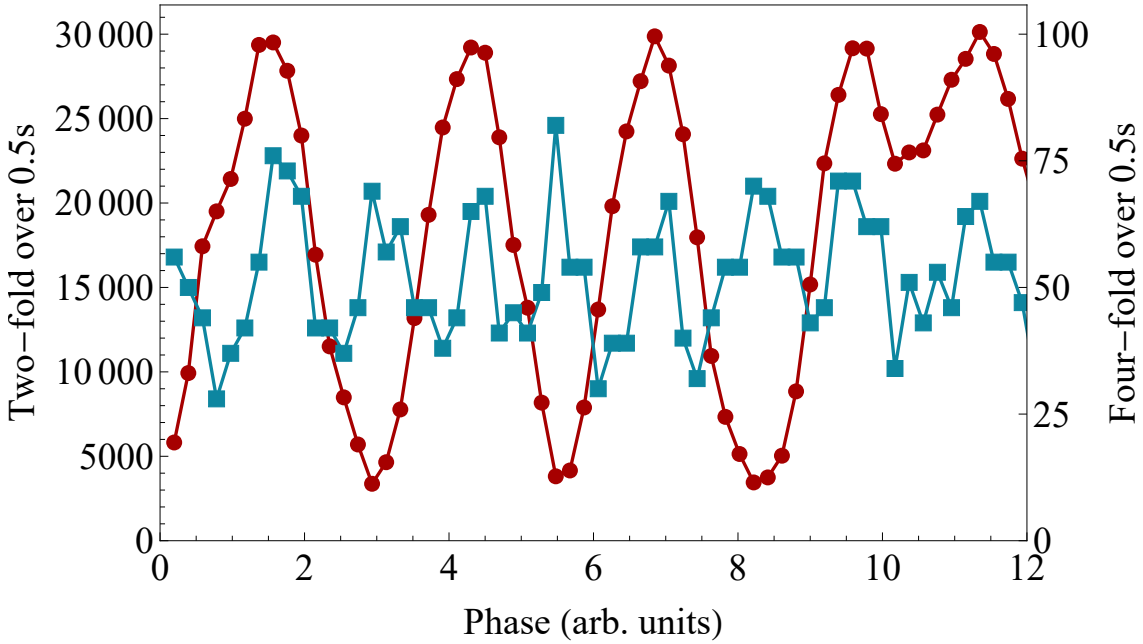

FIGURE A.10. Interference fringes in the two-fold (red) and fourfold (blue) coincidences, obtained in "real-time", while scanning a PZT as described in the text. The four-fold fringes can be seen to occur at twice the frequency of the two-fold fringes.

As stated in the main text, we have assumed that the three terms in the full state Eq. (A.3) are mutually incoherent. This is because our measurements are taken over a long timescale of a few hours where the optical phase drifts significantly and any phase-sensitive interference can be neglected. Over a shorter time-scale, we can measure this optical phase in real time by measuring fourfold coincidences with the two beamsplitters present, while scanning the PZT between both sources. A straightforward calculation taking into account the full state (A.3) shows that there is a term that oscillates at the sum frequency $\omega + \Omega \approx \omega_p$, where ω_p is the pump frequency, corresponding to about 415 nm in wavelength. In Fig. A.10, we plot the measured interference of the two-fold (red) coincidences against the four-fold fringes (blue), where the latter can be seen to modulate at twice the frequency of the two-fold modulation.

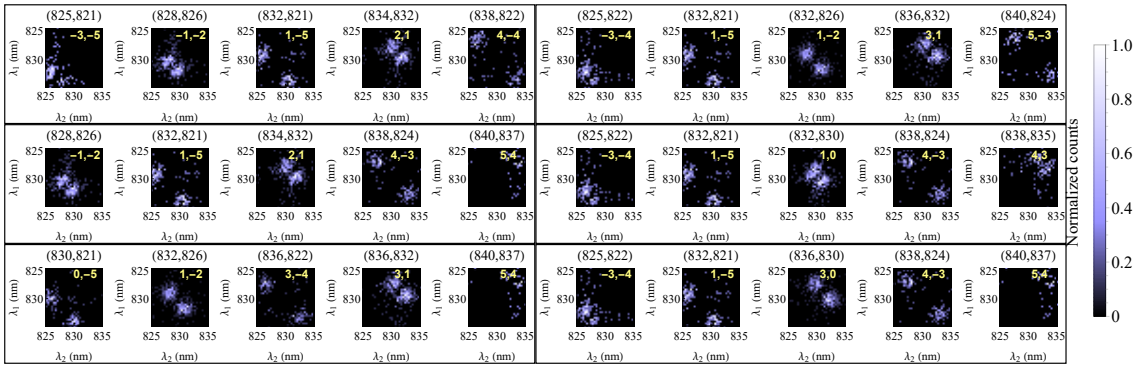

FIGURE A.11. Sets of orthogonal modes F_{jk} that have less than 15 % of mutual overlap. The insets label j and k.

A.9. Orthogonal modes

From Eq.(3.9), we see that the heralded state $|\Psi_{jk}\rangle$ is dependent on the modes $|\phi_j\rangle$ and $|\phi_k\rangle$, which, in the pure state case, results in a heralded joint spectrum (3.17) dependent on the outer products $\phi_j(\omega_1)\phi_k(\omega_2)$. For each heralding bin j and k, we label the heralded JSI from (3.9) as $F_n(\omega_1, \omega_2)$, where n indexes a pair (j, k). These are normalized as $\int \mathrm{d}^2\omega F_n(\omega_1, \omega_2) = 1 \; \forall \; n$ but are not orthogonal, even in the pure state case, *i.e* $\int \mathrm{d}^2\omega F_n(\omega_1, \omega_2) F_m(\omega_1, \omega_2) \neq \delta_{nm}$. Orthogonality is usually a corner stone in any quantum protocol, and it is therefore necessary to select the heralded states from our measurement that are orthogonal. To do so, we utilize our measurement of F_{jk} by measuring the spectral coincidences between the signal's photon heralded by a BSM on the idlers. We then obtain the set of JSI presented in Fig. 3.7(b).

First, it is important to notice the symmetry in (3.9), where $F_{jk} = F_{kj}$ for $j \neq k$. Since our TOFS are well-calibrated, it is reasonable to symmetrize our measured heralded JSI by averaging the experimentally obtained F_{jk} and F_{kj} (for $j \neq k$) thus defining the F_n functions. Then we compute the mutual overlaps $\int \mathrm{d}^2\omega F_n(\omega_1, \omega_2) F_m(\omega_1, \omega_2)$ and use an algorithm to select a set of modes $\{F_n\}$

which all have an overlap below a certain threshold of 15%. We represented a few of these JSI in Fig. A.11. Since the spectral range of our high resolution TOFS is limited, so is the range over which we can compute overlap, as can be seen from the modes that are labelled with a large j, k. Nevertheless, there is a sufficient amount of spectral coincidence in those cases to infer orthogonality with the other JSI.

Note that while this overlap is computed between the joint spectral intensities and not between the states, it can be shown that if the overlap in intensity is zero, then the states are necessarily orthogonal, hence the strategy is valid to select which $|\Psi_{jk}\rangle$ are mutually orthogonal. Therefore, it is fair to say that the JSI's F_{jk} from Fig. A.11 correspond to heralded states $|\Psi_{jk}\rangle$ that are all mutually orthogonal.

A.10. Miscellaneous functions and relations

Our theoretical derivation relies on the definition of the $\phi_{j(k)}(\omega)$ functions which renders computation easier thanks to the Gaussian approximation. These functions can be also written in a density matrix formalism.

Using the definitions from Sec.3.2, the $\phi_{j(k)}$ functions are defined from the JSA by:

$$f(\omega, \Omega_{j(k)}) = \sqrt{N_j}\phi_{j(k)}(\omega), \tag{A.39}$$

where N_j is a function that depends on the heralding frequency Ω_j, the JSA bandwidth over the idler axis σ_{I} and the amount of entanglement α. The reduced density matrix of the idler, given by Eq.(3.30), can then be written in the following

manner:

$$\begin{aligned}\rho_{\mathrm{I}}(\Omega_j, \Omega_k) &= \int \mathrm{d}\omega \; f(\omega, \Omega_j) f^*(\omega, \Omega_k) \\ &= \sqrt{N_j N_k} \int \mathrm{d}\omega \; \phi_j(\omega) \phi_k^*(\omega) \\ &= \sqrt{N_j N_k} \, \langle \phi_j | \phi_k \rangle \,, \end{aligned} \tag{A.40}$$

where we see that the idler density matrix can be linked to the overlap integral between the heralded signal states. The $N_{j(k)}$ functions are then found to be equal to the diagonal elements of the idlers density matrix:

$$N_{j(k)} = \rho_{\mathrm{I}} \left(\Omega_{j(k)}, \Omega_{j(k)} \right), \tag{A.41}$$

since the $\phi_{j(k)}$ are ℓ^2 normalized.

The signal density matrices then follow a similar derivation, with

$$\begin{aligned}\rho_{\mathrm{S}}(\omega, \omega') &= \int \mathrm{d}\Omega_{j(k)} \; f(\omega, \Omega_{j(k)}) f^*(\omega', \Omega_{j(k)}) \\ &= \int \mathrm{d}\Omega_{j(k)} \; N_{j(k)} \phi_{j(k)}(\omega) \phi_{j(k)}^*(\omega), \end{aligned} \tag{A.42}$$

and the diagonal elements are given by

$$\rho_{\mathrm{S}}(\omega, \omega) = \int \mathrm{d}\Omega_{j(k)} \; N_{j(k)} \left| \phi_{j(k)}(\omega) \right|^2 . \tag{A.43}$$

It is easy to show that in the case of similar sources, we also have the identity

$$\rho_{\mathrm{S}}(\omega, \omega') = \rho_{\mathrm{S}}^*(\omega', \omega). \tag{A.44}$$

Finally, the overlap between the modes ϕ_j and ϕ_k can also be written in term of the density matrices, as:

$$\langle \phi_j | \phi_k \rangle = \frac{\rho_{\mathrm{I}}(\Omega_j, \Omega_k)}{\sqrt{N_j N_k}} \tag{A.45}$$

A.10.1. Overlap

As shown previously, the overlap between the modes ϕ_j and ϕ_k is also written in term of the density matrices, as:

$$\langle \phi_j | \phi_k \rangle = \frac{\rho_{\mathrm{I}}(\Omega_j, \Omega_k)}{\sqrt{N_j N_k}} \tag{A.46}$$

$$\begin{aligned} \Gamma(\omega_1, \omega_2; \tau_{\mathrm{I}}) = &\left(\int \mathrm{d}\Omega f^*(\omega_1, \Omega) f(\omega_2, \Omega) e^{-i\Omega\tau_{\mathrm{I}}} \right) \times \\ &\left(\int \mathrm{d}\Omega' f^*(\omega_2, \Omega') f(\omega_1, \Omega') e^{i\Omega'\tau_{\mathrm{I}}} \right) \end{aligned} \tag{A.47}$$

which can be written more concisely as

$$\begin{aligned} \Gamma(\omega_1, \omega_2; \tau_{\mathrm{I}}) &= \left| \int \mathrm{d}\Omega \; f_1(\omega_1, \Omega) f_2^*(\omega_2, \Omega) \right|^2 \\ &= \left| \rho_{s1}(\omega_1, \omega_2) \rho_{s2}^*(\omega_1, \omega_2) \right|^2 \end{aligned} \tag{A.48}$$

by writing $f_1(\omega, \Omega) = f(\omega, \Omega)$ and $f_2(\omega, \Omega) = f(\omega, \Omega) e^{i\Omega\tau_{\mathrm{I}}}$, showing that this term is the overlap integral between the joint spectra of the sources. The second expression is obtained by defining the reduced density matrices for the signal photon of each source.

APPENDIX B

SFG THEORY SUPPLEMENTAL

B.1. Deriving the three-wave mixing transformation

Strictly speaking, the Hamiltonian describing the nonlinear interactions we consider is a time-dependent quantity, $\hat{H}(t)$, whereby a state $|\Psi_{\text{out}}\rangle$ evolves from an initial state $|\Psi_{\text{in}}\rangle$ according to

$$\begin{aligned} |\Psi_{\text{out}}\rangle &= \exp\Big[-\frac{i}{\hbar}\int_0^t \mathrm{d}t'\hat{H}(t')\Big]\,|\Psi_{\text{in}}\rangle \\ &\approx \left(1-\frac{i}{\hbar}\int_0^t \mathrm{d}t'\hat{H}(t')\right)|\Psi_{\text{in}}\rangle \end{aligned} \tag{B.1}$$

The relevant Hamiltonian for three-wave mixing has the form

$$\hat{H}(t) = \chi\int_V \mathrm{d}V\hat{E}_p^+(\mathbf{r},t)\hat{E}_s^-(\mathbf{r},t)\hat{E}_i^-(\mathbf{r},t) + \text{H.c.} \tag{B.2}$$

where $\hat{E}_j^{+(-)}$ denotes the positive (negative) frequency component of the j field operator, with $j = p, s, i$. V denotes the interaction volume, which we take to be infinite in the transverse direction (by assuming the field modes are well-confined within the crystal area), and of length L in the longitudinal direction. Finally, $\mathbf{r}$ and t denote the space and time coordinates, and $\tilde{\chi}$ describes the interaction strength. We expand the field operators into their plane-wave components,

$$\begin{aligned} \hat{E}_j^+(\mathbf{r},t) &= \int \mathrm{d}\omega_j A_j(\omega_j)\exp\Big[i(\mathbf{k}_j(\omega_j)\cdot\mathbf{r}-\omega_j t)\Big]\hat{a}_j(\omega_j), \\ \hat{E}_j^- &= (\hat{E}_j^+)^\dagger, \end{aligned} \tag{B.3}$$

where $A_j(\omega_j)$ is a slowly-varying function of ω. Substituting these into the Hamiltonian and absorbing all the slowly-varying functions into χ, we obtain

$$\begin{aligned}\hat{H}(t) =& \chi \int_V \mathrm{d}V \int \mathrm{d}\omega_p \mathrm{d}\omega_s \mathrm{d}\omega_i \hat{a}_p(\omega_p)\hat{a}_s^\dagger(\omega_s)\hat{a}_i^\dagger(\omega_i) \\ &\times \exp\Big[i(\mathbf{k}_p(\omega_p) - \mathbf{k}_s(\omega_s) - \mathbf{k}_i(\omega_i)) \cdot \mathbf{r}\Big] \\ &\times \exp\Big[-i(\omega_p - \omega_s - \omega_i)t\Big] + \text{H.c.}.\end{aligned} \tag{B.4}$$

Now we use this form of the Hamiltonian to compute output state (B.1) to first order in the expansion, whereupon we carry the integration over the transverse spatial directions to infinity. Additionally, we carry out the time integral from negative to positive infinity because the input and output states are observed long before and after the interaction time t, resulting in a delta-function in $(\omega_p - \omega_s - \omega_i)$ (energy conservation). All of this obtains

$$\begin{aligned}|\Psi_{\text{out}}\rangle \approx \Bigg[1 - i\chi \int_0^L \mathrm{d}z \int \mathrm{d}\omega_s \mathrm{d}\omega_i \exp\Big[i(\Delta\mathbf{k})_z z\Big] \\ \times \hat{a}_p(\omega_s + \omega_i)\hat{a}_s^\dagger(\omega_s)\hat{a}_i^\dagger(\omega_i) + \text{H.c.}\Bigg] |\Psi_{\text{in}}\rangle\,,\end{aligned} \tag{B.5}$$

where we have also absorbed the $\hbar$ into χ. Carrying out the integration over z provides the phase-matching function $\Phi(\omega_s, \omega_i)$, and we define the transformation

$$\hat{H} = \chi \int \mathrm{d}\omega_s \mathrm{d}\omega_i \Phi(\omega_s, \omega_i)\hat{a}_p(\omega_s + \omega_i)\hat{a}_s^\dagger(\omega_s)\hat{a}_i^\dagger(\omega_i) + \text{H.c}, \tag{B.6}$$

such that

$$|\Psi_{\text{out}}\rangle \approx \left(1 - i\hat{H}\right)|\Psi_{\text{in}}\rangle\,. \tag{B.7}$$

B.2. Relating the entanglement parameter α to the Schmidt number K

In section 5.3.3 we used the scenario of spectral teleportation to illustrate the role of entanglement in the measurement, on par with entanglement in the state, in a quantum protocol. To that end, we quantified the teleportation fidelity in terms of the correlation parameters α (β) of the bivariate Gaussian state $f_s(\omega, \omega')$ (measurement $f_m(\omega, \omega')$). This parameter has the advantage of being bounded by the interval $[-1, 1]$, with maximal entanglement at the boundaries, whereas more common measures of entanglement for pure states, such as the entropy and the Schmidt number, diverge for maximal entanglement. Here we show for completeness how the Schmidt number K depends functionally on α, while the same analysis holds for β.

The Gaussian JSA $f_s(\omega, \omega')$ from (5.41) has a Schmidt decomposition of the form

$$f_s(\omega, \omega') = \sum_{j=0}^{\infty} \sqrt{\lambda_j}\ u_j(\omega) v_j(\omega'), \tag{B.8}$$

where $\{u_j(\omega)\}$ is the orthonormal set of Hermite-Gauss functions spanning the spectral Hilbert space over ω, and the same is true of $\{v_j(\omega')\}$ [3]. The Schmidt coefficients λ_j are given by

$$\lambda_j = \operatorname{sech}^2 \zeta\ \tanh^{2j} \zeta, \tag{B.9}$$

satisfying $\sum_{j=0}^{\infty} \lambda_j = 1$, and where ζ is given by

$$\alpha = \tanh\ 2\zeta. \tag{B.10}$$

The Schmidt number K is then given by

$$K = \frac{1}{\sum_{j=0}^{\infty} \lambda_j^2} = \cosh 2\zeta. \tag{B.11}$$

Combining Eq. (B.10) and (B.11), we arrive at the simple relationship

$$K = \frac{1}{\sqrt{1-\alpha^2}}, \tag{B.12}$$

where, as expected, K is equal to unity for the case of no correlation, $\alpha = 0$, and diverges for maximal correlation, $\alpha = \pm 1$.

REFERENCES CITED

[1] S. Merkouche, V. Thiel, A.O.C Davis, , and B.J. Smith. Heralding multiple photonic pulsed bell-pairs via frequency-resolved entanglement swapping. 2021. In preparation.

[2] Vahid Ansari, John M. Donohue, Benjamin Brecht, and Christine Silberhorn. Tailoring nonlinear processes for quantum optics with pulsed temporal-mode encodings. *Optica*, 5(5):534, may 2018. ISSN 2334-2536. doi: 10.1364/OPTICA.5.000534. URL `http://arxiv.org/abs/1803.04316` `https://www.osapublishing.org/abstract.cfm?URI=optica-5-5-534`.

[3] Travis S. Humble. Spectral and spread-spectral teleportation. *Physical Review A - Atomic, Molecular, and Optical Physics*, 81(6):062339, 2010. ISSN 10502947. doi: 10.1103/PhysRevA.81.062339.

[4] M. Planck.

[5] A. Einstein. Über einen die erzeugung und verwandlung des lichtes betreffenden heuristischen gesichtspunkt. *Annalen der Physik*, 322(6):132–148, 1905. doi: https://doi.org/10.1002/andp.19053220607. URL `https://onlinelibrary.wiley.com/doi/abs/10.1002/andp.19053220607`.

[6] Paul A. M. Dirac. Quantum theory of emission and absorption of radiation. *Proc. Roy. Soc. Lond. A*, 114:243, 1927. doi: 10.1098/rspa.1927.0039.

[7] R. P. Feynman. Space-time approach to quantum electrodynamics. *Phys. Rev.*, 76:769–789, Sep 1949. doi: 10.1103/PhysRev.76.769. URL `https://link.aps.org/doi/10.1103/PhysRev.76.769`.

[8] Roy J. Glauber. The quantum theory of optical coherence. *Phys. Rev.*, 130: 2529–2539, Jun 1963. doi: 10.1103/PhysRev.130.2529. URL `https://link.aps.org/doi/10.1103/PhysRev.130.2529`.

[9] T. H. Maiman. Stimulated optical radiation in ruby. *Nature*, 187(4736):493–494, 1960.

[10] John F. Clauser. Experimental distinction between the quantum and classical field-theoretic predictions for the photoelectric effect. *Phys. Rev. D*, 9: 853–860, Feb 1974. doi: 10.1103/PhysRevD.9.853. URL `https://link.aps.org/doi/10.1103/PhysRevD.9.853`.

[11] D. T. Smithey, M. Beck, M. G. Raymer, and A. Faridani. Measurement of the wigner distribution and the density matrix of a light mode using optical homodyne tomography: Application to squeezed states and the vacuum. *Phys. Rev. Lett.*, 70:1244–1247, Mar 1993. doi: 10.1103/PhysRevLett.70.1244. URL https://link.aps.org/doi/10.1103/PhysRevLett.70.1244.

[12] Dik Bouwmeester, Jian-Wei Pan, Klaus Mattle, Manfred Eibl, Harald Weinfurter, and Anton Zeilinger. Experimental quantum teleportation. *Nature*, 390(6660):575–579, 1997.

[13] Marissa Giustina, Marijn A. M. Versteegh, Sören Wengerowsky, Johannes Handsteiner, Armin Hochrainer, Kevin Phelan, Fabian Steinlechner, Johannes Kofler, Jan-Åke Larsson, Carlos Abellán, Waldimar Amaya, Valerio Pruneri, Morgan W. Mitchell, Jörn Beyer, Thomas Gerrits, Adriana E. Lita, Lynden K. Shalm, Sae Woo Nam, Thomas Scheidl, Rupert Ursin, Bernhard Wittmann, and Anton Zeilinger. Significant-loophole-free test of bell's theorem with entangled photons. *Phys. Rev. Lett.*, 115:250401, Dec 2015. doi: 10.1103/PhysRevLett.115.250401. URL https://link.aps.org/doi/10.1103/PhysRevLett.115.250401.

[14] H. J. Kimble. The quantum internet. *Nature*, 453(7198):1023–1030, 2008. doi: 10.1038/nature07127. URL https://doi.org/10.1038/nature07127.

[15] Carlton M. Caves. Quantum-mechanical noise in an interferometer. *Phys. Rev. D*, 23:1693–1708, Apr 1981. doi: 10.1103/PhysRevD.23.1693. URL https://link.aps.org/doi/10.1103/PhysRevD.23.1693.

[16] Seth Lloyd. Enhanced sensitivity of photodetection via quantum illumination. *Science*, 321(5895):1463–1465, 2008. ISSN 0036-8075. doi: 10.1126/science.1160627. URL https://science.sciencemag.org/content/321/5895/1463.

[17] E. D. Lopaeva, I. Ruo Berchera, I. P. Degiovanni, S. Olivares, G. Brida, and M. Genovese. Experimental realization of quantum illumination. *Phys. Rev. Lett.*, 110:153603, Apr 2013. doi: 10.1103/PhysRevLett.110.153603. URL https://link.aps.org/doi/10.1103/PhysRevLett.110.153603.

[18] A. Einstein, B. Podolsky, and N. Rosen. Can quantum-mechanical description of physical reality be considered complete? *Phys. Rev.*, 47:777–780, May 1935. doi: 10.1103/PhysRev.47.777. URL https://link.aps.org/doi/10.1103/PhysRev.47.777.

[19] Albert B. Einstein, Max Born, and Hedwig Born. The born-einstein letters: Correspondence between albert einstein and max and hedwig born from 1916-1955, with commentaries by max born;. 1971.

[20] J. S. Bell. On the einstein podolsky rosen paradox. *Physics Physique Fizika*, 1: 195–200, Nov 1964. doi: 10.1103/PhysicsPhysiqueFizika.1.195. URL https://link.aps.org/doi/10.1103/PhysicsPhysiqueFizika.1.195.

[21] John F. Clauser, Michael A. Horne, Abner Shimony, and Richard A. Holt. Proposed experiment to test local hidden-variable theories. *Phys. Rev. Lett.*, 23:880–884, Oct 1969. doi: 10.1103/PhysRevLett.23.880. URL https://link.aps.org/doi/10.1103/PhysRevLett.23.880.

[22] Ryszard Horodecki, Paweł Horodecki, Michał Horodecki, and Karol Horodecki. Quantum entanglement. *Rev. Mod. Phys.*, 81:865–942, Jun 2009. doi: 10.1103/RevModPhys.81.865. URL https://link.aps.org/doi/10.1103/RevModPhys.81.865.

[23] Artur K. Ekert. Quantum cryptography based on bell's theorem. *Phys. Rev. Lett.*, 67:661–663, Aug 1991. doi: 10.1103/PhysRevLett.67.661. URL https://link.aps.org/doi/10.1103/PhysRevLett.67.661.

[24] M. J. Holland and K. Burnett. Interferometric detection of optical phase shifts at the heisenberg limit. *Phys. Rev. Lett.*, 71:1355–1358, Aug 1993. doi: 10.1103/PhysRevLett.71.1355. URL https://link.aps.org/doi/10.1103/PhysRevLett.71.1355.

[25] Taoufik Amri, Julien Laurat, and Claude Fabre. Characterizing quantum properties of a measurement apparatus: Insights from the retrodictive approach. *Physical Review Letters*, 106(2):020502, 2011. ISSN 10797114. doi: 10.1103/PhysRevLett.106.020502.

[26] S J van Enk. Photodetector figures of merit in terms of POVMs. *Journal of Physics Communications*, 1(4):045001, nov 2017. doi: 10.1088/2399-6528/aa90ce. URL https://doi.org/10.1088/2399-6528/aa90ce.

[27] W. K. Wootters and W. H. Zurek. A single quantum cannot be cloned. *Nature*, 299(5886):802–803, 1982.

[28] Charles H. Bennett, Gilles Brassard, Claude Crépeau, Richard Jozsa, Asher Peres, and William K. Wootters. Teleporting an unknown quantum state via dual classical and einstein-podolsky-rosen channels. *Phys. Rev. Lett.*, 70: 1895–1899, Mar 1993. doi: 10.1103/PhysRevLett.70.1895. URL https://link.aps.org/doi/10.1103/PhysRevLett.70.1895.

[29] Nicolas Gisin. Entanglement 25 years after quantum teleportation: Testing joint measurements in quantum networks. *Entropy*, 21(3), 2019. ISSN 10994300. doi: 10.3390/e21030325.

[30] Asher Peres and William K. Wootters. Optimal detection of quantum information. *Phys. Rev. Lett.*, 66:1119–1122, Mar 1991. doi: 10.1103/PhysRevLett.66.1119. URL https://link.aps.org/doi/10.1103/PhysRevLett.66.1119.

[31] Tamás Vértesi and Miguel Navascués. Certifying entangled measurements in known hilbert spaces. *Phys. Rev. A*, 83:062112, Jun 2011. doi: 10.1103/PhysRevA.83.062112. URL https://link.aps.org/doi/10.1103/PhysRevA.83.062112.

[32] Rafael Rabelo, Melvyn Ho, Daniel Cavalcanti, Nicolas Brunner, and Valerio Scarani. Device-independent certification of entangled measurements. *Phys. Rev. Lett.*, 107:050502, Jul 2011. doi: 10.1103/PhysRevLett.107.050502. URL https://link.aps.org/doi/10.1103/PhysRevLett.107.050502.

[33] Adam Bennet, Tamás Vértesi, Dylan J. Saunders, Nicolas Brunner, and G. J. Pryde. Experimental semi-device-independent certification of entangled measurements. *Physical Review Letters*, 113(8):080405, 2014. ISSN 10797114. doi: 10.1103/PhysRevLett.113.080405.

[34] M. Żukowski, A. Zeilinger, M. A. Horne, and A. K. Ekert. "event-ready-detectors" bell experiment via entanglement swapping. *Phys. Rev. Lett.*, 71:4287–4290, Dec 1993. doi: 10.1103/PhysRevLett.71.4287. URL https://link.aps.org/doi/10.1103/PhysRevLett.71.4287.

[35] B. Brecht, Dileep V. Reddy, C. Silberhorn, and M. G. Raymer. Photon temporal modes: A complete framework for quantum information science. *Physical Review X*, 5(4):041017, oct 2015. ISSN 21603308. doi: 10.1103/PhysRevX.5.041017. URL https://link.aps.org/doi/10.1103/PhysRevX.5.041017.

[36] E. H. Bernhardi, H. A.G.M. van Wolferen, L. Agazzi, M. R.H. Khan, C. G.H. Roeloffzen, K. Wörhoff, M. Pollnau, and R. M. de Ridder. Ultra-narrow-linewidth, single-frequency distributed feedback waveguide laser in al2o3:er3+ on silicon. *Opt. Lett.*, 35(14):2394–2396, Jul 2010. doi: 10.1364/OL.35.002394. URL http://opg.optica.org/ol/abstract.cfm?URI=ol-35-14-2394.

[37] Kevin A. O'Donnell and Alfred B. U'Ren. Observation of ultrabroadband, beamlike parametric downconversion. *Opt. Lett.*, 32(7):817–819, Apr 2007. doi: 10.1364/OL.32.000817. URL http://opg.optica.org/ol/abstract.cfm?URI=ol-32-7-817.

[38] Peter J. Mosley, Jeff S. Lundeen, Brian J. Smith, Piotr Wasylczyk, Alfred B. U'Ren, Christine Silberhorn, and Ian A. Walmsley. Heralded generation of ultrafast single photons in pure quantum states. *Phys. Rev. Lett.*, 100: 133601, Apr 2008. doi: 10.1103/PhysRevLett.100.133601. URL https://link.aps.org/doi/10.1103/PhysRevLett.100.133601.

[39] Christopher L. Morrison, Markus Rambach, Zhe Xian Koong, Francesco Graffitti, Fiona Thorburn, Ajoy K. Kar, Yong Ma, Suk-In Park, Jin Dong Song, Nick G. Stoltz, Dirk Bouwmeester, Alessandro Fedrizzi, and Brian D. Gerardot. A bright source of telecom single photons based on quantum frequency conversion. *Applied Physics Letters*, 118(17):174003, 2021. doi: 10.1063/5.0045413. URL https://doi.org/10.1063/5.0045413.

[40] Andrew M Weiner. Ultrafast optical pulse shaping: A tutorial review. *Optics Communications*, 284(15):3669–3692, 2011.

[41] Laura J. Wright, Michał Karpiński, Christoph Söller, and Brian J. Smith. Spectral shearing of quantum light pulses by electro-optic phase modulation. *Phys. Rev. Lett.*, 118:023601, Jan 2017. doi: 10.1103/PhysRevLett.118.023601. URL https://link.aps.org/doi/10.1103/PhysRevLett.118.023601.

[42] Michał Karpiński, Michał Jachura, Laura J. Wright, and Brian J. Smith. Bandwidth manipulation of quantum light by an electro-optic time lens. *Nature Photonics*, 11(1):53–57, 2017.

[43] J. M. Donohue, M. Mastrovich, and K. J. Resch. Spectrally engineering photonic entanglement with a time lens. *Phys. Rev. Lett.*, 117:243602, Dec 2016. doi: 10.1103/PhysRevLett.117.243602. URL https://link.aps.org/doi/10.1103/PhysRevLett.117.243602.

[44] James Ashby, Valérian Thiel, Markus Allgaier, Peru d'Ornellas, Alex O. C. Davis, and Brian J. Smith. Temporal mode transformations by sequential time and frequency phase modulation for applications in quantum information science. *Opt. Express*, 28(25):38376–38389, Dec 2020. doi: 10.1364/OE.410371. URL http://opg.optica.org/oe/abstract.cfm?URI=oe-28-25-38376.

[45] Andreas Eckstein, Benjamin Brecht, and Christine Silberhorn. A quantum pulse gate based on spectrally engineered sum frequency generation. *Opt. Express*, 19(15):13770–13778, Jul 2011. doi: 10.1364/OE.19.013770. URL http://opg.optica.org/oe/abstract.cfm?URI=oe-19-15-13770.

[46] Dileep V. Reddy and Michael G. Raymer. High-selectivity quantum pulse gating of photonic temporal modes using all-optical Ramsey interferometry. *Optica*, 5(4):423, apr 2018. ISSN 2334-2536. doi: 10.1364/OPTICA.5.000423. URL https://www.osapublishing.org/abstract.cfm?URI=optica-5-4-423.

[47] Jian-Wei Pan, Dik Bouwmeester, Harald Weinfurter, and Anton Zeilinger. Experimental Entanglement Swapping: Entangling Photons That Never Interacted. *Physical Review Letters*, 80(18):3891–3894, 1998. ISSN 0031-9007. doi: 10.1103/PhysRevLett.80.3891. URL https://link.aps.org/doi/10.1103/PhysRevLett.80.3891.

[48] Matthäus Halder, Alexios Beveratos, Nicolas Gisin, Valerio Scarani, Christoph Simon, and Hugo Zbinden. Entangling independent photons by timemeasurement. *Nature Physics*, 3(10):692–695, 2007. ISSN 1745-2473. doi: 10.1038/nphys700. URL http://www.nature.com/doifinder/10.1038/nphys700.

[49] Yingwen Zhang, Megan Agnew, Thomas Roger, Filippus S. Roux, Thomas Konrad, Daniele Faccio, Jonathan Leach, and Andrew Forbes. Simultaneous entanglement swapping of multiple orbital angular momentum states of light. *Nature Communications*, 8(1):632, dec 2017. ISSN 2041-1723. doi: 10.1038/s41467-017-00706-1. URL http://www.nature.com/articles/s41467-017-00706-1.

[50] Francesco Graffitti, Peter Barrow, Alexander Pickston, Agata M. Brańczyk, and Alessandro Fedrizzi. Direct generation of tailored pulse-mode entanglement. *Phys. Rev. Lett.*, 124:053603, Feb 2020. doi: 10.1103/PhysRevLett.124.053603. URL https://link.aps.org/doi/10.1103/PhysRevLett.124.053603.

[51] John Calsamiglia. Generalized measurements by linear elements. *Phys. Rev. A*, 65:030301, Feb 2002. doi: 10.1103/PhysRevA.65.030301. URL https://link.aps.org/doi/10.1103/PhysRevA.65.030301.

[52] C. K. Law, I. A. Walmsley, and J. H. Eberly. Continuous frequency entanglement: Effective finite hilbert space and entropy control. *Physical Review Letters*, 84(23):5304–5307, 2000. ISSN 10797114. doi: 10.1103/PhysRevLett.84.5304.

[53] Carl Eckart and Gale Young. The approximation of one matrix by another of lower rank. *Psychometrika*, 1(3):211–218, 1936.

[54] R Grobe, K Rzazewski, and J H Eberly. Measure of electron-electron correlation in atomic physics. *Journal of Physics B: Atomic, Molecular and Optical Physics*, 27(16):L503–L508, aug 1994. doi: 10.1088/0953-4075/27/16/001. URL https://doi.org/10.1088/0953-4075/27/16/001.

[55] Asher Peres. Separability criterion for density matrices. *Phys. Rev. Lett.*, 77: 1413–1415, Aug 1996. doi: 10.1103/PhysRevLett.77.1413. URL https://link.aps.org/doi/10.1103/PhysRevLett.77.1413.

[56] Sam A. Hill and William K. Wootters. Entanglement of a pair of quantum bits. *Phys. Rev. Lett.*, 78:5022–5025, Jun 1997. doi: 10.1103/PhysRevLett.78.5022. URL https://link.aps.org/doi/10.1103/PhysRevLett.78.5022.

[57] William K. Wootters. Entanglement of formation of an arbitrary state of two qubits. *Phys. Rev. Lett.*, 80:2245–2248, Mar 1998. doi: 10.1103/PhysRevLett.80.2245. URL https://link.aps.org/doi/10.1103/PhysRevLett.80.2245.

[58] G. Vidal and R. F. Werner. Computable measure of entanglement. *Physical Review A - Atomic, Molecular, and Optical Physics*, 65(3):032314, 2002. ISSN 10502947. doi: 10.1103/PhysRevA.65.032314.

[59] Olivier Morin, Jean-Daniel Bancal, Melvyn Ho, Pavel Sekatski, Virginia D'Auria, Nicolas Gisin, Julien Laurat, and Nicolas Sangouard. Witnessing trustworthy single-photon entanglement with local homodyne measurements. *Phys. Rev. Lett.*, 110:130401, Mar 2013. doi: 10.1103/PhysRevLett.110.130401. URL https://link.aps.org/doi/10.1103/PhysRevLett.110.130401.

[60] Z. Y. Ou, S. F. Pereira, H. J. Kimble, and K. C. Peng. Realization of the einstein-podolsky-rosen paradox for continuous variables. *Phys. Rev. Lett.*, 68:3663–3666, Jun 1992. doi: 10.1103/PhysRevLett.68.3663. URL https://link.aps.org/doi/10.1103/PhysRevLett.68.3663.

[61] Grant R. Fowles. *Introduction to modern optics*. Dover Publications, 2012.

[62] Peter Mosley. *Generation of Heralded Single Photons in Pure Quantum States*. PhD thesis, University of Oxford, 2007.

[63] Robert W. Boyd. *Nonlinear Optics, Third Edition*. Academic Press, Inc., USA, 3rd edition, 2008. ISBN 0123694701.

[64] Leonard Mandel and Emil Wolf. *Optical Coherence and Quantum Optics*. Cambridge University Press, 1995. doi: 10.1017/CBO9781139644105.

[65] Hendrik B. Coldenstrodt-Ronge, Jeff S. Lundeen, Kenny L. Pregnell, Alvaro Feito, Brian J. Smith, Wolfgang Mauerer, Christine Silberhorn, Jens Eisert, Martin B. Plenio, and Ian A. Walmsley. A proposed testbed for detector tomography. *Journal of Modern Optics*, 56(2-3):432–441, 2009. doi: 10.1080/09500340802304929. URL https://doi.org/10.1080/09500340802304929.

[66] S. J. van Enk. Time-dependent spectrum of a single photon and its positive-operator-valued measure. *Physical Review A - Atomic, Molecular, and Optical Physics*, 96(3):033834, 2017. ISSN 24699934. doi: 10.1103/PhysRevA.96.033834.

[67] David Bohm. *Quantum theory*. Prentice-Hall, New York, 1951.

[68] Charles H. Bennett and Stephen J. Wiesner. Communication via one- and two-particle operators on einstein-podolsky-rosen states. *Phys. Rev. Lett.*, 69: 2881–2884, Nov 1992. doi: 10.1103/PhysRevLett.69.2881. URL https://link.aps.org/doi/10.1103/PhysRevLett.69.2881.

[69] Richard Jozsa and Noah Linden. On the role of entanglement in quantum-computational speed-up. *Proceedings of the Royal Society of London. Series A: Mathematical, Physical and Engineering Sciences*, 459 (2036):2011–2032, 2003. doi: 10.1098/rspa.2002.1097.

[70] H. de Riedmatten, I. Marcikic, J. A. W. van Houwelingen, W. Tittel, H. Zbinden, and N. Gisin. Long-distance entanglement swapping with photons from separated sources. *Phys. Rev. A*, 71:050302(R), May 2005. doi: 10.1103/PhysRevA.71.050302. URL https://link.aps.org/doi/10.1103/PhysRevA.71.050302.

[71] M G Raymer, Andrew H Marcus, Julia R Widom, and Dashiell L.P. Vitullo. Entangled photon-pair two-dimensional fluorescence spectroscopy (EPP-2DFS). *Journal of Physical Chemistry B*, 117(49):15559–15575, 2013. ISSN 15206106. doi: 10.1021/jp405829n.

[72] K. J. Blow, Rodney Loudon, Simon J. D. Phoenix, and T. J. Shepherd. Continuum fields in quantum optics. *Phys. Rev. A*, 42:4102–4114, Oct 1990. doi: 10.1103/PhysRevA.42.4102. URL https://link.aps.org/doi/10.1103/PhysRevA.42.4102.

[73] S. Ramelow, L. Ratschbacher, A. Fedrizzi, N. K. Langford, and A. Zeilinger. Discrete tunable color entanglement. *Physical Review Letters*, 103(25): 253601, dec 2009. ISSN 00319007. doi: 10.1103/PhysRevLett.103.253601. URL https://link.aps.org/doi/10.1103/PhysRevLett.103.253601.

[74] Alessandro Fedrizzi, Thomas Herbst, Markus Aspelmeyer, Marco Barbieri, Thomas Jennewein, and Anton Zeilinger. Anti-symmetrization reveals hidden entanglement. *New Journal of Physics*, 11(10):103052, oct 2009. ISSN 1367-2630. doi: 10.1088/1367-2630/11/10/103052. URL http://stacks.iop.org/1367-2630/11/i=10/a=103052?key=crossref.add7c9c91107f1bc26

[75] N. Treps, V. Delaubert, A. Maître, J. M. Courty, and C. Fabre. Quantum noise in multipixel image processing. *Phys. Rev. A*, 71:013820, Jan 2005. doi: 10.1103/PhysRevA.71.013820. URL https://link.aps.org/doi/10.1103/PhysRevA.71.013820.

[76] Jonathan Roslund, Renné Medeiros De Araujo, Shifeng Jiang, Claude Fabre, and Nicolas Treps. Wavelength-multiplexed quantum networks with ultrafast frequency combs. *Nature Photonics*, 8(2):109–112, 2014.

[77] Valérian Thiel, Jonathan Roslund, Pu Jian, Claude Fabre, and Nicolas Treps. Quantum-limited measurements of distance fluctuations with a multimode detector. *Quantum Science and Technology*, 2(3):034008, jul 2017. doi: 10.1088/2058-9565/aa77d3. URL https://doi.org/10.1088/2058-9565/aa77d3.

[78] Víctor Torres-Company, Jesus Lancis, and Pedro Andres. Space-time analogies in optics. *Progress in Optics*, 56:1–80, 2011.

[79] Keisuke Goda and Bahram Jalali. Dispersive fourier transformation for fast continuous single-shot measurements. *Nature Photonics*, 7(2):102–112, 2013.

[80] Alex O. C. Davis, Paul M. Saulnier, Michał Karpiński, and Brian J. Smith. Pulsed single-photon spectrometer by frequency-to-time mapping using chirped fiber bragg gratings. *Opt. Express*, 25(11):12804–12811, May 2017. doi: 10.1364/OE.25.012804. URL http://www.opticsexpress.org/abstract.cfm?URI=oe-25-11-12804.

[81] Heonoh Kim, Sang Min Lee, and Han Seb Moon. Generalized quantum interference of correlated photon pairs. *Scientific reports*, 5(1):1–6, 2015.

[82] Yi-Han Luo, Han-Sen Zhong, Manuel Erhard, Xi-Lin Wang, Li-Chao Peng, Mario Krenn, Xiao Jiang, Li Li, Nai-Le Liu, Chao-Yang Lu, Anton Zeilinger, and Jian-Wei Pan. Quantum teleportation in high dimensions. *Phys. Rev. Lett.*, 123:070505, Aug 2019. doi: 10.1103/PhysRevLett.123.070505. URL https://link.aps.org/doi/10.1103/PhysRevLett.123.070505.

[83] Xiao-Min Hu, Chao Zhang, Bi-Heng Liu, Yu Cai, Xiang-Jun Ye, Yu Guo, Wen-Bo Xing, Cen-Xiao Huang, Yun-Feng Huang, Chuan-Feng Li, and Guang-Can Guo. Experimental high-dimensional quantum teleportation. *Phys. Rev. Lett.*, 125:230501, Dec 2020. doi: 10.1103/PhysRevLett.125.230501. URL https://link.aps.org/doi/10.1103/PhysRevLett.125.230501.

[84] Manuel Erhard, Mehul Malik, Mario Krenn, and Anton Zeilinger. Experimental greenberger–horne–zeilinger entanglement beyond qubits. *Nature Photonics*, 12(12):759–764, 2018. doi: 10.1038/s41566-018-0257-6. URL https://doi.org/10.1038/s41566-018-0257-6.

[85] Sofiane Merkouche, Valérian Thiel, and Brian J. Smith. Positive operator-valued measure for two-photon detection via sum-frequency generation. *Phys. Rev. A*, 103:043711, Apr 2021. doi: 10.1103/PhysRevA.103.043711. URL https://link.aps.org/doi/10.1103/PhysRevA.103.043711.

[86] Laia Ginés, Carlo Pepe, Junior Gonzales, Niels Gregersen, Sven Höfling, Christian Schneider, and Ana Predojević. Time-bin entangled photon pairs from quantum dots embedded in a self-aligned cavity. *Opt. Express*, 29(3): 4174–4180, Feb 2021. doi: 10.1364/OE.411021. URL http://www.opticsexpress.org/abstract.cfm?URI=oe-29-3-4174.

[87] Mikael Afzelius, Christoph Simon, Hugues de Riedmatten, and Nicolas Gisin. Multimode quantum memory based on atomic frequency combs. *Phys. Rev. A*, 79:052329, May 2009. doi: 10.1103/PhysRevA.79.052329. URL https://link.aps.org/doi/10.1103/PhysRevA.79.052329.

[88] Valérian Thiel, Alex O. C. Davis, Ke Sun, Peru D'Ornellas, Xian-Min Jin, and Brian J. Smith. Single-photon characterization by two-photon spectral interferometry. *Opt. Express*, 28(13):19315–19324, Jun 2020. doi: 10.1364/OE.396960. URL http://opg.optica.org/oe/abstract.cfm?URI=oe-28-13-19315.

[89] Wojciech Wasilewski, Piotr Kolenderski, and Robert Frankowski. Spectral density matrix of a single photon measured. *Phys. Rev. Lett.*, 99:123601, Sep 2007. doi: 10.1103/PhysRevLett.99.123601. URL https://link.aps.org/doi/10.1103/PhysRevLett.99.123601.

[90] S. P. Walborn, A. N. de Oliveira, S. Pádua, and C. H. Monken. Multimode hong-ou-mandel interference. *Phys. Rev. Lett.*, 90:143601, Apr 2003. doi: 10.1103/PhysRevLett.90.143601. URL https://link.aps.org/doi/10.1103/PhysRevLett.90.143601.

[91] Otfried Gühne and Géza Tóth. Entanglement detection. *Physics Reports*, 474 (1):1–75, 2009. ISSN 0370-1573. doi: https://doi.org/10.1016/j.physrep.2009.02.004. URL https://www.sciencedirect.com/science/article/pii/S0370157309000623.

[92] Palaiseau France) Aspect, Alain (Universite Paris-Saclay. Closing the Door on Einstein and. *Physics*, 8(December), 2015. URL http://physics.aps.org/articles/v8/123.

[93] J. Nunn, L. J. Wright, C. Söller, L. Zhang, I. A. Walmsley, and B. J. Smith. Large-alphabet time-frequency entangled quantum key distribution by means of time-to-frequency conversion. *Optics Express*, 21(13):15959, 2013. ISSN 1094-4087. doi: 10.1364/OE.21.015959. URL https://www.osapublishing.org/oe/abstract.cfm?uri=oe-21-13-15959.

[94] Frank Schlawin and Andreas Buchleitner. Theory of coherent control with quantum light. *New Journal of Physics*, 19(1):013009, jan 2017. doi: 10.1088/1367-2630/aa55ec. URL https://doi.org/10.1088/1367-2630/aa55ec.

[95] Barak Dayan. Theory of two-photon interactions with broadband down-converted light and entangled photons. *Physical Review A - Atomic, Molecular, and Optical Physics*, 76(4):043813, 2007. ISSN 10502947. doi: 10.1103/PhysRevA.76.043813.

[96] Quntao Zhuang, Zheshen Zhang, and Jeffrey H. Shapiro. Entanglement-enhanced lidars for simultaneous range and velocity measurements. *Physical Review A*, 96(4):1–6, 2017. ISSN 24699934. doi: 10.1103/PhysRevA.96.040304.

[97] Charles H Bennett, David P. DiVincenzo, Christopher A Fuchs, Tal Mor, Eric Rains, Peter W Shor, John A Smolin, and William K Wootters. Quantum nonlocality without entanglement. *Physical Review A - Atomic, Molecular, and Optical Physics*, 59(2):1070–1091, 1999. ISSN 10941622. doi: 10.1103/PhysRevA.59.1070.

[98] Charles H. Bennett, David P. DiVincenzo, Peter W. Shor, John A. Smolin, Barbara M. Terhal, and William K. Wootters. Remote state preparation. *Physical Review Letters*, 87(7):77902–1–77902–4, 2001. ISSN 10797114. doi: 10.1103/PhysRevLett.87.077902.

[99] Nicolas Sangouard, Bruno Sanguinetti, Noé Curtz, Nicolas Gisin, Rob Thew, and Hugo Zbinden. Faithful entanglement swapping based on sum-frequency generation. *Physical Review Letters*, 106(12):1–4, 2011. ISSN 00319007. doi: 10.1103/PhysRevLett.106.120403.

[100] Barak Dayan, Avi Pe'er, Asher A Friesem, and Yaron Silberberg. Nonlinear Interactions with an Ultrahigh Flux of Broadband Entangled Photons. *Physical Review Letters*, 94(4):043602, feb 2005. ISSN 0031-9007. doi: 10.1103/PhysRevLett.94.043602. URL https://link.aps.org/doi/10.1103/PhysRevLett.94.043602.

[101] Vahid Ansari, John M Donohue, Markus Allgaier, Linda Sansoni, Benjamin Brecht, Jonathan Roslund, Nicolas Treps, Georg Harder, and Christine Silberhorn. Tomography and Purification of the Temporal-Mode Structure of Quantum Light. *Physical Review Letters*, 120(21):213601, 2018. ISSN 1079-7114. doi: 10.1103/PhysRevLett.120.213601. URL https://doi.org/10.1103/PhysRevLett.120.213601.

[102] G. Daniel Jimenez, Veneranda G. Garces, and Kevin A. O'Donnell. Coherent reconstruction of pump beams through recombination of entangled photon pairs. *Phys. Rev. A*, 99:023853, Feb 2019. doi: 10.1103/PhysRevA.99.023853. URL https://link.aps.org/doi/10.1103/PhysRevA.99.023853.

[103] Marc Olivier Renou, Jedrzej Kaniewski, and Nicolas Brunner. Self-Testing Entangled Measurements in Quantum Networks. *Physical Review Letters*, 121(25):250507, 2018. ISSN 10797114. doi: 10.1103/PhysRevLett.121.250507.

[104] S. N. Molotkov. Quantum teleportation of a single-photon wave packet. *Physics Letters, Section A: General, Atomic and Solid State Physics*, 245(5): 339–344, 1998. ISSN 03759601. doi: 10.1016/S0375-9601(98)00423-X.

[105] S. P. Walborn, D. S. Ether, R. L. de Matos Filho, and N. Zagury. Quantum teleportation of the angular spectrum of a single-photon field. *Physical Review A - Atomic, Molecular, and Optical Physics*, 76(3):033801, 2007. ISSN 10502947. doi: 10.1103/PhysRevA.76.033801.

[106] S. Parker, S. Bose, and M. B. Plenio. Entanglement quantification and purification in continuous-variable systems. *Phys. Rev. A*, 61:032305, Feb 2000. doi: 10.1103/PhysRevA.61.032305. URL https://link.aps.org/doi/10.1103/PhysRevA.61.032305.

[107] Dashiell L. P. Vitullo, M. G. Raymer, B. J. Smith, Michał Karpiński, L. Mejling, and K. Rottwitt. Entanglement swapping for generation of heralded time-frequency-entangled photon pairs. *Physical Review A - Atomic, Molecular, and Optical Physics*, 98:023836, Aug 2018. doi: 10.1103/PhysRevA.98.023836. URL https://link.aps.org/doi/10.1103/PhysRevA.98.023836.

[108] Tiemo Landes, Michael G. Raymer, Markus Allgaier, Sofiane Merkouche, Brian J. Smith, and Andrew H. Marcus. Quantifying the enhancement of two-photon absorption due to spectral-temporal entanglement. *Opt. Express*, 29(13):20022–20033, Jun 2021. doi: 10.1364/OE.422544. URL http://opg.optica.org/oe/abstract.cfm?URI=oe-29-13-20022.

[109] Vahid Ansari, John M. Donohue, Markus Allgaier, Linda Sansoni, Benjamin Brecht, Jonathan Roslund, Nicolas Treps, Georg Harder, and Christine Silberhorn. Tomography and purification of the temporal-mode structure of quantum light. *Phys. Rev. Lett.*, 120:213601, May 2018. doi: 10.1103/PhysRevLett.120.213601. URL https://link.aps.org/doi/10.1103/PhysRevLett.120.213601.

[110] M. J. Collett and R. Loudon. Output properties of parametric amplifiers in cavities. *J. Opt. Soc. Am. B*, 4(10):1525–1534, Oct 1987. doi: 10.1364/JOSAB.4.001525. URL http://opg.optica.org/josab/abstract.cfm?URI=josab-4-10-1525.

[111] Rodney Loudon. *The quantum theory of light*. Oxford University Press, Oxford, 2010.

[112] Andrew M. Weiner. *Ultrafast-Pulse Measurement Methods*. John Wiley Sons, Ltd, 2009. ISBN 9780470473467. doi: https://doi.org/10.1002/9780470473467.ch3. URL https://onlinelibrary.wiley.com/doi/abs/10.1002/9780470473467.ch3.

[113] T. Binhammer, E. Rittweger, R. Ell, F.X. Kartner, and U. Morgner. Prism-based pulse shaper for octave spanning spectra. *IEEE Journal of Quantum Electronics*, 41(12):1552–1557, 2005. doi: 10.1109/JQE.2005.858781.

[114] Tiemo Landes, Markus Allgaier, Sofiane Merkouche, Brian J. Smith, Andrew H. Marcus, and Michael G. Raymer. Experimental feasibility of molecular two-photon absorption with isolated time-frequency-entangled photon pairs. *Phys. Rev. Research*, 3:033154, Aug 2021. doi: 10.1103/PhysRevResearch.3.033154. URL https://link.aps.org/doi/10.1103/PhysRevResearch.3.033154.

[115] Claudia Wagenknecht, Che-Ming Li, Andreas Reingruber, Xiao-Hui Bao, Alexander Goebel, Yu-Ao Chen, Qiang Zhang, Kai Chen, and Jian-Wei Pan. Experimental demonstration of a heralded entanglement source. *Nature Photonics*, 4(8):549–552, 2010. ISSN 1749-4885. doi: 10.1038/nphoton.2010.123. URL http://www.nature.com/doifinder/10.1038/nphoton.2010.123.

[116] Alex O. C. Davis, Valérian Thiel, and Brian J. Smith. Measuring the quantum state of a photon pair entangled in frequency and time. *Optica*, 7 (10):1317–1322, Oct 2020. doi: 10.1364/OPTICA.396933. URL http://www.osapublishing.org/optica/abstract.cfm?URI=optica-7-10-1317.

[117] Oriol Pietx-Casas, Gustavo Castro do Amaral, Tanmoy Chakraborty, Remon Berrevoets, Thomas Middelburg, Joshua A. Slater, and Wolfgang Tittel. Spectrally multiplexed hong-ou-mandel interference. 2021. URL http://arxiv.org/abs/2111.13610.